X-ray Evolution of Supernova Remnants in the Large Magellanic Cloud

Master's Thesis in Physics

Presented by

Vaibhav Shukla

on

30.11.2024

Dr. Karl Remeis-Sternwarte Bamberg
Erlangen Centre for Astroparticle Physics
Friedrich-Alexander-Universität Erlangen-Nürnberg

Supervised by

Prof. Dr. Manami Sasaki

Abstract

X-ray Evolution of MCSNRs

Supernovae (SNe) are extreme astrophysical events at the evolutionary end of massive stars and accreting white dwarfs. The explosion (*core-collapse* or *thermonuclear/Type Ia*, respectively) enriches the interstellar medium (ISM) with energy $\sim 10^{51}$erg and stellar matter: ejected in a forward shock as an expanding shell of hot gas/plasma. This extended structure forms a supernova remnant (SNR), with a *shell*, *plerion*, *composite*, or *mixed* morphology. X-rays ($\sim 0.2 - 5$ keV) are emitted from shock-heated ejecta-CSM interactions. SNRs, observed in X-rays, provide an important diagnostic tool to study various aspects of the local population of SNe: nucleosynthesis yields, explosion asymmetries, shock acceleration and CSM (circumstellar medium) properties.

Our galactic neighbor, Large Magellanic Cloud (LMC) harbors a rich population of SNRs, offering ample opportunities for both compilation and statistical studies on the population. Numerous multiwavelength (radio, optical, X-ray) surveys have left *candidate* SNRs, objects which need additional verification. We examine one such (optical) candidate, J0500-6512 in the LMC, and perform X-ray imaging and spectral analysis, following the observation (PI: Manami Sasaki) with XMM-Newton. The plasma properties derived from explicit spectral fitting of the source and instrumental/astrophysical background components correspond to typical old SNRs in the LMC. Combined with MCELS Hα images, this optical candidate is thus confirmed as a new MCSNR.

Estimating evolutionary epoch of SNRs requires (analytical or numerical) modeling. We find that the standard Sedov-Taylor (ST) model suitable for the II phase of evolution, fails for older remnants in the radiative phase. Therefore, there are some specific models for different phases and some general models with unified solutions. Further, a Python "calculator" for modeling complete SNR evolution exists, by Leahy & Williams [2017]. An adapted version of this code (called SNRpy) is employed in this study. A set of SN explosion and CSM parameters are taken as input for the software to calculate a consistent & continuous, spherically-symmetric SNR evolution with output (forward and reverse) shock radius, velocity, temperatures, emission measures (EMs), phase transition times, etc. in a graphical interface. We first implement the program to verify calculations of the underlying analytical models of Truelove & McKee [1999], Cioffi et al. [1988] and Cox & Anderson [1982]. We then come to back to characterize the evolutionary state of MCSNR J0500-6512, contrasting it from the pure-ST estimates. Later, we follow the work of Leahy [2017] who used SNRpy-like models to derive ages, explosion energies and CSM densities of a set of 50 SNRs based on their X-ray size, temperature and EM. We verify their results, and discuss the role of ISM on SNR evolution. Similar analysis with a newer set of 8 MCSNRs is also presented in that context.

The almost *complete* sample of SNRs in the LMC, following the works of Maggi et al. [2016], Bozzetto et al. [2017],..., Zangrandi et al. [2024] is later exploited to undertake statistical studies to derive global properties of the MCSNR population as a whole. Having compiled the latest and most exhaustive list of confirmed and candidate SNRs in the LMC, we study their size distributions and spherical symmetry using probabilistic methods of maximum-likelihood and kernel smoothing. We also explore the (in)dependence of age and size on each other and on other parameters such as the ambient medium density. The results and conclusions of the analyses are presented in their respective places.

Part I of this Thesis is the theoretical primer on SNRs: reviews the current state of knowledge about their origins, characteristics, classification, population and evolution, detailing various hydrodynamical phenomena involved and the models to explain them. Further, X-ray emission from shock-heated and synchrotron-accelerated hot plasma in SNRs is discussed in the light of high-resolution imaging spectroscopy with XMM-Newton, elucidating X-ray optics, telescopy, imaging and background modeling. In Part II, I describe the methods and results of analysis: i) on X-ray data of the XMM observation of J0500-6512 using Extended Source Analysis Software package of the Science Analysis System (XMM-ESAS), and XSPEC for spectral fitting; ii) with SNRpy; and iii) statistical methods. A summary of the qualitative and quantitative results is placed in the end, along with an outlook on future work.

Contents

List of Acronyms

1D one-dimensional
2D two-dimensional
3D three-dimensional

AGN active galactic nucleus
AMISE asymptotic mean integrated square error
AXB astrophysical X-ray background

BH black hole
BIMSE bootstrap integrated mean squared error

CCD charge-coupled device
CCO compact central object
CCSN core-collapse supernova
CIE collisional ionization equilibrium
CNM cold neutral medium
CSM circumstellar medium
CXB cosmic X-ray background

DTD delay time distribution

ED ejecta-dominated
EM emission measure

FOV field-of-view
FWHM full width at half-maximum
FX fluorescent X-rays

GRB gamma-ray burst
GTI good-time-interval

HIM hot ionized medium
HN hypernova

IGM intergalactic medium
IR infrared
ISM interstellar medium
ISMa interstellar matter

KDE kernel density estimate

LHB Local Hot Bubble
LMC Large Magellanic Cloud
LoS line-of-sight

MC Magellanic Cloud
MCS momentum-conservation shell
MHD magnetohydrodynamic
MISE mean integrated square error
MOS metal-oxide semiconductor
MW Milky Way

NEI non-equilibrium ionization
NS neutron star

OoT out-of-time

PDF probability density function
PDS pressure-driven "snowplow"
PIC particle-in-cell
PISN pair-instability supernova
PSF point spread function
PWN pulsar wind nebula

ROI region of interest
RRC radiative recombination continuum

SFH star formation history
SMC Small Magellanic Cloud
SN supernova
SNR supernova remnant
ST Sedov-Taylor

TNSN thermonuclear supernova

UV ultraviolet

VLBI very long baseline interferometry

WD white dwarf
WIM warm ionized medium
WNM warm neutral medium

List of Figures

List of Tables

Part I

Review

Chapter 1

Introduction

Our universe is made up of stars, matter that make up the stars, matter that the stars make and dark matter, clumped together by gravity into galaxies which are drifting away from each other in an expanding space-time accelerated by dark energy. The universe is "all that is or was or ever will be" [Sagan 1980], but the observable universe is finite in size and age. Its origin lies in an 'explosive expansion', called the Big Bang, some 13.8 billion years ago, of an extremely hot and infinitely dense core containing all the matter and energy in existence. A few-hundredth-years-old universe consisted of elementary particles like electrons, neutrinos, photons and quarks that coupled in triads to form some protons and neutrons. The temperature was 10^{11} K and density $\sim 4 \times 10^9$ cm^{-3}, so that particles and antiparticles were created out of pure energy and annihilated again. Only at the end of the first three minutes was the universe cool enough (10^9 K) for hydrogen (H) and helium (He) nuclei to form, and only after a few 100,000 years were H and He atoms (with electrons) formed. [Weinberg 1977]. The coalescence of this gas under gravity would then form the stars, galaxies and structures that we see in the universe, including ourselves.

This Thesis addresses the matter-energy in-between the stars of a galaxy, the interstellar medium (§1.1). We start with a description of its crucial role in lifecycle of stars and ecosystem of galaxies like our own, the Milky Way Galaxy (§1.1.1). Notably, the death of some stars injects some of stellar matter and all of gravitational-binding energy back into the medium in a momentary burst, a supernova (SN) explosion. Multiple such explosions are thought to regulate the multi-phase occurrence of the interstellar matter (§1.1.2), discussed in §1.1.2.1. Moreover, the astrophysical impact of supernovae on the ambient medium is in form of hydrodynamic shocks and electromagnetic radiation (§1.1.3). The first interaction of ejected shock-heated plasma with the circumstellar medium a expanding structure, the supernova remnant (SNR). These beautiful objects emit light in wavelengths from radio to optical to X-rays from thermal and non-thermal processes, possibly Fermi acceleration of cosmic rays! Thus, they are quintessential targets of multimessenger astronomy (§1.2).

My aim is to present a dynamic picture of supernova remnants, evolving from their explosive origins, traced by X-rays and analytical models. Following this introduction (§1), we review supernovae (§2), the origin of SNRs (§3), before delving into the processes responsible for their hydrodynamic evolution (§4). The X-ray emission processes and detection methods are broadly discussed in §5 in light of modern observatories capable of high-resolution imaging and spectroscopy of SNRs. This concludes the "Review" part of this Thesis. In "Research", in §6, we present the analysis of X-ray data of a particular extended source J0500–6512 observed with the *XMM-Newton* satellite, discussing the instrument and data reduction procedures, and deriving some results from the images and spectral fits. This is followed by evolutionary analysis

(§7) of not a single but a population of SNRs. A summary of the written work and outlook on future work is presented in §8. (The loophole that I exploit in this binary division of content is that any review involves some *research*, and no research can be done without a *review* of existing literature.) Supplementary material which is outsized or unfit for the flow of main content is attached in Appendix §A.

1.1 Interstellar Medium

The interstellar medium (ISM) of our Galaxy or the intergalactic medium (IGM) between galaxies, is the gas and dust, along with cosmic rays and magnetic fields, intertwined by electromagnetic and gravitational forces, that inhomogenously permeates the space between the stars in form of clouds or diffused [Ferrière 2001; Draine 2011]. Stars are embedded in this extremely tenuous medium, from their birth in molecular clouds to their demise as SNRs. The interstellar space is nowhere a vacuum, although the densities of interstellar matter (ISMa) amount to just few atoms per cm^3 up to $\sim 10^6$ cm^{-3}, which are negligible compared to Earth's atmosphere's $\sim 2 \times 10^{18}$ cm^{-3} [Dopita & Sutherland 2003].

Arguably the most beautiful part of the visible universe, ISM is crucial to galactic evolution. The interstellar gas, and more so, dust is often considered a nuisance due to its absorption and extinction effects in foreground along a line-of-sight (LoS). Conversely, ISM is manifested and characterized by obscuration, reddening and absorption lines in stellar spectra, as well as polarization of starlight, and through various emission mechanisms. ISMa is mostly observed in X-rays, ultraviolet (UV), optical, infrared (IR) and radio wavelengths.

1.1.1 Galactic Ecology

ISM is not just a passive substrate for stellar evolution but a vital partner in the galactic ecosystem. Interstellar gas is predominantly H and He. Currently, the elemental abundances of the ISM in the Milky Way (MW) are approximated by solar values. For example, around 70.4% of the ISM gas mass should be hydrogen (H), out of which 60% is neutral (HI), 23% is ionized (HII) and 17% is molecular (H_2), 28.1% of helium (He), and only 1.5% of rest of the elements [Ferrière 2001]. But, neithe r the composition nor distribution of the ISM is constant in time and space.

In the history of Universe, we can expect a point where most of the baryonic[1] matter was in form of "interstellar" gas, accumulation of which would subsequently lead to gravitational collapse in the densest regions (molecular clouds), i.e. star formation. Matter is locked in stars for millions or billions of years, before being released back to the ISM. This stellar feedback could be continuous as stellar winds, or sudden as supernovae. The fractional injection of stellar mass back to the ISM enriches the surrounding with heavier elements ("metals") synthesized inside the stars during or around the end of its lifetime. Some stars, quietly or explosively, shrink to a compact object, white dwarf (WD), neutron star (NS), or a black hole (BH) depending on their mass and metallicity (see §2.2.2).

Stars also inject energy in the ISM in form of (mostly UV) photons, a product of nuclear burning during their lifetimes, and then terminally from the kinetics of the ejecta from SNe (which are also known accelerators of cosmic rays). The ISM cools by radiating the photons away to the IGM. This cycle of mass and energy between the ISM and stars in the Galaxy is sketched in Fig. 1.1. Overall, the ISM is not in thermodynamic equilibrium. [Draine 2011]

[1] or, 'ordinary', as opposed to 'dark', matter: protons & neutrons, and including (leptonic) electrons

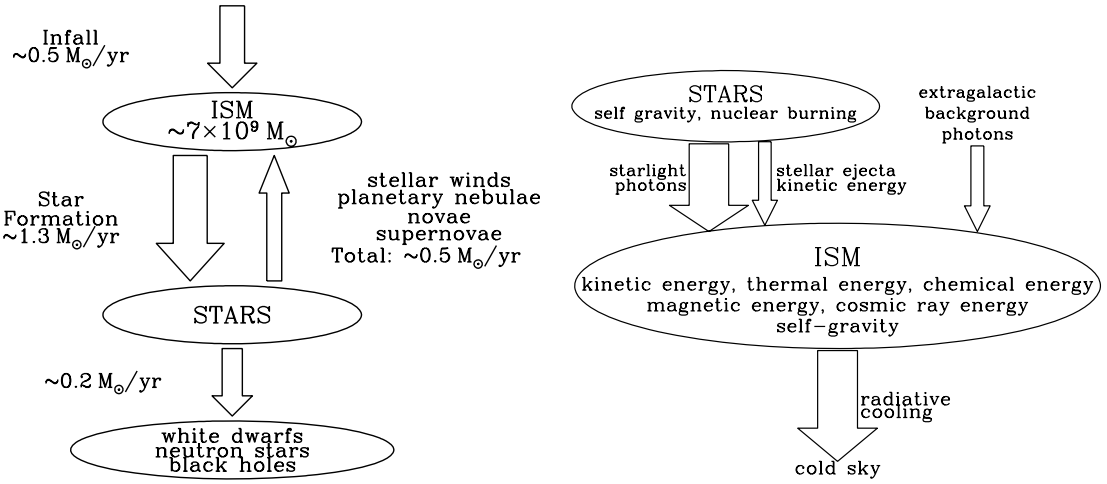

Figure 1.1: Flow of matter (**left**) and energy (**right**) in the Milky Way, a star-forming Galaxy with only ∼10% baryons in the ISM [Draine 2011]. Stellar winds and supernovae play a key role.

1.1.2 Multi-Phased Model

The main components that constitute the ISM are interstellar gas (atoms, molecules, ions, electrons), interstellar dust (tiny solid particles < 1 μm) and cosmic rays (relativistic charged particles, mostly protons & nuclei, and electrons & γ-photons). Further, electromagnetic radiation, e.g., from stars, heated gas & dust and the cosmic background, interstellar magnetic field and gravitational fields permeate the rest of the interstellar space. Galaxies are also known to host copious amounts of dark matter [e.g., Salucci 2019].

The interactions of these different components with each other and with neighboring stars result in a dynamic ISM. Events like stellar winds, supernova shock waves, magnetic fields and fast-moving charged particles add turbulence, heat, pressure, etc. ISMa thus spans a wide range of temperatures and densities. But we find that, we can categorize it into a few characteristic states or *phases*. First, a half of ISMa, by mass or number, exists as discrete clouds. These are relatively compact and occupy only 1-2% of the interstellar volume. These could be *dark clouds* of very cold ($\sim 10 - 20$ K) molecular gas, *diffuse clouds* of cold (~ 100 K) atomic gas or *translucent clouds* of both molecular and atomic gases with intermediate densities, temperatures and absorption. The rest of the ISMa is spread out in-between and is referred as the diffuse medium. [see Ferrière 2001, for a review]. This pervasive interstellar gas, which is often synonymous with ISM, is theorized and observed to exist in three phases: cold (neutral), warm (neutral or ionized), and hot (ionized) medium [Heiles & Kulkarni 1987]. The molecular clouds may be considered to consist of the cold, otherwise diffuse, gas, or as a separate (molecular) medium. And, interstellar dust, condensed molecular matter, is different altogether.

1.1.2.1 Three-Phase Model

The three-phase model for the ISM was developed by McKee & Ostriker [1977] by extending the two-phase model [Field et al. 1969] with active feedback from supernovae. In this theoretical approximation, most of the interstellar volume is occupied by a hot low-density medium, with discrete cold clouds dispersed through it. A SN blastwave propagates rapidly in this hot ionized medium (HIM). As the shocked gas cools, the cold neutral medium (CNM) is formed. Then, soft X-rays produced by the HIM penetrate the CNM clouds, heating the gas to form the "intercloud" warm neutral medium (WNM). The warm ionized medium (WIM) is formed from photo-ionization of this gas by hot young stars. The arguments are based on thermal

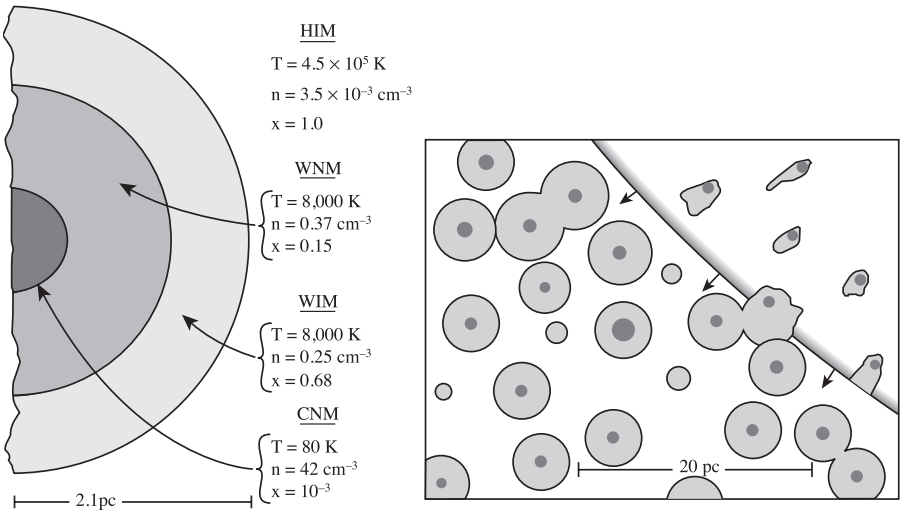

Figure 1.2: Illustration of the the three-phase model of McKee & Ostriker [1977], with typical temperature, density and scale of different phases, taken from Draine [2011]. On the **right**, we have a zoom-in on a SNR blast wave.

pressure equilibrium between different ISM phases, maintained by SNe: if ISM has initially a low pressure, SNRs would would overlap before they can fade away. The structure of this composite multiphase ISM created and regulated by SNRs is illustrated in Fig. 1.2, while the characteristics of the different phases is paragraphed below with the numbers representative of Galactic (MW) ISM from Dopita & Sutherland [2003].

Cold The cold phase of the interstellar medium consists of the molecular medium and the cold neutral medium. The molecular medium is an accumulation of molecular gas into discrete molecular clouds, which are very cold ($\sim$20 K) and very dense ($>10^3$ cm^{-3}), such as the dark clouds. This 'sub-phase' occupies the smallest fraction of volume ($\sim$1%), but a substantial mass ($\sim$30-60%) of the ISM. The diffuse component, CNM is cold, (mostly) neutral, atomic gas (HI), in form of dense sheets or filaments or diffuse clouds, with temperatures $\sim$100 K and densities $\sim$20-60 cm^{-3}. It is around 1-4% of the total volume. The cold phase is crucial to star formation.

Warm The warm "intercloud" medium, with $T\sim10^4$ K, consists of a neutral and an ionized component which are in pressure equilibrium. WNM has $T\sim$6000 K and $n\sim$0.3 cm^{-3}, and occupies a significant $\sim$30-40% of the volume, traced by the HI 21-cm emission line. This is in contradiction to the McKee & Ostriker [1977] model prediction of only 4.3% mass, a major shortcoming. Around 20% of the warm phase is partially ionized, primarily by the photoionizing UV radiation from hot young or massive (O & B) stars. This WIM is associated with HII regions, which are hotter ($T\sim$6000-12000 K) and denser ($n\gtrsim1$ cm^{-3}), but only occupy $\sim$2-4% of the total ISM volume.

Hot The hot phase is sparse plasma ($T\gtrsim10^6$ K, $n<0.01$ cm^{-3}) heated and ionized by strong shocks and radiation (§1.1.3) from stellar winds and explosions. HIM fills the interiors of SNRs and powers their blastwaves. Intrinsically thermally unstable, the gas in this phase cools via thermal conduction and emits soft ($\sim$0.1-2 keV) X-rays.

1.1.3 Shocks and Radiation

Shocks arise when matter moves faster than the local signal speed, particularly the speed of sound in the medium, or conversely when a supersonic fluid is obstructed. This creates ex-

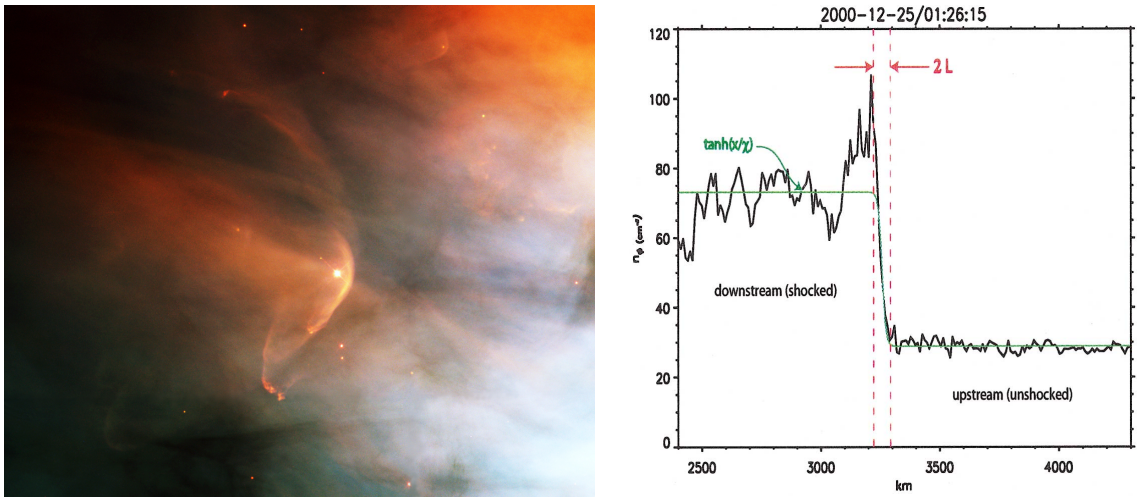

Figure 1.3: **Left**: Bow shock from 'collision' of wind from a young star, LL Ori, and the flow of Orion nebula [NASA/STScI/AURA]. **Right**: Bow shock transition of Earth, measured by ESA's Cluster II satellites [Bale et al. 2003]. The sharp density jump post-shock shows the narrowness of collisionless shocks.

treme discontinuities in the properties of the medium/flow called *shock waves* which compress and heat (gaseous) matter as they propagate. They can also accelerate particles to high energies. Further, shock heating and particle acceleration leads to emission of thermal and non-thermal radiation. Fig. 1.3 shows two examples of shocks, due to stellar (or solar) winds hindered by the ISMa (or a planet, Earth). The diagram on the right shows the discontinuity region across a shock, and how thin it could be.

Astrophysical shocks are abundant. These shocks in the interstellar medium are characterized by low densities $\sim 1\ \mathrm{cm}^{-3}$, which means that the heating cannot be accomplished by (Coulomb) particle-particle interactions, and are hence called *collisionless shocks* (see §4.1). Interstellar shocks are mostly produced by stars [McKee & Hollenbach 1980]. These could be from stellar winds creating bubbles in the interstellar gas, especially from hot & massive young, OB-type, Wolf-Rayet stars. By far, the strongest shocks are caused by supernovae. The interaction of energetic SN ejecta with the surrounding ISM forms a supernova remnant. We observe this as emission from the shock-heated plasma in X-rays, non-thermal synchrotron radiation from electrons accelerated at the shock-front in radio, and later in optical from cooled material. But, this is not the case for most (non-relativistic) collisionless shocks. The paradigm of such shocks are those in the heliosphere. These are the shocks from solar flares, coronal mass ejections, solar wind, etc. like the planetary or cometary bow shocks, interplanetary shocks and the solar termination shock. Although, most of these shocks do emit radio radiation at the local plasma frequency, it is energetically negligible, making them essentially 'dark shocks'. [Treumann 2009]. Thus, SNR shocks are special, in the sense that they emit, not just in one but *multiwavelength* regions. A number of hydrodynamic, thermodynamic and electromagnetic phenomena behind these emissions are discussed in §4.1, §4.2 and §5.1.

1.2 Multimessenger Astronomy

Science is a collaborative enterprise, astronomy more so. It humbles us to think of humanity as a whole, to ponder upon our existence on this "pale blue dot". The space is so vast and mostly empty that information is scarce. We need signals in as many forms as possible to understand

the astrophysical processes. Modern telescopes can pierce deep into the observable universe, not just in visible light but across the entire electromagnetic spectrum from radio waves to gamma-rays. More recently, the photons are complemented with observations of neutrinos, cosmic rays and gravitational waves. These are the 4 'messengers' of modern astronomy [Filipović & Tothill 2021]. Multiwavelength (or multifrequency) astronomy is thus a subset of the contemporary multimessenger astronomy.

The electromagnetic spectrum is divided into regions (of frequency): γ-ray (> 3 EHz), X-ray (30 EHz–30 PHz), ultraviolet (UV, 30 PHz–750 THz), optical (750 THz–430 THz), infrared (IR, 430 THz–3 THz), submillimeter (3 THz–300 GHz), microwave (300 GHz–3 GHz), and radio (< 3 GHz), based on the emission mechanisms that generate the radiation, the detection methods, or the spectral range allowed through the Earth's atmosphere [Filipović & Tothill 2021]. As varied as the ISM is, conditions for emission of virtually all kinds of radiation exist somewhere. The different phases emit and are observed in different wavebands [e.g., Draine 2011]:

- Dust is typically observed in the far-IR region due to its thermal emission.
- Molecules (like H_2, CO) are detected in the radio (e.g., the 2.6-mm CO line) and infrared wavebands, where their rotational and vibrational transitions fall.
- Cold and warm neutral media (HI) are primarily observed in the radio HI 21-cm line, and also in optical and UV absorption lines.
- HII regions are characterized by thermal radio continuum and optical line emissions.
- The hot ionized phase (coronal gas) is mainly studied through UV and X-ray emissions.

SNR plasmas, often in non-equilibrium ionization, show spectra dominated by continuum emission of X-rays via thermal bremsstrahlung and of radio synchrotron radiation (see §5.1). There is also line emission associated with electron-ion collisional excitation and recombination, especially from Fe K- and L-shell transitions. As their shock subdues and coronal plasmas cool with the adiabatic expansion and thermal X-ray emission, SNRs radiate in optical, particularly Hα lines and forbidden lines from N, O and S. Moreover, SNe emit most of their energy in form of neutrinos. Further, SNRs are connected to cosmic ray acceleration. Additionally, SNe are known creators and destroyers of dust, which helps cool SNR ejecta, and emits in infrared when heated. So, SNRs are true multimessenger sources. But, we focus on the X-ray properties of SNRs in this work.

1.2.1 X-ray Astronomy

X-ray astronomy is the study of electromagnetic radiation with energies 0.2–100 keV from extrasolar sources. We aim to determine the intensity, spectrum and direction of this radiation, to resolve the source to study its structure and other properties, and to study the effects of intervening ISM. Thanks to our atmosphere (Fig. 5.9), X-ray observations can only be performed with detectors flown on balloons, rockets and satellites. This adds to the existent optical constraints in focusing X-ray light (see §5.2.1). So, X-ray telescopes (§5.2.2) and other instruments must be small and rugged enough to be uplifted to space. Once up and running, the observer has to then isolate the source emission from a set of X-ray emitting and absorbing components in the LoS, the X-ray background (§5.2.4). This involves data reduction and analysis (as in §6.2), which will differ from the wider field of X-ray astronomical studies involving compact objects treated as "point sources". We will specifically discuss and analyze "diffuse emission" in the soft band (up to 10 keV) from extended sources (SNR plasmas), although many of the processes are fundamental to all kinds of X-ray phenomena in the Universe.

Chapter 2

Supernovae

In this chapter, we discuss the origin of supernova remnants, supernovae (SNe). Supernovae are extreme astrophysical events at the evolutionary end of (some) stars, an explosive death. The exploding star outshines the combined luminosity of its host galaxy; the peak luminosity ($\sim 10^{43}$ erg s^{-1}) exceeding that of the visible, luminous Universe! The explosion, which is either from a massive star unable to prevent gravitational collapse or white dwarfs in a thermonuclear runaway, releases $\sim 10^{53}$ erg of the gravitational "core-binding" energy and disperses stellar matter with $\sim 10^{51}$ erg of kinetic energy into the interstellar medium, leaving behind an expanding gaseous shell (SNR) possibly around a central compact object (CCO, a neutron star or a black hole). The progenitor appears as a "new star" (Latin: *nova*) from radiative heating of its photosphere, in the weeks and months to come.

Baade & Zwicky [1934] recognized that historical *novae* of this intensity were actually "supernovae" resulting from the transition of an ordinary star to a neutron star. They even suggested them likely sources of cosmic rays. As we will see in this chapter and the following, their predictions prove prophetic. We start with the history of supernova events in our Galaxy and beyond (§2.1) before discussing the SN classification scheme based on optical light-curve and spectra (2.2), and on the two fundamental explosion types (§2.2.1 and §2.2.2).

Supernovae have a strong influence on their local galactic environment, parent galaxy and even the intergalactic medium. The tumultuous events preceding the stellar explosion are known sites of synthesis of new, heavier elements. The energy and matter injected back to the interstellar environment leads to formation new, more metallic stars, to planetesimals and planets, and eventually living beings as us.

2.1 History

Historically, many civilizations observed bright "guest stars" in AD 1006, 1054, 1181. Later such events, in 1572 and 1604, named after Tycho (Brahe) and (Johannes) Kepler, were followed into their current epoch. The remnant of SN 1054 is the present-day Crab Nebula, which holds a pulsar (a fast-rotating neutron star) near its center. Another supernova, associated with the SNR Cas A, must have exploded around 1650–1680. In total, nine Galactic SNe have been observed in the history of last two millennia [Green 2002]. See Alsabti & Murdin [2017, partII] for a detailed review. The rate of occurrence of supernovae in a galaxy like our own is $\sim$2–3 per century. So, it was a pleasant surprise when the whole world observed the most recent SN 1987A in the nearby Large Magellanic Cloud, spanning the entire range of electromagnetic spectrum as well as in neutrinos! [Arnett et al. 1989]

Figure 2.1: Hubble Space Telescope image of SN 1994D (lower left) along with the galaxy NGC 4526. [Credit: NASA/ESA, The Hubble Key Project Team and The High-Z Supernova Search Team]

Systematic searches of SN events were initiated by F. Zwicky. Using Schimidt (optical) telescopes, he and his assistant J. J. Johnson, discovered nearly 20 SNe in 5 years. Based on light-curve and spectral measurements, the newly-discovered SNe were assigned to either one of the two broad *types*, discussed in §2.2. By 1990, the rate of discovery was 10–30 SNe per year, total being 700 [Bethe 1990]. Present-day *transient* monitoring programs such as iPTF[1], ASAS-SN[2], Pan-STARRS[3], and amateur astronomers are discovering several hundred SN per year. As a result, up to 2015, over 6500 SNe have been identified in external galaxies [IAU Central Bureau for Astronomical Telegrams 2015]. Fig 2.1 shows a beautiful example.

2.2 Classification

Supernovae are historically classified by their optical spectra and light-curves. The classification [due to Minkowski 1941] is based on the absence (Type **I**) or presence (Type **II**) of hydrogen (H) absorption lines in the spectrum. Type I has three subclasses (with early early-time spectra having): **Ia** (strong Si II), **Ib** (prominent He I) and **Ic** (neither Si II nor He I). Type II is divided into two distinct (photometric) subclasses: **II-L** (linear) and **II-P** (plateau) [see Filippenko 1997, and Fig. 2.3].

The optical classification scheme (shown diagrammatically in Fig. 2.2) is sliced into two broad classes based on explosion mechanisms: *thermonuclear* or *core-collapse*, i.e., the apparent

[1] `https://www.astronomerstelegram.org/?read=4807`
[2] `https://www.astronomy.ohio-state.edu/asassn/index.shtml`
[3] `http://pswww.ifa.hawaii.edu/pswww/`

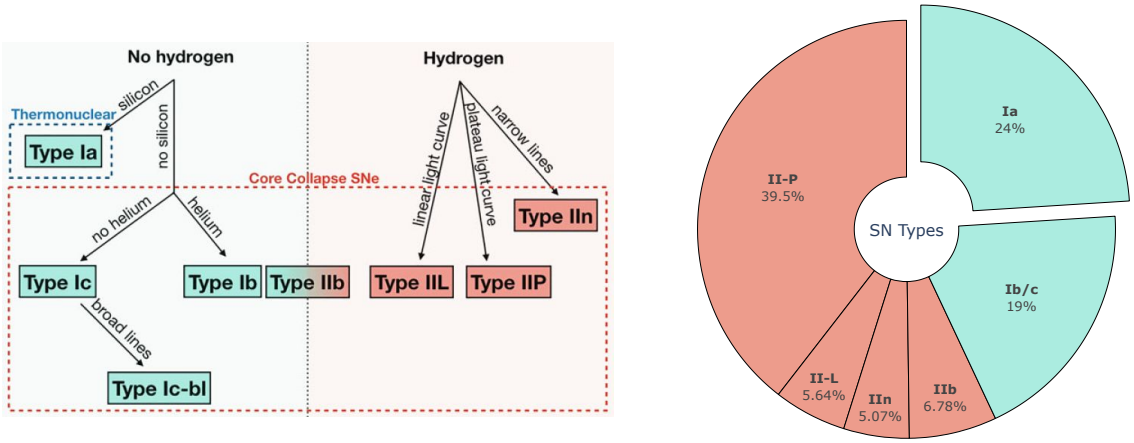

Figure 2.2: **Left**: Optical classes of SNe and two explosion mechanisms [Vink 2020]. **Right**: Fractions of SNe in different subtypes of Types I (green) and II (red) based on volume-limited observations of the nearby population by Li et al. [2011].

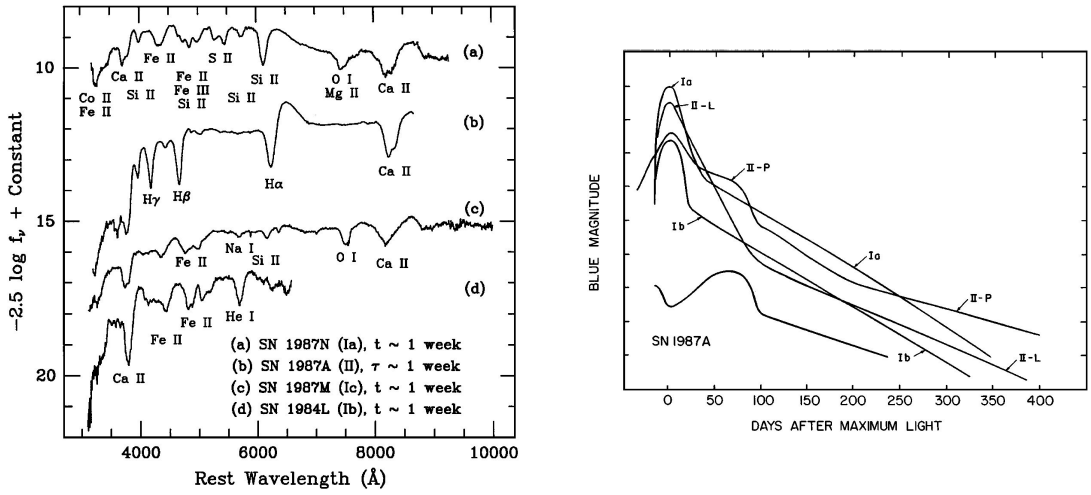

Figure 2.3: Early-time spectra and light-curves of the main SNe subtypes. t is the time after B-band maximum and τ is the time after core-collapse, both around 1 week in the spectra of observed 4 extragalactic SNe (**left**). Late-time spectra (e.g., after 5 months, not shown) and brightness evolution over time (**right**) provide further constraints for classification. [Filippenko 1997, Fig1,3]

variety across SNe spectra and photometry arises from different progenitors and environment of a thermonuclear supernova (TNSN or type Ia) or a core-collapse supernova (CCSN or types Ib, Ic, II) explosions. We discuss these below, noting that there are further subdivisions **Ibn**, **Icn**, **Ic-bl**, **IIn** depending on narrow or broad lines, and a transitional **IIb**. Plus, there is another supernova mechanism, the *pair-instability* supernova (PISN).

Thermonuclear supernovae (TNSNe) and pair-instability supernovae (PISNe) leave no stellar remnant, while core-collapse supernovae (CCSNe) usually leave a compact object, a NS or a BH. TNSNe have their physical origin in accreting WDs, while the CCSNe and PISNe originate from dying massive stars. That is why, type Ia SNe are mostly found in old stellar populations and late-type galaxies, while type II and others are associated with star-forming regions and galaxies.

2.2.1 Type Ia Supernova

Supernova of type Ia (SN Ia), devoid of H & He but showing strong Si II lines, constitute a rather homogeneous subclass. In particular, the peak absolute magnitude correlates with the width of the light-curve (broader light-curve SNe are more luminous) and color (redder SNe are more luminous). Thus, the luminosity can be calibrated so that apparent magnitude gives distance. Also, they are intensely bright, and hence observable in farthest galaxies of the visible Universe. For these reasons, SNe Ia are used as "standard candles" to measure cosmological distances and parameters, which leads to the discovery that the expansion of the Universe in accelerating, i.e., existence of a cosmological constant (Λ) ascribed to a dark energy [Riess et al. 1998; Perlmutter et al. 1999]. Specifically, the spectral and photometric observations of high-redshift (=distant) SNe Ia show that they are fainter than expected in a matter-dominated universe. Along with other probes [Aghanim et al. 2020], these observations concord to the currently standard "ΛCDM" model of the Universe with energy density comprising 4.9% baryonic matter, 26.8% dark (gravitating) matter and 68.3% dark energy [Zyla et al. 2020].

There are still some notable variations in the light-curve shape, color and peak among members of this class. These are usually specific peculiar SN events that differ from the "regular" or (spectroscopically) normal Ia supernovae. Prominent examples of such sub-classification are SN-1991T-like, SN-1991bg-like and SN-2002cx-like events. The first subtype is mostly ascribed to very luminous Ia events, second one to substantially less luminous Ia events compared to normal SN Ia. The early-time spectra of SN-2002cx-like events (also called SN Iax) is like SN-1991T but with peak spectra similar to normal type Ia SNe. [Alsabti & Murdin 2017, Ch12]. In any case, around 70% of SN Ia are normal events [Vink 2020]. Further, one talks about "Super-Chandra" events which has to do with the progenitor explosion mechanism, which we review in general below.

2.2.1.1 Progenitors

The observed characteristics of SNe Ia—including the lack of H or He & the homogeneity across spectra, the kinetic energy of the explosion being roughly equal to energy required to disrupt a degenerate carbon-oxygen core, and the correlation to old stellar populations—point to a definite involvement of white dwarfs in the explosion process. A SN Ia is thus surmised to be the thermonuclear explosion of a white dwarf that has acquired mass close to the Chandrasekhar limit ($\approx 1.4 M_\odot$). The exact progenitor system is not yet constrained, though two scenarios of close binaries are mainly discussed: the single-degenerate [Whelan & Iben 1973] and double-degenerate [Tutukov & Yungelson 1981; Iben & Tutukov 1984; Webbink 1984] models (see Fig. 2.4 for artistic illustrations). In the former, a carbon-oxygen WD star accretes matter off a non-degenerate companion – a main sequence, a subgiant, a redgiant, or a helium star – up to the Chandrasekhar mass around which it ignites and explodes in a thermonuclear runaway. In the latter, two WDs merge in a binary spiral, losing energy and angular momentum to gravitational waves, leading to a super-Chandra object that ignites and explodes. [see reviews by Wang & Han 2012; Maoz & Mannucci 2012]. The accretion could be a Roche-lobe overflow or wind-driven. The thermonuclear reactions inside the degenerate core propagate outwards and completely disrupt the C-O WD(s), converting carbon and oxygen into iron, releasing energy $\sim 10^{51}$erg. The light-curve is mainly powered by the radioactive decay of ^{56}Ni produced. The exact explosion mechanism is uncertain, particularly regarding the propagation of the nuclear burning front or 'flame' – whether it is always supersonic (pure detonation), or transitions from subsonic (deflagration) to supersonic (detonation) [see Hillebrandt et al. 2013, and Fig. 2.5].

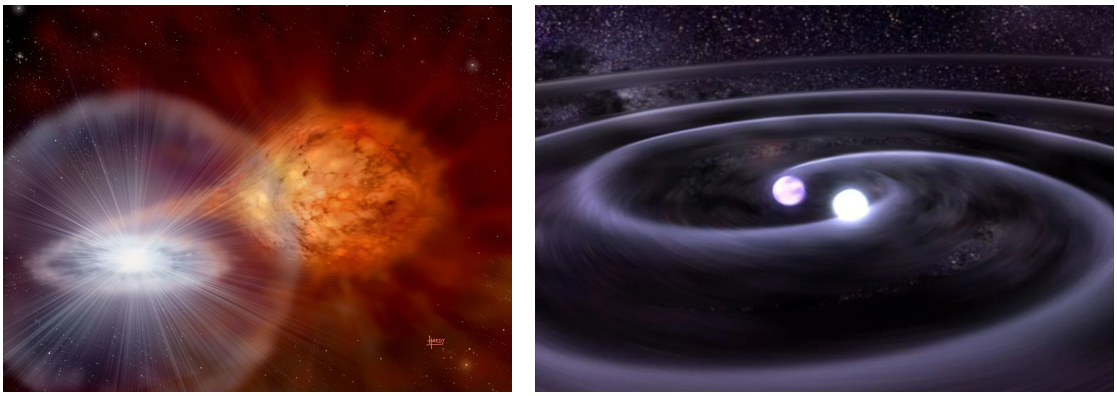

Figure 2.4: Artists' conceptions of the two main progenitor scenarios leading to a TNSN. **Left**: A WD engulfing material from a normal star [David A. Hardy & PPARC]. **Right**: A double-degenerate merger system [Tod Strohmayer (GSFC) & Dana Berry (CXC)].

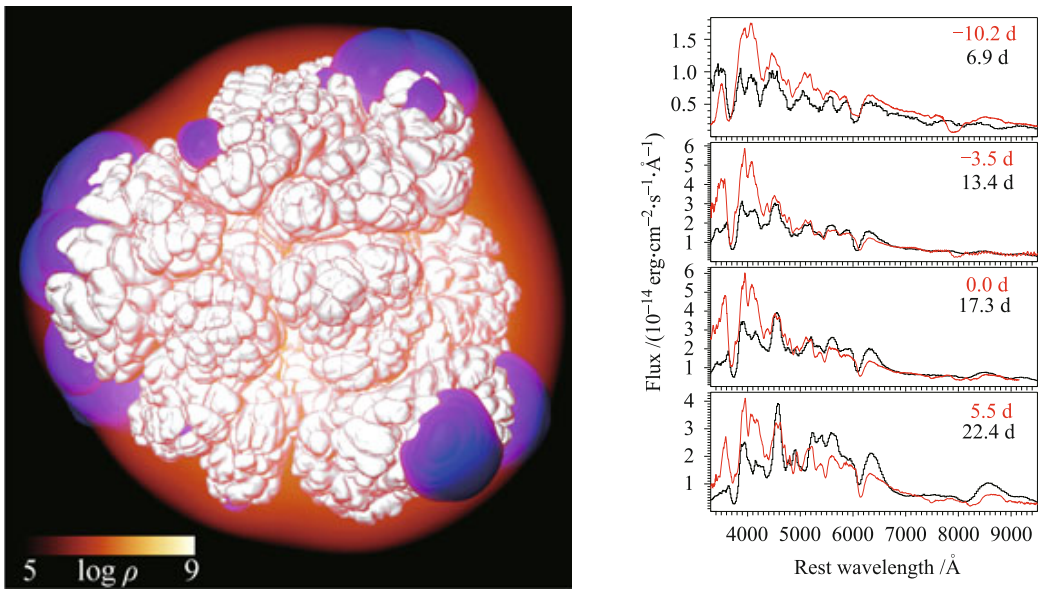

Figure 2.5: **Left**: A snapshot at 1 sec from Hillebrandt et al. [2013] hydrodynamic simulation of the so-called N100 model of a Chandrasekhar mass *delayed-detonation* 'normal' SN Ia explosion; density is in orange, deflagration levels are the white surfaces and detonation flames are in blue. **Right**: Synthetic spectra from the same simulation (black) at different epochs, reasonably reproducing the observed spectra from SN 2005cf (red).

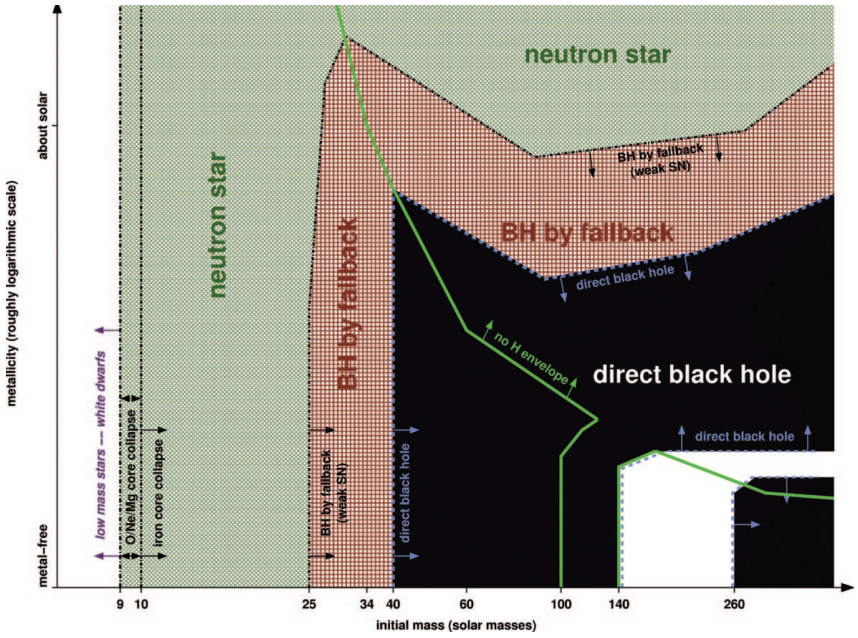

Figure 2.6: Fate of massive stars as a function of initial mass and metallicity [Heger et al. 2003].

2.2.2 Core-Collapse Supernova

Supernovae from the rest of the classes, which do not show Si lines in their spectra, i.e., SN Ib, Ic, II (marked in red in Fig. 2.2) are explosions from gravitational collapse of stellar cores. Unlike SN Ia that involve white dwarf(s), the progenitors of core-collapse supernovae are single massive stars at their evolutionary end. These are indeed the most common types of SNe, occurring only among young stellar populations and star formation regions of all galaxies.

As evident from Fig. 2.2, CCSNe show diverse spectral and photometric types. Most of them fall into one of the subtypes of II, showing hydrogen (prominently Hα) absorption and emission lines, respectively, in their early- and late-time spectra. Although, there is substantial heterogeneity in this class, most SNe II show either a linear ('L') or a plateau ('P') type light-curve in their early-time photometry. These are spectroscopically and physically related to SNe Ib/c. The absence of H (and He) in type Ib (and Ic) is arguably caused by stripping of outer hydrogen (and helium) envelope of the massive progenitor, either via stellar winds or binary interactions – these are then sometimes referred as "stripped-envelope SNe" (SESNe). This argument is supported by following SNe first classified as type II, but later morphed into hydrogen-less type Ib due to further mass-loss – such SNe are typed as IIb, e.g., SN 1993J [Vink 2020]. Then, there are also CCSNe of types IIn, Ibn, Icn and Ic-bl. The label 'n' refers to narrow ($\lesssim 200\,\mathrm{km\,s^{-1}}$) *emission* lines shown presumably from ejecta-CSM interactions. These could be H lines (SN IIn), He lines with weak or absent H lines (SN Ibn), or the narrow O and C lines but weak or absent H and He lines seen in the most recent SN Icn class [see Davis et al. 2023]. The peculiar Ic-bl type of SNe showing a blend of broad absorption lines are associated with gamma-ray bursts (GRBs) and X-ray flashes (XRFs) [Woosley & Bloom 2006]. There could be many more classes and subclasses to accommodate newly identified SNe, and new classification schemes are considered [see Alsabti & Murdin 2017, Ch.12]. What is mostly certain is the physical origin of SNe of all these types in explosion of massive stars.

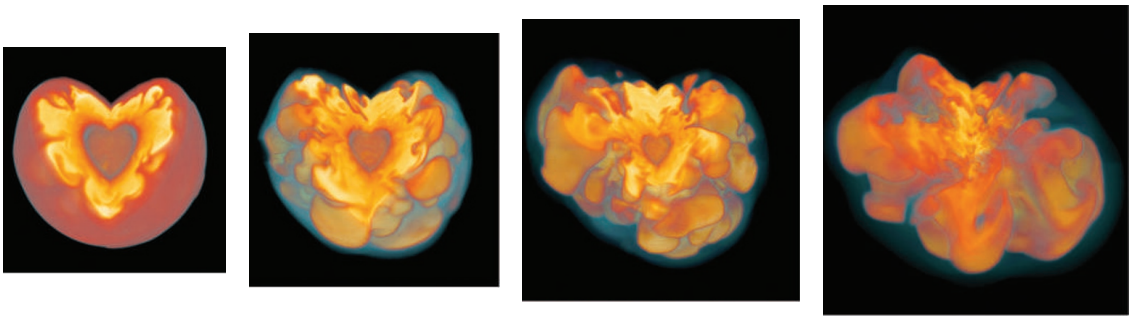

Figure 2.7: Four snapshots at times 0.1, 0.2, 0.3 and 0.5 s from a neutrino-driven, convection-aided core-collapse supernova's 3D hydrodynamic simulation. The slices show the proto-NS in the interior accreting hot matter and the effects of neutrino-heating in yellow and orange. The 'bounce' shock is shown in blue and has average radii growing as 200, 300, 500 and 2000 km, respectively, disrupting the outer material. Asphericity in the structure is apparent. [reproduced from Woosley & Janka 2005]

2.2.2.1 Explosion

A CCSN occurs when a massive star ($\gtrsim 8 M_\odot$) has passed through successive stages of H, He, C, Ne, O and Si fusion in its centre and is left with a dense Fe-rich core which collapses under its own gravity in a shock-induced explosion. The rapid contraction, aided by neutrino emissions, electron capture and photo-disintegration, is briefly & abruptly halted by neutron repulsion and the formation of a proto-NS, creating an outward ('bounce') shock wave which stalls due to accretion. Eventually, the proto-NS settles into a neutron-rich nucleus (a NS) if not crushed into a black hole, releasing energy at a rate $\sim 10^{53}$ erg s^{-1} in the process [see Woosley & Janka 2005, for details].

CCSNe are essentially neutrino-powered gravity bombs. Only $1–2 \times 10^{51}$ erg of the gravitational core-binding energy is released kinetically, while the rest is carried away by neutrinos. The energy deposition by neutrinos onto the collapsing stellar matter, called neutrino-heating, is considered to be the primary mechanism that revives the stalled shock (see Fig. 2.7) and leads to the explosion that we see as the supernova and later as a supernova remnant. That is, the outer stellar layers are ejected in a SN blast, while the interaction of the hot & fast ejecta and the blast wave with the ambient ISM creates a SNR.

Apart from neutrino transport, the role of asymmetries like spherical symmetry breaking and various instabilities like turbulent convection and SASI [see references in Müller et al. 2017] are being explored with multidimensional radiation-hydrodynamics simulations to account for explosions in a wide mass range of progenitors. Magnetic fields and rotation also likely play a crucial role, especially for explosions associated with GRBs and hypernovae (HNe). All in all, the decades-long problem of how massive stars die, how an imminent implosion is reversed to explosion, is converging at the resolution of microphysics of the nuclear, neutrino and turbulent processes around the nascent NS inside the collapsing core. We probably have all the necessary ingredients to detail core-collapse supernova explosion mechanisms, although the full answer is still years ahead as various theoretical, numerical, computational and observational challenges remain [see Woosley & Janka 2005; Janka 2012; Burrows & Vartanyan 2021, for reviews].

2.2.2.2 Nucleosynthesis

A clue to constrain some of the models is to probe elements produced in the violent nuclear processes occurring near the extremely dense and hot core, the nucleosynthesis yields. The innermost CCSNe ejecta contains Fe-, Si-group elements synthesized from protons and α-particles

left from nuclear disintegration of heavy elements in the collapsing core [Arnett 1996]. These include radioactive isotopes such as ^{56}Ni and ^{44}Ti. The decay chain

$$^{56}\mathrm{Ni} \xrightarrow{\tau=8.8\,\mathrm{days}} {}^{56}\mathrm{Co} \xrightarrow{\tau=111.3\,\mathrm{days}} {}^{56}\mathrm{Fe} + \gamma + e^{+}$$

causes copious γ-ray emission, heats the ejecta, shapes the SN or early SNR light curves. While SNe Ia, being a thermonuclear runaway of C-O WDs, are main producers of Fe in the universe, around half of isotopes heavier than Fe are evidently synthesized by nuclear processing CCSNe [Woosley & Janka 2005]. These are called "alpha-products" or "r-isotopes" because the key process occurring near the proto-NS is **r-process**, that is, *rapid neutron capture*. From outside, the yield of CCSNe is dominated by C, O, Ne, Mg, and other products of successive stellar burning during the shrinking stage of the massive progenitor.

2.2.2.3 Pair-Instability

The fate of very massive stars ($\gtrsim 140 M_{\odot}$, see the strange white region in Fig. 2.6) of low metallicity is even more dramatic. These are so-called Population III stars, predicted first generation of stars formed out of the metal-free primordial gas [e.g., Bromm et al. 1999]. Such stars cannot terminally form a stable Fe core; rather, enter into an electron-positron pair-instability during the O burning stage [Alsabti & Murdin 2017, Ch.1]. The pair production from collisions between nucleons and γ-rays drains the thermal pressure, and the O core collapses dynamically. The outcome is a PISN [Barkat et al. 1967; Bond et al. 1984], where the star is completely disrupted leaving no stellar remnant. It may manifest as a SN with abnormally long-duration light-curve or as a member of yet another SN class of "superluminous" supernova [SLSN, > -21 mag, Gal-Yam 2012].

Chapter 3

Supernova Remnants

Intricate, fascinating and spectacular objects on their own, supernova remnants are imprints of dead stars (supernovae) on the interstellar medium. SNRs are means to study the local population of SNe as they are visible for thousands of years after the initial burst of electromagnetic energy has faded away. After "first light", "maximum light" and "early decline" phases in a period of few weeks or months, SNe show emission lines—rather than absorption lines—from the *optically thin* ejecta. This "nebular phase" of a SN transitions into the I phase of SNR evolution, whereby the early-time SNR spectra or the late-time SN spectra are dominated by radioactive emission lines.

So, SNRs provide information about their progenitor as well as about the surrounding ISM. The magnetohydrodynamic interaction of the hot, fast, outermost ejecta with the innermost ambient medium, in weeks or 100–1000 years, creates a visible extended structure in the interstellar medium—the SN remnant. We talk about the dynamics of these interactions (shocks, phases and models) in §4, and what makes the structure visible (in X-rays, etc.) in §5. Here, we only talk about the morphology of the SNR structures (§3.1), and known SNR population and distribution (§3.2).

3.1 Morphological Classification

The supernova origin cannot be easily traced to type a remnant as a 'Ia-SNR' or a 'CC-SNR' or a subtype, although some direct methods and indirect indications exist (see §7.3.1.1). The classification scheme in practice is rather based on the morphological structure. From theories of progenitor explosion, ejecta expansion and emission, we expect the formation of a *shell* which should be roughly spherical with some asymmetry due to explosion mechanism itself and/or interactions with the ambient ISM.

As such, **shell-type** SNRs are the most common type of SNRs known. They have a ring-like morphology from the 2D projection of a spherical shell. Examples are Cas A, Tycho's SNR (SN 1572), Kepler's SNR (SN 1604) and Cygnus Loop [Vink 2020]. The brightened outer-edges ("limbs") seen in radio images mark the current location of the shock front [Alsabti & Murdin 2017, Ch78]. The interior is relatively 'hollow' in radio. There are many kinds of peculiar variations within this class that hosts more than 80% of all known Galactic SNR. For example, SN 1006 seems to have limb-brightening only on two opposites, suggesting a 'barrel-shaped' cylindrical morphology. Also, the shell is not always well-defined: the outer boundary could be irregular or blurry.

On the other hand, the radio brightness peaks near the center of some SNRs. Here, the mor-

phology of the shell has been modified by the presence of a pulsar driving a 'wind' of relativistic electrons and positrons into the medium, creating a pulsar wind nebula (PWN) [Gaensler & Slane 2006]. Such SNRs are called **composite** SNRs, as two mechanisms of radio (synchrotron) radiation are active. These are almost certainly CC-SNRs, even if the (almost) central neutron star is not visible, as is often the case. Prominent examples of this type are Kes 79 & Vela SNR in the Galaxy, and LMC SNR 0540-69.3.

And then, some SNRs have a 'filled center', i.e. the radio (synchrotron) emission is coming from all over the body of the SNR, with no indication of a shell. That is, the SNR shell has either disappeared or not formed at all, leaving a naked PWN [Alsabti & Murdin 2017, Ch77]. These are called **plerions**. Crab Nebula (SN 1054) is the prototypical example of this class, although puzzling in many ways [see Hester 2008]. Another example is the SNR (or PWN) 3C58, previously thought to be the remnant of SN 1181 [see Ritter et al. 2021].

Finally, we have a **mixed-morphology** class of SNRs, which have a (non-thermal) radio shell but a dominant center filled with thermal X-rays [Vink 2020]. They are also called 'thermal-composite' SNRs. Examples are older remnants like W44 and IC443. Such remnants need alternate evolutionary models, such as expansion in a cloudy ISM [such as White & Long 1991; Cox et al. 1999]. Fig. 3.1 shows an exemplar SNR of each of the 4 morphological types.

Apart from progenitor or explosion and morphology types, we can also classify supernova remnants by their age as 'young', 'mature', 'middle-aged' and 'old'. The range of time and epochs of transition are roughly defined by the phases of evolution, as discussed in §4.3.

3.2 Population and Distribution

How many supernova remnants are there? How many are observed and how many are expected? And, *how* are they discovered and classified? There are around 300 Galactic and 1200 extragalactic SNRs known today [Alsabti & Murdin 2017, Ch76], much lower than the theoretical estimates based on SN rates and visibility times. The incompleteness of the sample is more pronounced for Galactic SNRs than extragalactic ones, which on the other hand, cannot be resolved enough for a detailed study. The best target, hosting a rich a population of SNRs and close enough, are the Magellanic Clouds, especially the LMC, as we discuss below.

3.2.1 Galactic

Green [2024a] catalogs 310 Galactic SNRs, updated frequently as in Green [2024b]. SNRCat [Ferrand & Safi-Harb 2012][1] compiles 383 Galactic SNRs augmenting the radio with high-energy observations. The study of Galactic SNRs, though, especially in X-rays, is plagued by extreme distance uncertainties (because of numerous foreground and background sources) and foreground absorption due large column densities along the Galactic disk. Most of the (Galactic) SNRs have been discovered as radio sources, because: i) they emit in radio throughout their lifetime, ii) there is little to no extinction of radio sources in the Galaxy above 100 MHz, and iii) access to early and plenty of wide-field radio surveys [Vink 2020]. A small fraction have been discovered in optical wavelengths, and even smaller in X-rays.

The current numbers of observed supernova remnants in the Galaxy falls way short of the *expected* number. Based on an estimated SN rate of $\sim$3 per century and SNR visibility time of 10^5 years, MW should have 2000–3500 SNRs [Vink 2020]. So, observed number underestimates the true number by a large factor.

[1] `http://snrcat.physics.umanitoba.ca/`

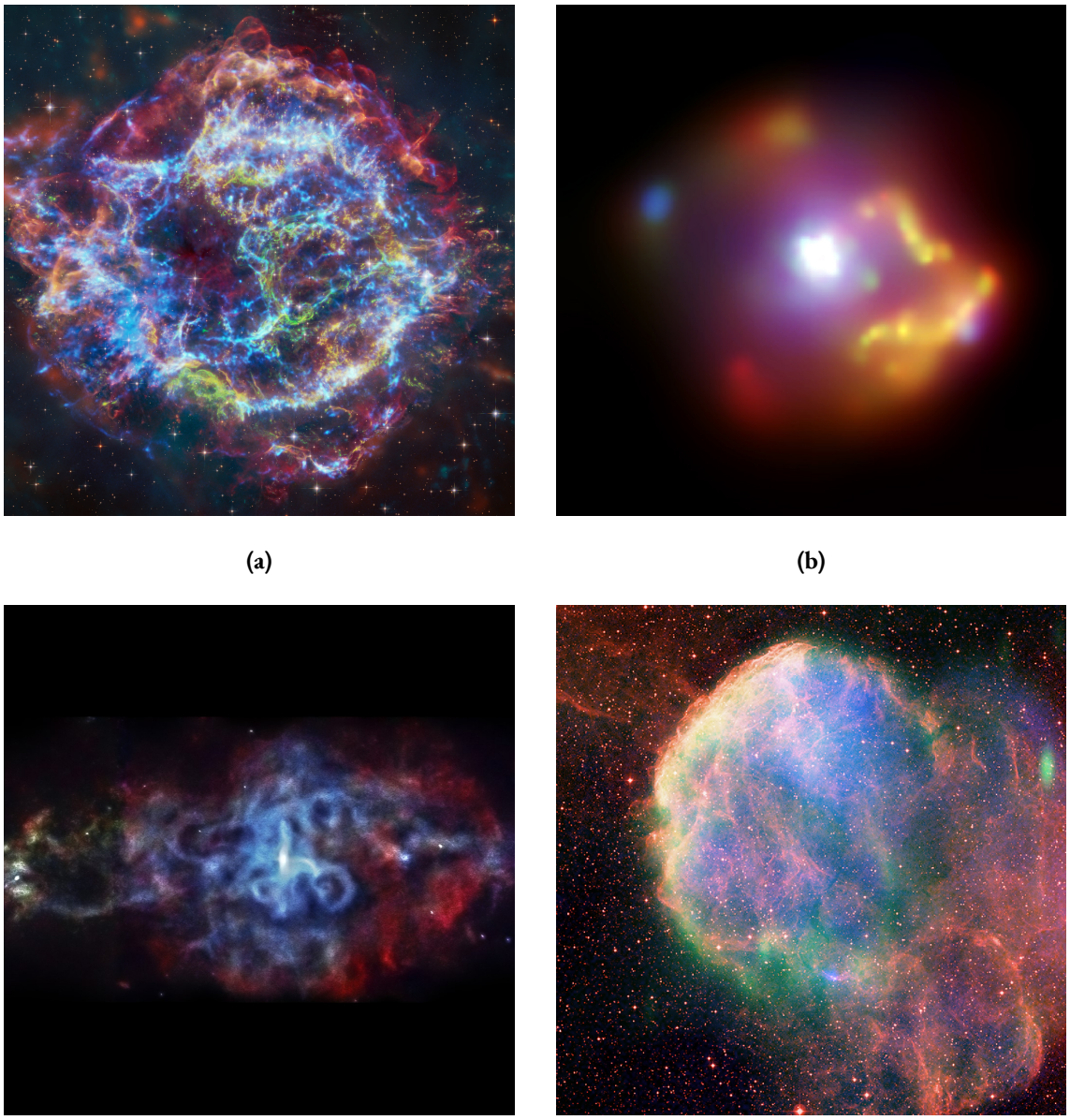

(a) **(b)**

(c) **(d)**

Figure 3.1: **(a)** A shell-type SNR Cas A in Chandra X-ray (blue), JWST infrared (RGB) and HST optical (red and white) [Credits: X-ray: NASA/CXC/SAO; Optical: NASA/ESA/STScI; IR: NASA/ESA/CSA/STScI/Milisavljevic et al., NASA/JPL/CalTech]. **(b)** A composite LMC SNR 0540-69.3, called 'twin of the Crab', in Chandra X-ray (RGB: 0.3–0.8–2.1–4 keV) [Credits: NASA/CXC/SAO]. **(c)** A plerion SNR 3C58 in Chandra X-ray (RGB: 0.5–1.2–2–7 keV) [Credits: NASA/CXC/SAO]. **(d)** A thermal-composite SNR IC443 (Jellyfish Nebula) in Chandra & ROSAT X-ray (blue), VLA radio (green) and DSS optical (red) [Credits: Chandra X-ray: NASA/CXC/B.Gaensler et al; ROSAT X-ray: NASA/ROSAT/Asaoka & Aschenbach; Radio Wide: NRC/DRAO/D.Leahy; Optical: DSS; Sonification: NASA/CXC/SAO/K.Arcand].

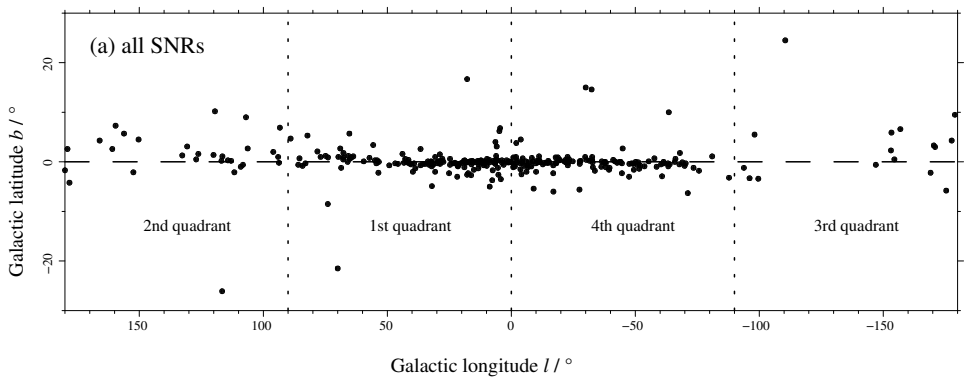

Figure 3.2: The distribution of SNRs with Galactic latitude and longitude from the latest catalog [Green 2024a, Fig3] showing concentration across the Galactic disk=star formation activity.

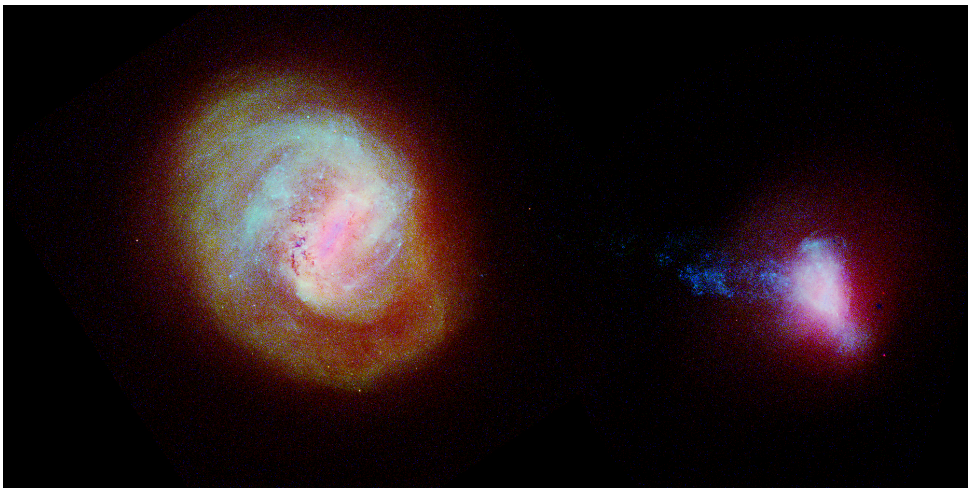

Figure 3.3: The Large and Small Magellanic Clouds in a composite image after Gaia DR3 [Credit: ESA/-Gaia/DPAC/Laurent Chemin/Gaia Collaboration et al. 2021].

The spatial distribution follows the star formation in the Galaxy, unsurprisingly (for CC-SNRs). Most SNRs (91.6%) lie within the Galactic latitude $b < \pm 5^\circ$ across the longitude (l), in Fig. 3.2. Type Ia SNRs need not be correlated with the b; so the outliers are most likely of a thermonuclear origin, e.g., SN1006 (G327.6+14.6) and Kepler's SNR (G4.5+6.8).

In terms of morphological types, 212 (+36?) shell-type, 20 (+18?) composite, and 9 pleri-ons are listed in [Green 2024b]. The mixed-morphology remnants class is not considered there, so the remaining 15 are objects with SNR 'candidacy'. The sample suffers from selection biases and incompleteness [Green 2005].

3.2.2 LMC

The Magellanic Clouds (MCs) are two satellite galaxies of the Milky Way in the Local Group. The larger among them, LMC is located at $\approx$ 50 kpc, while the Small Magellanic Cloud (SMC) is further away at $\approx$ 62 kpc with only $0.2\times$ mass [van der Marel 2004]. Both are classified as irregular dwarf galaxies, SMC more so. A 'stream' of HI gas, evidence of tidal interactions, forms the Magellanic Bridge between the two galaxies. Similar interactions are believed to have produced the Magellanic Stream which trails the MCs as they orbit the MW. See Fig. 3.3 and Gaia Collaboration et al. [2021].

Large Magellanic Cloud (LMC) is subjected to numerous multiwavelength studies, such

as, of SNRs in X-rays, radio and optical. Due to its physical properties and relative location, it is an ideal astrophysical laboratory to study star formation and the diffuse ISM. First, it is our closest star-forming galaxy, located at a relatively small & well known distance of $\approx$ 50 kpc [Pietrzyński et al. 2019; de Grijs et al. 2014]. Furthermore, this distance can be assumed to be approximately the same for all LMC objects because the galaxy is shaped like a disk which is thin ($0.3 - 1.5$ kpc) and inclined almost face-on ($30 - 40°$) [van der Marel et al. 2002; van der Marel 2004]. Thirdly, it is positioned away from the Galactic plane implying much smaller foreground absorbing column densities $< 10^{21}$ cm^{-2} [Dickey & Lockman 1990] as well as avoiding source confusion. Hence, the study of LMC is plagued less by systematic uncertainties than MW sources. Circling back, these characteristics make LMC a common target of various surveys, so a wealth of data in different bands from different telescopes is available.

As a result, our knowledge of the SNR population in the LMC is the most complete of any galaxy. The first LMC SNRs were N49, N63A and N132D, three HII "nebulae" proposed as candidates by Mathewson & Healey [1964] and confirmed by Westerlund & Mathewson [1966] from radio and optical observations. They were indeed the first *extragalactic* SNRs to be discovered. Since then, there have been notable additions to the population. First, Mathewson & Clarke [1973] went to discover 12 more LMC SNRs. The first X-ray astronomical satellite *Einstein* enabled Long et al. [1981] to identify 26 SNRs, confirm many earlier candidates. Mathewson et al. [1983] published a catalog of 25 SNRs with radio, optical, and X-ray data, which was expanded to 32 by Mills et al. [1984] and Mathewson et al. [1984, 1985].

Advancing to 1990s, *ROSAT* observations led to the discovery of several new SNRs, sometimes aided by optical spectroscopy [e.g., Smith et al. 1994; Chu et al. 2000]. Haberl & Pietsch [1999] cataloged ROSAT LMC X-ray sources including SNRs and SNR candidates. Many of these ROSAT candidates were revisited and confirmed [e.g., Maggi et al. 2014; Bozzetto et al. 2014; Kavanagh et al. 2015a,b] in the VLP (Very Large Programme) survey of the LMC (PI: F. Haberl) using the next best X-ray satellite *XMM-Newton*. This was alongside radio discoveries [e.g., Bozzetto et al. 2012b,a; de Horta et al. 2012] and others.

Comprehensive studies included catalogs of radio and optical SNRs [Filipovic et al. 1998], X-ray morphologies [Williams et al. 1999], UV emission [Blair et al. 2006], spectroscopic surveys [Payne et al. 2008], infrared surveys Seok et al. [2008, 2013], star formation by SNRs [Desai et al. 2010] and size distributions [Badenes et al. 2010].

Finally, Maggi et al. [2016] consolidated the sample to 59 confirmed LMC SNRs as seen in X-rays with XMM-Newton, analyzing individual spectral as well as some global properties of the population. The history thereafter is summarized in §7.2. The current sample stands at 78 confirmed and 46 candidate SNRs in the LMC after the all-sky surveys by another X-ray satellite *eROSITA* [Zangrandi et al. 2024] and continuous collaborative multiwavelength efforts—such as this work here.

For completeness, we mention that Maggi et al. [2019] performed a similar comprehensive study of SNRs in the Small Magellanic Cloud based on XMM-Newton data with a multiwavelength view. They compile and analyze a concatenated list of 21 confirmed and 2 candidate SMC SNRs.

3.2.3 Extragalactic

The SNRs in other (neighboring) galaxies are difficult to observe because their distances, however well-known, are large. It is hardly possible to study extragalactic (excluding MC) SNRs as extended sources. Nevertheless, various detailed population studies on the Local Group galaxies, M31 (Andromeda) and M33 (Triangulum) have been notably made.

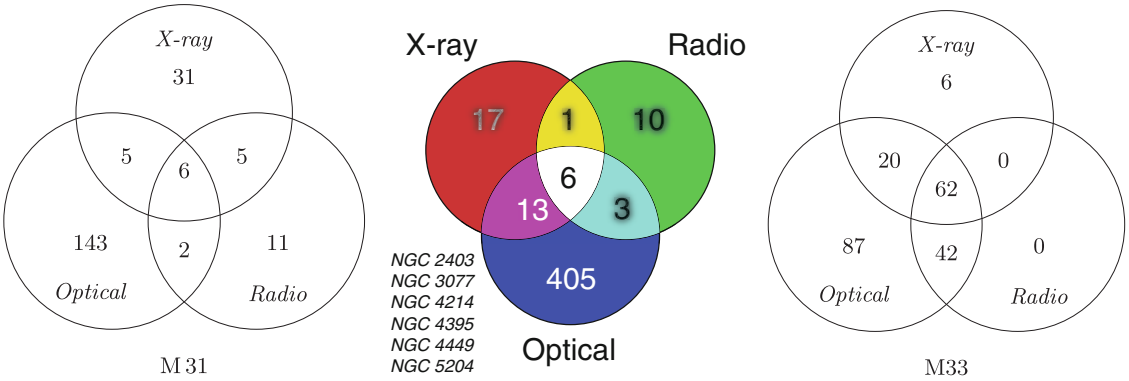

Figure 3.4: Venn diagrams for detection of extragalactic SNRs [Bozzetto et al. 2017; Vink 2020]

Sasaki et al. [2012] compiled a list of X-ray SNRs and candidates (26+20) in M31 from a deep XMM-Newton survey [Stiele et al. 2011]. Further, 154 optical candidates by [Lee & Lee 2014]. Huang et al. [2023] add to the catalog with a Legacy Survey (New-ANGELS) using archival XMM-Newton data. Long et al. [2010] present a large catalogue of 82 confirmed SNRs in M33, based on the Chandra ACIS survey of M33 (ChASeM33, Tüllmann et al. [2011]). Williams et al. [2015] did a deep XMM-Newton survey of M33 with more coverage, making the final, concatenated list of M33 SNRs to 90 objects.

Due to the large distances involved – from 0.79 & 0.84 Mpc for M31 & M33 respectively to 7 Mpc for M101 – spatial information is sparse. So, young extragalactic SNRs are too small to be resolved in X-rays. In radio, one requires very long baseline interferometry (VLBI) [Vink 2020]. Rather, most of the extragalactic SNRs known today were detected from optical observations (see Fig. 3.4); suggesting bias toward mature remnants.

Chapter 4

Supernova Remnant Evolution

Now that we have established the origin and existence of supernova remnants, we delve into the processes following the supernova explosion onto the circumstellar medium. The key process is the creation and propagation of the forward shock, also called the blastwave, which accompanies the injection of a large amount of kinetic and thermal energy in the ambient medium. We will first discuss the astrophysics of SNR shocks in §4.1 and §4.2. The fast-moving ejecta expands quickly into the surrounding medium, which gets shock-heated to X-ray-emitting temperatures. This first manifestation marks the birth of the extended object that we call a supernova remnant (SNR). We follow its dynamical evolution beyond this point, in §4.3. The four distinct evolutionary phases are discussed in some detail, followed by the standard analytical models (§4.4) that describe them.

The structure and content of this chapter derives from Vink [2011, 2020]. Both the review "*Supernova remnants: the X-ray perspective*" and the book "*Physics and Evolution of Supernova Remnants*", respectively, are highly recommended resources for SNR astrophysics.

4.1 Collisionless Shocks

Shocks (§1.1.3) are layers of rapid transition in fluid and thermodynamic properties of the plasma. The length scale of the transition layer for (astrophysical) shocks in the (sparse) interstellar medium is small compared to the (hydrodynamic) size scales. The mean free paths of particle-particle collisions as in Coulomb interactions of charges (electrons, protons, ions) in the interstellar medium is of the order of typical SNR radii [Vink 2020]. The collisional time scale is also quite long, compared to ages of young SNRs. Thus, shock heating cannot occur from Coulomb collisions, but through collisionless "collective effects" arising from plasma waves, fluctuating electromagnetic fields. Also, SNR shocks are strong, mildly relativistic and emit X-ray & radio radiation from heating & acceleration of particles.

4.1.1 Jump Conditions

As the thickness of the shock front is much smaller than its circumference, we can approximate SNR shocks as parallel planes. Assuming a comoving reference frame, we can apply the conservation laws of mass, momentum and energy on the flux of material "crossing" the shock to derive the so-called **Rankine-Hugoniot jump conditions** which allows us to determine the post-shock conditions from pre-shock conditions and vice versa. So as the shock propagates, the gas passing from the unshocked (*upstream*, 0) to the shocked (*downstream*, 2) region have

density ρ , pressure P, and internal energy U as:

$$\begin{aligned} \rho_0 v_0 &= \rho_2 v_2, \\ P_0 + \rho_0 v_0^2 &= P_2 + \rho_2 v_2^2, \\ \left(P_0 + U_0 + \frac{1}{2}\rho_0 v_0^2\right) v_0 &= \left(P_2 + U_2 + \frac{1}{2}\rho_2 v_2^2\right) v_2. \end{aligned} \tag{4.1}$$

$H \equiv P + U$ is the enthalpy and $\chi \equiv \frac{\rho_2}{\rho_0} = \frac{v_0}{v_2}$ is defined as the compression ratio. The strength of a shock depends on its speed relative to local sound speed, quantified by the (sonic) Mach number $M_s = v_0/c_s$. The general solution of Eq. 4.1, for high Mach numbers $\gtrsim 5$, reduces to give a density jump of factor 4:

$$\chi = \frac{(\gamma+1)M_s^2}{(\gamma-1)M_s^2+2} \overset{M_s\to\infty}{\approx} \frac{(\gamma+1)}{(\gamma-1)} = 4, \tag{4.2}$$

where $\gamma = 5/3$ is the specific heat ratio for non-relativistic monoatomic gases. One also gets the post-shock temperature and Mach number:

$$kT_2 = \frac{3}{16}\mu_2 m_p V_s^2 \tag{4.3}$$

$$M_{s,2} = [\gamma(\chi-1)]^{-1/2} \approx 0.45 \tag{4.4}$$

where μ_2 is the mean molecular weight of the downstream gas in units of proton mass m_p, and $V_s \equiv v_1$ is the shock speed. [Vink 2020]

4.1.2 Magnetohydrodynamics

We have ignored magnetic fields in the above description, although all collisionless shocks are magnetized [Treumann 2009]; inclusion implies additional terms in Eq. 4.1 for magnetic field lines parallel and perpendicular to the shock front, so that the following quantities are invariant across the shock front [McKee & Hollenbach 1980]:

$$\begin{aligned} &\rho v_\parallel, \\ &v_\parallel B_\perp - v_\perp B_\parallel, \\ &P + \frac{B_\perp^2}{8\pi} + \rho v_\parallel^2, \\ &\left(P + U + \frac{B_\perp^2}{4\pi} + \frac{1}{2}\rho v^2\right) v_\parallel - \frac{B_\perp B_\parallel}{4\pi} v_\perp. \end{aligned} \tag{4.5}$$

The magnetic field pressure leads to *Alfvén waves*, propagating transversely along the field lines with velocity $v_A = B_0/\sqrt{4\pi\rho}$ and an associated Mach number $M_A = v_1/v_A$. Combined with the gas pressure, the local signal speed is the velocity of the resulting magnetosonic waves $v_{ms} = \sqrt{v_A^2 + c_s^2}$, which propagate obliquely or perpendicular to the magnetic field. That is, the flow has to exceed this value, be super-sonic and super-Alfvénic, or super-magnetosonic with the magnetosonic Mach number $M_{ms} = v_1/v_{ms} > 1$, for a shock wave to form.

4.1.3 Shock Transition Layer

Collisionless shocks are microscopically thin [e.g., Treumann 2009] but not infinitely narrow as assumed so far. (See Fig. 1.3). The shock transition layer, usually called the shock front, is

not simply a boundary but a region that causes the abrupt changes in pressure and temperature between the upstream and downstream media. Indeed for high Mach numbers, the shock thickness is of the order of the mean free path of plasma particles, but it rapidly increases below $M_s \approx 2$ [Vink 2020]. Inside the transition layer (subscript 1), the Rankine-Hugoniot jump conditions need additional viscosity terms in momentum and enthalpy flux conservation:

$$\begin{aligned} P_0 + \rho_0 v_0^2 &= P_1 + \rho_1 v_1^2 - \frac{4}{3}\mu\frac{dv_1}{dz}, \\ \left(P_0 + U_0 + \frac{1}{2}\rho_0 v_0^2\right) v_0 &= \left(P_1 + U_1 + \frac{1}{2}\rho_1 v_1^2 - \frac{4}{3}\mu\frac{dv_1}{dz} - \kappa\frac{dT_1}{dz}\right) v_1, \end{aligned} \tag{4.6}$$

with μ and κ as coefficients of viscosity and heat conduction, respectively, and $+z$ is the direction of v_0 flow [Vink 2020]. Note that $\lambda = 3\mu/\rho\overline{v}$ is the mean free path of particles with an isotropic velocity distribution around the mean $\overline{v}$.

What happens inside the shock transition layer? The compression ratio (χ_1 here) increases monotonically ($1 \leq \chi_1 \leq \chi$). Viscous processes convert the incoming kinetic energy into thermal energy, 'smoothly' increasing the entropy of the gas. From this, the shock thickness is estimated to be $\Delta z \approx (1.08-1.62)\lambda$ for high Mach numbers [Vink 2020]. Further, the viscous processes cannot be Coulomb particle-particle collisions since the cross-section and collisional time scale, for single-scattering of two charged particles Z_1 & Z_2 with masses m_1 & m_2 and relative velocity v, are:

$$\sigma_{\rm pp} = 4\pi\frac{Z_1^2 Z_2^2 e^4}{v^4}\left(\frac{m_1+m_2}{m_1 m_2}\right)^2 \propto v^{-4} \tag{4.7}$$

$$\tau_{\rm pp} = \frac{1}{n\sigma_{\rm pp} v} \propto v^{-3} \tag{4.8}$$

which, for proton mass and typical shock velocity of 1000 km s^{-1}, gives a Coulomb mean free path, $\lambda_{\rm pp} \approx 32\, n_p^{-1}$ pc, and $\tau_{\rm pp} \approx 32\, n_p^{-1}$ kyr [Vink 2020]. These length and time scales are of the order of typical sizes and ages of observed SNRs. Thus, the shock front could not have been created by Coulomb (viscous) processes in a nascent SNR.

4.1.4 Thermalisation and Equilibration

Collisionless shocks are rather mediated by plasma waves and electric & magnetic fields in the shock transition layers, which thermalise the incoming particles. The source of viscosity in hot, dilute and fully-ionized plasmas such as in fast-moving SNR ejecta are non-local, non-binary 'anomalous collisions' between the particles and the existing electromagnetic fields. This leads to the mentioned 'collective interactions' that causes compression, heating, and increase in entropy. The microphysics behind the formation and evolution of collisionless shocks is complex beyond analytical treatment [see Treumann 2009, for a review]. It is best studied with particle-in-cell (PIC) simulations. These approximate the shock thickness by either the ion inertial length scale or the ion gyroradius. Although there are many uncertainties in the theory, it is clear that Δz is indeed much smaller than shock size scale [Vink 2020].

The main consequence of this is that for collisionless shocks, in general, the electron and proton temperatures are not equal: $kT_e \neq kT_p$ in Eq. 4.3. Indeed, observations of heliospheric and SNR shocks show that electrons are colder than the ions. As we cannot, a priori, assume that the complex plasma processes heat all electrons or ions equally, one resorts to models of electron/ion heating [reviewed in Ghavamian et al. 2013]. We only mentioned the shock front

as the viscous transition layer, characterized by sharp, localized changes in physical properties of matter. But, this main shock, often called the *subshock*, is preceded by a *shock precursor*. It is a region ahead of the subshock where plasma waves, electromagnetic radiation, and possibly cosmic rays are propagating. And, it is these cosmic ray precursors that are thought to be the most logical sites for electron heating in SNR collisionless shocks [Ghavamian et al. 2013]. The precursor length scale $\sim 10^{17}$ cm could be much larger than the subshock thickness $\sim 10^{7}$–10^{9} cm [Vink 2020].

Currently, shock temperatures are measurable with optical and UV spectroscopy on partial neutral media ("Balmer-dominated shocks"), $\sim 10^{15}$ cm downstream. X-ray spectra with current generation of telescopes allows measurement of electron temperatures but not the ion temperature. Future X-ray satellite missions with calorimeter-type spectrometers (like XRISM and ATHENA) will resolve this. For now it appears that $\beta \equiv T_e/T_p \propto V_s^{-2}$ [e.g., Ghavamian et al. 2013]. And, calculations show that it could take $\sim$10 kyr for electron and proton populations to equilibrate in temperature via Coulomb interactions [Vink 2020]. So, SNR plasmas are almost always out of ionization equilibrium, in so-called non-equilibrium ionization (NEI); opposed to the plasmas of cool stars and galaxy clusters which are in collisional ionization equilibrium (CIE). The electron-ion equilibration time is roughly inversely proportional to n_p ($\approx n_e$), so the parameter $\tau \equiv n_e t$ is often used as the ionization age of a supernova remnant. This is measurable in X-ray spectroscopy, using X-ray emission codes such as XSPEC. Broadly speaking, τ [10^{12}cm s^{-1}] $\lesssim 0.05$ indicates full non-equilibration between different charged species, ≈ 0.05–1 is when all ions are in equilibration with each other but not with the electrons, and finally, $\gtrsim 1$ means full equilibration in temperature [Vink 2011]. These considerations about kT and τ become practical when we analyze X-ray spectrum from a *likely* SNR ejecta plasma, in §6.2.3. Further for our evolutionary analysis in §7, we use the electron heating model of Cox & Anderson [1982].

4.2 Radiative Shocks

So far we discussed (collisionless) shocks arising from high-velocity ($\gtrsim$ 200 km s^{-1}) ejecta pushing against a tenuous medium ($\sim$ 1 cm^{-3}), compressing and heating plasma to high temperatures ($\sim 10^6$ K). We also mentioned cosmic-ray acceleration as a probable side-effect, which if significant, modifies the energy-flux conservation of the Rankine-Hugoniot relations by 'subtracting' a non-thermal component. There is another post-shock process of energy loss, namely radiation, where the usual jump conditions need not be valid. Such shocks can be referred to as radiative shocks.

For SNRs, this occurs from thermal continuum and line emissions (discussed in §5.1), cooling the plasma. The cooling timescale is derived from the cooling function Λ (volumetric rate of cooling) by dividing the enthalpy $U + P = \frac{\gamma}{\gamma-1}P$ by the emissivity $\epsilon = n_e n_p \Lambda$ as: [Vink 2020]

$$\tau_{\rm cool} = 5.7 \frac{kT}{n_e \cdot \Lambda(T)} \tag{4.9}$$

There comes a phase (see §4.3) in a SNR's evolution when radiative cooling becomes important. This is when the shock has slowed down to less than 200 km s^{-1} so that $v_2 \tau_{\rm cool} \approx V_s \tau_{\rm cool}/4$ becomes less than 1 pc [Vink 2020] and the cooling timescale falls below the age of the supernova remnant. Density increases to maintain the pressure balance, increasing the emissivity. This leads to knots and filaments seen in optical/UV images of older remnants. The first parcel of plasma to cool down and condense forms a *thin-shell* just behind the (sub)shock front.

Now, the pressure on the cooling plasma from the ambient medium can cause high compression ratios. Assuming that the cooling stops once $T_2 \approx T_0$, we can find the maximum χ for this (quasi) **isothermal shock** using the momentum-flux Eq. 4.1 as: [Vink 2020]

$$\chi_{\text{isothermal}} = \gamma M_s^2 \tag{4.10}$$

Another effect of this high compression is that magnetic field pressure becomes dominant. The modification in Rankine-Huguniot momentum-flux conservation in this case, including the perpendicular magnetic field term from Eq. 4.5, yields

$$\chi_{\text{magnetic}} = -\frac{1}{2}(\beta+1) + \frac{1}{2}\sqrt{(\beta+1)^2 + 8M_A^2} \tag{4.11}$$

for the compression ratio. Here β is not the electron-ion temperature ratio, but *plasma-beta*, the ratio between thermal and magnetic pressure [Vink 2020].

For completeness, we mention shocks mediated by magnetic precursors. These have important effects due to magnetosonic waves traveling far upstream and interacting with (charged & neutral constituents of) molecular clouds. If all the heating is done adiabatically within the magnetic precursor without the need of a viscous shock to satisfy the Rankine-Hugoniot jump conditions, then such shocks are called C-type ("continuous") shocks. If both precursor and subshock are needed, they are J-type ("jump") shocks. [Vink 2020]

4.3 Evolutionary Phases

Despite all the complexity, we can divide the evolution of supernova remnants into 4 discrete phases [Woltjer 1972] based on hydrodynamic interactions of ejecta with the ambient medium. The supersonic ejecta following the supernova explosion creates a shock and a shell in the circumstellar medium (CSM). The shock precedes the expanding shell. The ejecta-dominated (ED) phase I is characterized by dominance of initial ejected mass and explosion energy over effects of the medium, hence "free expansion". Soon, the mass swept-up by the shell exceeds the ejecta mass, so only the explosion energy remains important for the expansion. This marks the energy-conservation or Sedov-Taylor (ST) phase II of evolution, with negligible loss of energy, hence "adiabatic". Later, radiative losses become significant and we enter the pressure-driven "snowplow" (PDS) phase III where the expansion is driven by pressure from the hot low-density interior onto a cool dense shell which was formed behind the shock front. Eventually, the forward shock velocity approaches the local sound or Alfvénic velocity and the SNR terminates with a "merger" phase IV, indistinguishable from random motions in the large-scale ISM but leaving behind a plasma bubble. Seldom, in transition from phase III to IV, the SNR may lose its interior pressure before merging, leading to an additional momentum-conservation shell (MCS) phase, where the dense shell is coasted outward only by momentum-conservation, before becoming subsonic and fading away. We discuss these in detail below along with other intricacies like the reverse shock.

4.3.1 Free Expansion

Following the neutrino-driven turbulent (or else) gravitational explosion, supernova blast wave accelerates stellar ejecta outwards to speeds up to 30,000 km s^{-1} [Alsabti & Murdin 2017, Ch75]. This fast & hot material encounters the ISMa in the immediate vicinity of the progenitor star(s), the circumstellar medium (CSM). The properties such as the density structure (e.g., uniform or powerlaw decay) of the ejecta and the CSM depend on the progenitor (e.g.,

stellar wind or binary interactions). Regardless, this hindrance sets in a strong, astrophysical, collisionless, "forward" shock. And, it heats the CSM to X-ray emitting temperatures (see §5.1).

The initial phase of SNR evolution marked by this first interaction between ejecta and CSM is called the ejecta-dominated or ejecta-driven (ED) phase. It is characterized by rapid expansion of the shell, with minor deceleration. So, this phase I is also sometimes called the "free expansion" period. But, this could be misleading as one would expect that the forward shock velocity $V_{\rm fs}$ at any time t would evolve with the forward shock radius $R_{\rm fs}$ as

$$V_{\rm fs} = \frac{dR_{\rm fs}}{dt} = m\frac{R_{\rm fs}}{t} \tag{4.12}$$

with $m = 1$(?), that is, homologous expansion. And this is not the case; one expects (§4.4.1) and observes (in young remnants) this **expansion parameter** $m \equiv V_{\rm fs}\, t/R_{\rm fs}$ to be less than 1. There is a dependence on density profiles of ejecta and medium, as we will discuss in §4.4.

Certainly, there is negligible loss of energy from radiation as the expansion is powered by the kinetic energy from the initial explosion energy and mass of the ejecta (M_{ej}) is larger than the mass swept-up by the shock wave (M_{sw}). As a result, the ejecta, which was heated from the SN blast wave and radiation from radioactive SN nucleosynthesis yields, cools adiabatically. That is, there is a rapid decline in internal pressure. [Vink 2020]

4.3.1.1 Reverse Shock

The shock-heated shell does decelerate, almost as soon as it forms. So, soon the outermost, unshocked ejecta will catch-up and collide with the expanding shell. And if this collision is supersonic, it will create an *inward* shock wave, which re-heats the adiabatically cooled ejecta [McKee 1974]. This is called the reverse shock, and it creates a "contact discontinuity" (see Fig. 4.1) separating the (forward) shock-heated CSM and the (reverse) shock-heated ejecta. The two regions are in rough pressure equilibrium, but the boundary is not smooth or perfectly spherical. The wrinkles or 'fingers' seen in the diagram (Fig. 4.1), as well as in actual observations of many young remnants (Fig. 4.2), are mostly caused by **Rayleigh-Taylor instabilities**. The forward shock boundary shown spherical must also suffer from explosion asymmetries and convective instabilities (e.g., SASI, NS-kick, rotation, etc.) However, most 1D analytical and 2D numerical models assume spherical symmetry for simplicity. We do the same throughout this work.

4.3.2 Adiabatic

As $M_{sw} \approx M_{ej}$ with time, and the reverse shock has re-heated the freely-expanding ejecta to the very center of the SNR, the ED phase is said to be over [Draine 2011]. SNR enters its Sedov-Taylor phase, aged $t_{\rm ST}$, as now it can now be described by the *self-similar* solutions of Sedov [1959] and Taylor [1950a] for a "point explosion". The expansion is still approximately adiabatic in the sense that radiative losses are not yet energetically important, although (forward) shock-heating does increase the entropy of the gas. So, even though, both ED and ST phases can be called adiabatic, this term is also misleading. The main change when ejecta-dominance is over is that the ram pressure due to downstream unshocked ejecta expanding through the reverse shock has died out. So coming into the Sedov phase, the explosion energy powering the expansion of the shell is (reasonably assumed) the net sum of its internal energy and kinetic energy. For this reason, this II phase of SNR evolution is also called the *energy-conservation* phase.

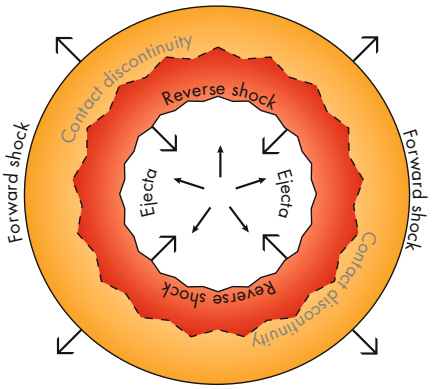

Figure 4.1: Schematic diagram of the regions heated by the forward (orange) and the reverse (red) shocks separated by a wrinkled contact discontinuity. The white regions outside and in the interior denote the unshocked or upstream CSM and the unshocked or colder ejecta, respectively. [Credits: Vink 2020]

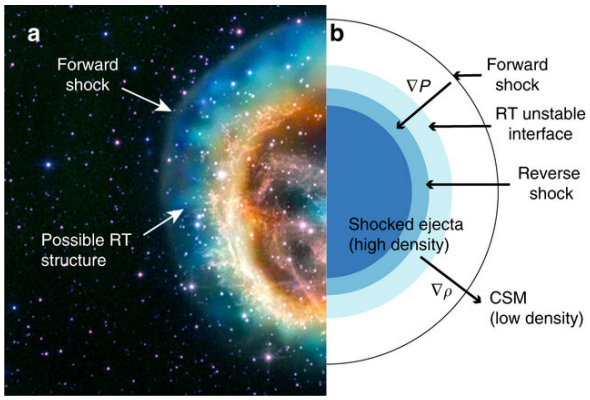

Figure 4.2: The structure of forward & reverse shocks and Rayleigh-Taylor (RT) instabilities in SMC SNR E0102.2-72. The **left**-half shows false-color image created from (Hubble) optical and (Chandra) X-ray data, while the **right**-half approximates the different regions associated with the shock wave interactions. [from Kuranz et al. 2018]

The Sedov-Taylor model(s) to describe the eponymous phase is discussed in §4.4.2. It does not take the ejecta mass into account ($M_{ej} = 0$), nor the complex internal structure of the SNR, on the expansion. And, the expansion parameter drops even more below unity ($m = 0.4$). Notably, two analytical models include the ejecta velocity & density structure in calculating the nonradiative evolution of supernova remnants. First, Chevalier [1982] describe the early (ED) evolution by assuming powerlaws for ejecta (and CSM) densities, giving m between 0.9 and 0.4. Secondly, the analytical model by Truelove & McKee [1999] enables smooth transition from the ED through ST phases, with the expansion parameter starting from that of Chevalier [1982] and asymptotically approaching that of Sedov [1959]-Taylor [1950a].

4.3.3 Snowplow

The PDS marks the beginning of the radiative phase of SNR evolution. This is when radiative losses have cooled the shell for a characteristic cooling timescale (see §4.2). This increases compressibility and emissivity, until magnetic fields limit them. The onset of this phase III is sudden, with formation of a cool dense shell [Blondin et al. 1998]. The radial expansion of is governed by momentum conservation, pressure-driven by the remnant interior which has much lower density and longer cooling time [Alsabti & Murdin 2017, Ch75].

The expansion parameter $m \approx 0.25$ at this stage ($t = t_{\rm rad}$), while the post-shock temperature and shock velocity have fallen below 0.5×10^6 K and 200 km s^{-1}, respectively [Vink 2011, 2020]. This phase is called the snowplow phase because the mass of the dense shell increases as it sweeps up the ambient gas [Draine 2011].

4.3.3.1 Momentum-Conservation Shell

MCS phase may occur in some (rare) cases when the SNR loses its interior pressure before merging with the large-scale ISM. This is known as the momentum-conservation shell phase, since the expansion is powered *only* by momentum-conservation of the shell. [Cioffi et al. 1988;

Leahy & Williams 2017]

4.3.4 Merger

The speed of the shock front (V_s) at the start of the PDS phase is still high enough to drive a strong shock through the interstellar gas. But, it gradually declines, approaching the local sonic speed (c_s), so that the compression ratio $\chi \rightarrow 1$. This epoch is usually called the merger time (t_{mrg}). As the downstream velocity and temperature become comparable or smaller than the turbulent speeds and temperatures of the ISM, the SNR "fades away" leaving little to no evidence of its existence. That is why, this IV phase is also called the fadeaway phase [Draine 2011]. SNRs do leave a plasma bubble which outlives them and overlapping of multiple SNRs plays a crucial role in regulating the observed structure of the galactic ISM (as disccused in §1.1.2).

4.4 Analytical Models

Considering the complex processes from the instantaneous injection of intense energy in the interstellar medium to the super-magnetosonic flow of high-temperature fully-ionized plasma, the most accurate visualization of evolution of a supernova remnant has to come from magneto-hydrodynamic (MHD) simulations in three dimensions [e.g., Kim & Ostriker 2015]. However, with so many variables to be taken into account such as turbulence, hydrodynamic instabilities, magnetic fields in an inhomogeneous multiphase ISM is even numerically difficult and computationally expensive. Further, some assumptions about "expected" initial conditions need to be made. Therefore, simpler analytical studies that approximate the general evolution of a (spherical) SNR blastwave in an (homogeneous) ISM have been constructed over time. Some of them are based on 1D hydrodynamical simulations. Much can be learnt from these models or solutions, without the need to resolve to the microphysics of SNR evolution

Self-similarity A class of models assumes that a SNR evolves in such a way that its overall structure or properties at different times are proportionally similar to each other. These are parameterized by certain self-similar parameters, which are a combination of basic SNR variables, such as explosion energy, ejecta mass, ambient density, age and radius. Self-similar solutions to otherwise a very complicated problem are known to capture the main characteristics of SNR evolution without resolving every small detail.

4.4.1 Chevalier Solutions for ED Evolution

Chevalier [1982] and Nadezhin [1985] independently derived self-similar solutions for the ejecta-dominated phase of SNR evolution. They assumed powerlaw distributions for ejecta and CSM with indices n and s, respectively. Further, they express the density as a function of velocity rather than radius, since initial expansion should be homologous. Chevalier [1982] assumed a "core-envelope" structure for the ejecta: a constant-density *core* surrounded by a powerlaw *envelope*.

$$\rho_n(v,t) = \begin{cases} \rho_{\text{core},0} \left(\frac{t}{t_0}\right)^{-3}, & \text{for } v \leq v_{\text{core}} \\ \rho_{\text{core},0} \left(\frac{t}{t_0}\right)^{-3} \left(\frac{v}{v_{\text{core}}}\right)^{-n}, & \text{for } v > v_{\text{core}} \end{cases} \tag{4.13}$$

where $v_{\rm core} = r_{\rm core}/t$ [Vink 2020]. And for the ambient medium, we have the density profile:

$$\rho_s(r) = \rho_0 \left(\frac{r}{r_0}\right)^{-s} \tag{4.14}$$

The profiles for ejecta mass M_{ej} and ejecta energy E_{ej} can be derived by appropriately integrating Eq. 4.13. We find that no solutions exist for $n \leq 5$ because as $v \to \infty$, E_{ej} diverges: all kinetic energy seems to be concentrated in the outermost ejecta. Combining Eqs. 4.13 and 4.14 gives the characteristic radius of the supernova remnant in this model:

$$R_c = A \cdot t^{\frac{n-3}{n-s}} \tag{4.15}$$

where A is a constant. This is actually the radius of constant discontinuity, and the exponent of t is the expansion parameter $m = (n-3)(n-s)$ for the Chevalier model [Vink 2020]. For $n \to 5$ the expansion approaches the Sedov-Taylor self-similarity (see §4.4.2). For other values of n and s, no analytical solution exists for the velocity, pressure or density in the interior, but numerical estimates are shown in Fig. 4.3. The model works as long as the reverse shock has not reached the core ejecta ($R_{\rm rs} < v_{\rm core} t$).

4.4.2 Sedov-Taylor Solutions for ST Evolution

The theory of the 'famous' self-similar solutions describing an adiabatic blastwave stems from the works of Sedov [1946, 1959], Taylor [1946, 1950a,b] and von Neumann [1947, 1963] attempting to understand the effects of nuclear explosions in (war-torn) Earth's atmosphere. Later, Shklovskii [1962] recognized its applicability to astrophysical explosions, SNR evolution. It is based on the shock-wave fluid dynamics of Rankine [1870] and Hugoniot [1889] and an application of the Buckingham [1914] π theorem, with some simplifying assumptions:

1. The explosion energy (E_0) is released & transferred instantly & completely to the ambient medium, which has a uniform density (ρ_0).
2. The blastwave is in the strong shock regime, i.e. $M_s >> 1$ and $P_0 = 0$ [Vink 2020].

Then, the (forward) shock radius and velocity evolve with time t as follows:

$$R_{\rm fs} = \left(\frac{\xi E_0 t^2}{\rho_0}\right)^{1/5} \tag{4.16}$$

$$V_{\rm fs} = \frac{dR_{\rm fs}}{dt} = \frac{2}{5}\left(\frac{\xi E_0}{\rho_0}\right)^{1/5} t^{-3/5} = \frac{2}{5} R_{\rm fs} t \tag{4.17}$$

where the dimensionless constant $\xi = 2.026$ for a non-relativistic, monoatomic gas ($\gamma = 5/3$) [Vink 2011]. Eq. 4.16 has been expressed as such, and also in terms of the (constant) pre-shock hydrogen density, in Eq. §6.6 in 6.3.3.

Eq. 4.17 shows that the expansion parameter is $2/5$ or 0.4 during the ST phase. But, this changes with the generalization $\rho(r) \propto r^{-s}$ for the ambient medium density profile with a powerlaw index s. Then, $R_{\rm fs} \propto t^m$ gives $m = 2/(5-s)$. Astrophysically, $s = 2$ is expected for CSM around a (massive) progenitor with a stellar wind [e.g., Chevalier 1982].

Assumptions 1 and 2 and Eqs. 4.16 and 4.17 above imply that Sedov-Taylor solutions do not consider the effects of SN ejecta. Therefore, they are good approximations once $M_{sw} > M_{ej}$. The internal structure (velocity, density, pressure, temperature) can be analytically calculated for Sedov [1959] self-similar explosions, as shown in Fig. 4.4. We can see that the density approaches zero near the center, and most of the mass is concentrated near the shock (radius here, $R_{\rm sh}$).

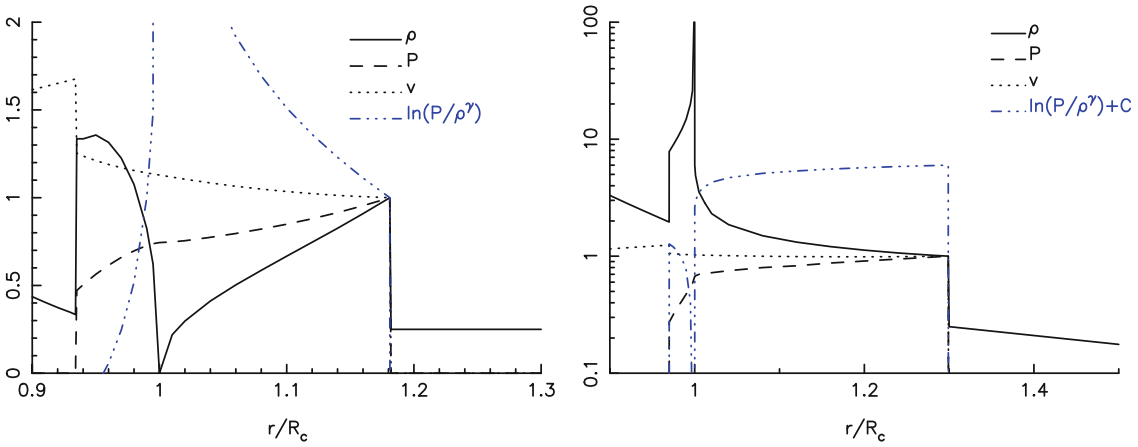

Figure 4.3: Density, pressure, velocity, and entropy profiles for Chevalier [1982] models with $s = 0$ (**left**) and $s = 2$ (**right**). $n = 7$. The normalization is with respect to the radius of contact discontinuity. [from Vink 2020]

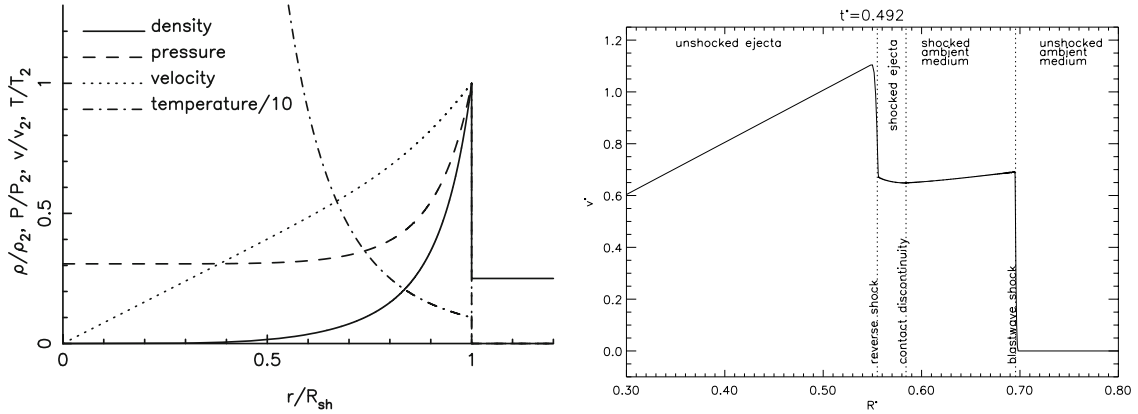

Figure 4.4: **Left**: Internal structure of a SNR according to Sedov-Taylor self-similarity. The values are scaled by corresponding values at *just* behind the shock. [from Vink 2020]. **Right**: A snapshot of velocity (v^*) distribution with radius (R^*) at $t^* = 0.492$ showing basic internal structure of a TM99 SNR evolution. Both $n = 0$ and $s = 0$.

4.4.3 Truelove-McKee Models for ED–ST Evolution

Truelove & McKee [1999], hereafter TM99, conducted a numerical analysis on the dynamics of SNR evolution prior to the radiative epoch, and presented a single unified analytical solution for all nonradiative supernova remnants with a given powerlaw structure. They construct characteristic dimensional parameters – for ejecta energy, ejecta mass and ambient density, using corresponding dimensionless quantities. The solutions agree with 1D hydrodynamic simulations from early ED to late ST phases.

They use the same assumptions for density profiles as Chevalier [1982], and define the following characteristic variables for mass, radius and time:

$$\begin{aligned} M_{\rm ch} &\equiv M_{\rm ej}, \\ R_{\rm ch} &\equiv M_{\rm ej}^{1/(3-s)} \rho_s^{-1/(3-s)}, \\ t_{\rm ch} &\equiv E_0^{-1/2} M_{\rm ej}^{(5-s)/(2(3-s))} \rho_s^{-1/(3-s)}. \end{aligned} \tag{4.18}$$

These give dimensionless age, $t^* = t_{\rm ch}/t$ and radii, $R^*_{\rm fs} = R_{\rm fs}/R_{\rm ch}$ & $R^*_{\rm rs} = R_{\rm rs}/R_{\rm ch}$ for

which models can be constructed for different values of the parameters n and s and some constants which are determined numerically [see Truelove & McKee 1999, for details]. Summarily, the forward and reverse shock evolution are described in two parts: a general ED solution and a general ST solution, separated at time/age $t_{\rm ST}$, ensuring smooth transition. The first part asymptotically approaches free-expansion for $n < 5$ and Chevalier solution for $n > 5$ when $t \to 0$. And, it has two forms depending on whether the reverse shock is in the envelope or the core. The second part approaches the ST solution as $t \to \infty$. The reverse shock radius has been assumed proportional to the forward shock radius in the ED phase, and has constant acceleration in the unshocked ejecta frame in ST phase.

The original TM99 model treated only uniform density CSM with index $s = 0$, but suggested extension to the $s = 2$ case suitable for stellar-wind profiles. These have been tried for specific remnants such as Cas A [Laming & Hwang 2003; Micelotta et al. 2016] or in general [Tang & Chevalier 2016]. We recognize that tuning such analytical models in accordance to observed SNR properties and, vice versa, deriving observational parameters from the models, is a powerful tool in understanding how supernova remnants evolve under different conditions. Fig. 4.4 (right) shows the radial profile of the dimensionless velocity in the ED–ST transitional period, simulated for an idealized, spherically-symmetric SNR with uniform ejecta expanding into uniform ISM. The structure of shocked and unshocked material created by the forward and reverse shocks can be clearly seen. We come back to the TM99 model in §7 and show the evolution of forward & reverse shocks, temperatures and emission measures with time, among other calculations. We employ a computer tool which combines the models discussed so far together and with models for the radiative phase discussed below.

4.4.4 Radiative Evolution

As discussed in §4.2 and §4.3.3, the adiabatic cooling and deceleration of expanding ejecta gives way to formation of a thin-shell and significant radiative energy losses. The supernova remnant transitions from energy-conservation to momentum-conservation regime, from nonradiative to radiative phase. The evolution of the forward shock is governed by:

$$M V_{\rm fs} = \frac{4\pi}{3} \rho_0 R_{\rm fs}^3 \frac{dR_{\rm fs}}{dt} = \text{constant} \tag{4.19}$$

The radiative evolution of SNRs has been treated by many authors [Cioffi et al. 1988; Blondin et al. 1998] using numerical simulations to approximate analytical solutions. The crucial difference from the earlier self-similar and unified models is that the expansion does not follow a powerlaw in time anymore. Although, earlier studies estimated $R_{\rm fs} \propto t^{2/7}$ [McKee & Ostriker 1977], ignoring internal cooling. Accounting for this internal radiation pressure [Kahn 1976], one also finds the momentum-conservation shell phase with $R_{\rm fs} \propto t^{1/4}$ [Oort 1951].

Secondly, no single *absolute* analytical model exists to describe the PDS and merger phases. The reason is evident from hydrodynamic simulations showing dynamical instabilities both during and after the transition; implying that the formation of the thin-shell and subsequent radiative evolution is, more than other phases, a complex multi-dimensional process, which may not be properly modeled in 1D. So, the validity of every model is contingent on its assumptions and methodology. Blondin et al. [1998] performed 1D and 2D simulations, assuming the cooling function (see Eq. 4.9) $\Lambda(T) \approx 10^{-16} \cdot T^{-1}$ erg cm^3 s^{-1}. This gives the age of transition to the radiative phase:

$$t_{\rm rad} \approx 2.9 \cdot E_{51}^{4/17} n_0^{-9/17} \times 10^4 \text{ yr} \tag{4.20}$$

The forward shock radius, velocity, swept-up mass and post-shock temperature of the ST blast-wave at this stage are calculated to be:

$$\begin{aligned} R_{\text{fs,rad}} &\approx 19.1 \cdot E_{51}^{5/17} n_0^{-7/17} \text{ pc} \\ V_{\text{fs,rad}} &\approx 260 \cdot E_{51}^{1/17} n_0^{2/17} \text{ km s}^{-1} \\ M_{sw,\text{rad}} &\approx E_{51}^{15/17} n_0^{-4/17} \times 10^3 M_\odot \\ T_{2,\text{rad}} &\approx E_{51}^{2/17} n_0^{4/17} \times 10^6 \text{ K} \end{aligned} \tag{4.21}$$

Here, n_0 is the number density of the ISM, and E_{51} is the explosion energy in units of 10^{51} erg.

Later in §7.1, we discuss and implement the analytical model of Cioffi et al. [1988], where the cooling function $\Lambda \propto T^{-1/2}$. They use an "offset" powerlaw where $R_{\text{fs}} \propto (t - t_{\text{off}})^{3/10}$ to approximately describe the complete radiative phase. This gives similar, but slightly different values for the ages corresponding to the snowplow phase (t_{PDS}) and thin-shell formation (t_{sf}). As CMB88 model also extends to the possible MCS phase and the final merger, this completes our set of analytical models that can be used to describe the whole evolution of supernova remnants (in 1 dimension). We discuss the different kinds of radiation from SNRs and the basic emission mechanisms in the next section (§5.1).

Chapter 5

X-ray Observation

As already indicated in the previous sections, supernova remnant are emitters of electromagnetic radiation across a wide range of wavelengths. What are these wavelengths and what causes this radiation, is the subject of §5.1. We mentioned thermal (§5.1.1) and non-thermal (§5.1.2) emissions. These are associated with shock-heating and particle-acceleration activities of the forward (or the reverse) shock, and are primarily in X-rays and radio, respectively. Then, rapid cooling and transition to radiative shocks results in copious optical/UV emission lines. Apart from line emission (§5.1.1.4), there is continuum emission due to a number of radiative mechanisms (§5.1.1.1, §5.1.1.2, §5.1.1.3).

In 5.2, we tackle the problems and advances in observing astrophysical X-rays. The basic optical principles in focusing and imaging X-ray beams is summarized in §5.2.1. The pivotal discovery of Wolter-optics and its application to astronomy, led to first X-ray telescopes (§5.2.2), the increasing resolution and sensitivity of which have been well-utilized by modern CCD cameras (§5.2.3). We also discuss interstellar extinction and sources of noise when observing extragalactic X-rays (§5.2.4), in preparation of subsequent X-ray data analysis (§6). The discussions in this chapter are somewhat generic to other astrophysical processes involving X-rays, and/or emission and detection of photons, not just SNRs.

5.1 Emission Processes

X-rays in the universe are produced by a variety of processes, broadly classified as thermal and non-thermal. The emission mechanisms include blackbody radiation, bremsstrahlung, line emission, recombination, synchrotron radiation and inverse-Compton scattering [Mewe 1999].

By thermal emission, we mean that the electrons in the electron-photon process are in a Maxwellian energy distribution. As SNR plasmas are optically thin, the important thermal emission mechanisms are line and continuum emissions. The primary source of continuum emission from SNRs is thermal bremsstrahlung, while line emission is associated with atomic transitions. The emitted photons at the typical $\sim 10^6$ K temperatures are in the X-ray energy range of 0.5–10 keV.

Non-thermal radiation, on the other hand, involves acceleration of electrons (or other charged particles) to relativistic velocities in a magnetic field. The electron distribution spans a large energy range in this case and can be approximated by a powerlaw. This is called synchrotron radiation, mostly detected in the radio bands, but can extend up to X-rays in young SNRs. Bremsstrahlung has a non-thermal origin as well. This is when the relativistic electron Compton *up-scatter* background photons, which are then "braked" by the plasma ions, and detected

in γ-rays [Vink 2020].

Apart from these, what we do not discuss, there is line emission of γ-rays and hard X-rays due to radioactive decays (of ^{56}Ni and ^{44}Ti) from a nascent SNR. Also, optical/UV line emission behind radiative shocks is prevalent in older remnants. Many forbidden lines (like [SII], [OIII], [NII]) are observed, since spontaneous de-excitation time is very long in astrophysical settings as in a SNRs.

5.1.1 Thermal X-ray Emission

SNR plasmas are heated to temperatures of a million Kelvin or more; so are plasmas of stellar coronae, galaxy clusters and the diffuse intergalactic medium. Such plasmas are optically thin, meaning that constituent atoms/ions of the plasma do not attenuate the passing X-rays. They are often called *coronal plasmas*, like the **coronal model** that describes them that was first applied on solar corona. The assumptions [Mewe 1999] of the coronal model for thermal emission (of X-rays) are also valid for supernova remnants, with some modifications. Most severe change is that SNR plasmas are not in ionization equilibrium [Vink 2020], as mentioned in §4.1.4. So, with the limitations of current generation of X-ray spectroscopic instruments, we are only able to measure the electron temperature with accuracy. Thankfully, it is the most important diagnostics for characterizing coronal plasmas. Most of the spectral properties of thermal emission (continuum shape, line ratios) are determined by the electron temperature of the plasma. Essentially, (most) X-ray emission is an electron-photon process. The excitations and ionizations are predominantly caused by electrons colliding with the ions. The ion temperature, if measured, is a diagnostic for thermal line broadening. Lastly, as the SNRs' X-ray-emitting plasmas are optically thin to X-rays, X-ray spectroscopy becomes a powerful tool to measure elemental abundances: of SN nucleosynthesis for young SNRs, and of the ISM for old SNRs.

5.1.1.1 Bremsstrahlung Continuum Emission

Thermal X-ray spectra of supernova remnants consist of continuum emission caused by bremsstrahlung, recombination and two-photon processes [Vink 2011]. The term "bremsstrahlung" (German for "braking radiation") is used to describe the radiation that is emitted when charged particles (mostly electrons) are decelerated (or accelerated) in presence of other charged particles (mostly nuclei) or an electric field. This is the most important continuum emission mechanism for SNRs, with most of the output in X-rays. In radio and infrared astronomy, it is commonly known as "free-free emission". As we expect a Maxwellian distribution of electrons producing the radiation, this form of continuum emission is specifically referred to as *thermal bremsstrahlung*. This can be contrasted from *non-thermal bremsstrahlung* or even *relativistic bremsstrahlung* when the population of electrons is shock-accelerated. Thermal bremsstrahlung is rather the result of electrons colliding with protons, He, or heavier nuclei.

A Maxwellian energy distribution $f(E)$ of electrons with temperature T_e is given by:

$$f(E) = 2\sqrt{\frac{E}{\pi}} \left(\frac{1}{k_B T_e}\right)^{3/2} \exp\left(-\frac{E}{k_B T_e}\right), \tag{5.1}$$

The emissivity for free-free emission from a plasma with electrons distributed around this function is given by:

$$\epsilon_{\text{ff}} = \frac{2^5 \pi e^6}{3 m_e c^3} \left(\frac{2\pi}{3 k_B m_e}\right)^{1/2} g_{\text{ff}}(T_e) T_e^{-1/2} \exp\left(-\frac{h\nu}{k_B T_e}\right) n_e \sum_i n_i Z_i^2 \,\text{erg}\,\text{s}^{-1}\text{cm}^{-3}\text{Hz}^{-1}, \tag{5.2}$$

where $g_{\rm ff}(T_e) \approx 1$ is the frequency-dependent Gaunt factor, and subscript i denotes various ion species [Vink 2011]. For plasmas with abundances closer to solar or 'cosmic' values, the normalization $n_e \sum_i n_i Z_i^2 \approx n_e n_H$. Integrating this quantity over the volume (dV) of emission gives the **emission measure (EM)** of the plasma, which is also used in the X-ray spectral fitting code XSPEC as the normalization factor (see Eq. 6.3).

5.1.1.2 Radiative Recombination Continuum

Radiative recombination occurs when a free electron (with energy E_e) is captured and *bound* into an atomic shell (with principal quantum number n) of an ion; hence the name "free-bound emission". A photon is emitted with an energy $h\nu_n = E_e + \chi_n$, with χ_n being the ionization energy of the final configuration. For a specific energy level, the emissivity due to the free-bound process is given by:

$$\epsilon_{\rm fb} = (\frac{2}{\pi})^{1/2} n_e n_{z+1} \frac{g_z}{g_{z+1}} \, c\,\sigma(h\nu) \left(\frac{h\nu}{\chi_n}\right) \left(\frac{\chi_n^2}{m_e c^2 kT}\right)^{3/2} \exp\left(-\frac{h\nu - \chi_n}{kT_e}\right) \text{ erg s}^{-1}\text{cm}^{-3}\text{Hz}^{-1}, \tag{5.3}$$

where n_{z+1} is the density of the ion with charge $z+1$, g_{z+1} and g_z are the statistical weights of the ion before and after recombination, and $\sigma(h\nu)$ is the photo-ionization cross-section for the final state of the ion [Vink 2011].

This process is actually the opposite of photoionization (discussed in §5.2.1 in the context of detecting X-rays through matter), and important for the ionization balance of SNR plasma. The emission itself is only quasi-continuous, as it produces line-like emission near the series limits for $kT \ll h\nu$, such as in photo-ionized or overionized plasmas. The continuum, called the radiative recombination continuum (RRC) dominates over bremsstrahlung for $kT \ll 0.1$ keV [Kaastra et al. 2008].

5.1.1.3 Two-Photon Emission

Another source of continuum emission from SNR plasmas, which are very low-density, is "two-photon emission". It occurs when a free electron collides with light nuclei exciting the bound electron from 1s to 2s (metastable) state. As quantum-mechanical selection rules forbid a radiative 2s→1s transition, the ion must be excited to even higher (e.g., 2p) state to be able to return to the ground state (1s). But, for sparse SNR plasmas, the probability of a second collision is very low: the electron relaxes by emitting two photons. The three types of thermal continuum emission mechanisms are summarized in Fig. 5.1 for a pure Si-rich plasma in NEI.

5.1.1.4 Discrete Line Emission

Fundamentally, line emission is a quantum mechanical process of atomic transitions. This involves transition probability matrices and Einstein coefficients, which we cannot divulge here[see Dopita & Sutherland 2003; Kaastra et al. 2008]. We just mention that the most important processes that shape the line emission spectra of SNR plasmas are collisional excitation & ionization, and radiative recombination (free-bound transition). The latter was already discussed in §5.1.1.2 as a source of free-bound continuum emission. Collisional processes of (atomic) excitation and ionization involve transition of an electron from a lower to a higher energy-level or ejection from the atom, respectively, due to 'collision' with a free electron. For SNRs these electron-ion collisions dominate over other forms, e.g., photo-excitation and photo-ionization. Also, collisional de-excitation can be neglected for the rarefied SNR plasmas.

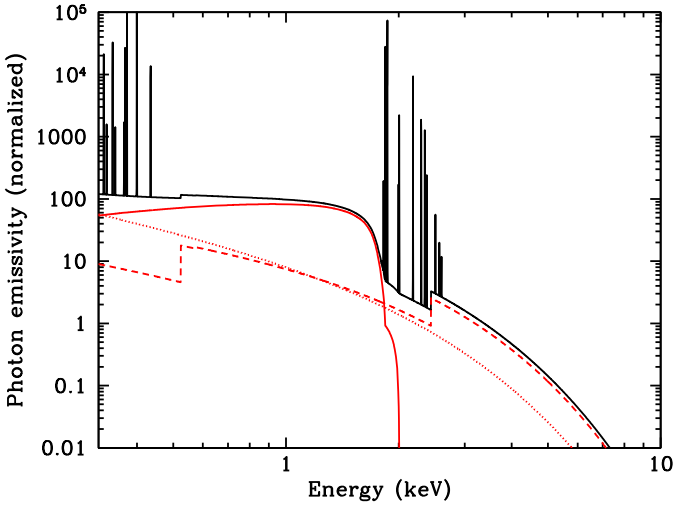

Figure 5.1: The emissivity of a pure silicon plasma out of ionization equilibrium (kT_e = 1 keV, $n_e t$ = 5×10^{10} cm^{-3} s). The total emissivity (black line) is the sum of contributions from free-free (dotted line), free-bound (dashed line) and two-photon (red solid line) emission processes. [from Vink 2011]

For temperatures $> 10^6$ K, which is the case for young and middle-aged remnants, most of the alpha-elements (O, Ne, Mg, Si, S, Ar, Ca) are in the He-like or H-like ionization stage, with line emission in the energy band from 0.5 to 10 keV. Fe and Fe-group elements emission lines in the 0.7–1.5 (L-shell transition) or the 6–8 keV (K-shell transition) ranges. [Vink 2020]. Fe line emission is an important diagnostic tool to constrain the state of plasma in SNRs, in determining kT_e and $n_e t$. And, if instrumental resolution is even better, "He-triplet" lines can be observed.

5.1.2 Non-Thermal X-ray Emission

If we talk about non-thermal emission from supernova remnant in general, we need to go beyond X-rays. Even though, SNRs could (and are observed to) emit non-thermal X-rays via synchrotron acceleration or non-thermal bremsstrahlung, the majority of radiation is in radio, from the same processes. Hence, here we discuss the basic mechanisms that lead to emission from a non-thermal population of particles.

5.1.2.1 Synchrotron Radiation

Synchrotron radiation is emitted by relativistic charged particles spiraling within a magnetic field. These are predominantly electrons (or positrons), being the lightest available charges. A particle with a charge Ze moving through a magnetic field of strength B experiences a **Lorentz force**:

$$\mathbf{F}_L = \frac{1}{c} Ze\, \mathbf{v} \times \mathbf{B}. \tag{5.4}$$

This centrifugal force does not change the magnitude of the particle's momentum but causes it to move in a circular trajectory perpendicular to the magnetic field. Adding the component of motion parallel to the field, the particle traverses a helix. Since the charged particle is accelerated, it radiates energy according to the (relativistic) **Larmor formula**:

$$\frac{dE}{dt} = \frac{2}{3} \frac{Z^2 e^2}{m^2 c^3} \gamma^2 \left[\left(\frac{dp}{dt} \right)_\perp^2 + \gamma^2 \left(\frac{dp}{dt} \right)_\parallel^2 \right], \tag{5.5}$$

where $\gamma = (1 - v^2/c^2)^{-1/2}$ is the Lorentz factor of the particle, and $p = \gamma m v$ is the relativistic momentum of the particle. This formula accounts for the fact that relativistic particles radiate more energy when their motion involves perpendicular acceleration relative to the direction of their velocity [Vink 2020]. Detailed calculations [Ginzburg & Syrovatskii 1965] show that a relativistic electron with energy E moving in a magnetic field of strength B emits synchrotron radiation, with maximum power at a characteristic frequency $\nu_{\rm ch}$, or energy:

$$h\nu_{\rm ch} = 19 \left(\frac{B_\perp}{100\,\mu\mathrm{G}} \right) \left(\frac{E}{100\,\mathrm{TeV}} \right)^2 \mathrm{keV}, \tag{5.6}$$

where $B_\perp \approx B\sqrt{2/3}$ is the component of the magnetic field perpendicular to the motion of the electron. From this, we can deduce the typical electron energy associated with radio emission from SNRs is about a GeV. For typical magnetic fields inside SNRs, B ranges from 10–500 μG, the emitting electrons would have energies in the range of 10–100 TeV [Vink 2011], which implies X-ray synchrotron radiation. This has been observed, e.g., in SN 1006 [Koyama et al. 1995].

5.1.2.2 Inverse-Compton Scattering

Another cause of non-thermal X-rays from supernova remnants has been considered to be the bremsstrahlung of lower-energy electrons via inverse-Compton effect. The expected output, however, is in GeV–TeV hard X-ray or γ-ray bands [Hinton & Hofmann 2009]. Inverse-Compton scattering is a electron-photon collision, where (comparatively) higher-energy electrons boost the photons to higher frequency. Since this process is not very important for SNRs, both theoretically and observationally, we avoid going into details here.

5.2 Detection Methods

Observing X-rays is a difficult task for a number of reasons. First, typical optical systems (silver mirrors, glass lenses for reflection/refraction) do not work for X-rays. The unfavorable interaction of X-ray photons with detector atoms (§5.2.1) limit us to the phenomenon of grazing-incidence reflection (§5.2.1.2). Even then, true imaging in astrophysical context could only be achieved by using a certain geometry of paraboloidal-hyperboloidal mirrors (§5.2.1.3) and nesting multiple of them together, leading to first X-ray telescopes (§5.2.2) aboard rockets and satellites. We briefly relate the history (§5.2.2.1) and characteristics (§5.2.2.2) of these in a general way, and discuss more detail in §6.1.1 for a specific satellite observatory. Similarly, we discuss CCDs in general in §5.2.3 before specifically discussing such cameras deployed in space (§6.1.2). Finally, X-ray background (5.2.4) is discussed.

5.2.1 X-ray Optics

5.2.1.1 Refraction and Photoabsorption

X-rays cannot be analogously refracted and reflected as visible light, a difficulty apparent since its discovery by Röntgen [1896]. This can be attributed to atypical optical constants in the X-ray electromagnetic band. Namely, the refractive index of all materials in X-rays is close to 1 (slightly lesser), unlike usual optics where it is greater than 1. The X-ray refractive index (n, Eq. 5.7) is determined by the properties of the (medium) atom interacting with the incoming (X-ray) photon (Eq. 5.8) [see Spiga 2005].

$$n = 1 - \delta + i\beta \tag{5.7}$$

$$n = 1 - \left(\frac{N_A r_e}{2\pi A}\right) \lambda^2 \rho (f_1 + i f_2) \tag{5.8}$$

In this model for n, the real part ($\delta \sim 10^{-4} - 10^{-5}$) accounts for refraction, while the imaginary part ($\beta \sim 10^{-5} - 10^{-6}$) mainly for photoabsorption; N_A is the Avogadro number, A is the atomic mass number, r_e is the classical electron radius, ρ is the mass density, while f_1 and f_2 are (semi-empirical) atomic scattering coefficients [compiled by Henke et al. 1993]: $f_1 \approx Z$ is the number of scattering electrons per atom and $f_2 = \sigma_{pe}/(2r_e\lambda)$ is proportional to the photoelectric cross-section.

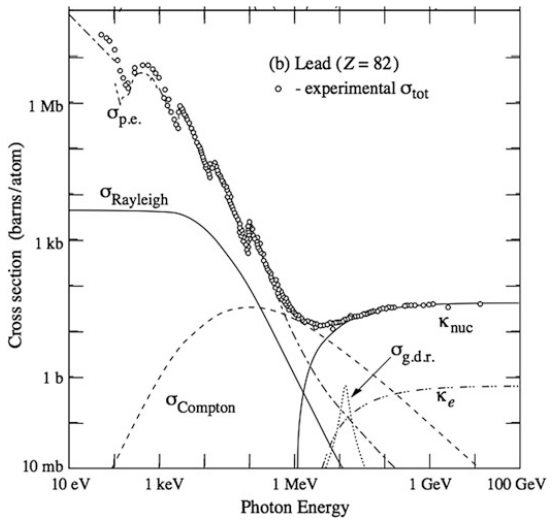

Figure 5.2: Interaction cross-section of lead (Pb) atoms with respect to photons over a large energy range. The total cross-section (σ_{tot}) at any given energy is the sum of cross-sections of different fundamental interactions like photoelectric effect ($\sigma_{p.e.}$), Rayleigh and Compton scattering, pair production in presence of nucleus (κ_{nuc}) or electron (κ_e), and photonuclear dissociation ($\sigma_{g.d.r.}$). 1 barn (b) = 10^{-28}m^2. [D'Auria 2018 from Tanabashi et al. 2018]

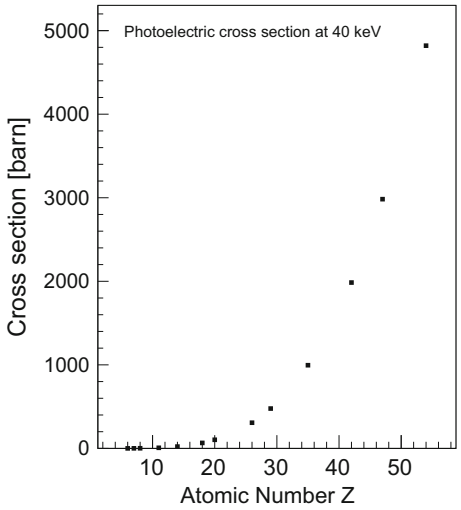

Figure 5.3: Interaction cross-section per atom for the photoelectric process for 40 keV X-ray photons, as a function of the atomic number of the absorber. Here, best fit: $Z^{4.2}$ variation. [D'Auria 2018 with NIST Data from Hubbell 1969]

The dominant photon-atom interaction process at X-ray energies ($0.1 - 100$ keV) is indeed absorption due to photoelectric effect. The "coherent" Rayleigh and "incoherent" Compton scattering also occur, and contribute to the total *cross-section* (viz. the quantum mechanical probability of interaction) and the *attenuation* of passing (X-)radiation. Other effects, such as pair production and photonuclear dissociation can be neglected. See Fig. 5.2.

X-ray photons excite the inner(most)-shell K, L, M,.. electrons out of their atoms, leading to *absorption edges* at corresponding shell-binding energies in the photoabsorption cross-section curve (discontinuities visible in Fig. 5.2). This is where prominent variations of the optical constants occur and lead to anomalous dispersion effects in the material [Pareschi et al. 2021].

The photoelectric cross-section depends on energy (E) of the incoming photon *and* on the atomic number (Z) of the absorber, in general, in a complicated manner, of the form $\sigma_{pe} \propto Z^n/E^m$, but reasonable approximations are with $m = 3$ or 3.5 and $4 < n < 5$ depending on

the energy range [D'Auria 2018; Angelis & Pimenta 2018; Fabjan & Schopper 2020]. That is, at a given photon energy, photoabsorption steadily increases with Z (see Fig. 5.3), and hence low-Z materials like carbon are less sensitive to photoelectric effect, while heavier elements like lead are good absorbers as well as better reflectors (used as radiation shields and X-ray screens) [Spiga 2005].

5.2.1.2 Grazing-Incidence Reflection

The closeness of n to 1 implying too long a focal length, and thick lenses implying too large an absorption, rule out refractive in favor of reflective optics for X-rays. Moreover, the extreme smallness of δ compared to unity implies that *reflectivity* from a mirror surface is always small, except at sufficiently small ("grazing") angles when the incident ray is *totally reflected*. This was first experimentally demonstrated by Compton [1923], and follows from application of Fresnel equations and Snell's law to the (X-ray optical) system [see Spiga 2005]. The critical angle can be approximated as:

$$\theta_C \approx \sqrt{2\delta} \propto \frac{\sqrt{\rho}}{E} \tag{5.9}$$

showing how it increases with the reflector density ρ and falls with increasing energy E (see Fig. 5.4). The reflection angles are always small anyway, e.g. $< 1°$ for soft X-rays ($0.1 - 10$ keV), and get worse for higher energy (hard) X-rays even with the densest coatings (which, of course, also increases the photoabsorption) [Pareschi et al. 2021]. It should also be noted that the mirror surface has to be very smooth (superpolished, with microroughness below a few angstroms) to approach the predicted reflectivity.

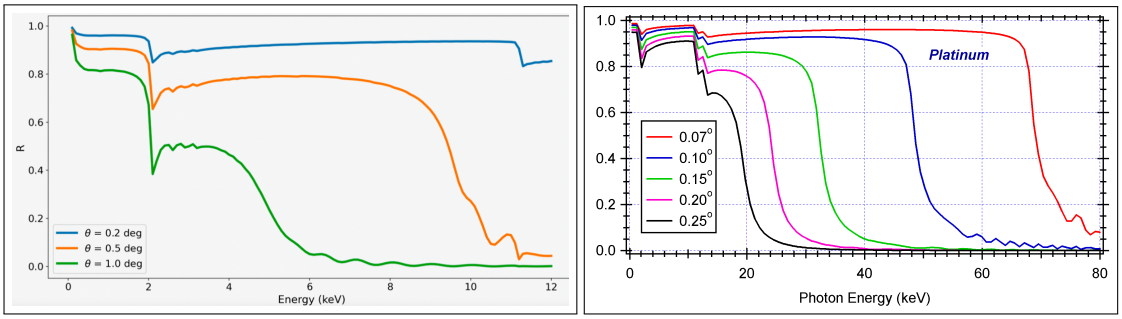

Figure 5.4: Typical reflectivity curves of Ir (left, Z=77, ρ=22.42 g/cm^3) and Pt (right, Z=78, ρ=21.46 g/cm^3) coated ideal surfaces: reflectivity (R, in fraction) as function of X-ray energy (E, in keV) for different grazing incidence angles. [Christensen & Ramsey 2022; Spiga 2005]

5.2.1.3 Wolter-I Mirror Configuration

Thus, for focusing and imaging X-rays, we are practically constrained to grazing-incidence reflective optical systems. Following Compton's [1923] work on total external reflection at grazing angles, Kirkpatrick & Baez [1948] produced first images with grazing-incidence mirrors. It was a double-reflection system with 2 mutually perpendicular, approximately paraboloidal mirrors. This design, the Kirkpatrick-Baez (KB) system, removes spherical aberrations but still suffers from coma aberrations.

A coma-free image requires the so-called Abbe sine condition to be satisfied at all points of the reflecting surface(s). For this, Wolter [1952a] proposed a family of configurations consisting of a paraboloidal mirror with either a hyperboloidal (types 1 and 2) or ellipsoidal (type 3) secondary mirror. The two conic section reflecting surfaces are coaxial and confocal. The most

popular geometry is of the Wolter type 1 (*Wolter-I*) shown in Fig. 5.5, an internally reflecting paraboloid-hyperboloid. It has the advantage of a short(er) focal length, with the added possibility of nesting confocal shells to increase photon collecting area, and easier & robust mirror manufacturing [Pareschi et al. 2021].

Other X-ray mirror configurations include a Schwarzschild variant of Wolter-I which exactly fulfills the Abbe sine condition for coma correction, discussed by Wolter [1952b] [Chase & VanSpeybroeck 1973], although various ray tracing programs [e.g., Werner 1977] favor the original Wolter-I optics. The fundamental parameters of this type (1) were first systematically assessed by VanSpeybroeck & Chase [1972] who laid down empirical formulas for angular resolution, point spread function and collecting area. Along with KB and Wolter systems, the focusing collimator or "lobster-eye" X-ray optics [Angel 1979] forms the third family of double-reflection grazing-incidence systems in astronomical applications.

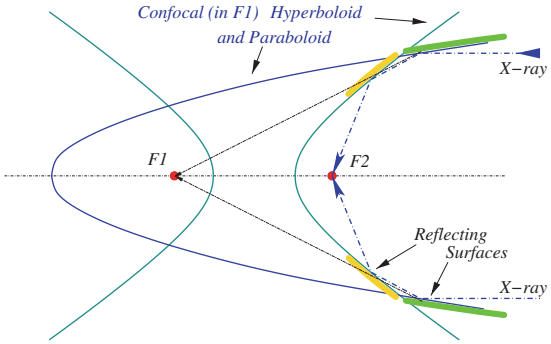

Figure 5.5: Wolter type 1 mirror configuration for X-ray telescopes. See source [Pareschi et al. 2021, Fig. 13] for types 2 and 3 also.

5.2.2 X-ray Telescopes

5.2.2.1 History

Giacconi & Rossi [1960] proposed the first application of grazing-incidence telescopy to X-ray astronomy. Their optic was simply a truncated paraboloidal mirror, capable merely of focusing the X-ray photons than any true imaging. This would soon change with fabrication of *nested confocal Wolter-I mirror shells* [Giacconi et al. 1969]. Notably, 2 years later, the group of Giacconi et al. [1962][1] would discover the first extra-solar X-ray source (Sco X-1) embedded in a diffuse isotropic cosmic X-ray background (CXB) using collimated detectors in Geiger mode flown on a rocket. The early missions were mostly rocket- or balloon-borne and directed at the Sun, our closest source of X-rays; worth mentioning is the imaging spectroscope aboard NASA's *Skylab* (1973-74) space station for studying solar X-ray emission.

The age of probing cosmic X-rays with satellites began with *Uhuru* [SAS-1, Giacconi et al. 1971] which performed the first all-sky X-ray survey and cataloged 339 X-ray sources, but *Einstein* [HEAO-2, Giacconi et al. 1979] was really the first high-resolution X-ray observatory in space. The treasure of scientific results obtained from Einstein include X-ray images of historical SNRs, Cas A and Crab nebula.

The following period and up to the late 1990s saw a number of X-ray missions from USA, Europe, Japan, Russia and India [see Santangelo et al. 2023 for a chronological history]. The

[1] Riccardo Giacconi deservedly won the Nobel Prize in Physics 2002 for his pioneering contribution to X-ray astrophysics. [Nobel Lecture: Giacconi 2003]

most significant, in science and in technology, were: ESA's *EXOSAT* (1983-1986), German *ROSAT* (1990-1999) and NASA's *RXTE* (1995-2012).

Chandra [CXO, Weisskopf et al. 2000], followed by *XMM-Newton* (§6.1) launched in 1999 marked a new generation of X-ray telescopes with high(est) spatial resolution and large(st) effective area (respectively) over a wide(r) energy band. The progress was continued with *Suzaku* (2005-2015), *NuSTAR* (2012-), *eROSITA* (2019-) and *XRISM* (2023-). The future will see more ambitious missions such as *ATHENA* (2037?-). See Tab. A.2 for an exhaustive list of X-ray-band satellite missions.

5.2.2.2 Characteristics

A X-ray telescope's quality is characterized by its ability to collect and focus photons over an energy range, quantitatively by effective area, angular resolution and spectral resolution. The sensitivity, i.e., the minimum detectable flux (photon energy per unit area per second) given by total source and background counts as the signal-to-noise ratio $S = C_s/\sqrt{C_s + C_b}$, depends on collecting area, exposure time, energy band and quantum efficiency of the detector.

The simplest system consists of a X-ray collimator (a system of channels) to limit the solid angle to a X-ray detector (such as a gas-filled proportional counter). Such collimated, opposed to focusing, telescope have a (poor) angular resolution which coincides to its field-of-view (FOV) and a sensitivity limited by detector area (as $\sqrt{A_d}$). Mirror optics, on the other hand, focuses the photon flux to a small detection point, thereby greatly reducing the background noise and resolving extended sources (see Fig. 5.6). Their sensitivity is improved in proportion to the effective area (A_e) of the mirrors. For comparison, *Chandra* has a mirror effective area ≈ 800 cm^2 at 0.25 keV, comparable to detector area of each of the two large-area proportional counters of *Uhuru*, but a sensitivity 10^5 times higher [Christensen & Ramsey 2022], and *Einstein* had a sensitivity 10^4 times the Geiger counters used in the discovery of Sco X-1.

The photon distribution in the focal plane is usually expressed in terms of PSF (point spread function): 2-dimensional distribution of photons from an object at infinity. Its 1D integral is called LSF (line spread function). The angular resolution is measured in terms of fractional encircled energy (EE) within a certain angle around the optical axis – usually half-energy width (HEW) or half-power diameter (HPD), at which 50% of photons are effectively focused onto the focal plane. Less accurately, LSF FWHM (full-width at half-maximum) is also used. They, along with effective area, determine the sensitivity. S is sometimes given in units of flux of the Crab SNR, considered a standard candle for X-ray instruments calibrations [Kirsch et al. 2005]. The spectral resolution is quoted in dimensionless $E/\Delta E$ to distinguish between the smallest energy difference at a given energy.

5.2.3 CCD Cameras

X-ray optics also allow the use of high-performance detectors in the focal plane. In early days of X-ray astronomy, imaging systems composed of gelatin-coated films, scintillating crystals or photocathode tubes were employed [see Giacconi et al. 1969]. This was revolutionized by the invention of charge-coupled devices (CCDs), imaging detectors based on semiconductor technology. The concept of CCDs was first sketched by Boyle & Smith [1970] of Bell Labs, who were awarded one-half of the Nobel Prize in Physics 2009 for their invention. Long been used as optical sensors in cameras, CCDs found application in X-ray astronomy with XMM-Newton and (failed) ABRIXAS missions.

The simplest solid-state particle/photon detector is a reverse-biased pn-junction diode. A photodiode is formed when an *intrinsic* semiconductor (like Si) is *doped* with "donor" (like P)

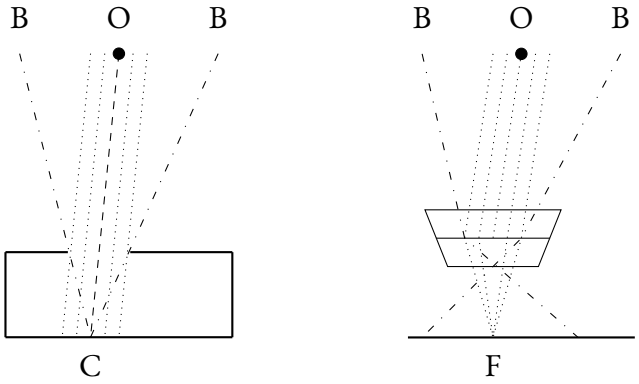

Figure 5.6: X-ray collimation vs. focusing: A collimator (**left**) simply projects the X-rays from a source O over a very large area of the detector C, including all the background B in its FOV; while mirrors (**right**) focus the parallel rays from the source on a tiny area on the detector F, essentially decoupling source and background.

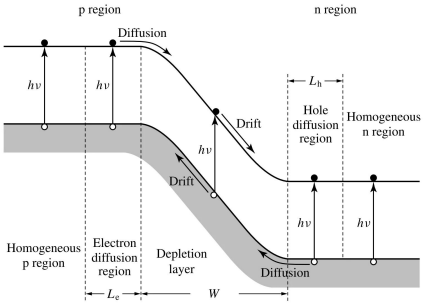

Figure 5.7: Schematic of a pn-junction photodiode, showing different regions of the semiconductor as well as the processes that lead to the photocurrent. [Fosco Connect 2023]

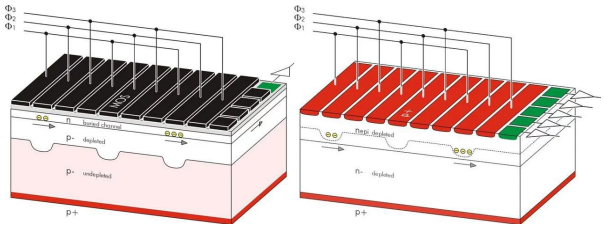

Figure 5.8: Schematic cross-sections of MOS (**left**) and pn (**right**) CCDs. In both, charge is shifted from left to right by applying 3 periodical voltage clocks connected to the MOS metal registers or pn implants. Each pn-CCD pixel column has its own readout amplifier, unlike MOS. [MPG HLL]

or "acceptor" (like B) atoms and the resulting *p*- and *n*-type *extrinsic* semiconductors are sandwiched together. A "reverse-bias" voltage enables detection of incident photons as changes in the current flow, as the photon energy causes transition of valence electron(s) to the conduction band (see Fig. 5.7). This works only for semiconducting solids as their "band-gap" energy is just enough for such photo-excitation ($\sim$3.7 eV for Si at $-90°$C). A two-dimensional array of photodiodes ("pixels"), along with apparatus for charge collection ("read-out") and current amplification ("amplifiers"), creates a CCD, an imaging detector [see McLean 2008, for details].

There are two common CCD types used in X-ray astronomy today: pn and MOS CCDs. The two diagrams in Fig. 5.8 show the basic design of the two types. As suggested by the name, pn-type CCDs have pn-junctions as pixel units. Usually, they are back-illuminated, i.e., photons enter from the bottom of the detector. X-ray pn CCDs were pioneered by Strüder et al. [2001] for the EPIC detector onboard XMM-Newton. Their structure has a large depletion volume and very good *quantum efficiency*, although the fabrication is more difficult. MOS CCDs have a insulating layer, historically of metal-oxide, between the gates and doped layers; hence the name metal-oxide semiconductor. They are easier to manufacture but more prone to radiation damage than pn CCDs. Two cameras based on this technology are installed on the XMM-Newton [Turner et al. 2001].

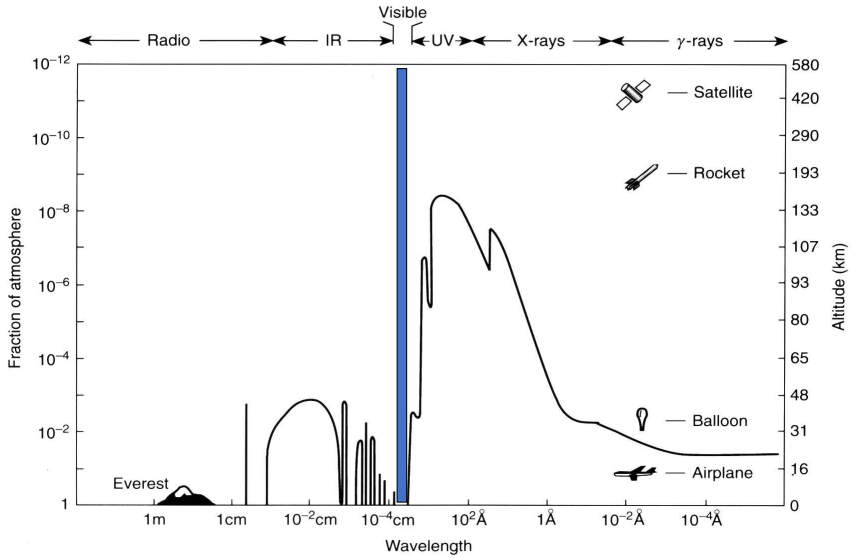

Figure 5.9: Atmospheric absorption of electromagnetic waves in terms of fraction (in atm) or column (in km) of atmosphere that absorbs half of the incoming radiation; a wide radio and a thin visible light "window" can be seen. [Santangelo et al. 2023]

5.2.4 X-ray Background

From emission at a source to detection in a CCD, X-rays are absorbed & scattered and contaminated by various celestial, solar, terrestrial and instrumental components. That is, the received signal is attenuated, and intermixed with "background" signals. Firstly, the detector's intrinsic readout mechanism and interaction with (low- or high-energy) particles or photons introduces a set of "instrumental" background. These may be induced by "soft" protons from solar flares (SPF) and (photon) emission from solar wind charge exchange (SWCX). Then, atmospheric attenuation of electromagnetic radiation is severe in the X-ray range (see Fig. 5.9), hence the need for deploying X-ray instruments on balloons, rockets and satellites. Apart from being the origin of SPF and SWCX, Sun is also a bright X-ray emitter. If not the target themselves, these contributions are a foreground nuisance to X-ray observations of distant sources, especially of extended & diffuse emission from astrophysical plasmas such as in a supernova remnant. We discuss the various instrumental background components in §6.1.2.3 for the particular case of XMM-Newton's EPIC CCDs, and how to model & subtract them in subsequent analysis (§6.2) of soft X-rays from a specific LMC SNR. Here we discuss the astrophysical causes of background components (AXB) including the CXB which permeates the whole sky.

5.2.4.1 AXB

Beyond Earth's atmosphere and Sun's heliosphere, X-rays are attenuated by ISMa. The reason is that X-rays photo-ionize and are photo-absorbed by the diffuse gas, molecules and dust grains in the ISM. The total photoionization cross-section is usually normalized to the total hydrogen number density N_H, also referred to as the *column density* along a line-of-sight. Apart from this absorbing component, there are emission sources of astrophysical X-rays, which we collectively call the astrophysical X-ray background (AXB) here. It has 3 or 4 components. At the 'softest' parts, the emission is known to be thermal and Galactic in origin. Closest to us, in the solar neighborhood is the Local Hot Bubble (LHB), a region of hot ($\sim 10^6$ K or $kT \approx 0.085$ keV) plasma [Henley & Shelton 2008]. Then there is additional thermal emission from plasmas in the Galactic halo. There is a cool ($\sim$0.1 keV) and a warm ($\sim$0.25 keV) component.

Finally, there is a diffuse component of the AXB, referred to as the CXB, that spans from ∼2–100 keV. It was discovered with the discovery of the first extrasolar X-ray source [Giacconi et al. 1962, Sco X-1], then mapped by the HEAO-1 observatory, and have been extensively since then. Currently, the soft part of its X-ray spectrum (<10 keV) have been almost entirely (80–90%) resolved as emission from discrete sources. These are mostly active galactic nucleus (AGN), with small contributions galaxy clusters and starburst galaxies [see Moretti et al. 2009, and references within]. For the purpose of X-ray spectral fitting this extragalactic background component is usually treated as a powerlaw with a index like $\Gamma = 1.46$ [see Chen et al. 1997].

Part II

Research

Chapter 6

X-ray Data Analysis

This chapter describes the X-ray observation of a SNR (candidate, confirmed hereafter) in the LMC, MCSNR J0500–6512. The instrument for data was EPIC (§6.1.2) on XMM-Newton and the software for analysis was XMM-ESAS (§6.1.3). The standard manual for reduction of XMM data have been thoroughly followed, and the step-by-step procedure is described in §6.2.1. This leads to creation of background-subtracted images of the source from the data, in bands suitable for soft diffuse emission from SNRs. Imaging analysis (§6.2.2) aids us in our investigation of what appeared to be thermal emission from SNR plasma or shock-heated ejecta. We fit the spectra of this "source", along with a "background" to physical X-ray emission & absorption models, in §6.2.3. The results, further calculations, and their consequences are discussed in §6.3.

6.1 XMM-Newton

X-ray Multi-Mirror Mission "Newton" (*XMM-Newton*) is a space observatory mission with three high-throughput (nested Wolter-I) X-ray telescopes and a (30 cm Ritchey–Chrétien) UV-optical telescope. The spacecraft, weighing 4 tonne & 10 m long, was launched by the European Space Agency (ESA) on an Ariane V504, on 1999 December 10, in a highly elliptical 48 hour Earth orbit. The payload, along with 3+1 telescopes, consists of 6 science instruments of three types: 3 European Photon Imaging Camera (EPIC, 2 -MOS + 1 -pn type CCD arrays) for X-ray imaging, 2 Refraction Grating Spectrometer (RGS) for high-resolution X-ray spectroscopy, and 1 Optical Monitor (OM) for UV-optical imaging & grism spectroscopy. (See Fig. 6.1) [Jansen et al. 2001; XMM-Newton SOC 2023]

6.1.1 Telescope

6.1.1.1 Mirror Modules

At the heart of XMM are the 3 X-ray telescopes, mirror modules (MMs), each an assembly of 58 Wolter-I mirror shells nested in a coaxial and confocal configuration (Fig. 6.2). The optics has a focal length of 7.5 m and grazing-incidence angles range from 17–40 arcmin. [de Chambure et al. 1999]

The mirrors were fabricated from superpolished gold coated mandrels using a nickel electroforming technique, innermost with diameter 30.6 cm & thickness 0.5 mm and outermost with 70 cm & 1 mm. The Au layer on Ni shells is $\sim$250 nm thick with microroughness $\leq$5 nm. [Aschenbach 2002]

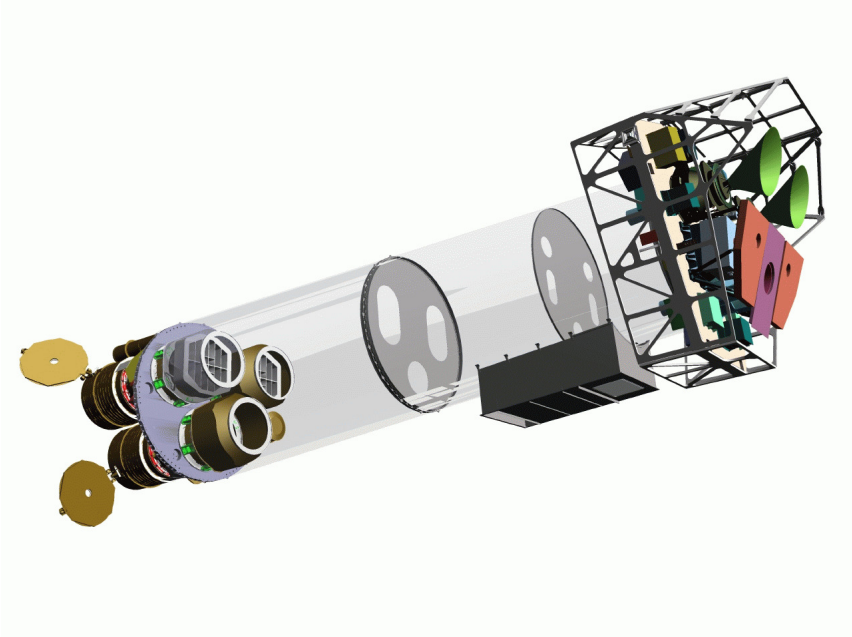

Figure 6.1: XMM-Newton spacecraft "open" view, showing two large payloads separated by a long tube. The X-ray telescopes, two with RGAs, are visible at the lower left. At the right end of the assembly, the focal instruments are shown: The EPIC-MOS cameras with their radiators (black/green "horns"), the radiator of the EPIC-pn camera (violet) and those of the (light blue) RFCs (in orange). The black box at the bottom of the bus is the outgassing device. [Dornier Satellitensysteme GmbH]

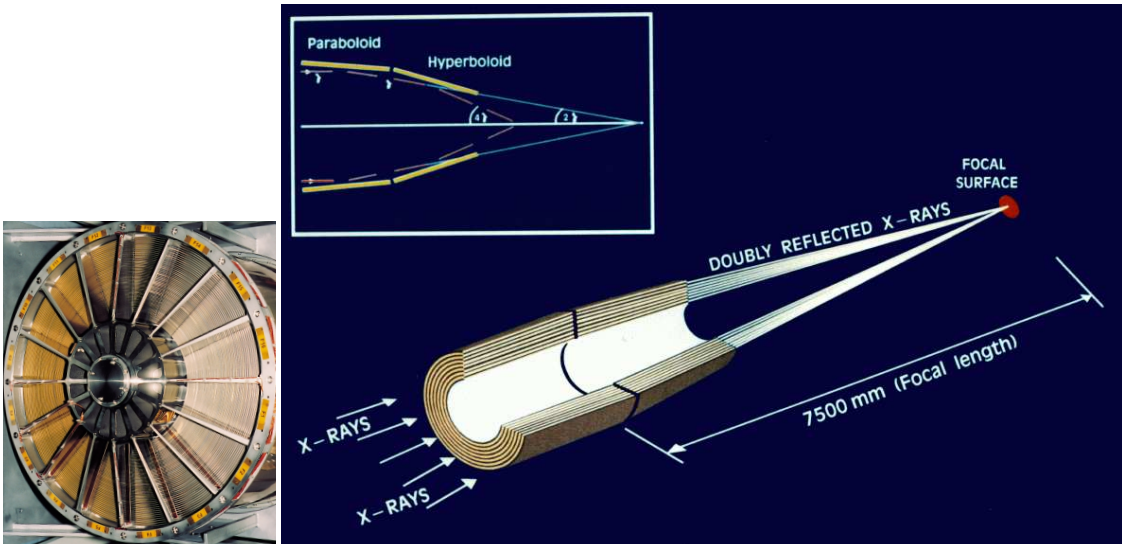

Figure 6.2: XMM Optics: 58 nested Wolter-I mirror shells bunched by 16 spokes. X-rays enter from the **left**, and are focused by successive grazing-incidence reflection from paraboloidal-hyberboloidal mirror system. [de Chambure et al. 1999; XMM-Newton SOC 2023]

The design provides an unprecedented effective collecting area ($\sim$1550 m^2 each at 1.5 keV) over a wide energy band (0.15–12 keV for EPIC) with high spectral (200–800 power for RGS) and good spatial ($\sim$15 arcsec) resolution [XMM-Newton SOC 2023]. See also §6.1.1.3.

The light path from 2/3 MMs to EPIC-MOS1 and -MOS2 is intercepted by an array of grazing-incidence gratings (RGAs), which disperse $\approx$ 40% to focal cameras (RFCs) of RGS1 and RGS2, leaving only $\approx$ 44% at the primary focus. The optics with EPIC-pn at the focus is shown in Fig. 6.2.

6.1.1.2 X-ray baffle

An inherent issue of grazing-incidence X-ray optics is the contamination from sources outside the field of view , so-called *straylight*. This happens from single reflection of rays off rear-end of the hyperbola, if the stray source is 20–80 arcmin off-axis (for XMM), which can inescapably reach the focal plane cameras. The images have then sharp "arcs" or ring-like structures.

To minimize this effect, the mirror modules are complemented with "pre-collimators" known as X-ray baffles in the front. They consist of 2 sieve plates with 58 annular apertures each, to act as thin cylindrical shells blocking singly-reflected rays. This has proved to be quite effective for straylight rejection (see §6.1.1.3 below).

6.1.1.3 Performance

In accordance to §5.2.2.2, the performance of XMM's optics is evaluated qualitatively by mirror sensitivity and image quality, quantitatively by effective area and angular resolution as well as by its straylight rejection efficiency.

The ability to focus photons is determined by the narrowness of the PSF. For MMs corresponding to EPIC-pn, EPIC-MOS1 + RGS1 and EPIC-MOS2 + RGS2, the on-axis HEW at 1.5 keV are found to be 16.6″, 16.8″ and 17.0″ respectively, for XMM in orbit [XMM-Newton SOC 2023] and matches the ground calibrations.

The ability to collect photon depends on the net[1] effective area of the mirrors at different energies. This is plotted in Fig. 6.3 for different telescope modules of XMM. The geometric area approaches 1900 cm^2 for energies up to 0.15 keV, $\sim$ 1500 cm^2 at 2 keV, 900 cm^2 at 7 keV and 350 cm^2 at 10 keV for each of the three telescopes on-axis; at 15 keV, it drops to $\sim$ 12 cm^2 [Aschenbach 2002], reminiscent of the reflectivity curves of Pt and Ir (Fig. 5.4) discussed in §5.2.1.2. Note also the deficiency for the spectrometers and the sharp drops at Au M absorption edge.

Additionally, XMM observations are affected by light from bright off-axis (<1.5°) stray sources, but 80% of it is efficiently rejected by the X-ray baffles [de Chambure et al. 1999].

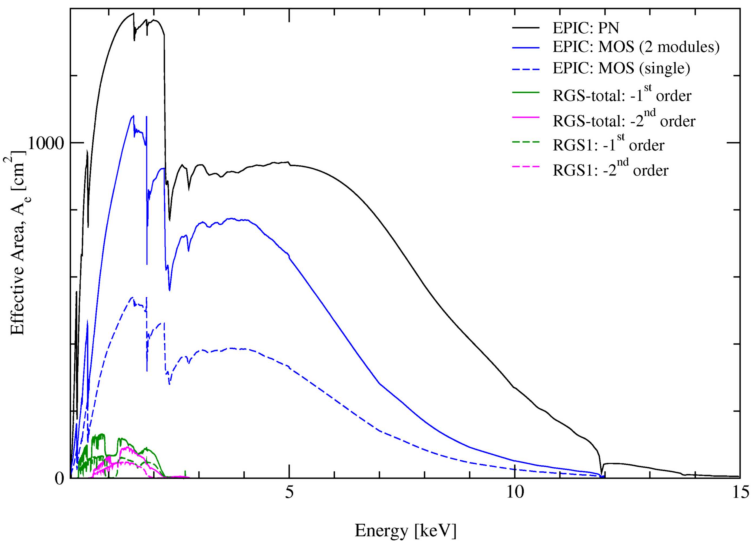

Figure 6.3: Net effective area of XMM telescope modules on a linear energy scale; extracted from instrumental response matrices; maximum is around 1.5 keV; sharp drop around 2 keV corresponds to Au M absorption edge. [XMM-Newton SOC 2023]

[1] i.e., here, the product of telescope effective area and detector quantum efficiency, $A_e \cdot \eta_E$

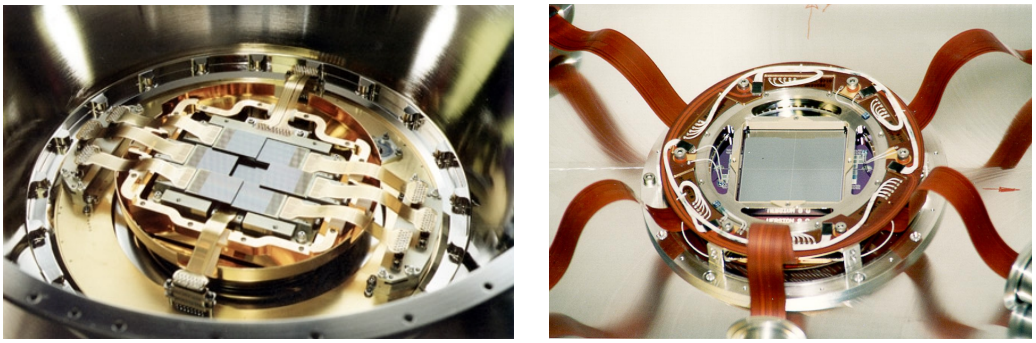

Figure 6.4: EPIC MOS (**left**) and pn (**right**) CCD chip arrays [Credits: ESA]

6.1.2 EPIC

As the name suggests EPIC is a photon imaging camera, a set of CCDs (§5.2.3). There are 2 EPIC-MOS and 1 EPIC-pn cameras in the focii of the 3 XMM telescopes. The two types of EPIC detectors are fundamentally different in chip geometry, pixel size, received flux, and time & energy resolutions. The two MOS cameras each consist of 7 *individual* CCD chips, while the PN camera is an *integrated* array of 12 CCD chips. Two of the seven MOS1 CCD chips, namely MI-3 and MI-6, have been rendered inactive due to micro-meteorite damages. The surface of PN is divided into 4 quadrants with 3 CCDs each.

Both the cameras cover an FOV of around 30' in the 0.2–12 keV band with an spectral resolution of $E/\Delta E \sim 20$–50 and an angular resolution of $HEW \sim 15$". The timing accuracy of PN supersedes that of MOS cameras with time resolution as low as 7μs. [XMM-Newton SOC 2023]

6.1.2.1 -MOS

EPIC-MOS detectors are based on metal oxide semiconductor technology, as mentioned in §5.2.3. There are 7 'EEV type 22' CCDs in the focal plane of each MOS camera [Turner et al. 2001], arranged as shown in Fig. 6.4. They have an high-resistivity epitaxial Si layer with an open-electrode structure. Since MOS cameras are behind RGSs, they receive less than half of the incident flux [XMM-Newton SOC 2023]. Also, since MOS detectors are not monolithic, the individual CCD chips overlap causing unusable "gaps".

It must be mentioned that the cameras need a cooling system as well as some radiation-shielding to operate properly. These are addressed by the MOS cryostat and the MOS radiator. The detectors are also equipped with (thick, medium and thin) filters to block optical/UV or even X-ray light, if required.

6.1.2.2 -pn

EPIC-pn detector is based on the concept of fully-depleted pn semiconductor technology [Strüder et al. 2001]. The readout of the PN chips is much faster than that of the MOS cameras, because each pixel column has its own readout node (as seen in Fig. 5.8). Secondly, they are back-illuminated, which shields them more from radiation, enhances their quantum efficiency. More, each of them receive $\geq$95% light of an on-axis point source from the their telescope [XMM-Newton SOC 2023].

The EPIC cameras can be operated in different combinations of PN and MOS CCDs and/or regions of data acquistion, called *science modes*: full frame, extendend full frame, large window, small window, timing and burst.

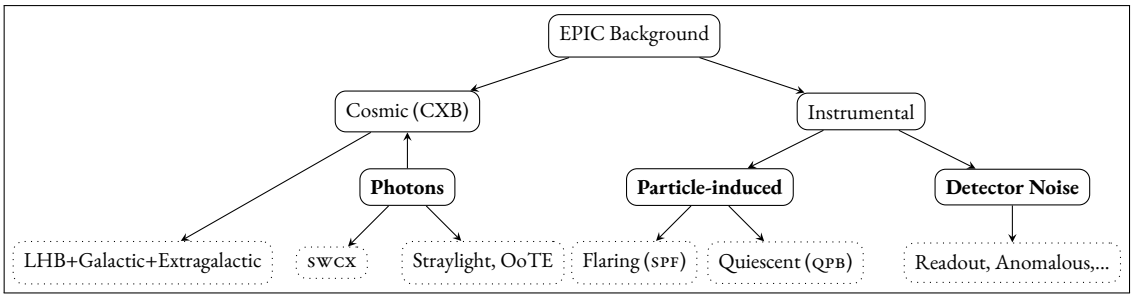

Figure 6.5: EPIC background components

6.1.2.3 Background

The X-ray background seen by EPIC can be classified into three components[2]: Photons, Particles and Electronic Noise.

First and foremost, the photon background includes the astrophysical X-ray background (AXB) of soft diffuse emission from the *LHB* & the *Galactic halo* and a hard X-ray *extragalactic background* from unresolved galaxies and AGNs (see 5.2.4.1). Secondly, solar wind charge exchange (SWCX) emission is a foreground contaminant. Then, light from stray sources, i.e., single reflections from outside the FOV, is a nuisance in some EPIC observations. Additionally, for -pn, a fraction ($\approx 6.3\%$) of recorded events are out-of-time (OoT), i.e., registered during readout of a CCD, which have to be corrected in the data analysis [XMM-Newton SOC 2023, 3.3.10].

As noted in Fig. 6.5, the non-cosmic background component of the EPIC CCDs is partly from detector noise (which is important for low energies, below 300 eV) but primarily particle-induced: an external 'flaring' component and an internal 'quiescent' particle background. The instrumental particle-induced background is caused by energetic particles interacting with the detectors, directly or via fluorescent X-rays produced from striking surrounding hardware. The flaring component is attributed to soft protons (low energy, $E_p < 100$ eV) from solar flares, funneled by the mirrors to the detectors, which 'appear' like X-ray photons. These soft proton flares (SPF) are highly temporally variable. The quiescent component of the particle background (QPB) is induced by high-energy particles (cosmic rays, $E \gtrsim 100$ MeV) penetrating the detector apparatus. It is variable on a longer timescale, hence more stable and easier to model & subtract (from the source spectrum).

The electronic noise in the detectors includes bright pixels or (parts of) columns, readout noise and negligible dark current [Carter & Read 2007]. Notably, in certain outer -MOS chips, artificial low-energy enhancements are observed. These are characterized by anomalously low hardness ratio and anomalously high background rate, called anomalous states [Kuntz & Snowden 2008]. The cause of this temporal anomaly is not yet known, nevertheless the procedure of identifying & excluding the affected CCDs is well-integrated into the standard data analysis of XMM EPIC-MOS data.

6.1.3 ESAS

XMM-Newton Science Analysis System (SAS) Extended Source Analysis Software (*XMM-ESAS*) package is a collection of tasks for analysis of EPIC observations of extended objects and the diffuse X-ray background. SAS, a suite of programs (tasks, scripts and libraries coded in

[2]Visit `https://www.cosmos.esa.int/web/xmm-newton/epic-background-components` for a table summarizing their temporal, spectral and spatial properties.

C++, Fortran 95, Perl and Python), is the main tool for reduction, extraction and analysis of all XMM data, incorporating ESAS for extended diffuse source data analysis.

We refer to the "ESAS Cookbook" prepared by Snowden & Kuntz [2023] for SAS 21.0, along with SAS 'guides' and 'Data Analysis Threads'[3] for data reduction, spectra extraction and creation of background-subtracted & exposure-corrected images of our source.

The initial steps are same for both spectroscopy and imaging. We start with the latest recalibrated event files, check (and remove, if any) CCDs in anomalous states, identify (and remove) time segments affected by soft proton flares, locate (and mask) point sources, and extract the (QPB) spectrum of the region of interest. This concludes with the spectral analysis, done elsewhere, e.g., XSPEC [Arnaud 1996]. For imaging, we still need a (rough) fitting of the spectrum (over FOV or ROI) to estimate (and filter) residual soft proton (SP) flare contamination [Kuntz & Snowden 2008]; similarly and probably for solar wind charge exchange (SWCX) emission [Snowden et al. 2004]. The QPB, SP and SWCX images are then produced and subtracted from the count image, divided by the exposure image to get a flux-calibrated image of the region. The general procedure, outlined in Fig. 6.6 as a flowchart of (E)SAS tasks, is as follows:

1. Setup (`cifbuild` & `odfingest`)
2. Initial Processing (`-chain` or `-proc`)
3. Soft Proton Flare filtering (`espfilt`)
4. Anomalous CCDs' detection (`emanom`)
5. Point Sources' excision (`cheese`)
6. Intermediate Spectra & Quiescent Particle Background creation (`-spectra` & `-back`)
7. Spectral Fitting
8. Image Production (`combimage` & `binadapt`)

There are various caveats and intermediate steps in the full analysis, such as generating custom point source list (`edetect_chain`) & region files (`region`), converting (e.g., detector to sky, `rotdet2sky`) coordinates, grouping spectral files (`specgroup`) and so on, which often require outside tools such as ds9 [4] [Joye & Mandel 2003], fv [5] [Pence & Chai 2012] and self-written scripts. These are summarized in the section (§6.2) below, while the complete set of tasks is appendiced (§A.1) for our specific observation, in a general "pipeline" with instructions.

6.2 Analysis

The analysis was partly done in SAS v20 and rest in v21. SAS v21 is significantly different from the previous versions, although the outlying procedure and, more importantly, the final result, is the same. The task names are similar, though simplified (e.g., `mos-spectra` to `mosspectra`). In the course of writing this, the analysis steps were reciprocated in SAS v21, but some of the output presented below was derived from previous SAS v20 analysis. We perform the data reduction and form background-subtracted images in three bands from 0.3 to 0.7 to 1.1 to 4.2 keV suited for thermal emission from SNRs. We then created regions around the source "SNR", i.e., a concentration of X-rays in the soft bands near the center of the FOV, and extracted spectral data for fitting with a thermal emission model. Some calculations, about the state and dynamics of the plasma, from the spectral fit are discussed in the subsequent §6.3.

[3] `https://www.cosmos.esa.int/web/xmm-newton/how-to-use-sas`
[4] `https://sites.google.com/cfa.harvard.edu/saoimageds9`
[5] `https://heasarc.gsfc.nasa.gov/docs/software/ftools/fv/`

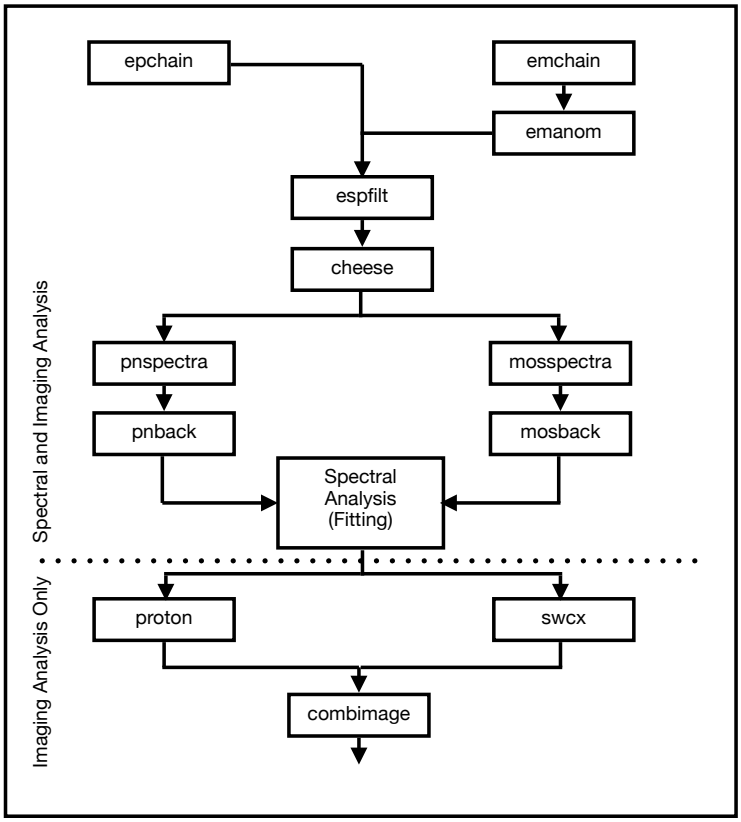

Figure 6.6: Flowchart of general order of tasks in ESAS processing for analysis of diffuse emission. [Snowden & Kuntz 2023]

6.2.1 Data Reduction

6.2.1.1 Observation

J0500–6512 was observed with XMM on 27 April 2023 (ObsID: 0901010201, PI: M. Sasaki) with EPIC-MOS1, -MOS2 and -pn exposure (IDs: S001, S002 and U002) times of 43.626, 43.608 and 39.848 ks, respectively. All 3 cameras were operated in the same "full-frame" mode and with a "medium" optical filter. The target is located at $05^{h}00^{m}55.20^{s}$ $-65°12'08.00''$ or J050055.20-651208.00 in R.A Dec (J2000) equatorial coordinates.

6.2.1.2 Setup

XMM telemetry is stored in observation data files (ODF), which are in a **FIT**S (Flexible Image Transport System) format, like most of the output, with a few **ASC**II summary files. Accordingly, we create two sub-directories, `odf` and `analysis`, in a main directory `/my_work/ObsID` and setup SAS v21 in there: with SAS installed and initialized, we `load` it as a `module` and point it (`setenv`) to the directory (`SAS_CCFPATH`) of current calibration files (CCF) and to `SAS_ODF`. SAS further needs a calibration index file (`.cif`) and an updated summary file (`*.SAS`) to be produced by tasks `cifbuild` and `odfingest` in the `analysis` and `odf` folders, respectively.

6.2.1.3 Event Files

The first step is to recreate event files. We use the commands `epchain` and `emchain` for this initial ESAS processing of raw ODF data. Among the output, we identify 4 files named `*EVLI*.FIT`

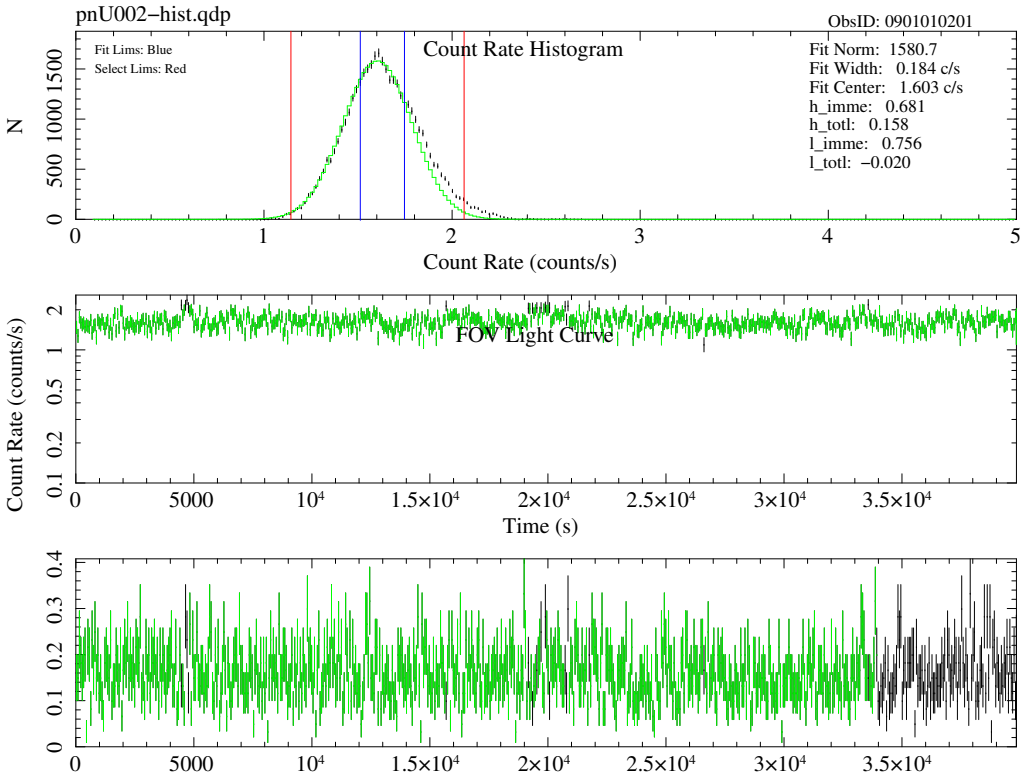

Figure 6.7: Diagnostic file for PN after `espfilt` showing (**top**) X-ray count rate histogram from FOV data fitted to a Gaussian (green curve) in a range (blue vertical lines) with 1.5σ limits (red vertical lines) for GTI and (**middle**) FOV & (**bottom**) corner light-curves in 2.5-8.5 keV band with accepted (green) and filtered out (black) data.

corresponding to MOS1, MOS2, PN and PN-OOT events, and rename them accordingly. Before proceeding further with analysis, we created a preliminary image using the task `evselect` to indeed see a concentration of soft X-rays in the centre.

6.2.1.4 Anomalous CCDs

The anomalous states of MOS CCDs is identifiable from rate-hardness diagrams based on unexposed region data. In ESAS, the routine `emanom`, invoked for the respective (M1 and M2) event files, outputs the hardness ratio of individual chips with flags **G**ood, **I**ntermediate, **B**ad, **O**ff, and **U**ndetermined. For our observation, all MOS chips were in normal (G) state, except, of course, the unusable (off) M1-3 and M1-6 chips lost in micrometeorite impacts.

6.2.1.5 SPF Filtering

Our observation was not significantly affected by soft proton flares. This is evident from the diagnostic output of the SP filtering routine `espfilt` (Fig. 6.7). It shows (for the PN `chain` event file here) a count rate histogram and two light-curves from FOV & corner data in 2.5-8.5 keV band; green points traverse over the accepted portions or good-time-interval (GTI), which is almost the whole observation duration, while the black points represent data likely affected by SPF, excluded by the filtering algorithm. The task fits the count peak to a Gaussian, determines GTI as time intervals with count rates $\pm 1.5\sigma$ and creates "cleaned" event files with (most) SP contamination removed. Any residual SP component inside the GTI event list has to be approximated by spectral fitting (in §6.2.3.1).

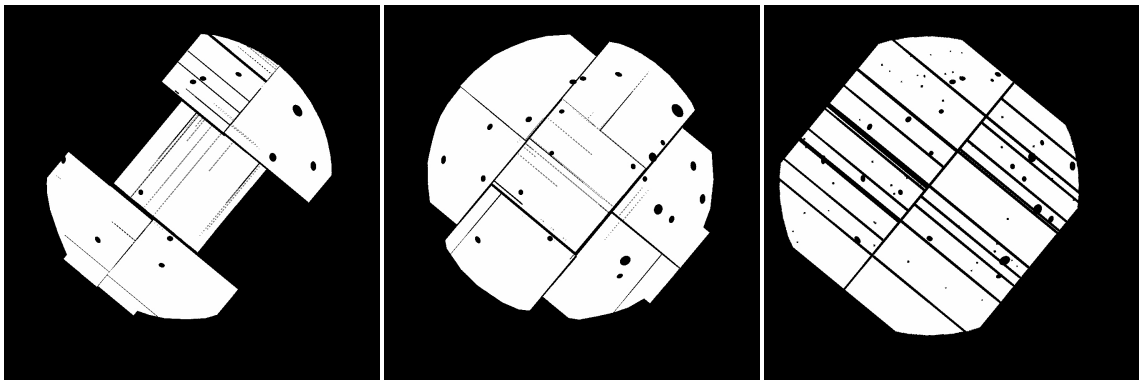

Figure 6.8: `cheese` point source mask images for MOS1, MOS2, PN

6.2.1.6 cheese

As we are interested in the diffuse emission, point sources in view are a statistical nuisance. We need to detect and mask them. This can be accomplished by the ESAS task `cheese`, which calls to SAS tasks for detecting point sources, creating region files and making "Swiss-cheese" masks. It generates source lists, exposure maps and masks (see Fig. 6.8) based on specified detection criteria such as PSF threshold scale in terms of local background, flux thresholds (in units of 10^{-14} erg cm^{-2} s^{-1}), minimum likelihood and minimum separation (in arcsec) of the sources. These are then used to create source-excluded spectra and images. Most of the default values suffice for us at this stage of analysis, .i.e., for full FOV. Later, we follow a "rolling our own" approach to locate and remove point sources, from regions around our (soft diffuse extended) source (SNR) emission (§6.2.2.3).

6.2.1.7 QPB Model

The next step in processing prior to spectral and imaging analysis is to model the quiescent particle background. The QPB spectrum, an imprint of penetrating particles on the detectors, is a continuum resembling a powerlaw that is not folded through the instrumental effective area. It varies spatially across the CCD chips and with location on each chip. The temporal variations are on scales longer than a single observation, except for anomalous states, and best characterized by the hardness ratio of (2.0–5.0 keV) / (0.5–1.2 keV) bands. Following the methodology of Kuntz & Snowden [2008] summarized in Snowden et al. [2008], the particle background can be modeled using corner (unexposed pixels) data and FWC (filter wheel closed position) data from corners & FOV (or region). The former provide a measure of QPB magnitude and shape, since corners should experience the same "internal" background as the portions of the detectors exposed to cosmic X-rays and soft protons. The latter, derived from observations when detectors were blocked to the sky (by a 1.05 mm thick Al filter) except to high-energy cosmic-ray particles, provide spatial distribution of QPB events.

These spectra are extracted from each ("non-anomalous") chip of MOS and all quadrants of PN by the `mosspectra` and `pnspectra` routines in ESAS. Further, energy band parameters can be specified to extract images as well. The extraction is either from the full FOV or a ROI specified by a *regionfile* (in detector coordinates), excluding the `cheese` point source regions. The model QPB spectra (in 0.3-8.0 keV) and images (in specified band) are produced by respective `mosback` and `pnback` runs. An example, diagnostic output for PN full FOV, is shown in Fig. 6.9.

Here again, a residual component, that of fluorescent X-rays (FX), instrumental lines in

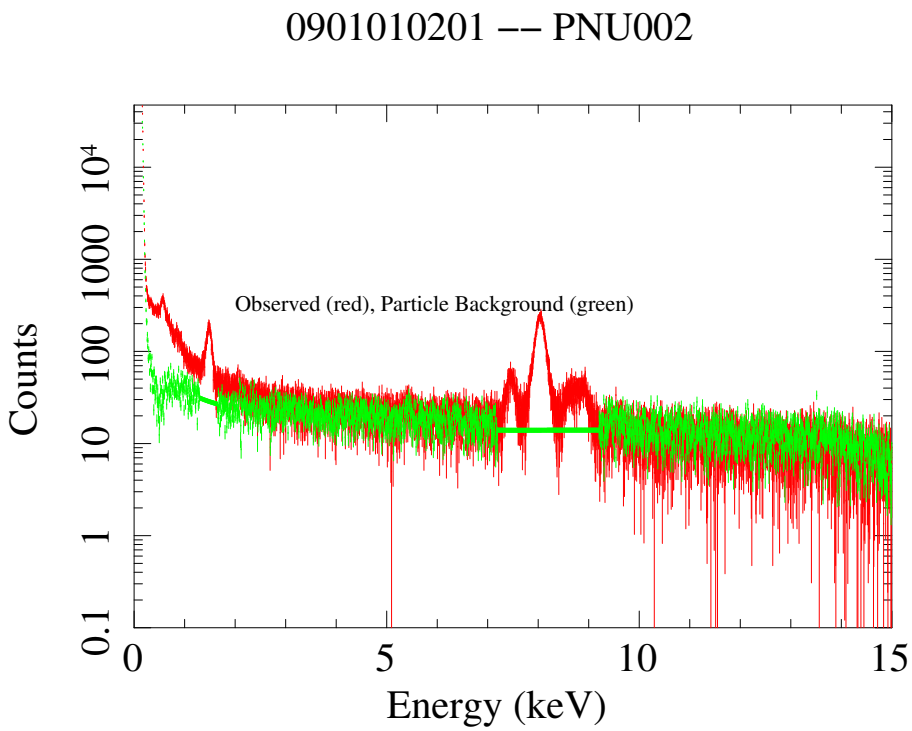

Figure 6.9: The observed full FOV spectrum (red) and the model QPB spectrum (green) constructed by `pnback` from FWC data. The smooth parts at $\sim$ 1.5 keV and around $\sim$ 7.5 keV correspond to FX lines that are fitted here as "bridges" in the continuum.

the otherwise featureless continuum, has to be fitted along with source spectra. The spectral fitting proceeds immediately with the output `*.pi`, `*.rmf` and `*.arf` files. And, we can already create QPB-subtracted images using `*-bkgimdet-*.fits`, although with FX and likely-contamination from SP & SWCX. We repeat the process for imaging in three (RGB) energy bands of 0.3-0.7, 0.7-1.1 and 1.1-4.2 keV, and for three different regions: full FOV, a polygon around the central SNR (source), and an annulus around the polygon (background) for spectral fitting (see Fig. 6.10). The spectral files are renamed region-wise and binned using FTOOL `grppha` for analysis with XSPEC in §6.2.3, while the particle background images in detector coordinates are saved for creating images in §6.2.2 below.

6.2.2 Imaging

As mentioned before, true imaging, i.e. representation of cosmic/extrasolar X-rays requires spectral fitting of some background components. Notably, FX lines, residual SP flares and SWCX emission has to be modeled. ESAS offers tasks to create model images of these contaminating components, then subtract them from the count image, combine different instruments' data and even apply an adaptive smoothing to have a background-subtracted & exposure-corrected image of our observation.

While the particle background is already modeled, instrumental lines will form (Gaussian) parameters in fitting of our source spectrum. The soft proton and solar wind charge exchange background are estimated by fitting the spectrum of the full FOV as a (broken) powerlaw and Gaussians, respectively; and using the resulting fit parameters, powerlaw index & norm and Gaussian norm in tasks `proton` and `swcx` to create model count images. The spectral fitting procedure, model and analysis is deferred to §6.2.3. Here we present the final images and the process of producing them.

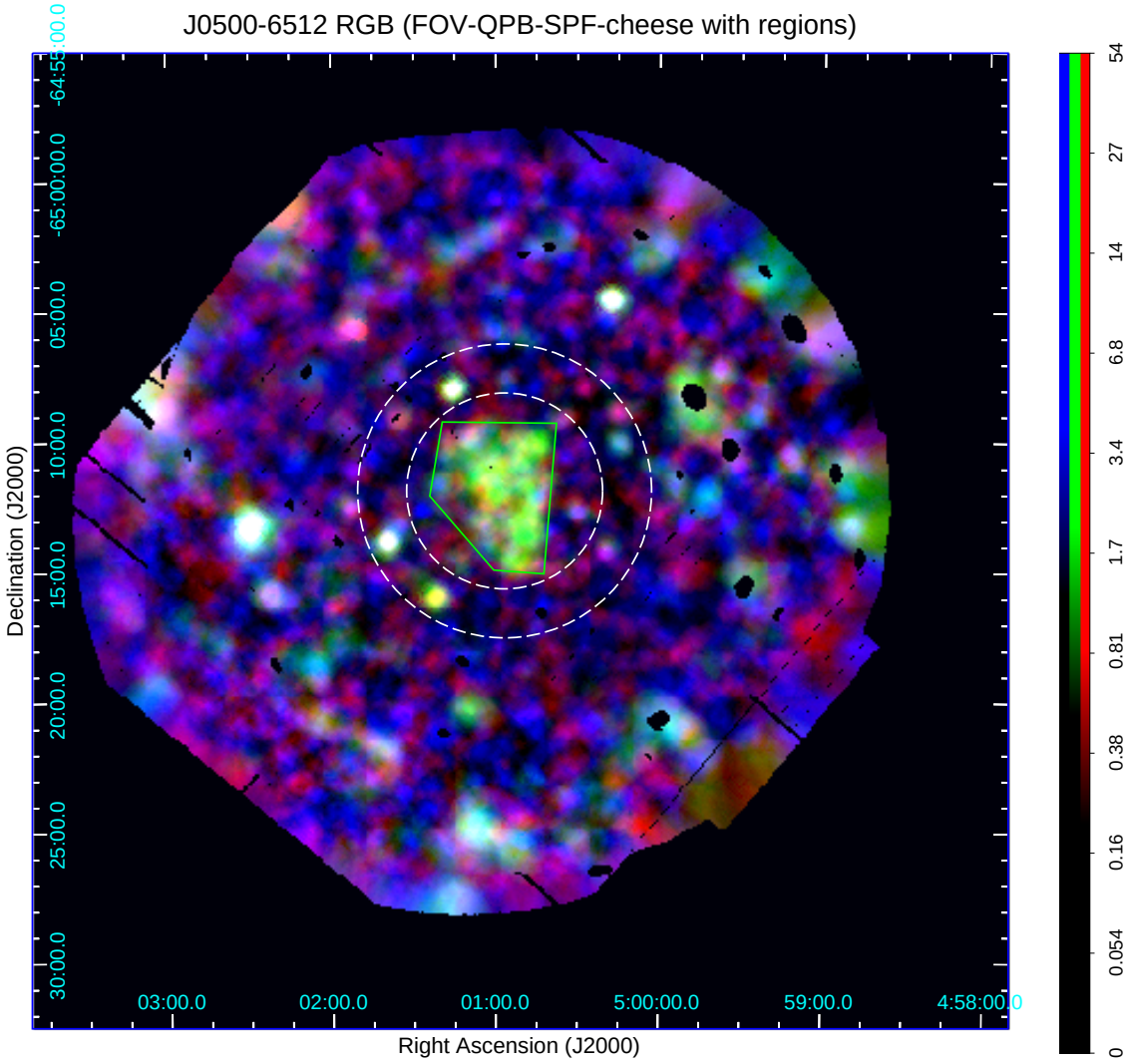

Figure 6.10: RGB image of MCSNR J0500−6512 in XMM-Newton bands of 0.3-0.7, 0.7-1.1 and 1.1-4.2 keV after QPB subtraction, SPF filtering, smoothing and combining the image of 3 detectors, in sky coordinates, with regions chosen for source (green polygon) and background (white dashed annulus) spectral fits marked. The intensity scale is $\log_{10}$ and color table gives conical FWHM in arcmin.

We, in fact, fitted both FX and SWCX lines only for spectrum of our chosen background and source regions. So, our full FOV images are only QPB and SPF subtracted (with or without point sources). This is warranted by the relatively low source counts, QPB being the dominant background and no indication of severe contamination from solar flares and winds from our diagnostics. We also define regions around our supposed SNR (a polygon and an annulus), thoroughly excluding point sources, from visual inspection of preliminary images.

6.2.2.1 proton and swcx

Starting with QPB `*bkgimdet*` images, we first convert them to `*bkgimsky*` i.e. to sky coordinates, by executing `rotdet2sky` which performs a reflection, an offset and a rotation. Next we produce the detector images (for the three detectors and in three bands each) by `proton` with parameters *speccontrol*=1, and *pindex* & *pnorm* from the powerlaw fit results of Tab. 6.1 after §6.2.3.1 residual SPF filtering.

A similar task called `swcx` takes input the scale factors (*gnormlist*) determined from spectral fitting of an arbitrary number of SWCX emission lines (*linelist*) and outputs the respective background image in detector coordinates. As justified above, this was not done this way in our analysis.

6.2.2.2 combimage and binadapt

Now the sky images of quiescent and SPF (and not SWCX) background are processed and combined across the 3 detectors/exposures with proper scaling by `combimage`. The final images are the result of `binadapt` that accounts for all the components (total counts, background, exposure and mask). We also bin the counts to 2 pixels and apply an adaptive filter with Gaussian kernel of 50 counts for "smoothing" the images. The three band images are then loaded as overlapping frames in red, green and blue colors in DS9 and annotated, shown in Fig. 6.10.

6.2.2.3 Source Detection and Region Selection

As we are interested in a scientific analysis of X-ray emission specifically from our astrophysical source, our next step is to isolate the corresponding regions. For this, we inspect the combined image (binned but not smoothed) and notice a concentration of soft X-rays (mostly in the green 0.7-1.1 keV band) near the FOV centre. We use DS9 to define a polygon around this extended structure, as well as an annulus around that polygon to use as "background" for spectral fitting.

Before that, we search for any remaining point sources to exclude, now directly calling the SAS task `edetect_chain`. We load the generated source lists onto the created exposure maps in 5 different bands for each of the 3 instruments as circular regions in DS9. The ones within the mentioned polygon and annulus are identified and saved as `.reg` files in sky (FK5) coordinates in degrees. These are then converted to detector coordinates using a Python script [J. Knies, priv. comm.]. So, we have 6 region files defining the source (SRC) and background (BKG) *without* point sources from which to extract MOS1, MOS2 and PN spectral data.

6.2.3 Spectral Analysis

The data reduction and imaging analysis of the previous sections culminates in this section with fitting of the extracted X-ray spectrum of the source SNR to appropriate models. We try to dissociate its different components of emission, absorption and noise from both instrumental and cosmic origins, to procure the purest possible information from our source. We follow the method of Maggi et al. [2012] of fitting the spectrum from a nearby region (BKG) to a

physically motivated model simultaneously with the source (SRC) spectrum rather than simply subtracting. The background and source models & fits are discussed in §6.2.3.2. First we fit the spectrum of the full FOV for the purpose of filtering SPF background in §6.2.3.1 below.

All spectral analysis was done with the X-ray spectral fitting software XSPEC v12.14.0h with χ^2 (Chi-Squared) fit statistic and a modified Levenberg-Marquardt minimization method [Levenberg 1944; Marquardt 1963 based on Bevington 2002].

6.2.3.1 Residual SPF Filtering

Although the bulk of SPF background is filtered out from observation data by removing "bad" time intervals by light-curve screening by `espfilt`, a residual amount might be present across the FOV, GTI and the spectrum. This longer-scale, lower-amplitude component can be modeled as a (broken) powerlaw which is not folded through the instrumental response [see Kuntz & Snowden 2008]. We use the PN, MOS1 and MOS2 spectra extracted from the full FOV, grouped & binned to a minimum 50 counts, and the following model in XSPEC:

```
con<1>(gauss<2>+gauss<3>+gauss<4>+gauss<5>+gauss<6>+gauss<7>+gauss<8>+gauss<9>)
    + apec<10>+TBabs<11>(apec<12>+apec<13>+pow<14>)
        + TBvarabs<15>*apec<16>*TBabs<17>)
```

The eight Gaussians correspond to EPIC instrumental lines. These were at 1.49 and 1.75 keV for MOS, and at 1.49, 7.11, 7.49, 8.05, 8.62 and 8.9 keV for pn detectors, 'frozen' with zero width (σ) and appropriately 'free' norm. No SWCX emission lines were included in this rough fitting of a model. The spectra were scaled by their net angular area from the 3 detectors viz. a (BACKSCAL) constant determined via ESAS `protonscale`.

The cosmic background comprises of 3 thermal components – from unabsorbed soft emission from the LHB and an absorbed column of cooler & another of hotter halo from the Galaxy or the IGM. We account for them by the "CIE" plasma model `apec` (Astrophysical Plasma Emission Code from AtomDB[6]) with $kT = 0.1$, 0.2 and 0.6 keV, respectively. The metal abundances were set to unity with respect to the `angr` [Anders & Grevesse 1989] solar abundance table. The powerlaw component with $\Gamma = 1.46$ represents the CXB from unresolved discrete X-ray sources [Chen et al. 1997]. The absorbing column density, `TBabs` N_H was initiated with value calculated for our sky position by a tool[7] based on HI4PI Collaboration et al. [2016], and eventually fitted and fixed to 3.67×10^{20} cm^{-2}.

Further away, the LMC absorption was accounted by the `TBvarabs` model with abundances half the solar values (except for He). It was set to 9.654×10^{20} cm^{-2}. Another component of foreground absorption was multiply added, for the intervening ISM to the LMC, with the same N_H. Finally, we fitted the *source* with another `apec` component, as plasma emission from LMC as a whole. Here, kT was 0.1 keV, but with abundance 0.5$\times$ solar and a redshift of 9×10^{-4} like the other two extragalactic components.

The SP contamination is added as separate powerlaw models with *diagonal response files* for the data [Snowden & Kuntz 2023]. The best-fit results of these are reported in Tab. 6.1. The full model has has (87+2)$\times$3 parameters, however many of them are tied together and/or frozen with an initial or a physically reasonable or an intermediate fit value. For us, for residual SPF filtering, the final fitted model yielded small negative values for the `powerlaw` photon indices for MOS. Hence, we fixed them to 0.1 and re-fitted, before use in `proton` and imaging (§6.2.2.1). The spectra with models folded through the response of PN, MOS1 and MOS2 intruments is shown in Fig. 6.11.

[6] `http://atomdb.org/`

[7] `https://heasarc.gsfc.nasa.gov/cgi-bin/Tools/w3nh/w3nh.pl`

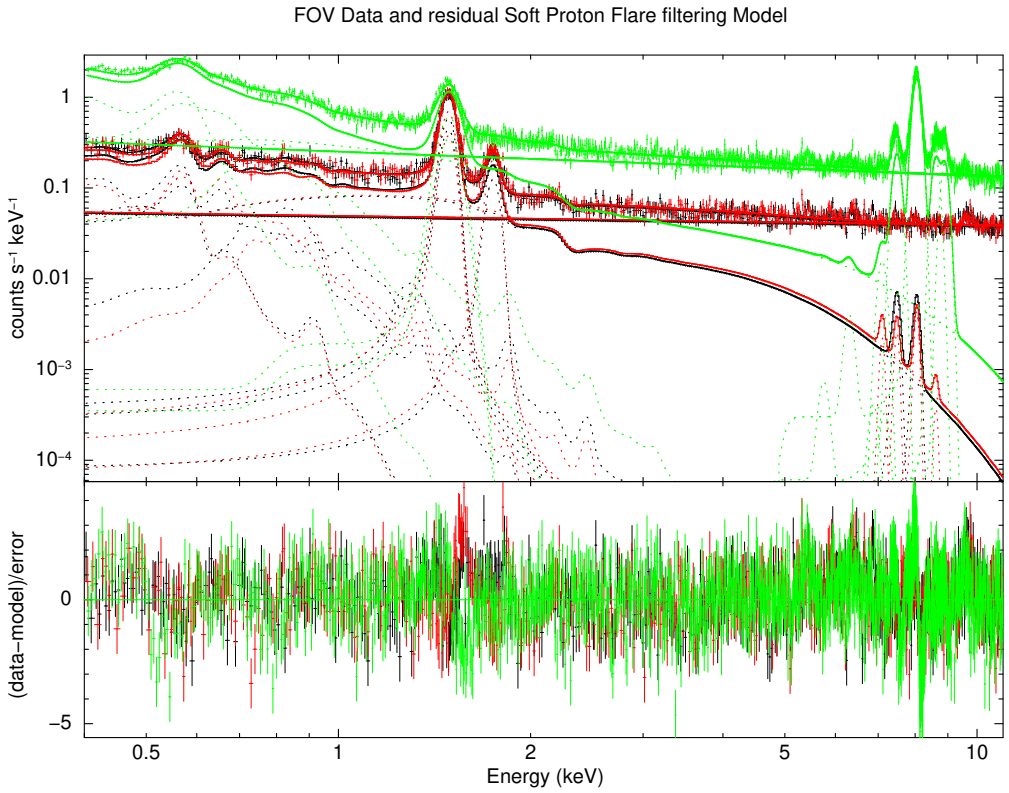

Figure 6.11: Residual SPF Filtering spectral fit: PN, MOS1 and MOS2 with respective powerlaw curves (straight lines) and additive components (dotted curves).

6.2.3.2 Background+Source Model

The final spectral model consists many of the same components as before (i.e. §6.2.3), but the fitting procedure is more rigorous. It follows the methods along the lines of Maggi et al. [2012, 2014, 2016], Kavanagh et al. [2015b] and Zangrandi et al. [2024], following the prescriptions of Snowden et al. [2008] and background modeling of Kuntz & Snowden [2008]. The same versions of XSPEC and AtomDB, along with photoabsorption cross-sections of Balucinska-Church & McCammon [1992] and elemental abundances of Wilms et al. [2000] were used. The background and source spectra (viz. extracted from BKG and SRC regions) were grouped and binned to a minimum of 30 counts for use of χ^2-statistic.

The main XSPEC model can be written, and its various background, foreground, instrumental and source components can be disentangled, as follows:

```
con<1>(gauss<2>+gauss<3>+gauss<4>+gauss<5>+gauss<6>+gauss<7>+gauss<8>)
        + TBabs<9>(TBvarabs<10>*vnei<11>)
    + con<12>(apec<13>+TBabs<14>(apec<15>+apec<16>+TBabs<17>*pow<18>)))
```

First, the seven Gaussians here (#2–8) are for fitting SWCX lines with zero widths but free normalizations. These were C VI (0.46 keV), O VII (0.57 keV), O VIII (0.65 keV), O VIII (0.81 keV), Ne IX (0.92 keV), Ne IX (1.02 keV) and Mg VI (1.35 keV). The instrumental lines of MOS and PN were fitted as separate models, along with SPF powerlaws. The Gaussians were at 1.49 and 1.75 keV for Al K and Si Kα florescence, respectively in this case, since we are only interested in the soft part of the spectrum.

We again have an unabsorbed `apec` component (#13) to account for the thermal emission from the LHB, and two absorbed `apec` components (#15–16) for the Galactic halo plasma. The temperatures were found or fixed to $kT \approx 0.1$, 0.17 and 0.79, respectively. The absorbed

Table 6.1: Fit results for SPF background powerlaw models for the 3 detectors, with chi-squared/(degrees of freedom) fit statistics. The last row is the total test statistic divided by the number of bins used.

Model	Parameter	Value	χ^2/dof
MI:pow<1>	PhoIndex	0.1 (frozen)	600.91/508
	norm	0.048 ± 0.00052	
M2:pow<1>	PhoIndex	$0.1 =$ MI:p1	688.25/515
	norm	0.050 ± 0.00054	
PN:pow<1>	PhoIndex	0.263 ± 0.02	2158.73/1300
	norm	0.253 ± 0.01	
			3447.90/2323

powerlaw (#18) again accounts for CXB with photon index frozen at 1.46, but now we also need to include absorption by the column of LMC behind the source, using another `TBabs` (#17) component. The latter was found to be $\approx 1.996 \times 10^4$ cm^{-2}.

Crucially, the source spectrum was fitted with a variable NEI [Borkowski et al. 2001] model called `vnei`, modulated by foreground Galactic (#9) and LMC (#10) absorptions. While the Galactic `TBabs` column density was frozen to the value (3.63×10^{20} cm^{-2}) calculated from the HI map [Dickey & Lockman 1990], the LMC `TBvarabs` N_H was one of the free parameters. We used abundances as $0.5\times$ solar value of `wilm` table for all elements except for H and He [Westerlund 1997]. The background was fitted first, and then the fitted parameters were frozen and tied in fitting the corresponding source spectrum. The background spectra were scaled by constants (#12), ratios of areas of SRC and BKG regions for each of the three instruments (MOS1, MOS2, PN).

The total number of parameters in this case were $(99\times6)+(5\times2)+(8\times4)$. See the density of lines in Fig. 6.13. However, most of them correspond to the astrophysical and instrumental backgrounds and were fitted separately already; many of them tied together across the instruments. So, the BKG best-fit results were frozen parameters in fitting the SRC spectra. Eventually, optimal fit was obtained (see Fig. 6.14) with just 4 free parameters: the foreground absorbing column density of LMC `TBvarabs` $N_{H\,\mathrm{LMC}}$, the plasma (electron) temperature `vnei` kT, ionization timescale `vnei` τ and `vnei` norm. The best fit results with 90% confidence intervals obtained from the `error` command of XSPEC and further verification from `steppar`, are noted in Tab. 6.2. See also, Fig. 6.12 to see a variation of the χ^2 value. Later, we also thawed the O and Fe abundances (in `vnei`) away from the fixed $0.5\times$ solar value (Tab. 6.3). The command `flux` was also executed to calculate the luminosity of the source in a given energy range (0.3–4.2 keV).

Table 6.2: Values from best `fit` and `error` (90% confidence intervals) of the free parameters, adjusted according to `steppar` (see Fig. 6.12).

Parameters	$N_{H\,\mathrm{LMC}}$ (10^{22} cm^{-2})	kT (keV)	τ (10^{11} s cm^{-3})	norm (10^{-4} cm^{-5})	χ^2/dof
best-`fit`$\pm$`error`	$0.02^{+0.18}_{-0.02}$	$0.46^{+0.07}_{-0.13}$	≈ 3.47	$0.51^{+0.07}_{-0.12}$	744.29/775

Table 6.3: `vnei` abundances of oxygen and iron from best `fit` with `error` (90% confidence intervals).

Elements	O ($\times$ solar)	Fe ($\times$ solar)	χ^2/dof
best-`fit`$\pm$`error`	$0.54^{+2.85}_{-0.42}$	$0.62^{+0.69}_{-0.19}$	743.21/775

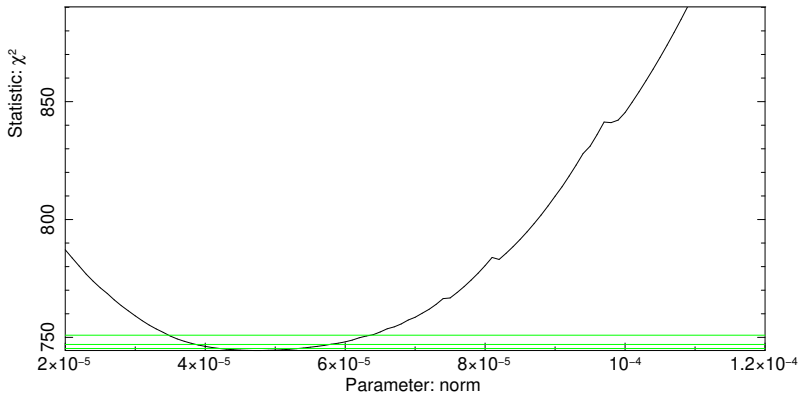

Figure 6.12: Variation of χ^2-fit statistic with `steppar` variation on `vnei` norm

6.3 Results

The main results of the spectral fitting of the source (SNR plasma) emission are summarized below:

1. The spectral model was well fit, with a reduced χ^2 of ≈ 0.96. The overfitting might be due to a high quality data, if not from using a more complex model than necessary. The plots of all 6 spectra and source only are shown in Figs. 6.13 and 6.14, along with `delchi` residuals. For BKG spectrum and individual spectra with various additive components of the model, see §A.3.1.
2. The plasma temperature kT, ionization timescale $\tau = n_e t$ and the normalization of the source component model `vnei` were determined in the spectral fitting and are listed in Tab. 6.2 with errors approximately encompassing the 90% confidence range of the parameters. Some calculations and consequences on the observed values are discussed in §6.3.2. The $N_{H\,\mathrm{LMC}}$ fraction of $\approx 0.2 \times 10^{21}$ cm^{-2} seem consistent with the observations of Maggi et al. [2016] for the region.
3. Varying the abundances of specific elements did not change the fit significantly. Although freeing O and Fe yielded respective abundances 0.51 and 0.61, the errors were too large for any conclusion regarding the origin type of SNR (CCSN or Type Ia). See Tab 6.3.

6.3.1 Multiwavelength Comparison

Our background-subtracted & exposure-corrected XMM-EPIC images in red ($R = 0.3 - 0.7$ keV), green ($G = 0.7 - 1.1$ keV) and blue ($B = 1.1 - 4.2$ keV) bands, as in Fig. 6.10, shows a bulge of soft X-ray emission near the FOV centre. The dominant green region was approximated by an irregular polygon (SRC) with dimensions listed in Tab. 6.4. We ascribe that as X-ray emission from the ejecta, which has been shocked-heated in the course of expansion of the SNR. In optical MCELS[8] Hα image (Figs. 6.15, 6.16), we see a faint shell, a ring-like structure arguably due to 2D projection of a sphere. We approximate the edges of this shell to

[8]The **M**agellanic **C**loud **E**mission-**l**ine **S**urvey [Smith & MCELS Team 1999]

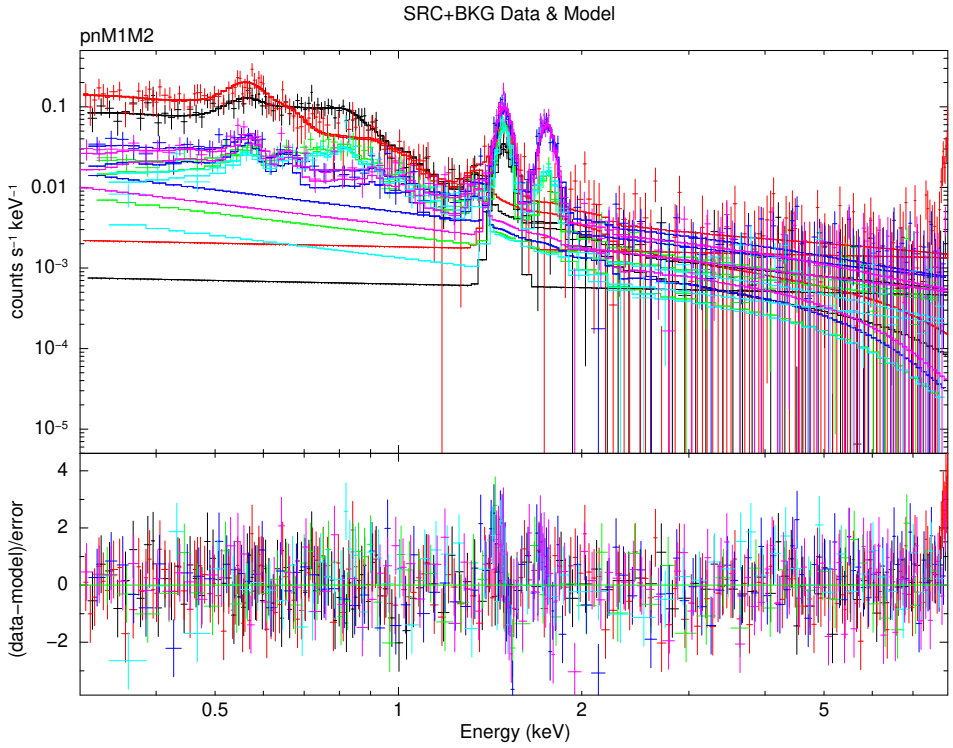

Figure 6.13: The final spectral fit result for the chosen background and source of J0500-6512. The color coding of the points & solid lines follow the order: PN-SRC, PN-BKG, MOS1-SRC, MOS1-BKG MOS2-SRC, MOS2-BKG data & folded model, respectively. The plot is rebinned for visual clarity. Additive model components are not shown. The residuals are `delchi` viz. error = square-root of model counts.

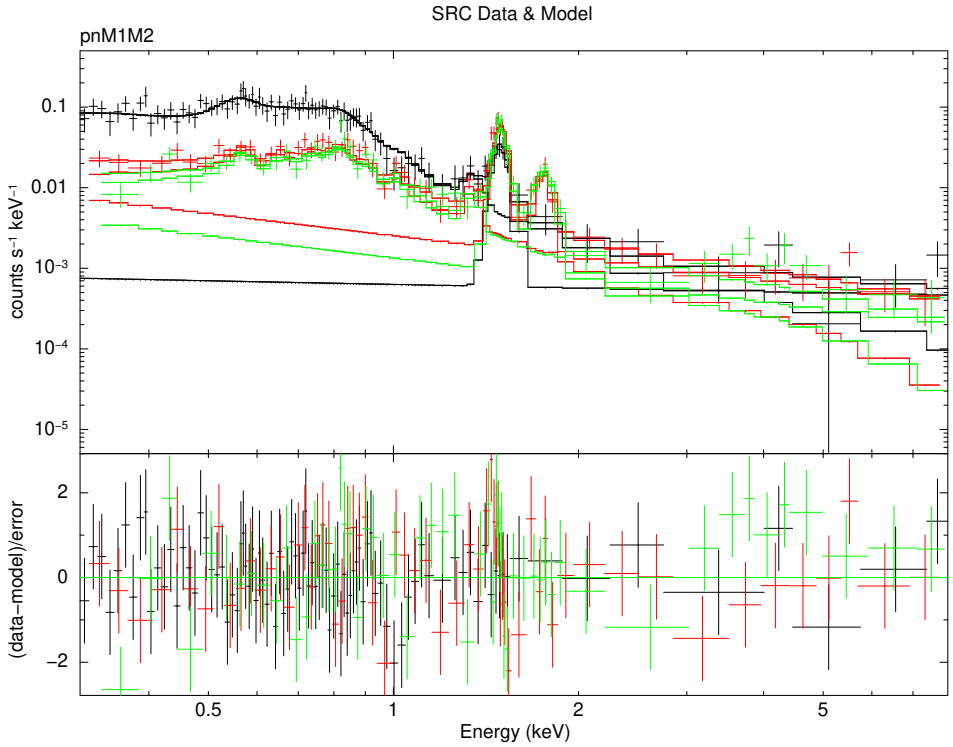

Figure 6.14: Spectral fit result for the source spectra. Black, red and green points & solid lines show PN, MOS1 and MOS2 data & folded model, respectively. The plot is rebinned for visual clarity. A FX line and SPF powerlaws are also shown. The residuals are `delchi` viz. error = square-root of model counts.

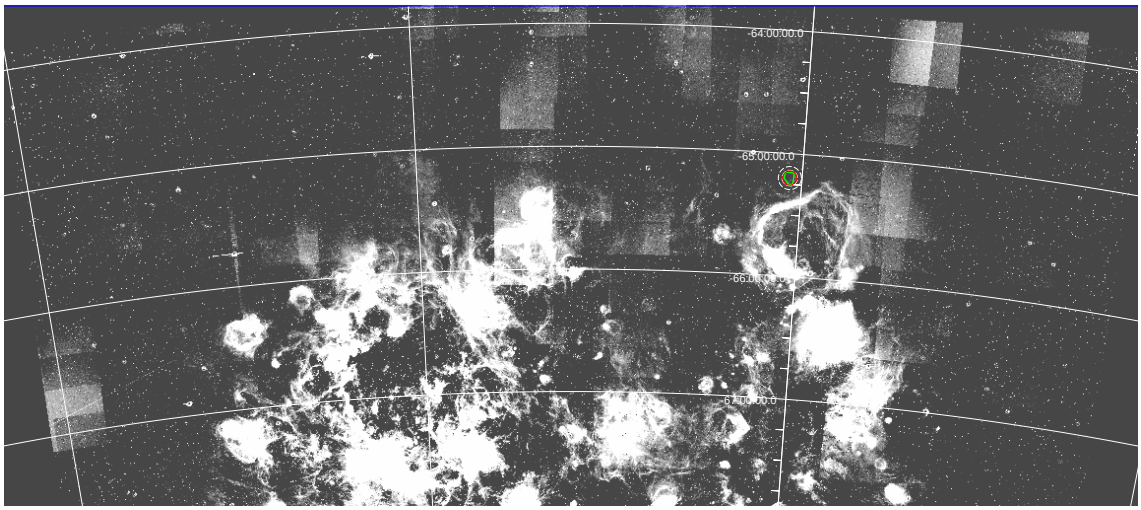

Figure 6.15: MCELS Hα image [Smith & MCELS Team 1999] with our analysis regions around MCSNR J0500–6512 marked.

Table 6.4: Geometrical parameters for our analysis regions, using DS9.

Dimensions (″)						Centre (RA, Dec)
SRC Polygon (green)						
a	*b*	*c*	*d*	*e*	*diag*	
263.326	348.426	116.065	225.658	173.151	421.322	75.238°, −65.202°
BKG Annulus (dashed white)						
	$r_+ = 224.894$		$r_{++} = 338.841$			75.236°, −65.198°
Shock Circle (red)						
		$r = 210.661$				75.236°, −65.198°

be shock radius of the expanding SNR. (We recognize that the LMC's tilt along the LoS may introduce up to 10% distance error for SNRs closer to the southern versus northern end of the LMC [Bozzetto et al. 2017].)

Based on the optical and X-ray emission structure from the source, we classify it as a *mixed-morphology* remnant, i.e. an optical shell filled with X-rays in the centre, and with no known PWN in vicinity. And with respect to the stage of evolution and estimated age (§6.3.3), we can call it a *middle-aged* SNR, with low shock-velocity, visibility in optical and start of the radiative cooling. More accurate estimate on its evolutionary state is made in §7.2.1.

6.3.2 Plasma Properties

From our spectral fit results (Tab. 6.2), we can derive physical properties of the X-ray emitting plasma. Particularly, the normalization of the `vnei` component gives us useful information about the state of the plasma.

$$\underset{\text{(norm)}}{K} = \frac{10^{-14}}{4\pi[d_A(1+z)]^2}\int n_e n_H \, dV \, [\text{cm}^{-5}] \tag{6.1}$$

where d_A is the angular diameter distance to the source, z is the redshift, dV is the volume element and n_e & n_H are the electron & hydrogen densities. With $z = 0.000927739 \approx 0$, we assume $d_A \approx d_{\text{LMC}} = 49.59 \pm 0.55$ kpc, the physical distance to the LMC [Pietrzyński et al. 2019] as the distance d to our remnant. Further, with LMC metallicity of $0.5\times$ solar

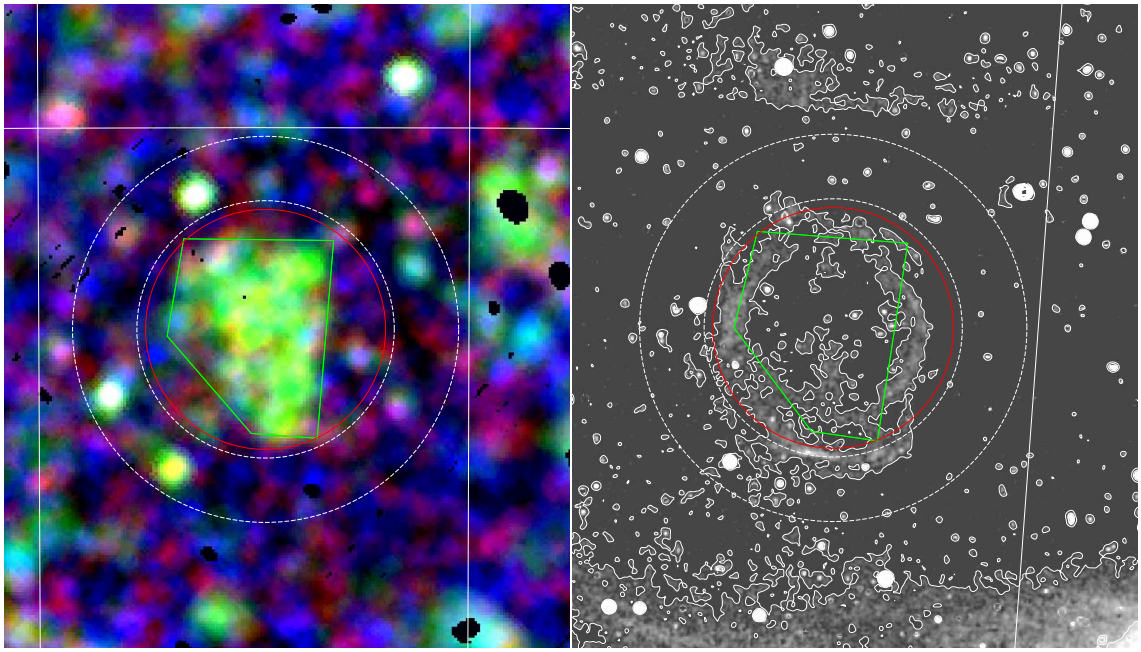

Figure 6.16: Comparison of XMM EPIC RGB (**left**) and MCELS Hα (**right**) images, latter with contours (levels 10, smoothing 4, min-max with limits 0-184), with analysis regions and coordinate grid lines, zoomed in around J0500–6512. The red circle delineates the maximal extent of the SNR, with chosen diameter = diagonal side of the SRC polygon and centre = BKG annulus. For scale, the "thin" gap between the red and the dashed white circle is ≈ 3.45 pc.

abundances, $n_e = 1.2 n_H$ [Sasaki et al. 2011]. Hence, we have the H nuclei number density:

$$n_H = \left(\frac{4\pi K d^2 \times 10^{14}}{1.2 V f} \right)^{\frac{1}{2}} \; [\mathrm{cm}^{-3}] \tag{6.2}$$

where we included the term f in the $norm$ integral as the filling factor and assumed an uniform density for the plasma. From K, we can also directly calculate the EM of the source:

$$EM = \int n_e n_H \, dV = (10^{14} \, 4\pi d^2) \, K \; [\mathrm{cm}^{-3}] \tag{6.3}$$

The calculated values based on $d = d_{\mathrm{LMC}}$ and norm K from best-fit of the source spectral model are listed in Tab. 6.5. For n_H, we enclose the emitting plasma in a sphere of radius $r = 210.661'' \pm 14.223'' = 50.67 \pm 3.45$ pc around the maximal extent of the soft diffuse X-ray emission ('diagonal' side of the 'green' SRC polygon region) with inner circle of the BKG annulus as the upper error. The geometry was inferred by comparing the morphology of the remnant in XMM EPIC X-ray against MCELS Hα optical image (see Fig. 6.16 and Tab. 6.4). The volume was thus $V = \frac{4}{3}\pi r^3$ with $f \approx 0.5$ (see Fig. 6.17 for variations). Knowing n_H, we constrain the pressure (P) of the plasma from its temperature (`vnei` kT with the Boltzmann constant $= 8.617 \times 10^{-8}$ keV K^{-1}) using:

$$P/k = 2.31 f^{-1/2} \, n_H \, T \; [\mathrm{cm}^{-3} \, \mathrm{K}] \tag{6.4}$$

From the `flux` F_X of the plasma obtained from the spectral-fit model integrated over the band 0.3–4.2 keV, we estimate the luminosity L_X of the source as:

$$L_{X\,\mathrm{SRC}} = 4\pi d^2 \cdot F_X \approx (1.176 \pm 0.026) \times 10^{29} \mathrm{erg\,s}^{-1} \tag{6.5}$$

Table 6.5: Results of calculations on the X-ray emitting plasma

d (kpc)	r (pc)	f	T (10^6 K)	EM (10^{57} cm^{-3})	n_H (10^{-2} cm^{-3})	P/k (10^5 cm^{-3} K)
$49.59^{\pm 0.55}$	$50.67^{\pm 3.45}$	0.5	$5.34^{+0.81}_{-1.51}$	$1.50^{+0.209}_{-0.355}$	$1.25^{\pm 0.128}$	$2.18^{+0.40}_{-0.65}$

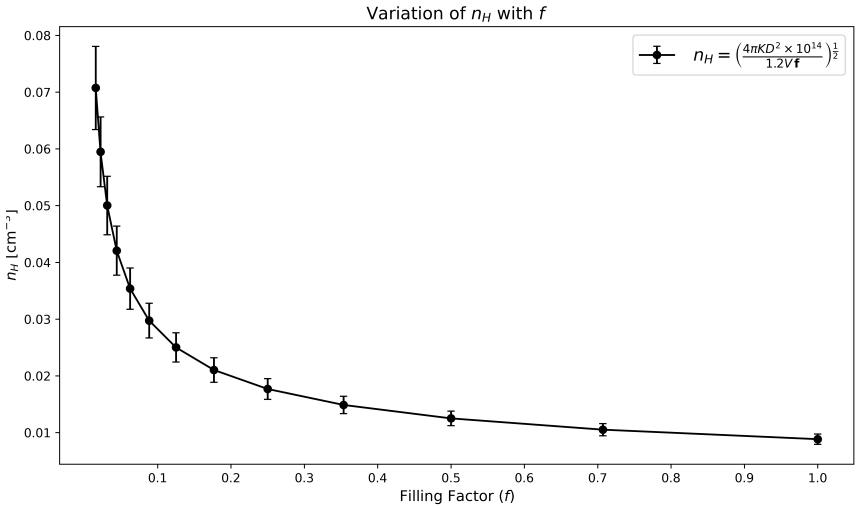

Figure 6.17: Variation of n_H with the filling factor f of the assumed spherical volume.

Thus, our remnant falls in the category of very faint, possible older remnants of the LMC population. The very low photon statistics limit further concrete analysis about the properties, e.g., progenitor type, evolution phase, etc. So, we rely on some assumptions based on existing theory and observations. The first and simplest is to use the Sedov-Taylor solutions, introduced in §4.4.2.

6.3.3 Sedov-Taylor Estimates

If we assume that the remnant is in its II or adiabatic phase of evolution, we can calculate some of its parameters based on Sedov-Taylor self-similar solution, using the results of our imaging and spectral analysis. The radius of the SNR (or rather of the forward shock) depends on initial explosion energy, age and density of the ambient medium according to [Vink 2020]:

$$R_{\rm fs} = 1.15 \left(\frac{Et^2}{\rho_0}\right)^{\frac{1}{5}} [\rm cm] = 5.0 \left(\frac{n_0}{1\,\rm cm^{-3}}\right)^{-\frac{1}{5}} \left(\frac{E_0}{10^{51}\,\rm erg}\right)^{\frac{1}{5}} \left(\frac{t}{1000\,\rm yr}\right)^{\frac{2}{5}} [\rm pc] \qquad (6.6)$$

and its derivative, the forward shock velocity is then:

$$V_{\rm fs} = \frac{2}{5} R_{\rm fs}\, t \qquad (6.7)$$

Now, we know or assume that the maximal extent of the X-ray emission coincident with the Hα shell-like structure, traces the circle of forward shock of our (spherically-symmetric) SNR. That is, $R_{\rm fs} \approx r$. We first assume a pre-shock hydrogen density of 0.1 cm^{-3} and explosion energy of 0.5×10^{51} erg [e.g., Leahy 2017]. This gives us an estimated age and a shock velocity, as listed in Tab. 6.6. The plots in Fig. 6.19 show the analytical evolution of forward shock radius and velocity according to Eqs. 6.6 and 6.7 with time. The values of t_0 and $V_{\rm fs}$ at the observed

radius vary significantly with the assumed environment (n_0) and explosion energy (E or E_0 or E_{51}) of the SNR, as seen in Fig. 6.18.

Clearly, the crude assumption of a constant expansion parameter ($2/5$) falls short here. So, in the next chapter (§7), we attempt to improve modeling the evolution for a population of SNRs in the LMC, including the newly added MCSNR J0500-6512.

Table 6.6: Sedov-Taylor estimates on MCSNR J0500–6512

$R_{\rm fs}$ (pc)	n_0 ($\rm cm^{-3}$)	E_0 (10^{51} erg)	t_0 (10^3 yr)	$V_{\rm fs}$ ($\rm km\ s^{-1}$)
$50.67^{\pm 3.45}$	0.1	0.5	$146.207^{\pm 24.887}$	$136^{\pm 24}$

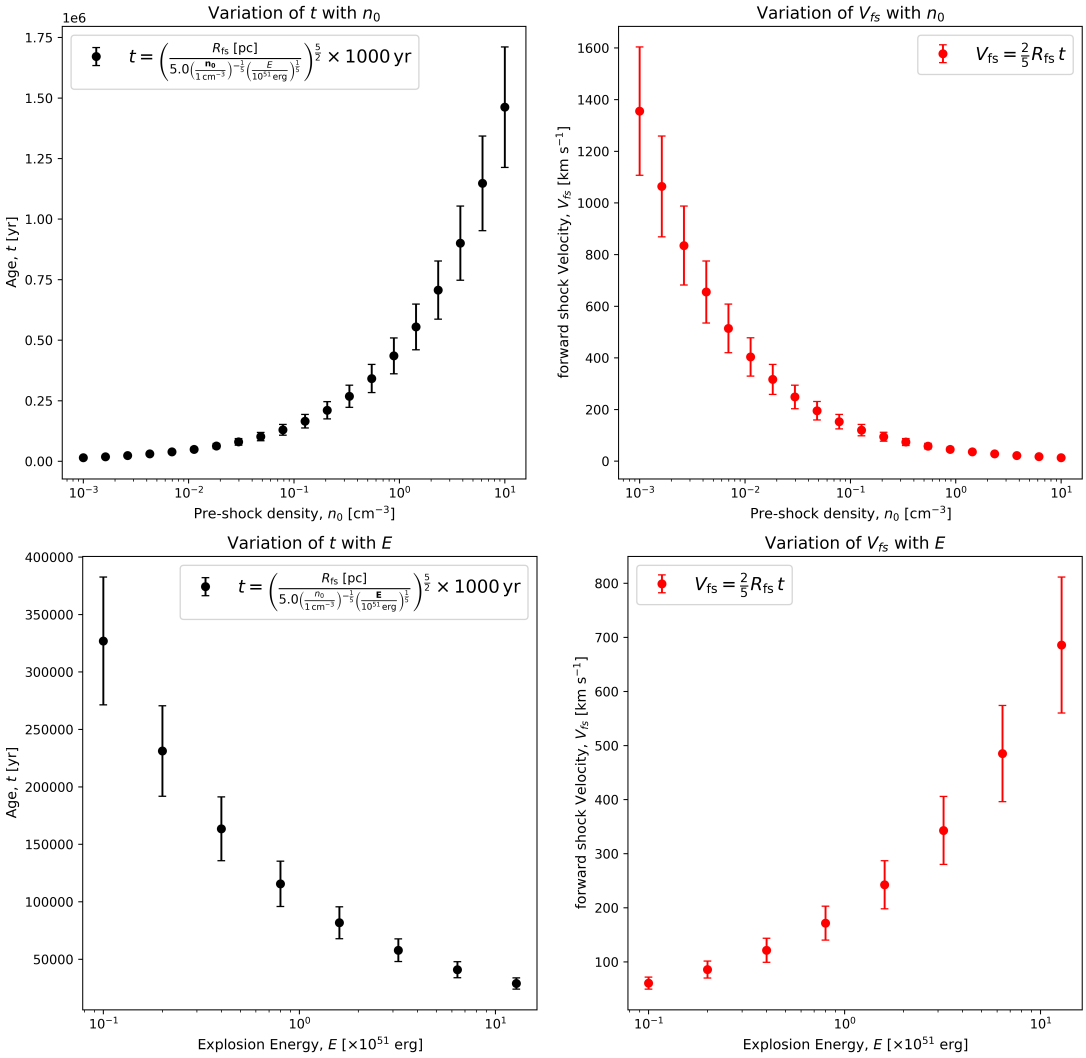

Figure 6.18: Variations of t_0 (**left**) and $V_{\rm fs}$ (**right**) with n_0 and with E_0, given the observed radius and $E_{51} = 0.5$ (for **top**) or $n_0 = 0.1\ \rm cm^{-3}$ (for **bottom**), according to Sedov-Taylor solution.

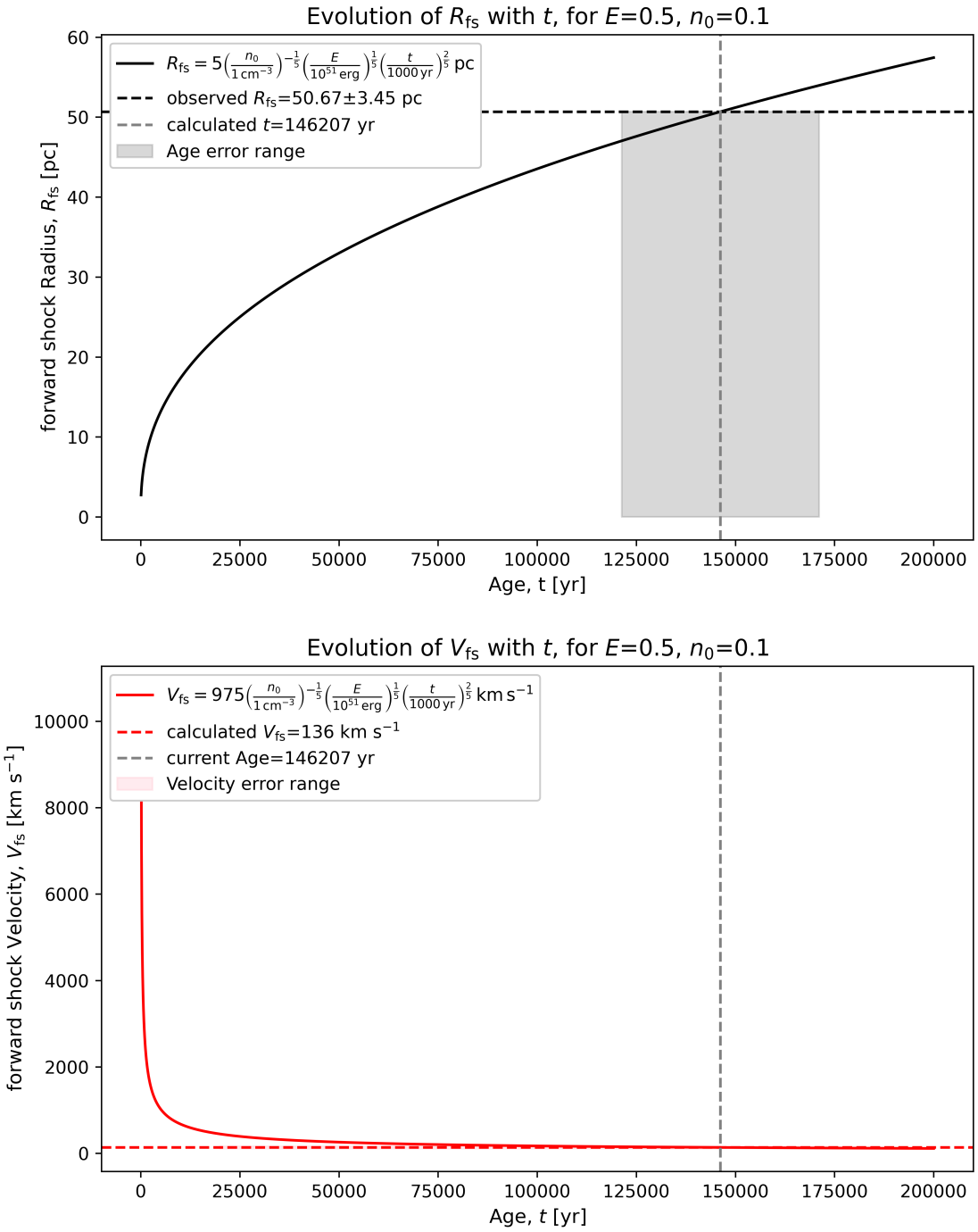

Figure 6.19: Sedov-Taylor evolution of forward shock radius and velocity with age of the SNR assuming $E_{51} = 0.5$ and $n_0 = 0.1$. Based on the observed $R_{fs} = 50.67 \pm 3.45$ pc, current t_0 and V_{fs} are calculated and shown by dotted lines.

Chapter 7

Population Evolution Analysis

We follow our X-ray (XMM-Newton) data analysis of a single LMC SNR (J0500–6512) with a population study using multiwavelength observations and evolutionary models on all known supernova remnants in the Large Magellanic Cloud. Such a study provides constraints on the physical processes that originated the SNRs and the galactic ISM environment where they evolve [Badenes et al. 2009]. Currently, a mere fraction of Galactic SNRs are studied well enough to characterize their evolutionary state [Leahy 2017], which depends on the SN progenitor (explosion type, explosion energy, ejected mass) as well the ambient ISM (abundance, densities). LMC, our closest and well-observed star-forming galaxy, offers optimal opportunities to survey, classify, compile and catalog SNRs. The current LMC SNR sample is the most complete of any galaxy (see §7.2 and references therein). Numerous analyses on global properties such as spatial & size distributions, luminosities, chemical compositions, phases or age distribution, lifetimes or rates, emission spectral indices, spherical symmetries, local environments, etc. have been made on the MCSNR population. Most of these population studies are powered by multiwavelength astronomy. We discuss and follow some of them in this chapter, focusing on a *population evolution analysis*.

As summarized in 4.4, SNR evolution is subject of many theoretical studies. Woltjer [1972], Chevalier [1982], Cox & Anderson [1982], Cioffi et al. [1988], Blondin et al. [1998] and Truelove & McKee [1999] have studied and surmised analytical models for different phases of SNR evolution in different conditions. The predicted properties need to be verified from measurements of SNR parameters such as size, age, X-ray temperature (kT), emission measure (EM), explosion energy, ejecta mass, etc. As most of these quantities are not fairly known for individual remnants, one relies on assumptions and statistics. In an attempt to *generalize* SNR evolution, we employ a theoretical modeling tool along with a large collection of confirmed or candidate SNRs of LMC to gain some insights into the population. We begin with a description of the tool (§7.1) SNRpy, followed by a summary of data & works used (§7.2). We add one more source to the list of MCSNRs based on our X-ray data analysis and previous studies on J0500-6512; and determine its evolutionary state. This is followed by a series of statistical analyses on the consolidated population data in §7.3, following previous studies and using SNRpy.

7.1 SNRpy

SNRpy [Leahy & Williams 2017, hereafter LW17] is a supernova remnant evolution modeling calculator in Python, a GUI[1] software which takes some SNR parameters as input, performs calculations based on analytical models for different phases of evolution, and gives some plots & values as output. The interface in Fig. 7.1 shows the variable input parameters and output plot & values for evolution of a typical LMC Ia SNR.

The input parameters are age (t_0 yr), initial explosion energy (E_0 $\times 10^{51}$ erg), ejecta mass (M_{ej} $\times \mathrm{M}_\odot$) and ejecta density powerlaw (n = 0 to 14) related to the SNR; and density powerlaw (s = 0 or 2), number density (n_0 cm^{-3}), temperature (T_0 K), cooling adjustment factor (ζ_m) and turbulence speed (σ_v km/s) for the ambient ISM. One can also adjust the, otherwise automatically calculated, electron-ion temperature ratio (T_e/T_i). It also allows you to enter abundances of elements H, He, C, N, O, Ne, Mg, Si, S, and Fe in the CSM and ejecta, manually or choosing from the pre-defined tables: Solar/LMC and CC/Ia, respectively. Some input parameters are changed or added when we change the 'model type' from 'standard' to 'fractional energy-loss', 'hot low-density', or 'pure ST' alternative evolutionary models.

The calculations are based on the analytical solutions of Truelove & McKee [1999] (or TM99) for phases ED through ST, with early ED evolution following the self-similar solutions of Chevalier [1982] and Nadezhin [1985]. The radiative phases are evolved according to the dynamics of Cioffi et al. [1988] (hereafter CMB88) solutions, augmented with the earlier phases. The details are in sections 3.1 & 3.2 of LW17 and §7.1.1 below.

For a given set of input parameters, abundances and model type, the software calculates time arrays of radius, velocity, temperature and emission measure of the forward and reverse shock fronts. The 4 output plots of the variables ($R_{\mathrm{fs/rs}}$, $V_{\mathrm{fs/rs}}$, $EM_{\mathrm{fs/rs}}$ and $T_{\mathrm{fs/rs}}$) versus time (t) can be viewed one-by-one, in linear or log *x*- and *y*-scales and for different ranges of *x* or time. Further, it calculates and prints values of electron temperatures, radii and velocities associated with forward and reverse shocks at the specified age ($t = t_0$). Phase transition times (t_{ST}, t_{PDS}, t_{mrg}) as well as reverse shock 'peak' and 'lifetime' are shown. Some tests on how these values and the plots vary by varying different parameters (while keeping others fixed) are presented in §7.1.3, verifying the results of LW17 and the underlying analytical models.

Some limitations on the working and usage of the program are noted here:

1. The evolution calculations for density profile of the pre-shock medium $\rho_0 \propto r^{-s}$ work only up to the ED and ST phases for the $s = 2$ case which is suitable for progenitors with stellar winds (In this case, the CSM input parameters are the wind mass-loss and speed). So, only the constant density case, $s = 0$ is considered throughout.
2. As "Emissivity" outputs like surface brightness profile and luminosity are also limited to certain cases, namely whenever self-similarity exists, those results are not very useful for most of our cases and are hence not included in the analysis.
3. There were some technical problems in extracting and manipulating emission measure and temperature versus time data from the code; those calculations and plots are hence used in a limited capacity.
4. Lastly, although it was to possible to model alternate evolutionary models, we stick to the "Standard" path of evolution for our remnants. A future study can look more deeply in the specific environment and conditions of individual SNRs and model them accordingly.

[1] Graphical User Interface: here, a *window* with graphical and interactive elements "popping-up" from a *.py script

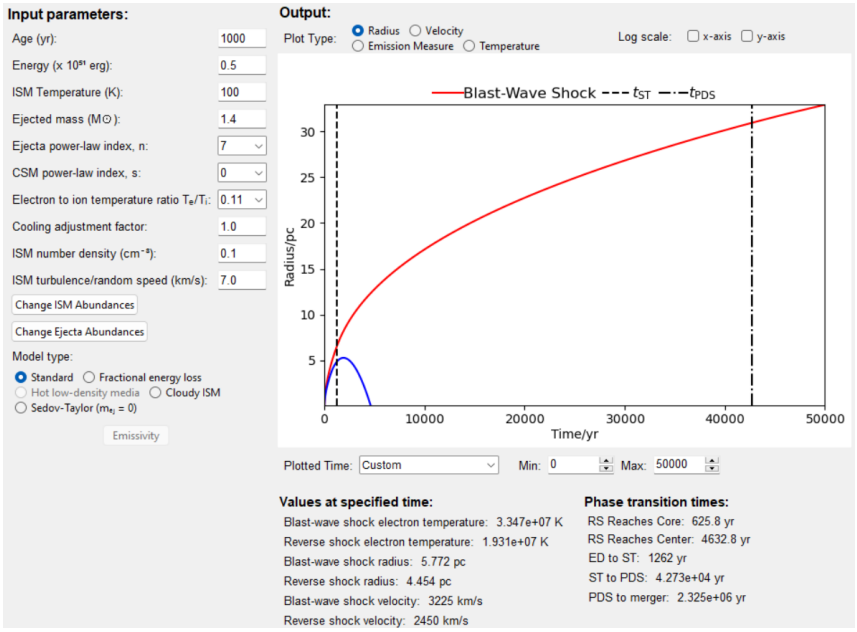

Figure 7.1: SNRpy interface with typical values for LMC SNRs. The changed input parameter values are of t, E_0, n and n_0, while rest are default. The ISM and ejecta abundances are set to "LMC" and "Type Ia", respectively, and the x-axis limit of the plots is from 0 to 50,000 yr. The current plot is for (forward in red and reverse in blue) shock radius, with "Standard" model calculations. Some results at $t = 1000$ yr are shown on the bottom right, and $t_{\rm phase}$ on the bottom left ($t_{\rm ST}$ and $t_{\rm PDS}$ are also shown on the plot with dashed and dash-dotted lines).

7.1.1 Shock Evolution Models

The model(s) assumes a spherical symmetry following TM99, so that the system reduces to one spatial dimension. TM99 uses characteristic radius and time scales (see §4.4.3). For the $s = 0$ case, these are:

$$R_{\rm ch} = \left(\frac{M_{\rm ej}}{\rho_0}\right)^{1/3} \quad \text{and} \quad t_{\rm ch} = \frac{E_0^{-1/2} M_{\rm ej}^{5/6}}{\rho_0^{1/3}} \quad \Longrightarrow \quad V_{\rm ch} = \frac{R_{\rm ch}}{t_{\rm ch}}. \tag{7.1}$$

and the characteristic shock temperature (for constant CSM density, $\rho = \rho_0 = \mu_H m_H n_0$):

$$T_{\rm ch} = \frac{3}{16} \frac{\mu_I m_H}{k_B} V_{\rm ch}^2 \tag{7.2}$$

where n_0 is the ambient ISM hydrogen number density, μ_H & μ_I are the mean mass per hydrogen/ion, m_H is the mass of a hydrogen atom, k_B is the Boltzmann constant; E_0 is the initial explosion energy and $M_{\rm ej}$ is the ejected mass. For the case where $s = 2$ (CSM with $\rho = \rho_s \propto r^{-2}$):

$$R_{\rm ch} = \frac{M_{\rm ej}}{\rho_s} \quad \text{and} \quad t_{\rm ch} = \frac{E_0^{-1/2} M_{\rm ej}^{3/2}}{4\pi\rho_s} \tag{7.3}$$

where $\dot{M}$ is the wind mass-loss rate and v_w is the wind velocity in mass density $\rho_s = \frac{\dot{M}}{4\pi v_w}$.

The remnant is assumed to be cooling according to the function

$$\Lambda = 1.6 \times 10^{-19} \zeta_m T^{-1/2} \text{ erg cm}^3 \text{ s}^{-1} \tag{7.4}$$

with the metallicity factor ζ_m. This gives the epoch of thin-shell formation, $t_{\rm sf}$, and advent of the radiative phase, $t_{\rm PDS} = t_{\rm sf}/e$, from CMB88, and finally the merger phase when $V_s < \beta\sqrt{c_s^2 + \sigma_v^2}$. We have:

$$t_{\rm sf} = 3.61 \left(\frac{E_{51}^{3/14}}{n_0^{4/7} \zeta_m^{5/14}} \right) \times 10^4 \,{\rm yr} \quad \text{and} \quad t_{\rm mrg} = 153 t_{\rm PDS} \left(\frac{E_{51}^{1/14} n_0^{1/7} \zeta_m^{3/14}}{\beta c_6} \right)^{10/7} \tag{7.5}$$

assuming the factor $\beta = 2$ which distinguishes the shock from the thermal sound speed, $c_s = \sqrt{\gamma k_B T_0/(\mu_H m_H)}$ and turbulent motions, σ_v in the ISM. Here, E_{51} is E_0 in units of 10^{51} erg and $c_6 = \sqrt{c_s^2 + \sigma_v^2}$ per 10^6 cm s^{-1}.

Summarily, the shock evolution in SNRpy starts with the self-similar solutions of Chevalier [1982] for the early ED phases and then follows the treatment of TM99 for unified ED to ST phases. Specifically, the authors (LW17) use the tables 3, 5, 8, 9 and equations 47, 48, 49, 57, 58, 75, 76, 77, 81, 82, 83, 84 of TM99 for non-radiative evolution of forward and reverse shocks with different ejecta profiles (n). The radiative phases (PDS, MCS and merger) follow the CMB88 model calculations, but with a linear interpolation for the shock velocity to avoid discontinuity at the transition point.

Further, for defining shock temperatures, SNRpy takes electron heating into account, following the analytical approximation of Cox & Anderson [1982]. The electron-ion equilibration timescale and the temperature ratio due to Coulomb collisions are given as:

$$t_{\rm eq} = 5000 \cdot E_{51}^{3/14} n_0^{-4/7} \tag{7.6}$$

$$\frac{T_e}{T_i} \equiv g = 1 - (1 - g_0) \cdot \exp\left[- \left(\frac{5f}{3} \right)^{0.4} \left(1 + 0.3 \left(\frac{5f}{3} \right)^{0.6} \right) \right] \tag{7.7}$$

with $g_0 = 0.03$ as the lower limit,

$$f = \frac{\ln(\Lambda)}{81} \cdot \frac{4 n_0}{T_s^{3/2}} (t - t_0) \quad \text{and} \quad \ln(\Lambda) = \ln\left(1.2 \times 10^5 \sqrt{\frac{T_s}{4 n_0}} T_e \right) \tag{7.8}$$

This allows the calculation of electron/ion temperatures from g and shock velocity as:

$$\frac{T_e}{\mu_e m_H} + \frac{T_i}{\mu_i m_H} = \frac{3 V_s^2}{16 k_B} \tag{7.9}$$

See LW17 for more details. As implementation, the output plots of shock temperature evolution are shown in Figs. 7.4, 7.5, 7.6 (bottom right).

7.1.2 Emission Calculations

In addition to calculating the evolution of the forward and shock radii, the program also provides measures of SNR emissivity. We already introduced emission measure (EM) as the volume-integral of $n_e \cdot n_H$ and its relation to the normalization of spectral model fitted for the X-ray-emitting plasma. In SNRpy (LW17), the authors define a dimensionless EM:

$$dEM = EM/(n_{e,s} n_{H,s} R_s^3) \tag{7.10}$$

where s denotes values *just* inside the shock front, so that $n_{H,s} = 4 n_H$. Similarly, dimensionless temperature is defined as:

$$dT = \frac{1}{T_s \cdot EM} \int n_e(r) n_H(r) T(r) dV \tag{7.11}$$

which gives a *emission-weighted temperature*, $dT \times T_s$. These normalizations only work for the self-similar phases of evolution when the interior density profile is constant.

The program also approximates the emission coefficient, $I(b, \nu) = \int j(\nu) ds$ by assuming that the emissivity $\epsilon(\nu) = n_e n_H / j(\nu)$ depends only on the current temperature $T(r)$ and not, for example, on the ionization timescale $\tau = n_H t$. So, the integral taken along SNR LoS at impact parameter b from the SNR center gives the surface brightness at given frequency ν. Only thermal bremsstrahlung is considered as the emission mechanism. The luminosity at a given energy (range) $L_\nu(dE)$ is also calculated, by integrating the surface brightness or the emssion coefficient over the SNR area.

7.1.3 Implementation

The 1D SNR evolution calculator code is distributed as an open-source software under the 3-Clause BSD License in a public repository [2]. We use the original code with minor modifications [by J. Knies, priv. comm.]. It consists of 3 Python modules for calculation, GUI and plotting, integrated into the main module, `snr.py`.

As a first step, we vary the density profile of the ejecta as $n = 0$, 1, 2, 4, 6, 7, 8, 9, 10, 11, 12, 13 and 14, keeping $s = 0$ and other parameters fixed. The resulting evolution of shock radii with time is plotted in Fig. 7.2 for a CC SNR with $E_0 = 10^{51}$ erg, $M_{\rm ej} = 1 M_\odot$ and solar ISM with $s = 0$, $n_0 = 2$ cm^{-3}, $T_0 = 100$ K, $\zeta_m = 1$ and $\sigma_v = 7$ km/s. It can be seen that the forward shock radius ($R_{\rm fs}$) does not vary significantly for different n: decreases slightly with increasing n, but is lowest for $n = 7$ and highest for $n = 4$. The reverse shock evolution variation with n is more complex: $R_{\rm fs}$ peak higher for larger n being largest for $n = 14$, but the reverse shock lifetime is longest for $n = 2$. These results were using identical input parameters as Fig2 of LW17 and corroborate with theirs. Repeating the same calculations with Ia SNR with $E_0 = 0.5 \times 10^{51}$ erg, $M_{\rm ej} = 1.4 M_\odot$ and LMC ISM with $s = 0$, $n_0 = 0.1$ cm^{-3}, $T_0 = 100$ K, $\zeta_m = 1$ and $\sigma_v = 7$ km/s, as shown in Fig. 7.1, we plot the radial and velocity evolution curves for different n, in Fig. 7.3. The time-evolution of forward and reverse shock radii now is qualitatively similar to Fig. 7.2 albeit with $\approx 6\times$ jump in the scale. As we will see, this is primarily due to an order-of-magnitude smaller value of n_0. Presently, we resolve to use $n = 7$ for the ejecta density for all our subsequent modeling calculations. This is expected for type Ia explosions [Colgate & McKee 1969], while CC SNRs should have $n > 5$ [Chevalier & Fransson 1994]. Also, the built-in theory is most compatible with this number, and observational errors usually dominate over the variations caused by n. Same goes for various M_{ej}, as shown in Fig. 7.4. We vary the ejecta mass from 0.1$-$10 M$_\odot$ in 20 multiplicative steps, and plot also the EM and shock temperatures. Forward shock radius and forward shock velocity are still not quite variable, but the reverse shock parameters are enlarged with increasing M_{ej}. We fix $M_{ej} = 1.4$ M$_\odot$ in our future calculations, unless stated otherwise. This assumption works well to model forward shock radii of (possibly observed) SNRs. We find that SNR explosion energy and ISM number density are the most impactful input parameters on the forward shock evolution. In Figs. 7.5 and 7.6, we vary E_0 (in units of 10^{51} erg) from 0.17 to 1.5 and n_0 from 0.01 to 1 cm^{-3}, while keeping the rest of the parameters to the "typical Ia LMC SNR" value. These parameter values and their range of variations follow the results and 1σ errors, respectively, of Leahy [2017]'s evolutionary analysis on the population of supernova remnants in the Large Magellanic Cloud, as will be discussed below.

[2] `https://github.com/denisleahy/SNRmodels`

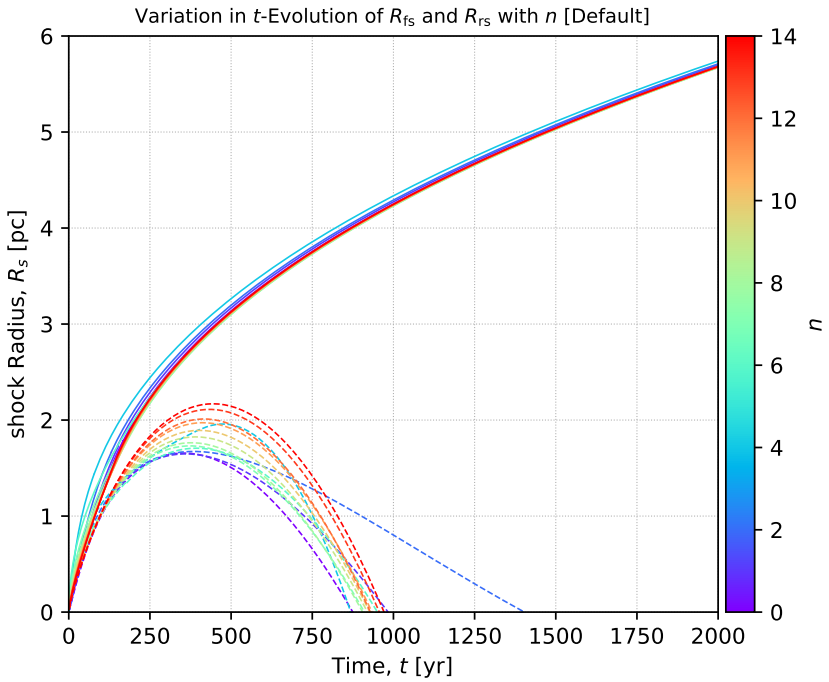

Figure 7.2: Variation in the time-evolution of the forward (solid lines) and reverse (dashed lines) shock radii with ejecta density powerlaw index n. Here, the input parameters are same as in Fig2 of LW17: CC, $E_0 = 1$, $M_{ej} = 1$ and Solar, $s = 0$, $n_0 = 2$, $T_0 = 100$, $\zeta_m = 1$, $\sigma_v = 7$.

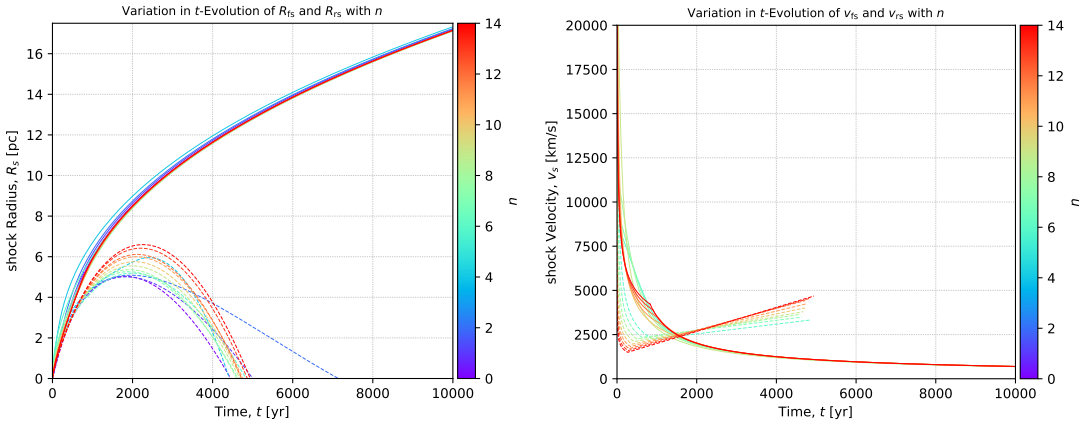

Figure 7.3: Variation in the time-evolution of the forward (solid lines) and reverse (dashed lines) shock radii (**left**) and shock velocities (**right**) with ejecta density powerlaw index n. Curves for v_s for $n < 6$ are skipped as the models exclude such calculation. Here, the input parameters are from Fig. 7.1: Ia, $E_0 = 0.5$, $M_{ej} = 1.4$ and LMC, $s = 0$, $n_0 = 0.1$, $T_0 = 100$, $\zeta_m = 1$, $\sigma_v = 7$. Notice the large change in scale as compared to Fig. 7.2.

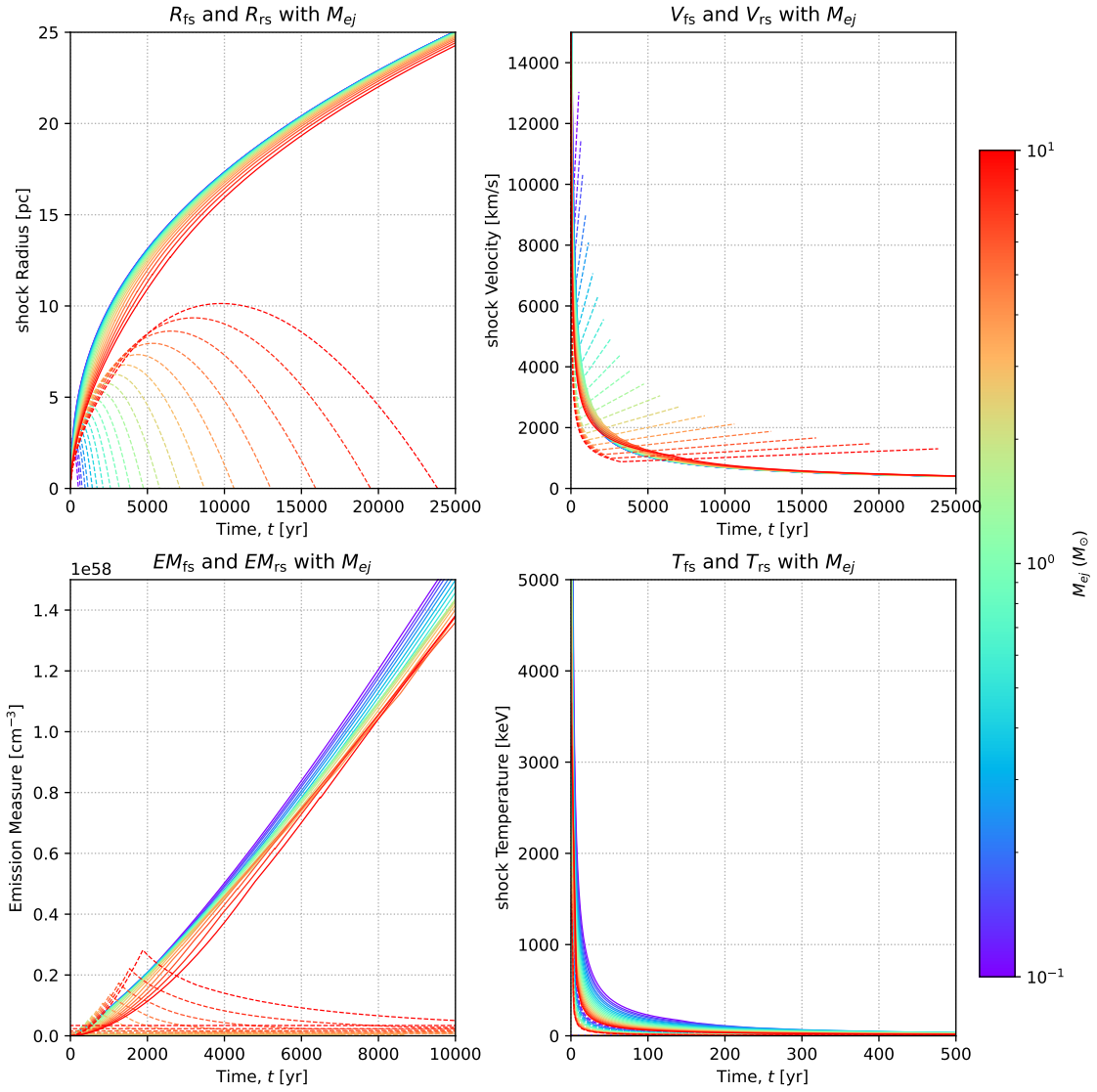

Figure 7.4: Time-evolution of the forward (solid lines) and reverse (dashed lines) shock radii (**top left**), velocities (**top right**), emission measures (**bottom left**) and temperatures (**bottom right**), varying with ejecta mass (M_{ej}, logarithmic color bar). Other inputs are same as in Fig. 7.3, i.e., for a "typical Ia LMC SNR".

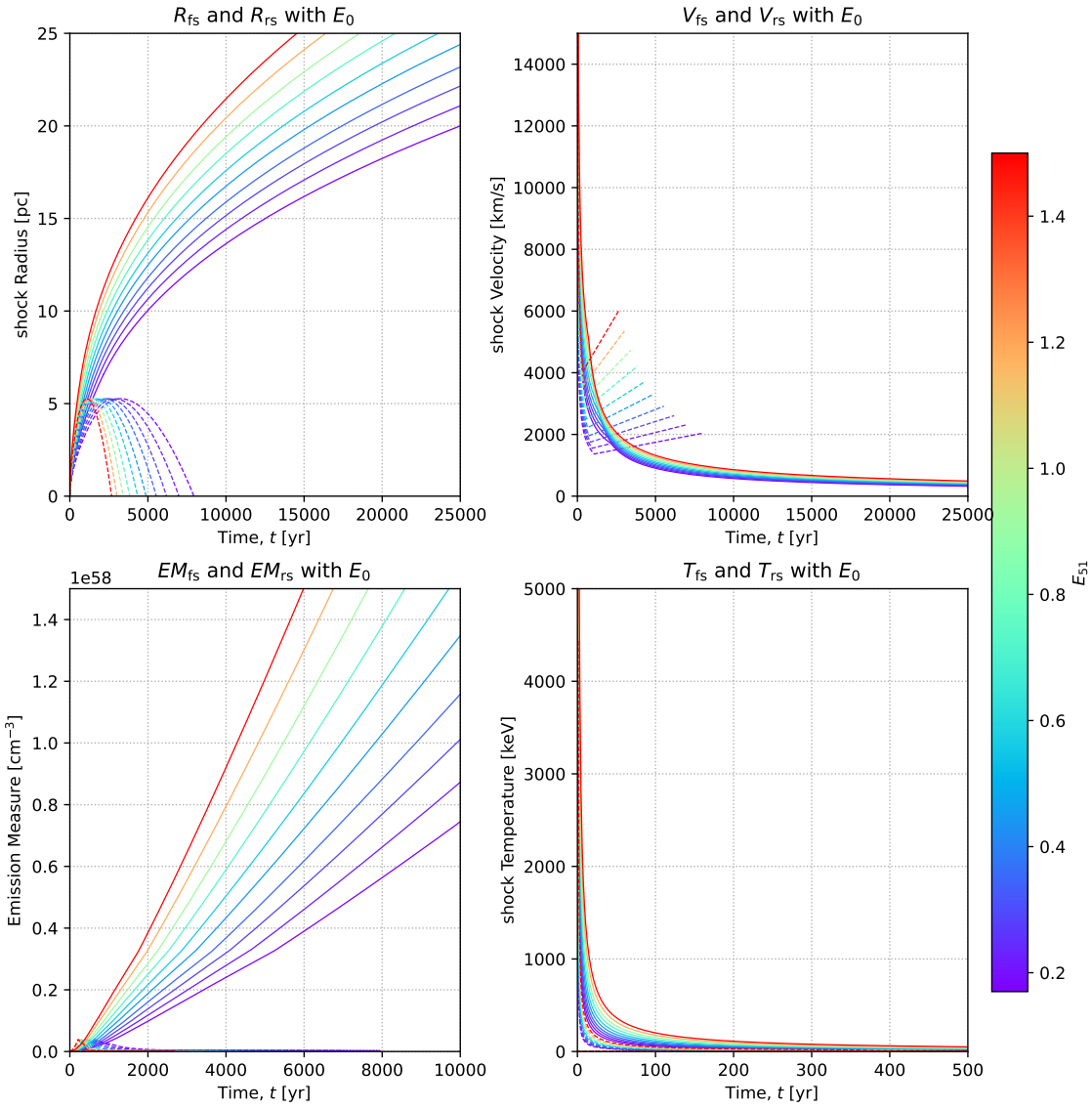

Figure 7.5: Time-evolution of the forward (solid lines) and reverse (dashed lines) shock radii (**top left**), velocities (**top right**), emission measures (**bottom left**) and temperatures (**bottom right**), varying with explosion energy E_{51} (linear color bar). Inputs and scales are same as in Fig. 7.4.

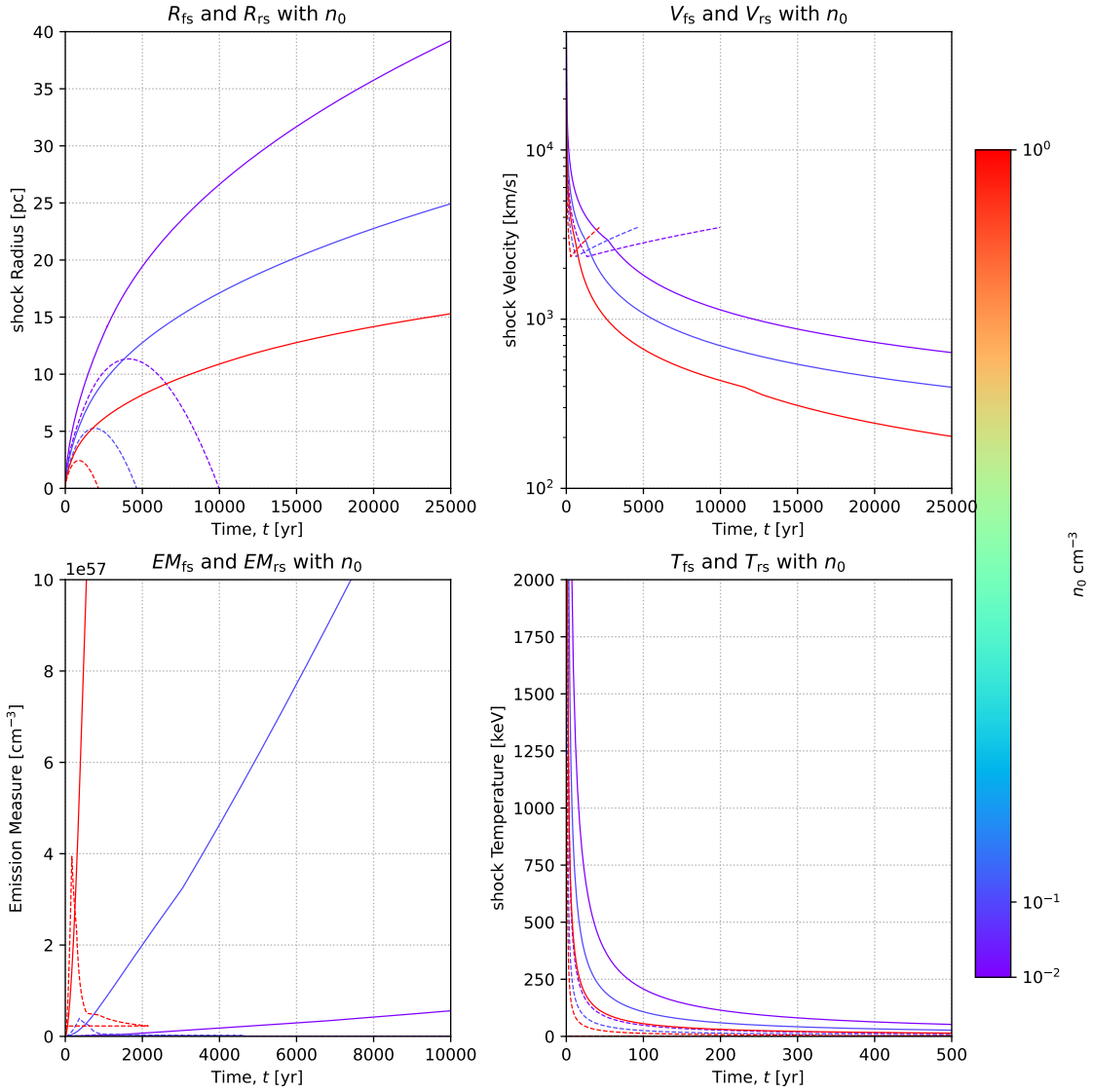

Figure 7.6: Time-evolution of the forward (solid lines) and reverse (dashed lines) shock radii (**top left**), velocities (**top right**), emission measures (**bottom left**) and temperatures (**bottom right**), varying with pre-shock densities n_0 of 0.01, 0.1 and 1 cm^{-3}. Other inputs are same as in Fig. 7.5 with $E_{51} = 0.5$, but some scales are different.

7.2 MCSNRs

In terms of data, we begin with the definitive X-ray catalog of Maggi et al. [2016]. M16 compiled a list of 59 confirmed SNRs in the LMC, including 51 observed with XMM-Newton, 3 with Chandra, 2 with ROSAT and only 3 with no X-ray data. The paper introduces the naming convention with prefix "MCSNR J" followed by right ascension and declination "hhmm–ddmm" of identified remnants (e.g., SNR 1987A is MCSNR J0536–6916), which we adopt here as most other studies on the population of SNRs in the MCs.

X-ray observations alone are not convincing evidence for existence of a supernova remnant, although they provide crucial information about the plasma and medium from the emission. Thus, we have *confirmed* or bona fide SNRs and *candidates* that show some characteristics of a SNR. Counterpart radio and/or optical range observations are usually needed to confirm (or reject) the candidates. There are fundamentally three criteria to classify an object as an SNR: a non-thermal radio spectral index, with $\alpha < -0.4$ (where $S_\nu \propto \nu^\alpha$, S_ν is the flux density and ν is the frequency), the presence of diffuse X-ray emission, and an elevated [SII]/Hα ratio ≥ 0.4, indicative of high-velocity shocks [notably Filipović et al. 1998]. Two of these three characteristics are usually enough to confirm a SNR, while just one makes it a candidate. Fig. 7.7 shows this multiwavelength approach.

Bozzetto et al. [2017] (hereafter B17) identified 15 candidate MCSNRs based on optical & radio surveys and classification criteria of Filipovic et al. [1998], and performed a statistical study on the augmented sample of 74 SNRs in the LMC, the most complete of any galaxy. This will be our second source of data, as many of the candidates suggested in this study have so far been confirmed as bona fide SNRs. Yew et al. [2021] (or Y21) presented optical candidates (16) and confirmed (3) MCSNRs, increasing the numbers to 62 and 20, respectively. The selection and classifications were primarily based on morphology and [SII]/Hα ratio obtained from narrow-band imaging observations (MCELS) and spectroscopic follow-up (WiFeS). These were generally from an older, larger and fainter population.

Further studies [Maitra et al. 2019, 2021; Sasaki et al. 2022] confirmed 2 more radio B17 candidates and one optical Y21 candidate, until Kavanagh et al. [2022] (hereafter K22) added 7 new MCSNRs to the list by follow-up X-ray (XMM-Newton) analysis on 8 candidate (and 2 previously confirmed) SNRs in the LMC. Six of these were B17 candidates, one from Haberl & Pietsch [1999]. Thus, there were 71 confirmed SNRs with a number of candidates. Bozzetto et al. [2022] presented 14 SNR candidates from radio (ASKAP) surveys, confirming one of them & one of the previous 20 candidates as MCSNRs. This adds up to 73 confirmed and 32 candidate SNRs in the LMC.

Most recently, Zangrandi et al. [2024] (elsewhere Z24), with the latest operational X-ray telescope (eROSITA[3]) which surveyed the whole sky including the entire LMC, updated the MCSNR catalog to 77+47 confirmed+candidates (see Fig. 7.8). Finally, this work (§6.2) adds one more, MCSNR J0500-6512 (§7.2.1), to the confirmed list. This makes up the current concatenated sample of 78 confirmed and 46 candidate SNRs in LMC.

Besides these search, compilation and classification studies on specific objects, a number of statistical and evolutionary studies on the population as a whole have been made. We mention, summarize, follow and contribute to some of them below, extending the analysis to the increased pool of MCSNRs. But, before proceeding further, we reiterate the justification for "Why only LMC SNRs are analyzed?":

1. The shock radius, one of the most important input parameters in our studies, must be inferred from the observed angular size and distance of the remnant, which is quite certain

[3] eROSITA is neither latest nor operational anymore due to Japan's XRISM and Russia's war, respectively.

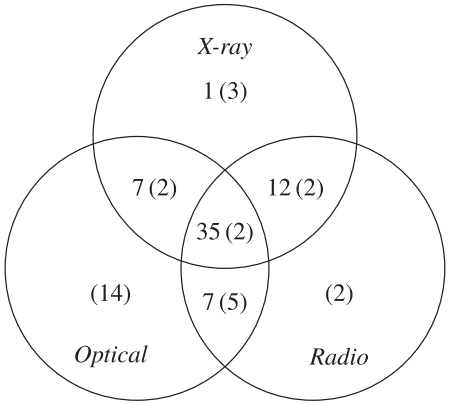

Figure 7.7: Venn diagram from Yew et al. [2021] showing 62 confirmed and 20 candidate LMC SNRs with observations in one or more electromagnetic regions.

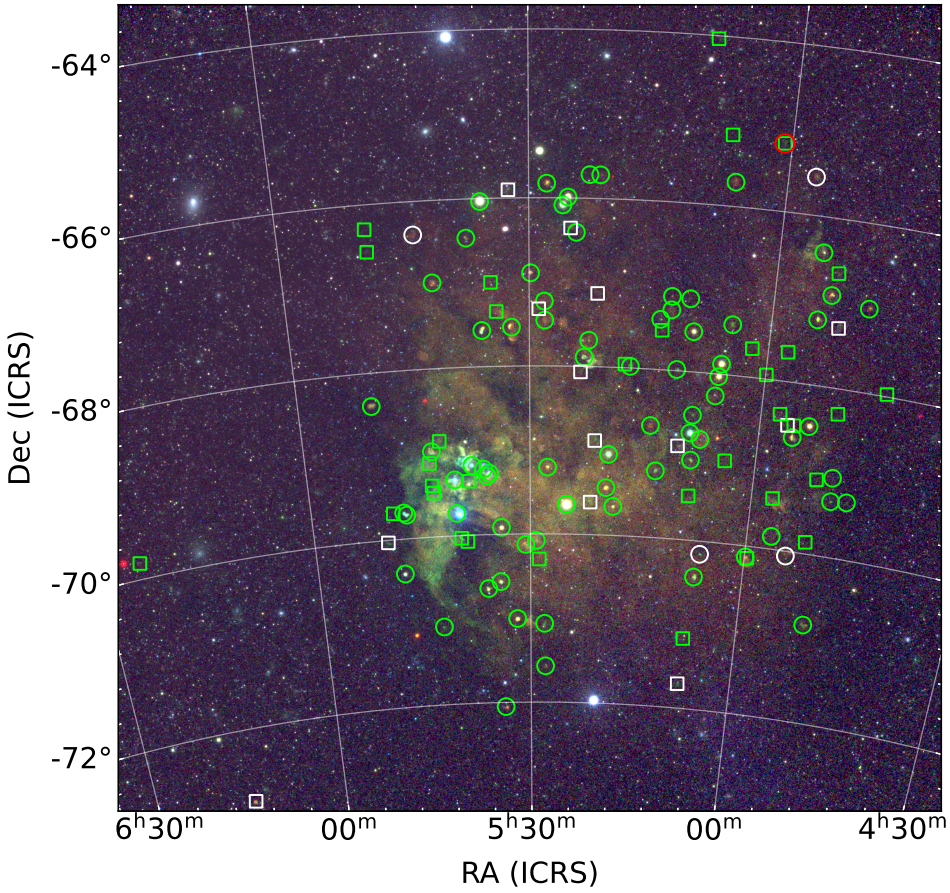

Figure 7.8: LMC in RGB (0.2–0.7–1.1–5 keV) with the current sample of confirmed (circle)s and candidate (squares) SNRs, from the eROSITA all-sky surveys [Z24, reproduced with permission]. MCSNR J0500-6512 is shown by a red circle enclosing the green square.

for occurrences in LMC.

2. The X-ray temperature and EM have to be extracted from careful modeling of the spectra, which needs good photon statistics. The lower X-ray absorbing column density along LMC LoS favors this.
3. The multiwavelength coverage of LMC, availability of data and studies is another reason for our priority. The obvious next step will be to explore extragalactic SNRs in the Local Group.

7.2.1 J0500-6512

A large, elongated SNR candidate was identified in the optical survey of Yew et al. [2021] with MCELS [SII]/Hα $\approx$ 0.8. The spectroscopic follow-up on 2017.10.22 with WiFeS [Dopita et al. 2007] showed [SII] and [NII] lines but did not diagnose for the 'blue' [OIII] and [FeII] lines. Their spectra and images are shown in Fig. 7.9, and other information in Tab. 7.1. The average size (in parsec) was derived from the average of the major and minor axes of the ellipse delineating the maximal extent of the optical emission and assuming a distance of 50 kpc. The lack of OB-type stars might indicate a type Ia origin, but this could not be ascertained. The electron density (n_e) based on the ratio of [SiII] lines and assumed $T_e = 10^4$ K is at the "low density limit" which suggests an old age.

Table 7.1: J0500-6512 optical observation information from Yew et al. [2021]. The fluxes of the different emission lines is relative (counts) with 23-25% error.

Obs Date	RA J2000	Dec J2000	$D_{maj} \times D_{min}$ arcsec	D_{av} pc	PA °	MCELS [SII]/Hα	OB stars #
2017.10.22	$05^h00^m58.5^s$	−65°12'15.3"	480×360	100.8	80	0.8	0/0

Lines Å	Hα 6563	[NII] 6583	[SII] 6716	[SII] 6731	[SII]/[SII] 6716/6731	[NII]/Hα	[SII]/Hα	n_e cm^{-3}
Flux	1111	152	540	359	1.5	0.18	0.81	low

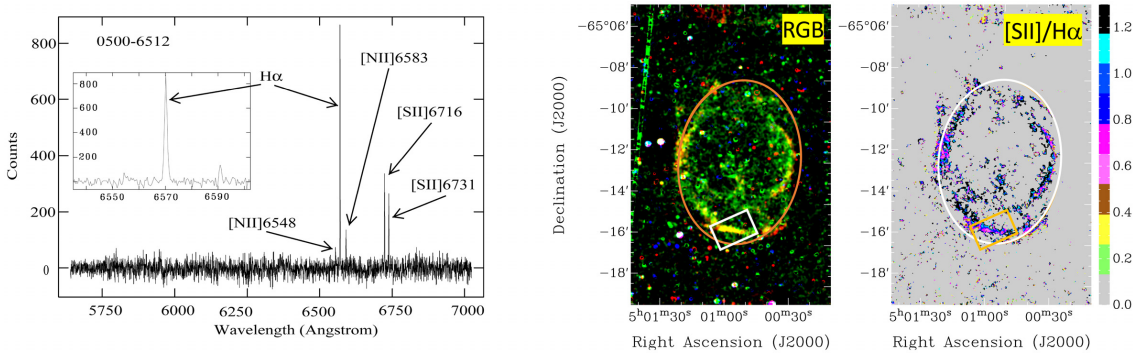

Figure 7.9: J0500-6512 (**left**:) spectra from one arm of the WiFeS spectrograph showing Hα & other optical lines and (**middle** and **right**:) images from MCELS data in Hα-[SII]-[OIII] RGB and [SII]/Hα ratio produced by Yew et al. [2021, FigA.5].

The age of J0500-6512 was estimated assuming Sedov-Taylor evolution from an initial energy of 0.5 $\times 10^{51}$ erg in an ISM of density 0.1 cm^{-3} in §6.3.3 to be ∼146207 yr. The forward shock velocity was also deduced from its radius known from X-ray and optical images. The

large size, presence of optical emission and long age for typical ranges of E_0 and n_0 implies that our remnant is well-past its Sedov phase. The ST solution, which ignores the ejected mass (i.e., $M_{ej} = 0$), is thus no longer applicable for MCSNR J0500-6512. To get a better estimate on age and evolutionary state of J0500-6512, we apply the 'standard' SNRpy model for a 'typical Ia LMC SNR', i.e., with $E_{51} = 0.5$, $n_0 = 0.1$, $M_{ej} = 1.4$, $n = 7$, etc. onto the observed $R_{\rm fs}$. The resulting time-evolution of shock radii and velocities are over-plotted onto the 'pure ST' model of Fig. 6.19, in Fig. 7.10. The contrast in the two models is visible in, for example, the age (t_0) estimate viz. the epoch at which the forward shock radius in ≈ 50.67 pc. SNRpy gives $t_0 \approx 176.500$ kyr. The transition times from ED to ST ($t_{\rm ST}$), ST to PDS ($t_{\rm PDS}$, current) and PDS to merger ($t_{\rm mrg}$) are approximately 1.262 kyr, 42.730 kyr, 2.325 Myr, respectively. The forward shock would only be moving at ≈ 89.52 km s^{-1}. Obviously, the evolution is contingent on the assumptions of explosion energy and pre-shock density, so that both the age and $V_{\rm fs}$ are variable on scales of several orders of magnitude, as seen in Fig. 6.18, 7.5, 7.6.

7.3 Analysis

7.3.1 Source Matching

For a consistent analysis and clean presentation, lists of all known SNRs and candidates in the LMC were searched and all relevant information on their properties was retrieved and merged. This compiled table with its first few columns is shown in Tab. A.1. It has 124 sources, numbered 1 to 78 for confirmed and c1 to c46 for candidate MCSNRs in the LMC, following the work of Z24 and the promotion of J0500-6512 to the confirmed category. The "SNr" or serial number is assigned to each source to be the unique identifier in case of mismatch in MCSNR names among different catalogs. The names and RA & Dec coordinates are from Z24. Alternate name (alias), wherever available, and references are also provided for cross-matching and more information.

7.3.1.1 Typing

The origin type of some MCSNRs is known from their morphology, ejecta composition, presence of a compact central object (CCO), light echoes, or historical observation [see 6 and B in M16, and references therein]. These are *secured* CC or TN type SNRs, listed in Table A.1 of M16. Further, M16 tentatively type all the remnants based on two metrics: "number of blue early-type stars in the immediate vicinity" $N_{\rm OB}$ and "ratio of CCSNe and TNSNe expected from the observed distribution of stellar ages in the neighborhood" $r = N_{\rm CC}/N_{\rm TN}$. The number of OB-type stars was counted from color-magnitude diagrams for stars within 100 pc of each remnant, while r was calculated using the delay time distribution (DTD) $\Psi_i(\tau)$ [Maoz & Badenes 2010] and the stellar mass formed M_i in the LMC in 3 time-intervals i as:

$$r = \frac{\Psi_1 M_1}{\Psi_2 M_2 + \Psi_3 M_3} \tag{7.12}$$

We use this criteria based on local star formation history (SFH) or the "hints" obtained from $N_{\rm OB}$ and r, along with the provided "Hint-spec" based on spectral analysis M16, Tables C.1, 6 and 7, taking their arithmetic mean, assign a *tentative* type to each of the 59 remnants. After comparing with the 25 secured SNRs, we correct 2 wrongly-assigned type: J0506−7026 (secured TN) and J0509−6844 (N103B, secured TN). Also 4 other remnants with undecided types were kept CC: J0453−6829 (low $N_{\rm OB}$, secured CC), J0455−6839 (N86), J0505−6802

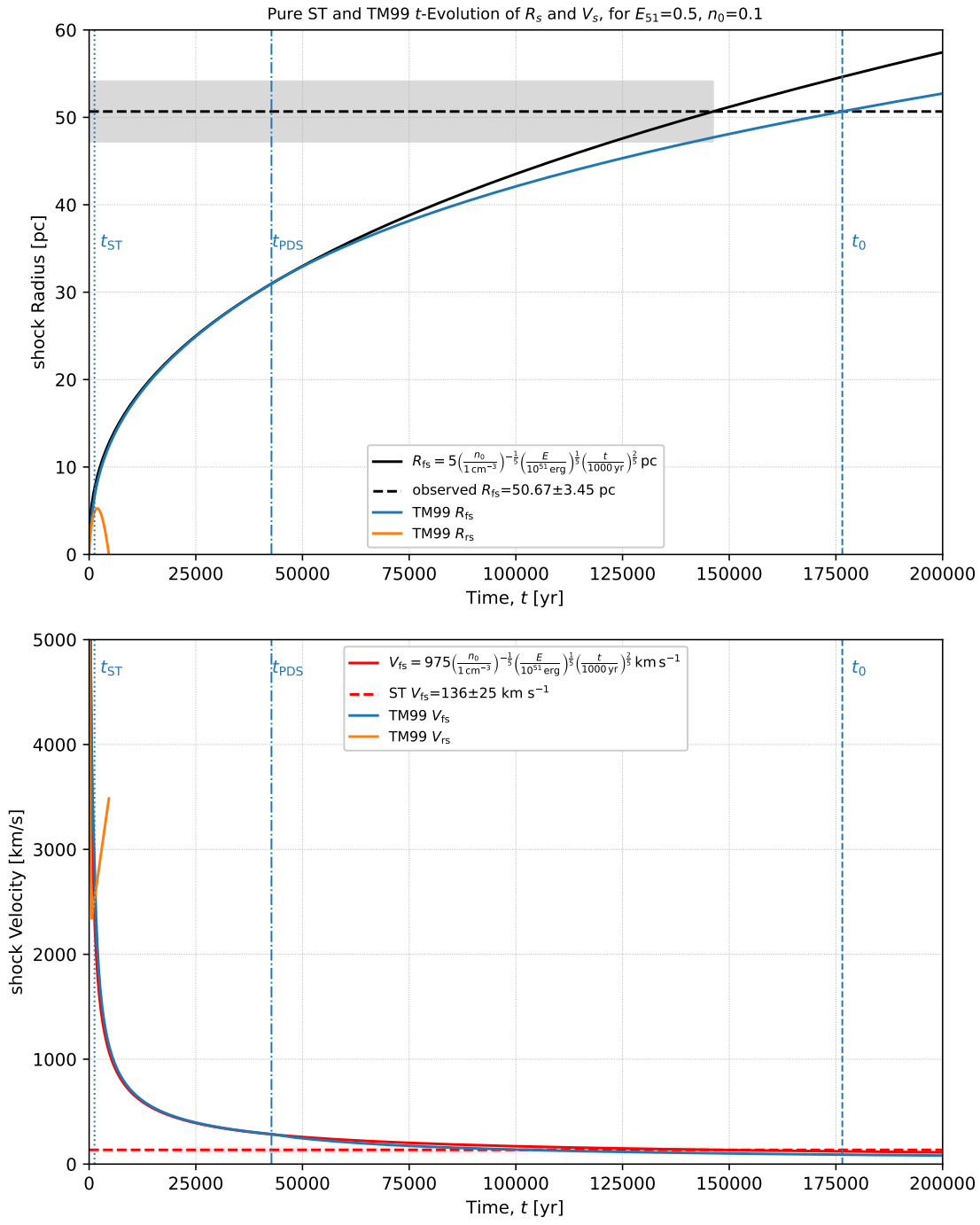

Figure 7.10: J0500-6512: Pure ST compared to SNRpy evolution

(N23, secured CC) and J0517−6759. We also verify the types of tentative SNRs from B17, who also lists "questionable" CC/TN types. These are used as the "new" tentative types, whenever available; though for the certain (including "PWN") and unknown ("X") type SNRs, M16 secured and tentative classifications are used.

This gives us the ratio $N_{\rm CC}/N_{\rm TN} = 34/25 = 1.36$, where 12 CC and 16 TN SNRs have a secured type. The implications of explosion type will be discussed in subsequent sections.

7.3.1.2 Dating

Unless a SNR can be associated with a historically observed SN event (§2.1), one must rely on indirect measures to estimate its age. The most common way is to use the observed "size", i.e., the extent of radio, optical or X-ray emission, and apply evolutionary models (especially the Sedov-Taylor solutions) with some assumptions to constrain a rough age or phase. As this has been done for a number of LMC remnants by various authors, we simply extract the data collected by M16 and B17. We also use the evolutionary properties derived by K22 for their 8 SNRs, and, of course the analysis of Leahy [2017] 51/59 M16 SNRs. Maitra et al. [2019, 2021] also provide Sedov age estimates from the observed radii, shock temperatures and ionization equilibration state.

7.3.2 Size Distribution

Most observational studies on MCSNRs have the SNR size as an output. For the LMC, a common distance of 50 kpc is assumed for all SNRs and enables us to convert their angular sizes to physical sizes. M16 defines and lists the *maximal* extent of their 59 SNRs seen in X-ray images and contours. B17 compiles the sizes of the same from multiwavelength sources (primarily MCELS images with aid from XMM, Chandra, ROSAT, and radio surveys). We show a size comparison in Fig. 7.11 by plotting the radius quoted in B17 versus the radius quoted in M16 for each SNR. The average of major and minor axes was taken as the diameter, as most of the remnants are seen asymmetric (elliptical). As noted in B17, their sizes are around 10% smaller than those of M16. This is somewhat surprising as one would expect radio/optical emission to trace the outermost rim of SNRs better; X-rays might be coming from the interior ejecta. But, a higher resolution in imaging might explain this. This can be seen in the figure as most of the points lying below the $y = x$ line and from the (negative) deviation of the best linear fit. The shape and fill of the numbered data points representing the SNRs expose their (tentative or secured) types.

The distribution of sizes is one of the most studied characteristics of SNR populations, especially for the MCs and commonly in the radio continuum and particularly for shell-type SNRs. In particular, the radio surface brightness Σ of SNRs seem to be correlated with their diameter D. As both the radio flux density S_ν and the solid angle Ω are inversely proportional to distance-squared, $\Sigma_\nu \equiv S_\nu/\Omega = L_\nu \pi^{-2} D^{-2}$ is distance-independent. That is, with time viz. growing size, SNRs should appear less luminous. This was observed and studied to derive the general statistical correlation $\Sigma = AD^{-\beta}$ (see Fig. 7.12). This is called the **Σ−D relation**, based on the theoretical work of Shklovskii [1960] but mostly empirical [e.g., Urošević et al. 2005]. The relation is controversial [e.g., Green 2005] especially when used to estimate distances from the observed surface brightness, and thus statistical dependence on more SNR parameters such as explosion energies and ambient densities [Bandiera & Petruk 2010; Kostić et al. 2016] have been suggested to probe the underlying (theoretical) electron acceleration and time evolution of SNRs.

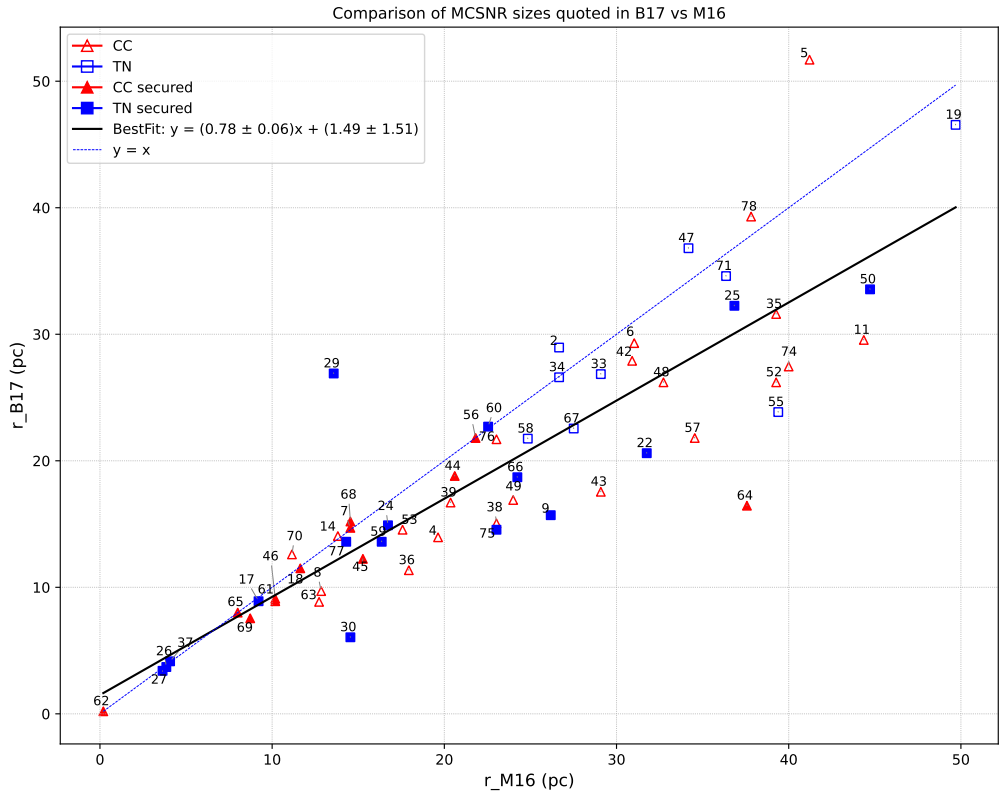

Figure 7.11: B17 vs. M16 size comparison of 59 LMC SNRs. r_{M16} is half the maximal X-ray size and r_{B17} is half the arithmetic mean of major & minor axes of (multiwavelength) extent. Distance is assumed to be 50 kpc throughout. Red triangles and blue squares show CC and TN type SNRs, respectively. Filled points denote SNRs with a secured CC/TN type. The identity line and best linear fit to the points are also plotted.

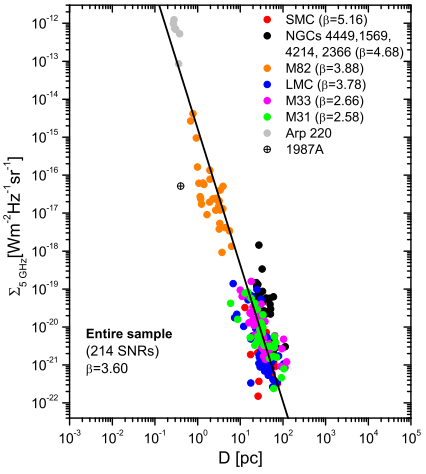

Figure 7.12: $\Sigma-D$ relation fitting using orthogonal regression by B17 on a composite sample of extragalactic SNRs including 40/59 from the LMC.

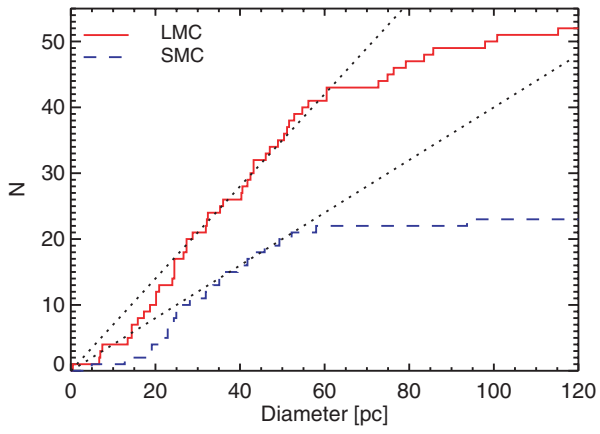

Figure 7.13: Cumulative size distribution of 77 LMC and SMC SNRs by Badenes et al. [2010] showing a linear trend with cut-off at diameter=60 pc.

7.3.2.1 Cumulative Diameter Distributions

We cannot follow up these studies here, except noting that sizes of MCSNRs seem to follow a linear cumulative distribution [Bandiera & Petruk 2010; Badenes et al. 2010]. The trend have been attributed to most MCSNRs being in ED phase or to selection effects. Badenes et al. [2010] rather show that on a bigger (although not 100% complete) sample of LMC and SMC SNRs, the roughly linear cumulative size distribution (see Fig. 7.13) can be explained if most SNRs are in the ST phase, decelerating towards the radiative phase, and in a broad range of ISM densities. We perform the same analysis on our datasets, shown in Fig. 7.14, and reiterate the same conclusions. The cumulative distribution of physical diameters is plotted for LMC SNRs from Z24 (inclusive of J0500-6512, i.e. our final sample), M16, B17 and Y21. All 4 distributions, though not directly comparable due different sample sizes and instrumental measurements, are roughly linear in SNR size up to a certain 'cut-off'. To estimate the slope of the distributions, we perform maximum-likelihood fits on each, similar to Badenes et al. [2010, Fig. 7.13]. Here, the model $dN/dr = n(r)$ is assumed a powerlaw of the form:

$$n(r) = \frac{N(\alpha+1)}{r_{\rm cut}^{\alpha+1}} r^{\alpha} \tag{7.13}$$

where $N = \int_{r_{\rm min}}^{r_{\rm cut}} n(r)dr$ is the enclosed number of remnants. The likelihood of the model is defined as the product of Poisson probabilities, and its maximum gives the maximum-likelihood solution that we use:

$$(\alpha+1)_{ml} = \frac{N}{N \ln r_{\rm cut} - \sum_{j>0} \ln r_i} \quad \text{and} \quad \Delta\alpha = \frac{\alpha+1}{\sqrt{N}} \tag{7.14}$$

This yields the following results for α based on different minimum and cut-off diameters (note that the symbol r is used here for size) for the different MCSNR data sources, summarized in Table 7.2.

Table 7.2: Maximum-likelihood fit for cumulative size distributions on different MCSNR datasets.

Source	α	$r_{\rm min}$ [pc]	$r_{\rm cut}$ [pc]
Z24+	0.42 ± 0.13	20	110
M16	0.33 ± 0.18	8	90
B17	0.54 ± 0.19	15	70
Y21	0.67 ± 0.45	20	100

7.3.2.2 Smoothed Diameter Distributions

We can further explore the distribution of sizes and more using **kernel density estimate (KDE)**, a non-parametric statistical method for estimating the probability density function (PDF) of a random variable based on smoothing individual data points. For a given set of n independent and identically distributed measurements $\{x_1, x_2, \ldots, x_n\}$, the KDE is given by:

$$\hat{f}(x) = \frac{1}{nh} \sum_{i=1}^{n} K\left(\frac{x - x_i}{h}\right) \tag{7.15}$$

where $K(\cdot)$ is the kernel function, typically chosen as a Gaussian kernel,

$$K(u) = \frac{1}{\sqrt{2\pi}} e^{-u^2/2} \tag{7.16}$$

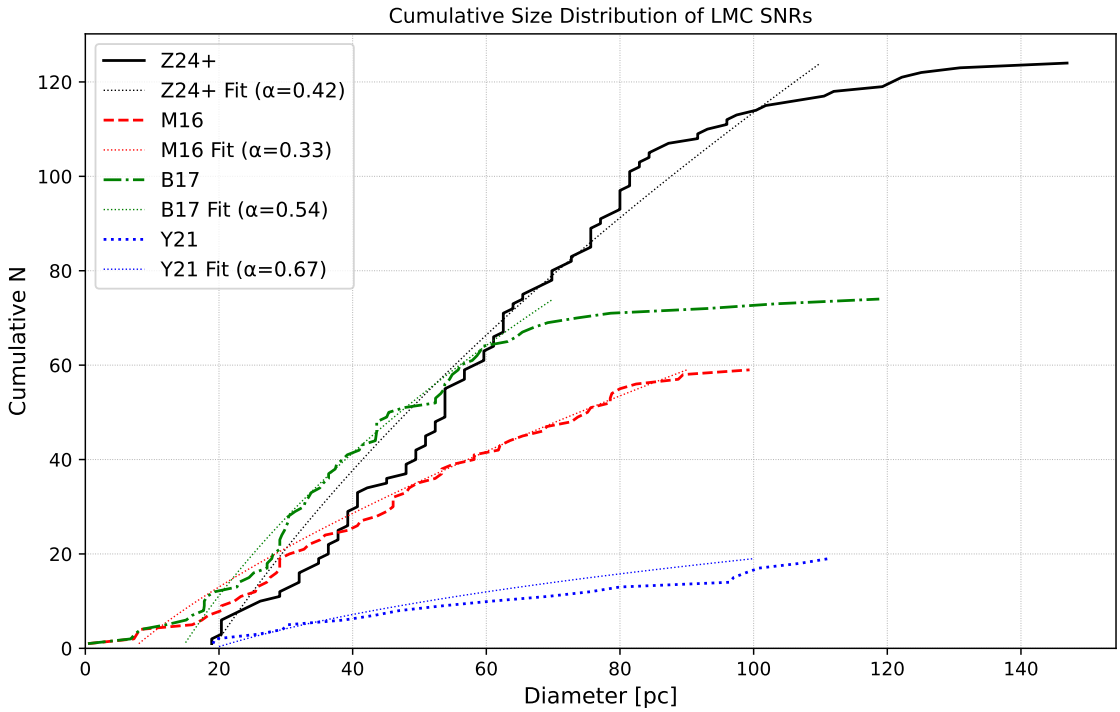

Figure 7.14: Cumulative size distribution of LMC SNRs of Z24; M16; B17; Y21 with maximum-likelihood powerlaw fits following [Badenes et al. 2010].

and h is the bandwidth, which controls the smoothness of the density estimate. For selecting the kernel bandwidth h, one usually minimizes the so-called mean integrated square error (MISE): $\int_{-\infty}^{\infty} \left(f(x) - \hat{f}(x)\right)^2 dx$ or rather the asymptotic MISE (AMISE) as $n \to \infty$ and $h \to 0$. We rather follow the kernel smoothing method of B17 where an optimal bandwidth is found using the bootstrap MISE (BIMSE), which minimizes the error by using smooth bootstrap resampling:

$$\text{BIMSE}(h) = \frac{1}{B} \sum_{i=1}^{B} \int_{-\infty}^{\infty} \left(\hat{f}_i^*(x) - \hat{f}(x)\right)^2 dx \tag{7.17}$$

where B is the number of bootstrap resamplings and $\hat{f}_i^*(x)$ is the kernel density estimate for the i-th bootstrap resample. The smooth bootstrap requires a "plugin" bandwidth h_0 for resampling, and for each resampled data point x_i^*, a Gaussian offset $\theta \sim \mathcal{N}(0, h_0^2)$ is added, yielding: $x_i^{**} = x_i^* + \theta$. This resampling process is repeated for each bootstrap sample, and the resulting density estimates are used to compute the BIMSE. The process is more intensive but more robust because unlike AMISE, the BIMSE shows a distinctive minimum that can be reliably used to select the optimal bandwidth h [see B17, Fig4].
The procedure to minimize BIMSE(h) is similar to B17:

1. We start with an initial rule-of-thumb bandwidth, based on Silverman's 1986 method, with standard deviation $\hat{\sigma}$ and the sample size n, as:

$$h_0 = 1.06 \cdot \hat{\sigma} \cdot n^{-1/5} \tag{7.18}$$

2. For each h value, $B = 500$ smooth bootstrap resamplings were performed to calculate the KDE for each resample. Python functions `resample` and `gaussian_kde` from classes `sklearn.utils` and `scipy.stats`, respectively, were employed. This can be

expressed as:

$$\text{Bootstrap Sample} = \text{Resample}(X) + \mathcal{N}(0, h^2) \tag{7.19}$$

3. A golden section search [Kiefer 1953] was applied which iteratively narrows the interval containing the minimum value by evaluating the BIMSE at four points, using the Python function `scipy.optimize.minimize_scalar`. This gives the optimal bandwidth

$$h^* = \arg\min_h \text{BIMSE}(h) \tag{7.20}$$

4. The confidence intervals were determined from the 500 bootstrap resamples. KDE was computed for each on h^* and confidence bands are the desired quantiles (viz. 2.5% and 97.5% for 95% intervals) at each x-value.
5. The mode of the distribution was estimated by identifying the location of the highest peak in the KDE, i.e.,

$$\hat{x}_{\text{mode}} = \arg\max_x \hat{f}(x) \tag{7.21}$$

The mean μ and median m were calculated from the data as:

$$\mu = \frac{1}{n}\sum_{i=1}^{n} x_i \quad \text{and} \quad m = \text{median}(x_1, x_2, \ldots, x_n) \tag{7.22}$$

The uncertainty in these estimates was assessed using the standard deviation of bootstrap estimates. For efficiency, Gaussian values were computed only within five standard deviations from the mean, with values outside this range treated as zero.

The results for average diameters of SNRs cataloged in B17, Y21 and Z24 are shown in Figs. below. The KDE-smoothed probability density distributions are plotted with 95% confidence intervals, mean, mode and median. First, our plot and calculations (Fig. 7.15, left) corroborate with that of B17 [Fig8, top]; as they should since we are using the same method on the same dataset. We get a mean diameter of 41 ± 3 pc for their population of 74 confirmed and candidate (many of which have been so far confirmed) MCSNRs, which is exactly same as their rounded-off value. Mode and median, 36 ± 3 pc and 37 ± 3 pc are also verified within the uncertainty ranges. So, this provides a benchmark for applying the method and then comparing with SNR data of other authors. Y21 [Fig3] use the kernel smoothing procedure of Maggi et al. [2019], which is computationally cheaper, to calculate the diameter distribution of their 16 SNRs and candidates. So, our repeated analysis with the KDE-BIMSE method does not yield the exact same result. Nevertheless, the qualitative outcomes match: diameters are around 2 times larger compared to B17 sample, the confidence interval is larger due to corresponding large errors, mean diameter = 63 ± 7 is larger than that for the B17 case and within error bounds of Y21 calculation.

Then, we apply the method on SNR sizes compiled by Z24. They draw circles or ellipses to enclose the region of soft diffuse X-ray emission seen in the eRASS:4 images. This includes the emission from known MCSNRs in the LMC as well previous candidates and new eROSITA candidates, a total of 124 objects. We produce smoothed KDE distributions for all as well for 78 confirmed ones, in Fig. 7.16. The PDFs are visually and qualitatively similar to B17, although the average diameter is 62 ± 2 pc i.e. around 33% higher and actually close to the older optical population of Y21. This can be ascribed to addition of fainter, older remnants in the sample and lower resolution & photon statistics of the eROSITA surveys. This is also evident from the reduced sizes of 78 confirmed remnants with a mean at 59 ± 3 pc, which is still higher than previous most X-ray and multiwavelength studies. Follow-up observations on poorly-observed bona fide SNRs and newly-discovered candidates with more sensitive instruments and longer exposure times is demanded for future statistical work in this direction.

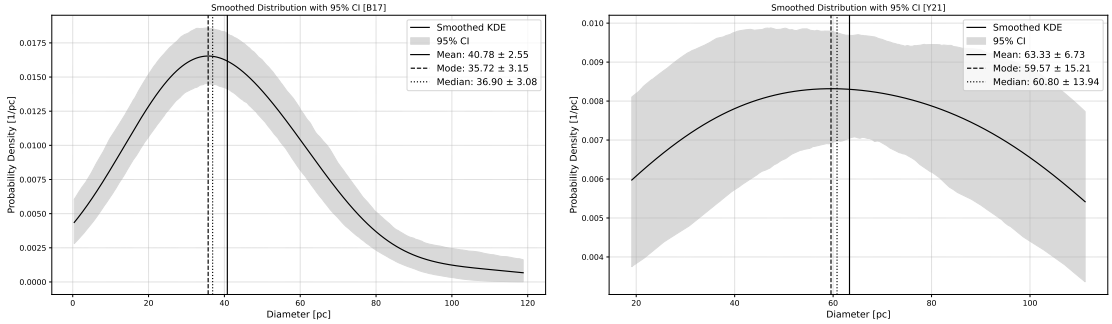

Figure 7.15: KDE BIMSE smoothed diameter distributions of MCSNRs: 59+15 of B17 (**left**) and 19 of Y21 (**right**). The gray fill delineates the 95% confidence interval. The mode has been computed from the KDE peak, while the mean & median from the data.

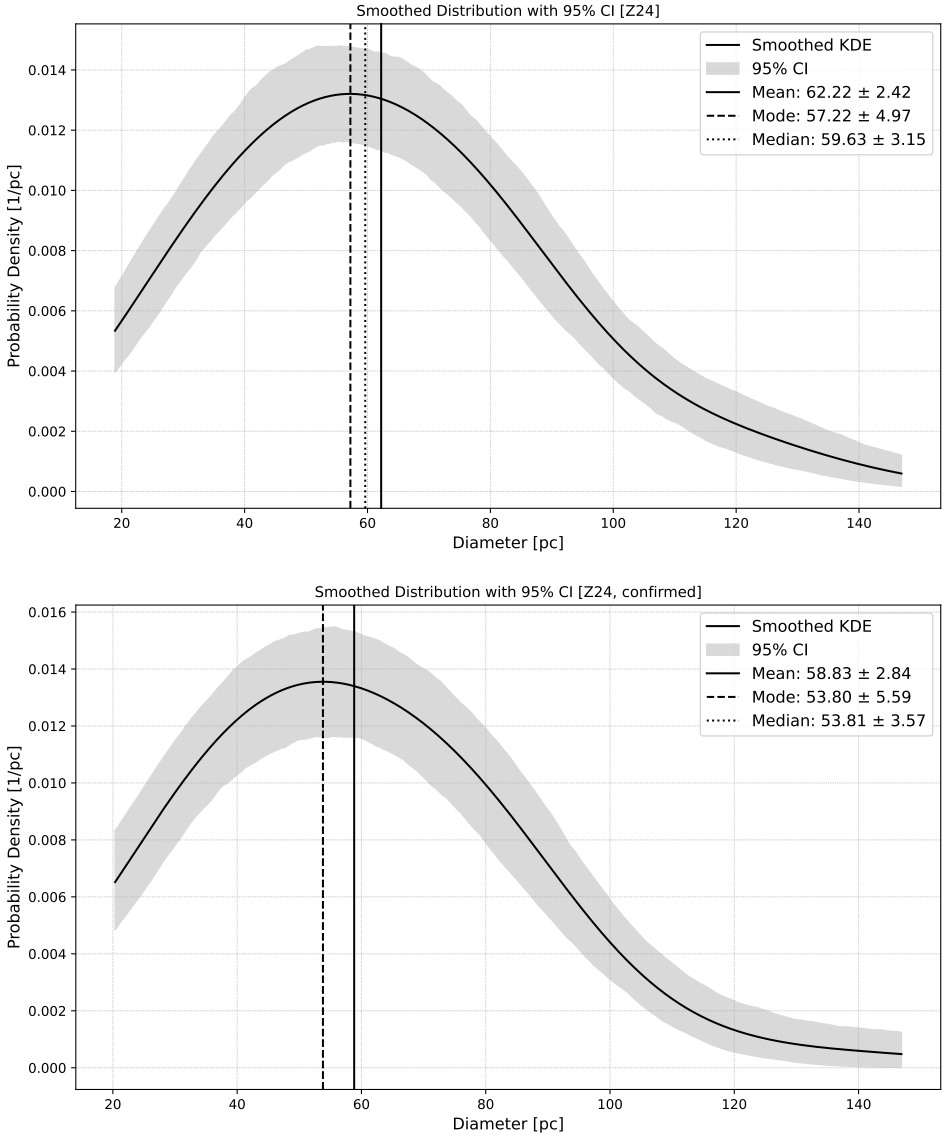

Figure 7.16: Same as Fig. 7.15 but for all 124 objects (**left**) and 78 confirmed MCSNRs (**right**) of Z24. The optimal bandwidths were 15.2 pc and 15.6 pc, respectively.

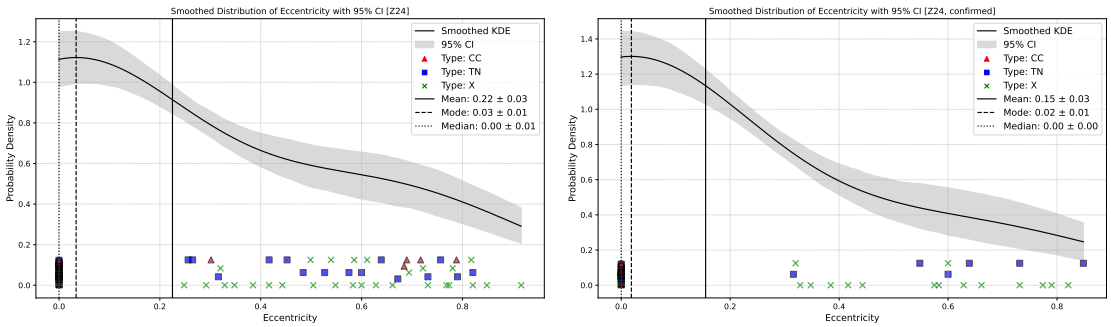

Figure 7.17: Kernel smoothing PDF of eccentricity of all (**left**) and confirmed (**right**) MCSNRs of Z24. Data points are colored/shaped according to SNR progenitor types and plotted along the x-axis in bins extending into respective vertical columns.

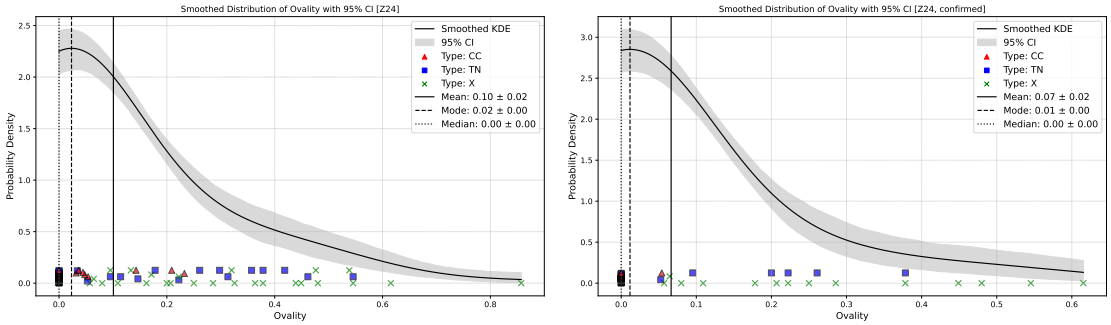

Figure 7.18: Same as Fig. 7.17 but for ovality.

7.3.3 Spherical Symmetry

In order to quantify how circular MCSNRs appear in different surveys, we also apply the KDE method described above on eccentricity calculated as $e = \sqrt{1 - \frac{b^2}{a^2}}$ from the observed minor and major axes, respectively. It has been suggested [e.g., Lopez et al. 2011] that a more spherical (thermal X-ray) SNR morphology may imply a type Ia origin. B17 explored this using ovality, defined as $\frac{2(a-b)}{a+b}$, as as measure of spherical symmetry. We follow their method of KDE by minimizing BIMSE, but rely on the mathematically-robust e values to estimate the deviation from a perfect circle ($e = 0$). The PDF is reconstructed in Fig. 7.17 with 95% confidence bands. For comparison, the PDF for ovality is also calculated on both the complete set of B17 (not shown) and the complete set of Z24 (Fig. 7.18) SNRs.

We also plot the data points (SNRs) with progenitor types (CC, TN or unknown) as horizontal scatter with the ones falling in the same bin in vertical columns. Based on the data, a bin size of 25 was chosen. The first (disappointing) observation is that most of the remnants have 0 eccentricity and ovality, i.e., they are circular. The mean of the eccentricity distribution is 0.22 ± 0.03 for the full sample and 0.15 ± 0.03 for the confirmed SNRs. The mode and median are almost zero. Similarly for the ovalities, means are 0.1 ± 0.02 and 0.07 ± 0.03, respectively, with null median and mode $\approx 0.01 - 0.02$. The values are more comparable to SNR population of the SMC [see Maggi et al. 2019, Fig5, top right] than LMC SNRs. Secondly, no distinctions of the SNR type can be made based on the distribution of 'CC' and 'TN' points across the eccentricity and ovality PDFs. Thus, as for B17, there seems no correlation between explosion type and sphericity for this set of measurements. Deeper and higher resolution observations are required before any conclusions can be drawn from these analyses.

7.3.4 Age and Size

As age of SNRs is hardly known except for historical ones, often their size is used as a proxy for age. (Again, one needs an accurate distance to the SNR to convert its angular extent to length units.) Moreover, most SNRs should be in the ST phase of their expansions, with radii growing adiabatically as [Badenes et al. 2010]:

$$r \sim E_0^{1/5} \rho_0^{-1/5} t^{2/5}, \tag{7.23}$$

where E_0 is the kinetic energy of the explosion, ρ_0 is the ambient gas density, and t is the time. Reasonably assuming a constant SN rate in the LMC over the past few kyr, $\tau^{-1} = \frac{dN}{dt} =$ *constant*, the naively expected size distribution of SNRs in their Sedov phase is

$$\frac{dN}{dr} = \frac{dN}{dt}\frac{dt}{dr} \sim r^{3/2}. \tag{7.24}$$

Although, this is contradictory to the almost uniform ($dN/dr \sim r^0$) distribution seen in §7.3.2.1, it can be interpreted as a consequence of transition from Sedov to radiative phase with $r_{\rm PDS}$ depending on ρ_0 [Badenes et al. 2010].

We explore this further using SNRpy and age & size data available on a number of MCSNRs. Many authors supplement their LMC remnant studies, imaging and spectral analysis, with an age estimate. Most of these estimates are based Sedov assumptions (like Eq. 7.23) combined with the 'radius' seen in high-resolution multiwavelength images. Some studies use more parameters and approximations which are specific to their remnant(s), such as whether the reverse shock is visible, whether there is an excess of Fe or O in spectra, plasma temperatures, emission measures, state of ionization, proper motion measurements, etc. A compilation of these pseudo-measurements of SNR ages can be found in M16 [Table A.1] and B17 [Table 1], for example. We use these values, with uncertainties wherever provided, in combination with quoted sizes (halving average diameter as before), and we overplot the *observed* ($r_{\rm obs}$, $t_{\rm 0obs}$) points corresponding to different MCSNRs onto the radial evolution plots from SNRpy.

Since the parameter with most variability is the ambient density (remember §1.1.2.1) and it causes the severest change in SNR evolution according to the analytical models like ST (Eq. 7.23) and TM99 (Fig. 7.6, top right), we vary n_0 from 0.0125–3.2 cm^{-3} in multiplicative steps of 2, while keeping other parameters to fixed. Particularly, $E_{51} = 0.5$, $M_{ej\odot} = 1.4$, powerlaw indices are $s = 0$ & $n = 7$ and abundances are for LMC & type Ia explosion. The resulting radius versus time (or age) curves are shown in Figs. 7.19 and 7.20 with data from M16 and B17, respectively. The secured ('s') and tentative types for respective SNR progenitors are also indicated. Reverse shock radii are only plotted for reference.

These plots can be viewed in certain different ways. One way is to assume that all or most LMC SNRs explode with similar energies and ejecta mass, so that only the ambient density is defining factor for evolution of the forward shock. The assumption is somewhat theoretically motivated from the physics (or numerical simulations) of SN explosion and ISM. In any case, the variation in at least the forward shock radius is minor when changing E_0, M_{ej} and n, as seen before in §7.1.3. Then, we can find a point, say #7 in Fig. 7.19, intersecting a curve gives the pre-shock density (here, 0.1 cm^{-3}) around that remnant. This will only be indicative of the actual value as the specifics of the SNR have not been taken into account. But we can further make the same assumptions for the explosion energy, and then for the ejecta mass, and so on, iteratively, to arrive at the observed $r_{\rm obs}$ at a given $t_{\rm 0obs}$. The method is similar to that of Leahy [2017], which we explain in the next section (§7.3.5).

Secondly, we can view the **curves** as theoretical evolution of a type Ia SNR in LMC with a certain explosion energy, ejecta mass, etc. but uncertain medium density, and the **points** as

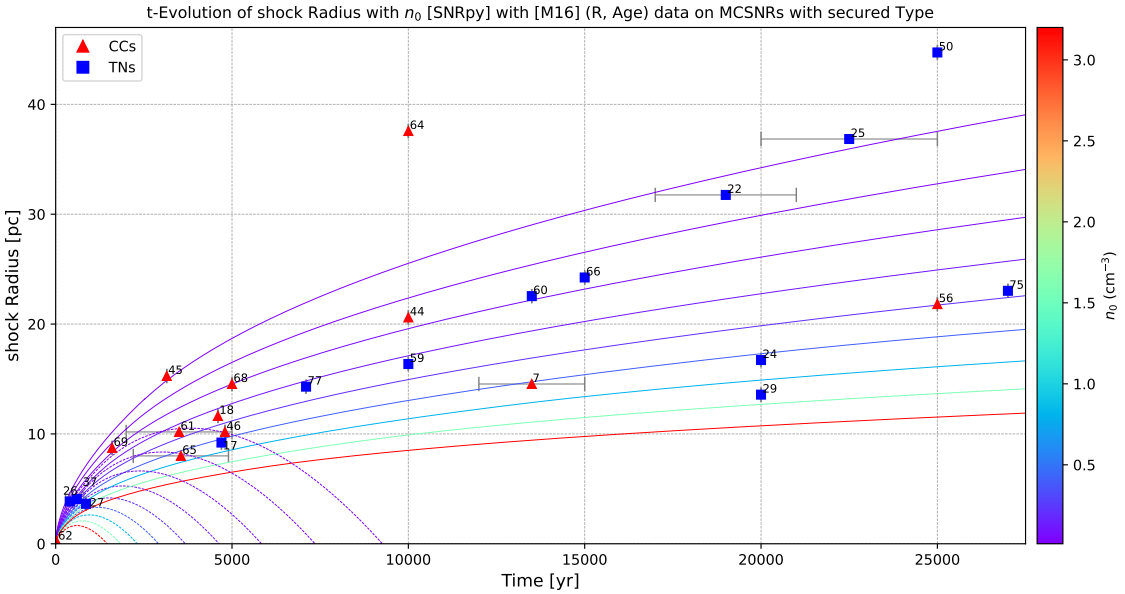

Figure 7.19: r versus age for M16's secured type SNRs onto SNRpy time-evolution of shock radii for various n_0 and "typical LMC" SNR parameters. Error bars for ages are drawn, whenever available.

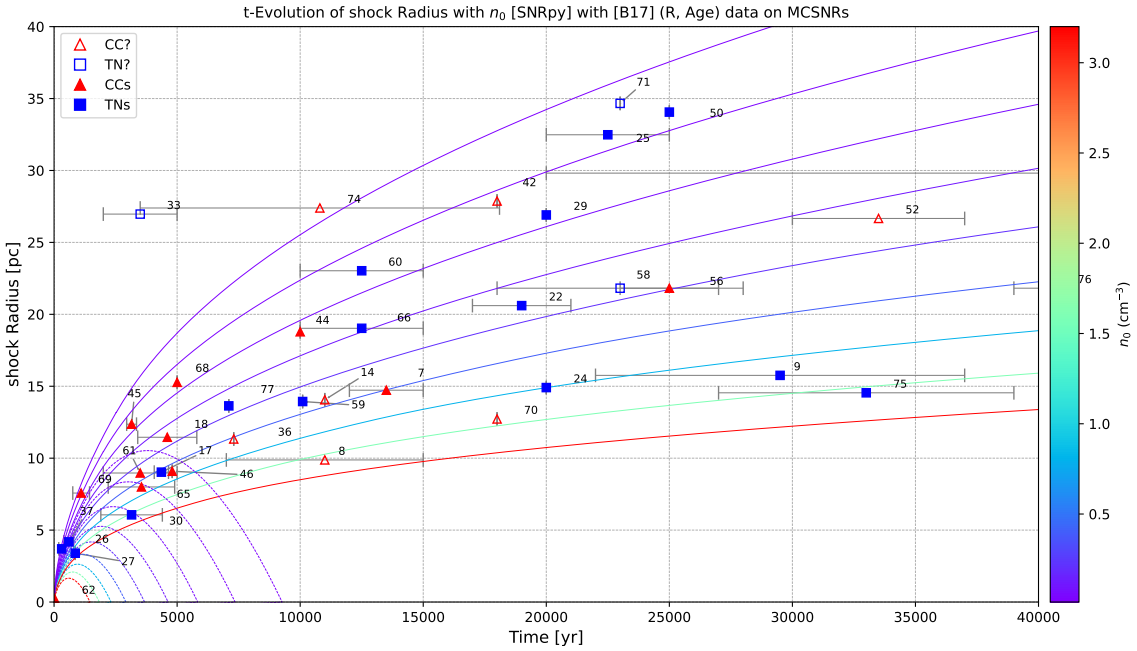

Figure 7.20: Same as Fig. 7.19 but for B17's SNRs data, upto 40 kyr; zoom-in on Fig. A.3 with the unique SNr number.

observational data of forward shock radius at different times of the same SNR. Then, the r_i and t_{0i} for the different data points i are not independent of each other. In fact, we expect

$$r_i \propto t_{0i} \sqrt{\frac{E_0}{M_{ej}}} \tag{7.25}$$

in the ED–ST phase, according to the TM99 model. That is, the *generalized* radius r_i should be evolving, increasing with time, or the shock velocity slowing down in proportion to $(E_0/M_{ej})^{1/2}$. This roughly seems to be the case in the plots: higher radial correlates to older age. And, the vertical divergence arguably reflects our uncertainties in our assumption of the values of E_0 and M_{ej} for a given n_0. If we now assume that n_0 could be of any value in our chosen range 0.0125–3.2 cm^{-3} for our SNR, we have roughly generalized the evolution of all SNRs in our LMC sample. We can see that almost all SNR points lie within this range of ambient density, given a typical set of SNR parameters. The outliers are most likely SNRs evolving in an atypical environment with unusually more (e.g., near a molecular cloud) or less (e.g., in a superbubble) ISM densities, if the age estimate is not inaccurate.

We must be careful not to draw much from these merely indicative plots, since we have haven't looked into the sources and methods of individual authors involved in the calculation of MCSNR ages. So, for example, we cannot be sure how independent $r_{\rm obs}$ and $t_{\rm 0obs}$ really are. A more rigorous and detailed study, looking into observational information of each SNR, is required in order to comment on the global properties of the LMC environment. We can just say that we verify the previous results of Badenes et al. [2010] and Leahy [2017] (see below) that: i) Visibility and evolution of SNRs is primarily dependent on the ambient density, ii) SNRs explode in a large range (here, 2 orders of magnitude) of ambient densities, and less affected by the initial energy and mass. This, in turn, verifies the expectations of McKee & Ostriker [1977], Truelove & McKee [1999], Cioffi et al. [1988], etc.

7.3.5 Energetics

Leahy [2017] (or L17) applied SNRpy (or SNRpy-like) models on the sample of 50 SNRs of M16 to study the energetics and birthrates of SNRs in the LMC. They constrained the initial explosion energy, age and pre-shock density of the sample from the known forward shock radii, X-ray temperatures and emission measures. They find the most-probable $E_0^{51} = 0.5^{\div 3}_{\times 3}$ and mean $n_0 = 0.1^{\div 8}_{\times 8}$ cm^{-3} with 1σ dispersions from log-normal fits on the distributions, and for ages $\leqslant$ 20,000 yr, a constant birthrate of 1/500 yr for the LMC SNRs. In Fig. 7.21, we show their analysis set in terms of time-evolution of the forward shock of each SNR, given E_0, n_0 and t_0, assuming type Ia ejecta abundance with powerlaw index $n = 7$, $M_{ej} = 1.4 M_\odot$, LMC constant density ISM $s = 0$, and other default inputs in SNRpy. This reproduces (roughly) the shock radii of all the SNRs observed by M16 and used as input by L17. The curves are only plotted up to this point or their calculated age. The dotted 'extensions' to the curves denote upper error on the age. The calculated explosion energies and ambient densities are represented by color gradient of the curves. The color bar is so scaled since $R_{\rm ch} \propto (E_0/n_0)^{(1/5)}$ according to Eq. 7.1.

Without the physically-motivated normalization in Fig. 7.21, we get Fig. A.4, i.e. a set of 50 SNRs with all same but different (E_0, n_0) input values for each of which the forward shock radius at certain t_0 is equal to their observed radius $r_{\rm obs}$. In other words, the 'endpoints' of the curves represent the ($r_{\rm obs}$, $t_{\rm 0obs}$) points for a larger M16 MCSNR sample. But, now, the age was calculated theoretically in a consistent way, using the evolutionary models that we have followed so far, with not just the observed radius (X-ray maximal extent) but the interior structure of

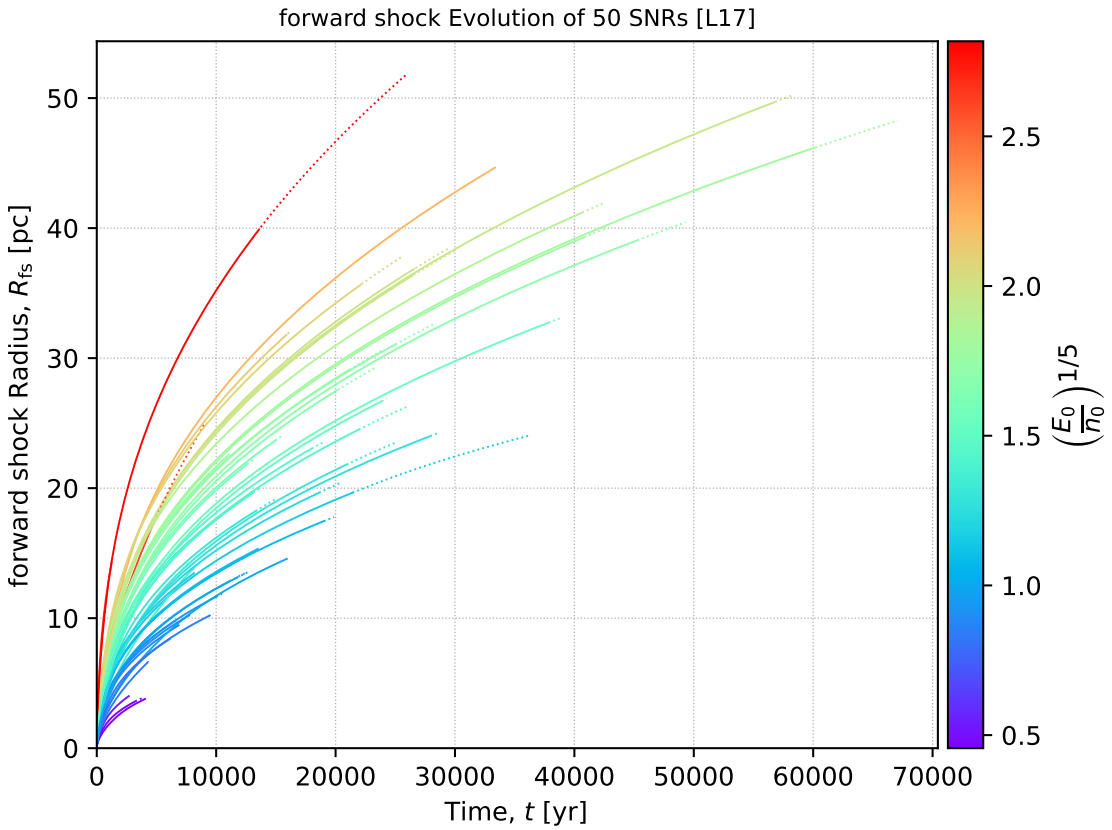

Figure 7.21: Forward shock evolution of L17's 50 SNRs up to the calculated ages (upper limit, t_0+error) or the input radii, with the calculated explosion energies and ambient densities represented by appropriately scaled color bar. See Fig. A.4 to identify the MCSNRs, not shown here for clarity.

the SNR (X-ray temperature and emission measure). So, the applying similar generalization arguments as before (§7.3.4), Fig. 7.21 shows the time-evolution of forward shock radius of a SNR with varying ambient density. The effect of E_0 is negligible here: the curves roughly follow a smooth (vertical) transition; the higher the n_0, the slower r_i grows.

Further interpretations are deferred to future studies. The quantitative results from this are already presented in L17. Thus, we move to the next dataset, where such analysis is possible. K22 not only performed X-ray imaging and spectral analysis on their candidate and confirmed MCSNRs, but also did evolutionary estimates on 8 of them. So, apart from SNR sizes, which we use to calculate the forward shock radii, they list estimated ages, explosion energies, ejecta masses and current forward shock velocities. These are based on Sedov-Taylor solutions. We put the mean of their E_0, n_0, M and *Age* in SNRpy to plot the forward shock evolution (Fig. 7.22), similarly with the $(E_0/n_0)^{(1/5)}$-scaled color bar. The endpoints of the curves do not exactly coincide with the observed radii due to the large uncertainties given for the input parameters. However, the same pattern is visible: the greater the ratio E_0:n_0, the faster the shock expands into the medium. So, we have corroborated the ST calculations with TM99 modeling. Although, there are overlaps, we can see a roughly smooth transition from SNr #16 to #3. Assuming a common explosion energy $E_{51} \equiv 0.5$, we can say that K22 SNRs are evolving in the range $0.0086 \approx 0.01 - 0.166 \approx 0.2$ cm^{-3} of ambient densities.

Although, a similar analysis as L17 on this dataset is possible, i.e. using SNRpy with an initial E_0, n_0 and age to calculate a model and then iterating the values of the 3 parameters until the model converges to the observed radius, plasma temperature and emission measure,

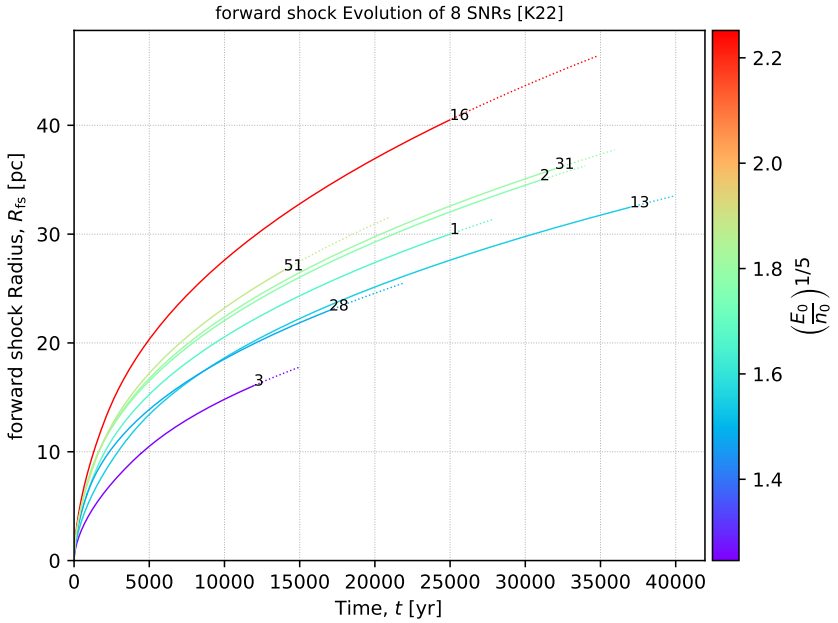

Figure 7.22: Same as Fig. 7.21 but for K22's 8 SNRs (numbered)

we refrained from doing this here. The first reason for that is the relatively small dataset (of just 8 MCNSRs) which probably just represents a population of faint mature SNRs; secondly, K22 make a case for 4 of them (#s 2, 13, 31, 51) as "typical Sedov-phase" remnants and 3 of them with unusual morphological/spectral properties. So, as one assumption is as good as any other, we rely on theirs. A better estimate on SNR explosion and environment properties is possible with models tailored to the specific requirements, demanded by existing observations, of individual SNRs. For example, inclusion of stellar wind ($s = 2$ case in SNRpy), use of the more accurate radiative (PDS) phase model by Bandiera & Petruk [2004] instead of CMB88 model, alternate evolutionary models [White & Long 1991; Liang & Keilty 2000; Tang & Wang 2005], etc. in combination with literature survey on each SNR to determine the suitable model and input parameters.

Chapter 8

Conclusion

The aim of this thesis was to thoroughly study the evolution of supernova remnants from both theoretical and observational perspectives—in X-rays and of LMC: *X-ray Evolution of MC-SNRs*. Further, we wanted to understand their impact on their interstellar environment and vice-versa, the role of the ISM on SNRs. This led us to a detailed review on the properties of the interstellar medium in chapter §1, astrophysics of supernova explosions in chapter §2, and the interconnection leading to supernova remnants in chapter §3. There we condensed the current information about the SNR population in our Galaxy and neighboring galaxies, summarizing the literature on discoveries of confirmed and candidate SNRs in the Large Magellanic Cloud. We review some more recent works on the LMC SNR population in the last chapter §7. We compile data from multiple sources on sizes, types, ages, energetics, etc. and cross-match to create a concatenated list of 78 bona fide and 46 candidate LMC SNRs. We use this data and opportunity to do statistical studies on the population as a whole: cumulative sizes distributions, kernel density estimates, and spherical symmetry. These build up on previous similar studies done on a smaller dataset. Our findings corroborate with their [Bozzetto et al. 2017; Badenes et al. 2010] results.

In chapter §4, we took a deep dive into the violent and often complex processes that occur from the interaction of SN ejecta with the surrounding CSM or the large-scale ISM. The microphysics of shocks and radiation in astrophysical plasmas may have indicated that analytical treatment of SNR evolution is practically impossible. Even numerical magnetohydrodynamic simulations must suffer from limitations of theory and resources, never providing a realistic or complete picture of the evolution. As it turns out, one-dimensional analytical models with some basic assumptions provide reasonable approximations to how supernova remnants evolve. They allow us to demarcate the life of a remnant into 2 major and 4 or 5 minor phases, from the non-radiative free-expansion and adiabatic phases to the radiative phases until the SNR merges with the ISM. The standard and most-commonly used model is the Sedov-Taylor self-similar solution for a point-explosion with good resemblance to the II phase of SNR evolution. However, it is insufficient to describe a large number of remnants which are too young or too old.

This includes the remnant MCSNR J0500-6512, which we analyze in this work in chapter §6 as an extended source in the LMC emitting diffuse soft X-rays. It was proprietarily observed with the EPIC CCDs onboard XMM-Newton as a follow-up to an optical observation [Yew et al. 2021]. A candidate earlier, we confirm it as a new MCSNR. The spectral analysis, succeeding the (X-ray and optical) imaging, gives a plasma temperature $kT = 0.46^{+0.07}_{-0.13}$ keV which seems consistent with old large ($R = 50.67^{\pm 3.45}$ pc, here) remnants. An ionization timescale of $\approx 3.47 \times 10^{11}$ s cm^{-3} indicated CIE, again pointing an old age. We estimated the EM $\approx 1.5^{+0.21}_{-0.96} \times 10^{57}$ cm^{-3} and luminosity $\approx 1.176^{\pm 0.026} \times 10^{29}$erg s^{-1} in 0.3–4.2 keV.

We went on to assume an explosion energy (0.5×10^{51} erg) and ambient density (0.1 cm^{-3}) and apply the ST solution to estimate an age (≈ 146207 yr) and shock velocity (≈ 136 km s^{-1}) of the remnant, which is clearly an overestimate, pointing to the failure of the model to accurately follow radiative SNRs. (We discussed the various mechanisms of X-ray emission in chapter §5, along with detection techniques. We particularly describe the optics and performance of the high-throughput X-ray telescope, XMM-Newton, in chapter §6. The general and specific data reduction pipeline for such analyses of EPIC data is also presented.)

That is why several other analytical solutions aided by 1D numerical hydrodynamic simulations are in practice for better modeling. We prefer one of them, by Truelove & McKee [1999], for most of our evolutionary analysis, augmented with models for the later phases as well as with calculations for emission, electron-ion equilibration, etc., in chapter §7. First we elaborate the tool used in this study, SNRpy [Leahy & Williams 2017], that calculates the SNR evolution, given some input parameters, which we first test. We then apply it on MCSNR J0500-6512 to contrast the evolution from a 'pure ST' solution. Later, we employ it to demonstrate the evolution of SNRs in variable ambient densities, using size and age data available from two sources of our compiled MCSNR list. We attempted to *generalize* SNR evolution with the ambient medium playing the major role. Finally, we verify the results of Leahy [2017] in modeling 50 MCSNRs. Similar picture emerges as radial evolution varies almost smoothly and primarily according to the changes in the ambient densities. Applying similar methodology on 8 more MCSNRs, we approximate the range of ISM number densities in which these remnants must be evolving. These latter analyses need a final word before we can come to any general conclusions.

What is particularly necessary from future studies are improvements in our current analytical models, especially for the later radiative phases. We also need to be able to fully model CC-SNRs whose progenitor probably had a stellar wind, and those that are interacting with a molecular cloud or evolving in a complicated ISM. Many mysteries, even with well-studied objects such as the Crab Nebula or Cas A, exist that need theoretical resolution. Tuning these analytical models in accordance to observed SNR properties and, vice versa, deriving observational parameters from the models, is demonstrably a powerful tool in understanding how supernova remnants evolve under different conditions. On the observational side, high-resolution imaging spectroscopy in X-rays as well deeper multiwavelength surveys are required to extract as much information on individual remnants as possible. There is still incompleteness in our Galactic and extragalactic SNR populations, hindering the progress of global statistical studies. Even though, we recognize that observing time of major observatories is limited and expensive, we believe that the number of supernova remnants in the LMC and elsewhere will likely increase, as it has in the last 70 years. We already see a trend of new observatories such as eROSITA targeting the MCSNR population, with follow-ups using XMM-Newton. Future observations with XRISM and upcoming ATHENA will provide a more detailed view of SNRs in X-rays. With the growing number of observations and studies on supernova remnants, our general understanding of these fascinating objects will continue to grow.

Appendix A

Supplements

A.1 Scripts

The following is the command line script used in XMM-ESAS analysis of J0500-6512:

```
#!/bin/tcsh

# 1. SETUP
setenv OID 0901010201
setenv my_work /userdata/data/vashukla/XMM
cd ${my_work}/${OID}/analysis
module unload isis
module load xmmsas
rm *.cif
rm ${my_work}/${OID}/odf/*.SAS
setenv SAS_VERBOSITY 3
setenv SAS_SUPPRESS_WARNING 3
setenv SAS_IMAGEVIEWER ds9
setenv SAS_CCF ${my_work}/${OID}/analysis/ccf.cif
setenv SAS_ODF ${my_work}/${OID}/odf
cifbuild withccfpath=no analysisdate=now category=XMMCCF calindexset=$SAS_CCF fullpath=
    yes
odfingest odfdir=$SAS_ODF outdir=$SAS_ODF
setenv SAS_ODF ${my_work}/${OID}/odf/*SUM.SAS
sasversion
ls -ltr

# 2. Initial ESAS Processing
epchain runradmonfix=N
epchain runradmonfix=N withoutoftime=true
emchain

mv P0901010201M1S001MIEVLI0000.FIT mos1S001.fits
mv P0901010201M2S002MIEVLI0000.FIT mos2S002.fits
mv P0901010201PNU002PIEVLI0000.FIT pnU002.fits
mv P0901010201PNU002OOEVLI0000.FIT pnU002-oot.fits
rm P*.FIT

# 3. Anomalous CCDs
emanom eventfile=mos1S001.fits keepcorner=no
emanom eventfile=mos2S002.fits keepcorner=no

# 4. SPF Filtering
espfilt eventfile=mos1S001.fits method=histogram withsmoothing=yes smooth=51 rangescale
    =6 allowsigma=3
espfilt eventfile=mos2S002.fits method=histogram withsmoothing=yes smooth=51 rangescale
    =6 allowsigma=3
espfilt eventfile=pnU002.fits method=histogram withsmoothing=yes    smooth=51 rangescale
    =15 allowsigma=3 withoot=Y ootfile=pnU002-oot.fits

# 5. Point Source excision
```

```
cheese mos1file=mos1S001-allevc.fits mos2file=mos2S002-allevc.fits pnfile=pnU002-allevc.fits pnootfile=pnU002-allevcoot.fits scale=0.4 ratetotal=1 ratesoft=1 ratehard=1 dist=50 mlmin=15 elowlist=200 ehighlist=7200 keepinterfiles=yes
# ## ratetotal=1 ratesoft=1 ratehard=1 mlmin=15 keepinterfiles=yes are default values, hence redundant

# 6. QPB spectra and images
mosspectra eventfile=mos1S001-allevc.fits pattern=12 withsrcrem=yes elow=300 ehigh=700 ccds="T T F T T F T" keepinterfiles=yes
mosspectra eventfile=mos2S002-allevc.fits pattern=12 withsrcrem=yes elow=300 ehigh=700 ccds="T T T T T T T" keepinterfiles=yes
pnspectra eventfile=pnU002-allevc.fits ootevtfile=pnU002-allevcoot.fits pattern=0 withsrcrem=yes elow=300 ehigh=700 quads="T T T T" keepinterfiles=yes

mosback inspecfile=mos1S001-fovt.pi elow=300 ehigh=700 ccds="T T F T T F T"
mosback inspecfile=mos2S002-fovt.pi elow=300 ehigh=700 ccds="T T T T T T T"
pnback inspecfile=pnU002-fovt.pi inspecoot=pnU002-fovtoot.pi elow=300 ehigh=700 quads="T T T T"

# # 6B. & 6C. Repeat 6. for elow=700 ehigh=1100 & elow=1100 ehigh=4200

ls *fovt*.pi *bkg.pi *.rmf *.arf *-fovimspdet.fits
ls *bkgimdet*
mkdir spectra_full backim_full

cp mos1S001-fovt.pi spectra_full/mos1S001-fovt-full.pi
cp mos1S001-bkg.pi spectra_full/mos1S001-bkg-full.pi
cp mos1S001.rmf spectra_full/mos1S001-full.rmf
cp mos1S001.arf spectra_full/mos1S001-full.arf
cp mos1S001-fovimspdet.fits spectra_full/mos1S001-fovimspdet-full.fits

cp mos2S002-fovt.pi spectra_full/mos2S002-fovt-full.pi
cp mos2S002-bkg.pi spectra_full/mos2S002-bkg-full.pi
cp mos2S002.rmf spectra_full/mos2S002-full.rmf
cp mos2S002.arf spectra_full/mos2S002-full.arf
cp mos2S002-fovimspdet.fits spectra_full/mos2S002-fovimspdet-full.fits

cp pnU002-fovt.pi spectra_full/pnU002-fovt-full.pi
cp pnU002-fovtoot.pi spectra_full/pnU002-fovtoot-full.pi
cp pnU002-bkg.pi spectra_full/pnU002-bkg-full.pi
cp pnU002.rmf spectra_full/pnU002-full.rmf
cp pnU002.arf spectra_full/pnU002-full.arf
cp pnU002-fovimspdet.fits spectra_full/pnU002-fovimspdet-full.fits
cp pnU002-fovtootsub.pi spectra_full/pnU002-fovtootsub-full.pi

cp *300-700* *700-1100* *1100-4200* backim_full/

# # 6D. & 6E. QPB spectra for region = BKG & SRC
mosspectra eventfile=mos1S001-allevc.fits pattern=12 withsrcrem=yes elow=400 ehigh=1250 ccds="T T F T T F T" keepinterfiles=yes withregion=yes regionfile=bkgd-MOS1.txt
mosspectra eventfile=mos2S002-allevc.fits pattern=12 withsrcrem=yes elow=400 ehigh=1250 ccds="T T T T T T T" keepinterfiles=yes withregion=yes regionfile=bkgd-MOS2.txt
pnspectra eventfile=pnU002-allevc.fits ootevtfile=pnU002-allevcoot.fits pattern=0 withsrcrem=yes elow=400 ehigh=1250 quads="T T T T" keepinterfiles=yes withregion=yes regionfile=bkgd-PN.txt

mosback inspecfile=mos1S001-fovt.pi ccds="T T F T T F T"
mosback inspecfile=mos2S002-fovt.pi ccds="T T T T T T T"
pnback inspecfile=pnU002-fovt.pi inspecoot=pnU002-fovtoot.pi quads="T T T T"

mkdir spectra backim_bkgd

cp mos1S001-fovt.pi spectra/mos1S001-fovt-bkgd.pi
cp mos1S001-bkg.pi spectra/mos1S001-bkg-bkgd.pi
cp mos1S001.rmf spectra/mos1S001-bkgd.rmf
cp mos1S001.arf spectra/mos1S001-bkgd.arf
cp mos1S001-fovimspdet.fits spectra/mos1S001-fovimspdet-bkgd.fits

cp mos2S002-fovt.pi spectra/mos2S002-fovt-bkgd.pi
cp mos2S002-bkg.pi spectra/mos2S002-bkg-bkgd.pi
cp mos2S002.rmf spectra/mos2S002-bkgd.rmf
cp mos2S002.arf spectra/mos2S002-bkgd.arf
cp mos2S002-fovimspdet.fits spectra/mos2S002-fovimspdet-bkgd.fits
```

```

cp pnU002-fovt.pi spectra/pnU002-fovt-bkgd.pi
cp pnU002-fovtoot.pi spectra/pnU002-fovtoot-bkgd.pi
cp pnU002-bkg.pi spectra/pnU002-bkg-bkgd.pi
cp pnU002.rmf spectra/pnU002-bkgd.rmf
cp pnU002.arf spectra/pnU002-bkgd.arf
cp pnU002-fovimspdet.fits spectra/pnU002-fovimspdet-bkgd.fits
cp pnU002-fovtootsub.pi spectra/pnU002-fovtootsub-bkgd.pi

cp *400-1250* backim_bkgd/

mosspectra eventfile=mos1S001-allevc.fits pattern=12 withsrcrem=yes elow=400 ehigh=1250
    ccds="T T F T T F T" keepinterfiles=yes withregion=yes regionfile=src-MOS1.txt
mosspectra eventfile=mos2S002-allevc.fits pattern=12 withsrcrem=yes elow=400 ehigh=1250
    ccds="T T T T T T T" keepinterfiles=yes withregion=yes regionfile=src-MOS2.txt
pnspectra eventfile=pnU002-allevc.fits ootevtfile=pnU002-allevcoot.fits pattern=0
    withsrcrem=yes elow=400 ehigh=1250 quads="T T T T" keepinterfiles=yes withregion=yes
     regionfile=src-PN.txt

mosback inspecfile=mos1S001-fovt.pi ccds="T T F T T F T"
mosback inspecfile=mos2S002-fovt.pi ccds="T T T T T T T"
pnback inspecfile=pnU002-fovt.pi inspecoot=pnU002-fovtoot.pi quads="T T T T"

cp mos1S001-fovt.pi spectra/mos1S001-fovt-src.pi
cp mos1S001-bkg.pi spectra/mos1S001-bkg-src.pi
cp mos1S001.rmf spectra/mos1S001-src.rmf
cp mos1S001.arf spectra/mos1S001-src.arf
cp mos1S001-fovimspdet.fits spectra/mos1S001-fovimspdet-src.fits

cp mos2S002-fovt.pi spectra/mos2S002-fovt-src.pi
cp mos2S002-bkg.pi spectra/mos2S002-bkg-src.pi
cp mos2S002.rmf spectra/mos2S002-src.rmf
cp mos2S002.arf spectra/mos2S002-src.arf
cp mos2S002-fovimspdet.fits spectra/mos2S002-fovimspdet-src.fits

cp pnU002-fovt.pi spectra/pnU002-fovt-src.pi
cp pnU002-fovtoot.pi spectra/pnU002-fovtoot-src.pi
cp pnU002-bkg.pi spectra/pnU002-bkg-src.pi
cp pnU002.rmf spectra/pnU002-src.rmf
cp pnU002.arf spectra/pnU002-src.arf
cp pnU002-fovimspdet.fits spectra/pnU002-fovimspdet-src.fits
cp pnU002-fovtootsub.pi spectra/pnU002-fovtootsub-src.pi

mkdir backim_src
cp *400-1250* backim_src/
cd backim_src/
ds9 *fovimsky* &
# ## to verify the region where the spectra was extracted from

# 7. Spectral Fitting of FOV
cd ${my_work}/${OID}/analysis/spectra_full
# # 7A. Grouping spectral files
grppha
mos1S001-fovt-full.pi
mos1S001-full-grp.pi
chkey BACKFILE mos1S001-bkg-full.pi
chkey RESPFILE mos1S001-full.rmf
chkey ANCRFILE mos1S001-full.arf
group min 50
exit

grppha
mos2S002-fovt-full.pi
mos2S002-full-grp.pi
chkey BACKFILE mos2S002-bkg-full.pi
chkey RESPFILE mos2S002-full.rmf
chkey ANCRFILE mos2S002-full.arf
group min 50
exit

grppha
pnU002-fovtootsub-full.pi
pnU002-full-grp.pi
```

```
chkey BACKFILE pnU002-bkg-full.pi
chkey RESPFILE pnU002-full.rmf
chkey ANCRFILE pnU002-full.arf
group min 50
exit

# # 7B. Determine solid angle
protonscale mode=1 maskfile=mos1S001-fovimspdet-full.fits specfile=mos1S001-fovt-full.pi
protonscale mode=1 maskfile=mos2S002-fovimspdet-full.fits specfile=mos2S002-fovt-full.pi
protonscale mode=1 maskfile=pnU002-fovimspdet-full.fits specfile=pnU002-fovt-full.pi

# # 7C. Creating and loading xspec script
xspec - sp.xcm

# 8. Imaging
# # 8A. Create residual SPF filtered image
# # proton with pindex and pnorm from sp.xcm best-fit powerlaw models
cd ${my_work}/${OID}/analysis
proton imagefile=mos1S001-fovimdet-300-700.fits specfile=mos1S001-fovt-full.pi elow=300
    ehigh=700 speccontrol=1 pindex=0.1 pnorm=0.048013
proton imagefile=mos2S002-fovimdet-300-700.fits specfile=mos2S002-fovt-full.pi elow=300
    ehigh=700 speccontrol=1 pindex=0.1 pnorm=0.049540
proton imagefile=pnU002-fovimdet-300-700.fits specfile=pnU002-fovt-full.pi elow=300
    ehigh=700 speccontrol=1 pindex=0.263328 pnorm=0.253091

proton imagefile=mos1S001-fovimdet-700-1100.fits specfile=mos1S001-fovt-full.pi elow=700
     ehigh=1100 speccontrol=1 pindex=0.1 pnorm=0.048013
proton imagefile=mos2S002-fovimdet-700-1100.fits specfile=mos2S002-fovt-full.pi elow=700
     ehigh=1100 speccontrol=1 pindex=0.1 pnorm=0.049540
proton imagefile=pnU002-fovimdet-700-1100.fits specfile=pnU002-fovt-full.pi elow=700
    ehigh=1100 speccontrol=1 pindex=0.263328 pnorm=0.253091

proton imagefile=mos1S001-fovimdet-1100-4200.fits specfile=mos1S001-fovt-full.pi elow
    =1100 ehigh=4200 speccontrol=1 pindex=0.1 pnorm=0.048013
proton imagefile=mos2S002-fovimdet-1100-4200.fits specfile=mos2S002-fovt-full.pi elow
    =1100 ehigh=4200 speccontrol=1 pindex=0.1 pnorm=0.049540
proton imagefile=pnU002-fovimdet-1100-4200.fits specfile=pnU002-fovt-full.pi elow=1100
    ehigh=4200 speccontrol=1 pindex=0.263328 pnorm=0.253091


# # 8B. Convert images from detector to sky coordinates
# # # a. rotate qpb (mosback & pnback) images from det to sky
rotdet2sky intemplate=mos1S001-fovimsky-300-700.fits inimage=mos1S001-bkgimdet-300-700.
    fits outimage=mos1S001-bkgimsky-300-700.fits withdetxy=false withskyxy=false
rotdet2sky intemplate=mos2S002-fovimsky-300-700.fits inimage=mos2S002-bkgimdet-300-700.
    fits outimage=mos2S002-bkgimsky-300-700.fits withdetxy=false withskyxy=false
rotdet2sky intemplate=pnU002-fovimsky-300-700.fits inimage=pnU002-bkgimdet-300-700.fits
    outimage=pnU002-bkgimsky-300-700.fits withdetxy=false withskyxy=false

rotdet2sky intemplate=mos1S001-fovimsky-700-1100.fits inimage=mos1S001-bkgimdet
    -700-1100.fits outimage=mos1S001-bkgimsky-700-1100.fits withdetxy=false withskyxy=
    false
rotdet2sky intemplate=mos2S002-fovimsky-700-1100.fits inimage=mos2S002-bkgimdet
    -700-1100.fits outimage=mos2S002-bkgimsky-700-1100.fits withdetxy=false withskyxy=
    false
rotdet2sky intemplate=pnU002-fovimsky-700-1100.fits inimage=pnU002-bkgimdet-700-1100.
    fits outimage=pnU002-bkgimsky-700-1100.fits withdetxy=false withskyxy=false

rotdet2sky intemplate=mos1S001-fovimsky-1100-4200.fits inimage=mos1S001-bkgimdet
    -1100-4200.fits outimage=mos1S001-bkgimsky-1100-4200.fits withdetxy=false withskyxy=
    false
rotdet2sky intemplate=mos2S002-fovimsky-1100-4200.fits inimage=mos2S002-bkgimdet
    -1100-4200.fits outimage=mos2S002-bkgimsky-1100-4200.fits withdetxy=false withskyxy=
    false
rotdet2sky intemplate=pnU002-fovimsky-1100-4200.fits inimage=pnU002-bkgimdet-1100-4200.
    fits outimage=pnU002-bkgimsky-1100-4200.fits withdetxy=false withskyxy=false

# # # b. rotate spf (proton) images from det to sky
rotdet2sky intemplate=mos1S001-fovimsky-300-700.fits inimage=mos1S001-protimdet-300-700.
    fits outimage=mos1S001-protimsky-300-700.fits
rotdet2sky intemplate=mos2S002-fovimsky-300-700.fits inimage=mos2S002-protimdet-300-700.
    fits outimage=mos2S002-protimsky-300-700.fits
```

```
222 rotdet2sky intemplate=pnU002-fovimsky-300-700.fits inimage=pnU002-protimdet-300-700.fits
      outimage=pnU002-protimsky-300-700.fits
223
224 rotdet2sky intemplate=mos1S001-fovimsky-700-1100.fits inimage=mos1S001-protimdet
    -700-1100.fits outimage=mos1S001-protimsky-700-1100.fits
225 rotdet2sky intemplate=mos2S002-fovimsky-700-1100.fits inimage=mos2S002-protimdet
    -700-1100.fits outimage=mos2S002-protimsky-700-1100.fits
226 rotdet2sky intemplate=pnU002-fovimsky-700-1100.fits inimage=pnU002-protimdet-700-1100.
    fits outimage=pnU002-protimsky-700-1100.fits
227
228 rotdet2sky intemplate=mos1S001-fovimsky-1100-4200.fits inimage=mos1S001-protimdet
    -1100-4200.fits outimage=mos1S001-protimsky-1100-4200.fits
229 rotdet2sky intemplate=mos2S002-fovimsky-1100-4200.fits inimage=mos2S002-protimdet
    -1100-4200.fits outimage=mos2S002-protimsky-1100-4200.fits
230 rotdet2sky intemplate=pnU002-fovimsky-1100-4200.fits inimage=pnU002-protimdet-1100-4200.
    fits outimage=pnU002-protimsky-1100-4200.fits
231
232 # # 8C. Image combining and massaging
233 combimage prefixlist='1S001 2S002 U002' withpartbkg=true withspbkg=true withswcxbkg=
    false withcheese=true cheesetype=t elowlist=300 ehighlist=700 alpha=1.7
234 combimage prefixlist='1S001 2S002 U002' withpartbkg=true withspbkg=true withswcxbkg=
    false withcheese=true cheesetype=t elowlist=700 ehighlist=1100 alpha=1.7
235 combimage prefixlist='1S001 2S002 U002' withpartbkg=true withspbkg=true withswcxbkg=
    false withcheese=true cheesetype=t elowlist=1100 ehighlist=4200 alpha=1.7
236
237 binadapt prefix=comb elow=300 ehigh=700 withpartbkg=true withspbkg=true withswcxbkg=
    false withmask=false withbinning=true binfactor=2 withsmoothing=true smoothcounts=50
238 binadapt prefix=comb elow=700 ehigh=1100 withpartbkg=true withspbkg=true withswcxbkg=
    false withmask=false withbinning=true binfactor=2 withsmoothing=true smoothcounts=50
239 binadapt prefix=comb elow=1100 ehigh=4200 withpartbkg=true withspbkg=true withswcxbkg=
    false withmask=false withbinning=true binfactor=2 withsmoothing=true smoothcounts=50
240
241 # 9. Spectral Fitting of SNR
242 # # 9A. Grouping... = Repeat 7A. twice with *full* replaced by *src* and *bkgd*
243 # # 9B. Spectral fitting of BKG
244 # # 9C. Spectral fitting of SRC with BKG best-fit parameters frozen
245 cd ${my_work}/${OID}/analysis/spectra
246 python3 bkg+src.py
```

A.2 Tables

Table A.1: Concatenated list of all MCSNRs and candidates [after Zangrandi et al. 2024]. The MCSNR names and coordinates are from Z24, Alias names are taken from literature wherever available ([HP99] is for Haberl & Pietsch [1999]). A unique serial number (SNr.) is assigned to each MCSNR or candidate (prefixed with the letter 'c').

SNr.	MCSNR	RA	Dec	Alias
1	J0447-6918	04:47:12	-69:19:16	
2	J0448-6700	04:48:25.2	-67:00:25	[HP99] 460
3	J0449-6903	04:49:34	-69:03:34	
4	J0449-6920	04:49:20	-69:20:20	
5	J0450-7050	04:50:27	-70:50:15	B0450-709
6	J0453-6655	04:53:10.2	-66:54:52	N4
7	J0453-6829	04:53:37.7	-68:29:38	B0453-685, LHG 1
8	J0454-6626	04:54:49	-66:25:32	N11L
9	J0454-6713	04:54:27.2	-67:13:20	N9
10	J0454-7003	04:54:19.8	-70:03:27	
11	J0455-6839	04:55:29.2	-68:39:01	N86
12	J0456-6533	04:56:50.7	-65:32:44	
13	J0456-6950	04:56:38	-69:50:55	
14	J0459-7008	04:59:51.9	-70:07:50	N186D
15	J0500-6512	05:00:53.2	-65:11:46	
16	J0504-6723	05:04:46.1	-67:23:59	
17	J0505-6753	05:05:41.9	-67:52:45	DEM L71, N63A
18	J0505-6802	05:05:54.7	-68:01:50	N23
19	J0506-6541	05:05:59.8	-65:42:37	DEM L72
20	J0506-6815	05:06:07.1	-68:15:43	
21	J0506-7009	05:06:15.8	-70:09:20	
22	J0506-7026	05:06:50	-70:25:53	[HP99] 1139, DEM L80
23	J0507-6847	05:07:33.6	-68:47:27	
24	J0508-6830	05:08:50	-68:30:50	
25	J0508-6902	05:08:37	-69:02:54	[HP99] 791
26	J0509-6731	05:09:30.6	-67:31:20	B0509-67.5, LHG 14
27	J0509-6844	05:08:59	-68:43:35	N103B
28	J0510-6708	05:10:11.4	-67:08:04	[HP99] 635
29	J0511-6759	05:11:17.4	-67:59:10	
30	J0512-6707	05:12:27	-67:07:18	[HP99] 483
31	J0512-6716	05:12:24.7	-67:16:55	DEM L81
32	J0513-6724	05:13:43	-67:24:10	
33	J0513-6912	05:13:12	-69:12:20	DEM L109, N112
34	J0514-6840	05:14:12.9	-68:40:15	HP 700
35	J0517-6759	05:17:11.7	-67:58:50	HP 607
36	J0518-6939	05:18:41.7	-69:39:20	N120A
37	J0519-6902	05:19:33.3	-69:02:21	B0519-690, LHG 26
38	J0519-6926	05:19:44	-69:26:08	B0520-694, LHG 27
39	J0521-6543	05:21:39	-65:43:07	DEM L142
40	J0522-6543	05:22:53.5	-65:43:09	
41	J0522-6740	05:22:33.7	-67:41:04	
42	J0523-6753	05:23:05.5	-67:53:20	N44I

SNr.	MCSNR	RA [hh:min:s]	Dec [hh:min:s]	Alias
43	J0524-6624	05:24:20.8	-66:24:28	DEM L175a, N48E
44	J0525-6559	05:25:24.1	-65:59:26	N49B
45	J0525-6938	05:25:02.9	-69:38:43	N132D
46	J0526-6605	05:25:59.4	-66:05:04	N49A
47	J0527-6550	05:27:54	-65:49:38	DEM L204
48	J0527-6714	05:28:07.9	-67:13:43	B0528-6716, DEM L205
49	J0527-6912	05:27:39.7	-69:12:20	B0528-692, LHG 40
50	J0527-7104	05:28:01.2	-71:04:23	[HP99] 1234
51	J0527-7134	05:27:49.9	-71:34:08	
52	J0528-6727	05:28:05	-67:27:20	DEM L205, [HP99] 498
53	J0529-6653	05:29:49.2	-66:53:34	DEM L214, DEM L316A
54	J0529-7004	05:29:11.4	-70:04:40	
55	J0530-7008	05:30:39	-70:07:30	DEM L218
56	J0531-7100	05:31:56	-71:00:19	N206
57	J0532-6732	05:32:14	-67:32:10	B0532-675
58	J0533-7202	05:33:53.3	-72:02:57	RASS 236
59	J0534-6955	05:34:00.4	-69:55:03	B0534-699, LHG 89
60	J0534-7033	05:34:14.9	-70:33:46	DEM L238
61	J0535-6602	05:35:44.9	-66:02:09	N63A, DEM L71
62	J0535-6916	05:35:27.7	-69:16:15	SNR1987A
63	J0535-6918	05:35:47.2	-69:18:14	Honeycomb
64	J0536-6735	05:35:56.2	-67:34:07	DEM L241, N59B
65	J0536-6913	05:36:15.4	-69:13:07	B0536-6914
66	J0536-7039	05:36:01.3	-70:38:26	DEM L249
67	J0537-6628	05:37:30.9	-66:27:52	DEM L256
68	J0537-6910	05:37:47.4	-69:10:17	N157B, 30 Dor B
69	J0540-6920	05:40:10.3	-69:19:59	B0540-693, N158A
70	J0540-6944	05:40:06.1	-69:44:00	N159
71	J0541-6659	05:41:49.5	-66:58:44	[HP99] 456
72	J0542-7104	05:42:42	-71:04:29	
73	J0543-6624	05:43:48.6	-66:23:51	
74	J0543-6858	05:43:05.9	-68:59:03	DEM L299
75	J0547-6941	05:47:23.2	-69:41:23	DEM L316A, DEM L214
76	J0547-6943	05:46:59.2	-69:43:05	DEM L316B
77	J0547-7025	05:47:48.2	-70:24:54	B0548-704, LHG 53
78	J0550-6823	05:50:30.9	-68:23:43	DEM L328
c01	J0444-6758	04:44:27.8	-67:58:13	
c02	J0450-6818	04:50:12.4	-68:18:05	
c03	J045145.7-671724	04:51:45.7	-67:17:24	
c04	J0451-6906	04:51:38.9	-69:06:26	
c05	J0451-6951	04:51:52.7	-69:51:41	
c06	J0452-6638	04:52:42.2	-66:38:43	
c07	J0455-6830	04:55:36.8	-68:30:35	
c08	J045625.5-683052	04:56:25.5	-68:30:52	
c09	J0457-6739	04:57:33	-67:39:05	
c10	J0457-6823	04:57:33.6	-68:23:39	
c11	J0457-6923	04:57:07.8	-69:23:58	[HP99] 544
c12	J0459-6757	04:59:55	-67:57:01	
c13	J0459-7008b	04:59:38.7	-70:08:37	

SNr.	MCSNR	RA [hh:min:s]	Dec [hh:min:s]	Alias
c14	J0502-6739	05:02:02.5	-67:39:31	
c15	J0504-6901	05:04:04.8	-69:01:12	
c16	J0506-6509	05:06:49.1	-65:09:19	
c17	J050750.8-714241	05:07:50.8	-71:42:41	
c18	J0507-7110	05:07:35.3	-71:10:15	[HP99] 530
c19	J0508-6928	05:08:46.5	-69:28:16	
c20	J0509-6402	05:09:15.5	-64:02:07	
c21	J051028.3-685329	05:10:28.3	-68:53:29	
c22	J0513-6731	05:13:26.9	-67:31:53	
c23	J0517-6757	05:17:53.6	-67:57:25	
c24	J052126.5-685245	05:21:36.6	-67:07:41	
c25	J052136.6-670741	05:21:26.5	-68:52:45	
c26	J052148.7-693649	05:21:48.7	-69:36:49	
c27	J052330.7-680400	05:23:30.7	-68:04:00	
c28	J052502.7-662125	05:25:02.7	-66:21:25	
c29	J052849.7-671913	05:28:49.7	-67:19:13	
c30	J0528-7018	05:28:46	-70:17:57	
c31	J053224.5-655411	05:32:24.5	-65:54:11	
c32	J0534-6700	05:34:42.4	-66:59:55	
c33	J0534-6720	05:34:04.9	-67:20:51	
c34	J0538-6921	05:38:14.7	-69:21:24	
c35	J0538-7004	05:38:44.9	-70:04:24	
c36	J0539-7001	05:39:35.5	-70:01:52	[HP99] 1063
c37	J0542-6852	05:41:59.3	-68:52:01	
c38	J0543-6906	05:43:27	-69:07:21	
c39	J0543-6923	05:43:16.5	-69:23:27	
c40	J0543-6928	05:43:06.3	-69:28:42	
c41	J0548-6941	05:48:49.2	-69:41:22	
c42	J054949.7-700145	05:49:49.7	-70:01:45	
c43	J0549-6618	05:49:30.4	-66:17:37	
c44	J0549-6633	05:49:25.6	-66:33:46	
c45	J061438.1-725112	06:14:38.1	-72:51:12	
c46	J0624-6948	06:24:13.5	-69:48:31	

Table A.2: X-ray satellite missions and their respective durations and energy ranges as of Jun 2024 [after Santangelo & Madonia 2014, Table2].

Satellite	**Mission Duration**	**Energy Range (keV)**
SAS-1 (Uhuru)	Dec 1970 – Mar 1973	2–20
OAO-3 (Copernicus)	Aug 1972 – Dec 1980	0.1–10
ANS	Aug 1974 – Jun 1977	0.1–30
Ariel 5	Oct 1974 – Mar 1980	0.3–40
Taiyo	Feb 1975 – Jun 1980	5.9–11.5
SAS-3	May 1975 – Apr 1979	0.1–60
HEAO-1	Aug 1977 – Jan 1979	$0.2–10^3$
HEAO-2 (Einstein)	Nov 1978 – Apr 1981	0.2–20
Hakucho	Feb 1979 – Apr 1985	0.1–100
Ariel 6	Jun 1979 – Feb 1982	1–50 + 0.25
HEAO-3	Sep 1979 – May 1981	$50–10^4$
Hinotori	Feb 1981 – Jul 1991	$0.2–9 \cdot 10^3$
Temna	Feb 1983 – Dec 1988	0.1–60
Astron	Mar 1983 – Jun 1989	2–25
EXOSAT	May 1983 – Apr 1986	0.05–50
Ginga	Feb 1987 – Nov 1991	1–500
Granat	Dec 1989 – Nov 1998	$2–10^5$
ROSAT	Jun 1990 – Feb 1999	0.1–2.5 + 0.062–0.206
BBXRT	2–11 Dec 1990	0.3–12
DXS	13–19 Jan 1993	0.15–0.28
ASCA	Feb 1993 – Mar 2001	0.4–10
ALEXIS	Apr 1993 – Apr 2005	0.066, 0.071, 0.095
RXTE	Dec 1995 – Jan 2012	2–250
BeppoSAX	Apr 1996 – Apr 2002	0.1–300
ARGOS	Feb 1999 – Jul 2003	1–15
Chandra	Jul 1999 –	0.1–10
XMM-Newton	Dec 1999 –	0.15–12
HETE-2	Oct 2000 – Mar 2008	0.5–400
INTEGRAL	Oct 2002 –	$3–35 + 15–10^4$
Swift	Nov 2004 –	0.3–150
Suzaku	Jul 2005 – Sep 2015	0.3–600
MAXI	Jul 2009 –	0.5–30
NuSTAR	Jun 2012 –	6–79
AstroSat	Sep 2015 –	0.3–8
Hitomi	Feb – Mar 2016	0.3–600
NICER	Jun 2017 –	0.2-12
SRG (eROSITA)	Jul 2019 –	0.2-8, 5-30
IXPE	Dec 2021 –	2-8
XRISM	Sep 2023 –	0.3-12
eXTP	2027?	2-30
ATHENA	2037?	0.3-12

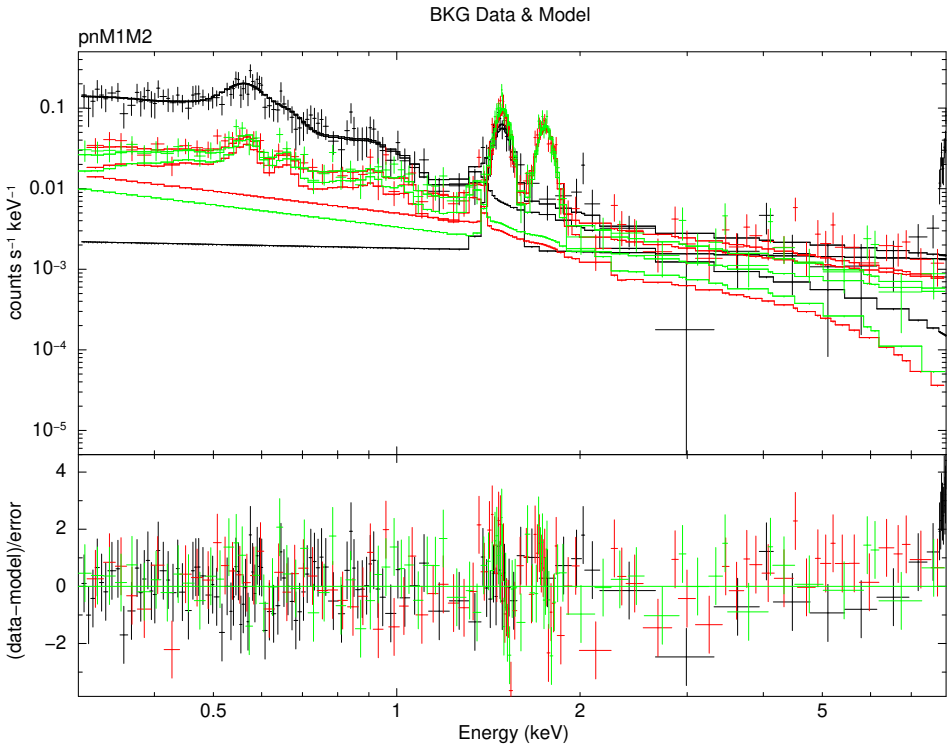

Figure A.1: Spectral fit result for the background. Black, red and green points & solid lines show PN, MOS1 and MOS2 data & folded model, respectively. The plot is rebinned for visual clarity. Additive model components are not shown. A FX line and SPF powerlaws are also shown. The residuals are `delchi` viz. error = square-root of model counts.

A.3 Figures

A.3.1 Spectral Fits

A.3.2 Population Evolution Curves

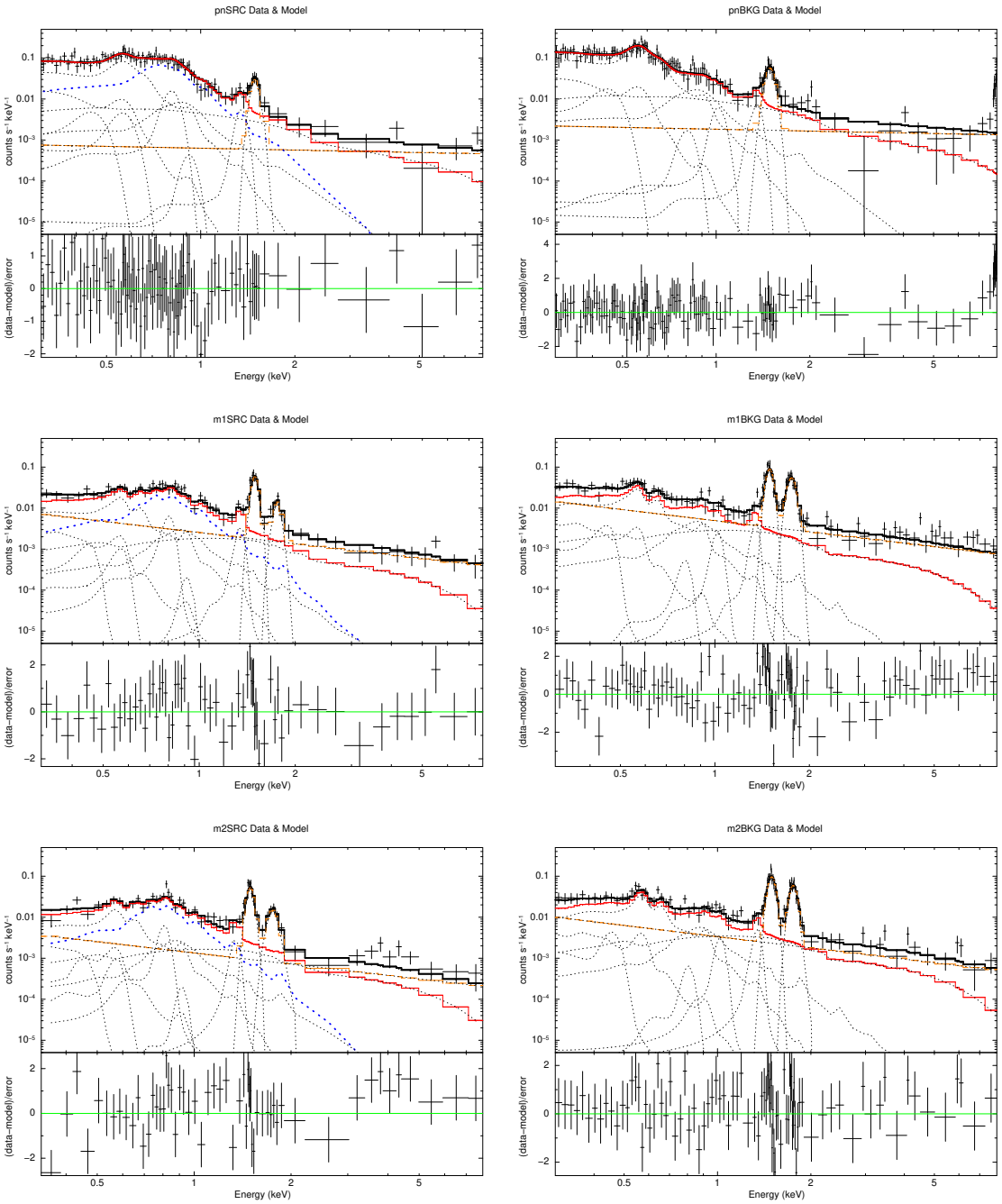

Figure A.2: MCSNR J0500-6512 individual spectra from fitting of BKG (**right**) & SRC (**left**) of PN (top), MOS1 (middle) and MOS2 (bottom) data. Black points and solid lines represent data and folded model. Red solid line is fitted line without the instrumental line (dashed orange). The dotted lines denote various additive components of the spectral model; `vnei` shown in thick blue.

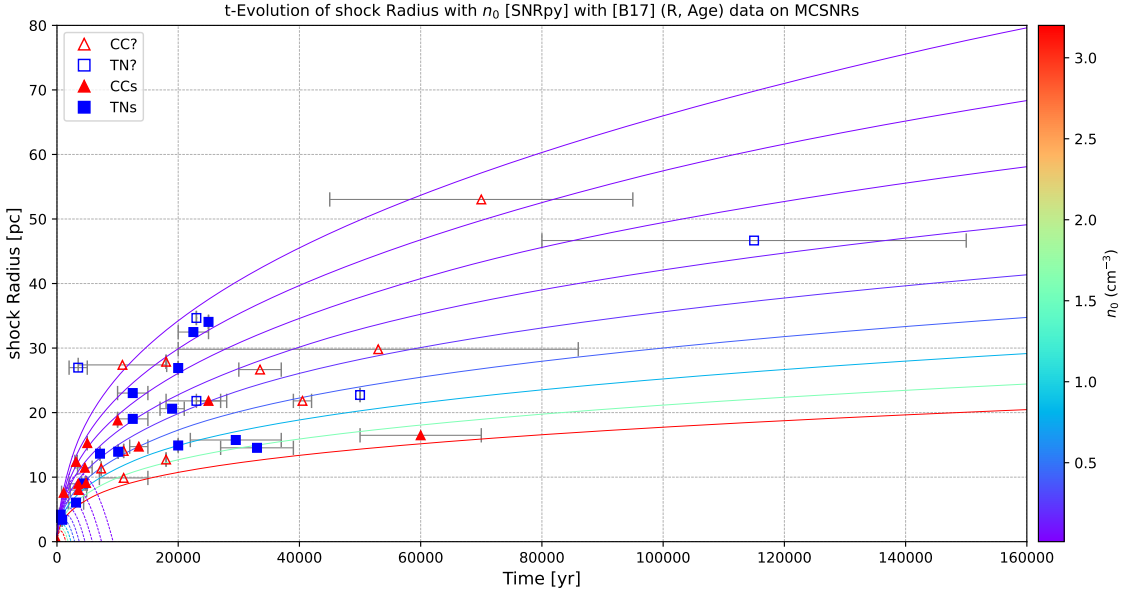

Figure A.3: r versus age for B17's SNRs onto SNRpy time-evolution of shock radii for various n_0 and "typical LMC" SNR parameters. Error bars for ages are drawn whenever available. Uncertainties is sizes is 0.3 pc for each, not drawn.

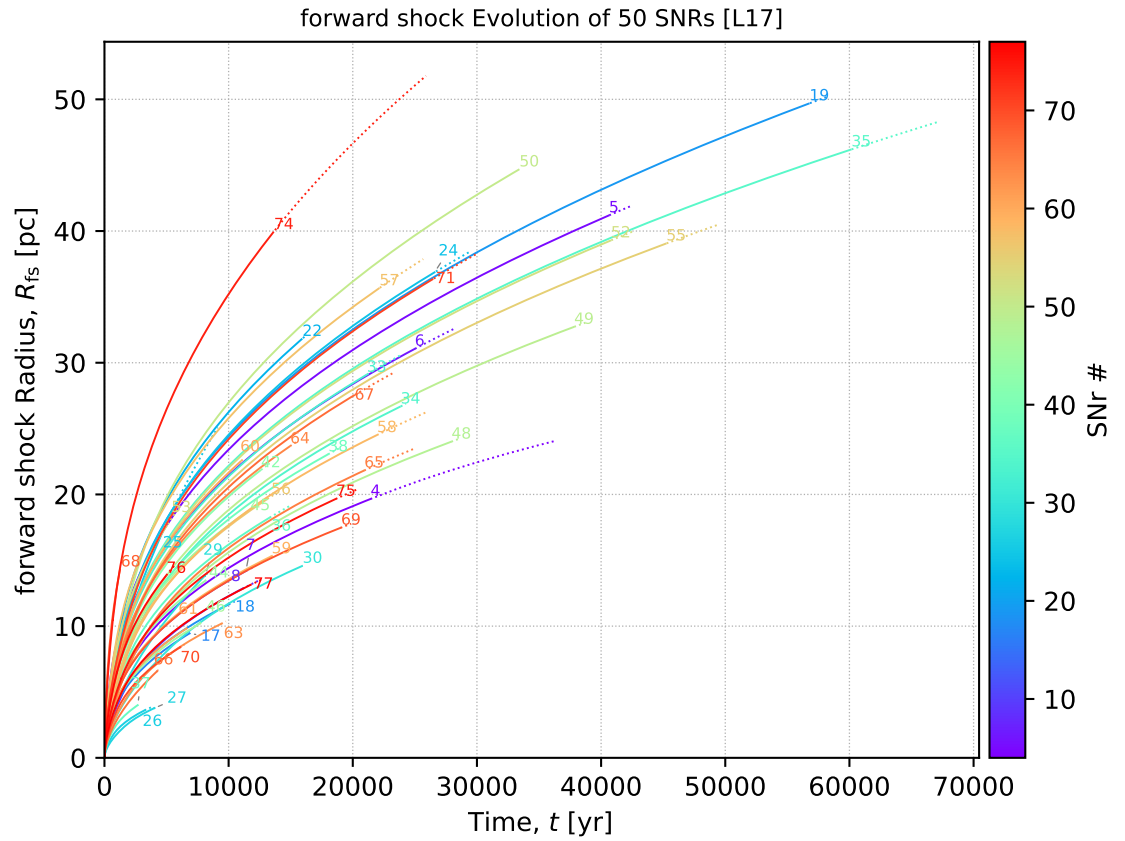

Figure A.4: Forward shock evolution of L17's 50 SNRs up to the calculated ages (upper limit, t_0+error) or the input radii, same as Fig. 7.21 but numbered and color graded by their serial number identifiers from Tab. A.1.

Acknowledgments

This work was supported by many people and organizations, directly or indirectly. An important portion of this study was based on observations with XMM-Newton, an ESA science mission funded by its member states. For data reduction, we use ESAS, a sub-collection of command line tasks of SAS, a software suite managed by the XMM-Newton Science Operations Centre (SOC). We are thankful to the authors of the ESAS Cookbook [Snowden & Kuntz 2023]. In further analysis, we use XSPEC, an X-ray spectral fitting package by Arnaud [1996]; DS9, an imaging tool funded by Chandra X-ray Science Centre (CXC); FV, a graphical program to manipulate FITS files developed at the High Energy Astrophysics Science Archive Research Center (HEASARC) at NASA Goddard Space Flight Center (GSFC). Along the way, I also use Python libraries such as matplotlib [Hunter 2007], NumPy [Harris et al. 2020], SciPy [Virtanen et al. 2020]. This research also uses images from the Magellanic Clouds Emission Line Survey (MCELS, Smith & MCELS Team [1999]), an optical survey performed using University of Michigan (UM) Curtis Schmidt telescope at Cerro Tololo Inter-American Observatory (CTIO). Another major portion of our study employed SNRpy, a Python program created by Leahy et al. [2017] to consistently calculate SNR evolution. I'd like to extend my gratitude to Jonathan K. for making the script work for my analysis; also to Sara S. for help during ESAS analysis; rest goes to Federico Z. for providing the spectral models, tables & images from his submitted paper, and non-quantifiable support throughout. I'd also like to thank the good people of Dr. Karl Remeis Observatory Bamberg and the working environment there. Foremost, I would always be indebted to my supervisor, Prof. Dr. Manami Sasaki for continuous encouragement and patient support. My research and interest in diffuse ISM and SNRs is owed to her lectures, works and guidance.

This thesis was written in the LaTeX markup language and compiled using XeTeX, a typesetting system based on Donald E. Knuth's TeX, on Overleaf, a commercial server-based editing and publishing platform. The body text is set in 12 point Egenolff-Berner (EB) Garamond, a revival of Claude Garamont's humanist typeface; the version used was designed by Duffner & Pardo [2023] and licensed to Google Fonts. The word cloud was created using the library *wordcloud* by Andreas Mueller. The writing was, of course, preceded by reading of books, papers and theses, which were often found using *astrophysics data system* (ads), a digital library of astronomy and physics research works operated by the Smithsonian Astrophysical Observatory (SAO) under a NASA grant. The authors of the literature used also deserve credit beyond the numerous citations in this work. Finally, I would like to thank my family for their emotional and financial support in all my endeavors; friends for making the daily life easier and fun; and myself for a tiny bit of perseverance.

References

Aghanim, N., Akrami, Y., Ashdown, M., et al. 2020, Astronomy & Astrophysics, 641, A6, doi: 10.1051/0004-6361/201833910

Alsabti, A. W., & Murdin, P., eds. 2017, Handbook of Supernovae (Cham: Springer International Publishing), doi: 10.1007/978-3-319-21846-5

Anders, E., & Grevesse, N. 1989, Geochimica et Cosmochimica Acta, 53, 197, doi: 10.1016/0016-7037(89)90286-X

Angel, J. R. P. 1979, The Astrophysical Journal, 233, 364, doi: 10.1086/157397

Angelis, A. D., & Pimenta, M. 2018, Introduction to Particle and Astroparticle Physics, 2nd edn., Undergraduate Lecture Notes in Physics (Springer Cham), XXX, 733, doi: 10.1007/978-3-319-78181-5

Arnaud, K. A. 1996, in Astronomical Society of the Pacific Conference Series, Vol. 101, Astronomical Data Analysis Software and Systems V, ed. G. H. Jacoby & J. Barnes, 17

Arnett, D. 1996, Supernovae and Nucleosynthesis, Princeton Series in Astrophysics (Princeton, NJ: Princeton University Press), 496. https://press.princeton.edu/books/paperback/9780691011479/supernovae-and-nucleosynthesis

Arnett, W. D., Bahcall, J. N., Kirshner, R. P., et al. 1989, Annual Review of Astronomy and Astrophysics, 27, 629, doi: 10.1146/annurev.aa.27.090189.003213

Aschenbach, B. 2002, in X-Ray Optics for Astronomy: Telescopes, Multilayers, Spectrometers, and Missions, ed. P. Gorenstein & R. B. Hoover, Vol. 4496, International Society for Optics and Photonics (SPIE), 8 – 22, doi: 10.1117/12.454367

Baade, W., & Zwicky, F. 1934, Proceedings of the National Academy of Sciences, 20, 254, doi: 10.1073/pnas.20.5.254

Badenes, C., Harris, J., Zaritsky, D., et al. 2009, The Astrophysical Journal, 700, 727, doi: 10.1088/0004-637X/700/1/727

Badenes, C., Maoz, D., & Draine, B. T. 2010, Monthly Notices of the Royal Astronomical Society, 407, 1301, doi: 10.1111/j.1365-2966.2010.17023.x

Bale, S. D., Mozer, F. S., & Horbury, T. S. 2003, Physical Review Letters, 91, 265004, doi: 10.1103/PhysRevLett.91.265004

Balucinska-Church, M., & McCammon, D. 1992, The Astrophysical Journal, 400, 699, doi: 10.1086/172032

Bandiera, R., & Petruk, O. 2004, Astronomy & Astrophysics, 419, 419, doi: 10.1051/0004-6361:20035950

—. 2010, Astronomy and Astrophysics, 509, A34, doi: 10.1051/0004-6361/200912244

Barkat, Z., Rakavy, G., & Sack, N. 1967, Physical Review Letters, 18, 379 – 381, doi: 10.1103/PhysRevLett.18.379

Bethe, H. A. 1990, Reviews of Modern Physics, 62, 801, doi: 10.1103/RevModPhys.62.801

Bevington, P. R. 2002, Data Reduction and Error Analysis for the Physical Sciences, 3rd edn. (McGraw-Hill)

Blair, W. P., Ghavamian, P., Sankrit, R., et al. 2006, The Astrophysical Journal Supplement Series, 165, 480, doi: 10.1086/505346

Blondin, J. M., Wright, E. B., Borkowski, K. J., et al. 1998, The Astrophysical Journal, 500, 342, doi: 10.1086/305708

Bond, J. R., Arnett, W. D., & Carr, B. J. 1984, The Astrophysical Journal, 280, 825, doi: 10.1086/162057

Borkowski, K. J., Lyerly, W. J., & Reynolds, S. P. 2001, The Astrophysical Journal, 548, 820, doi: 10.1086/319011

Boyle, W. S., & Smith, G. E. 1970, The Bell System Technical Journal, 49, 587, doi: 10.1002/j.1538-7305.1970.tb01790.x

Bozzetto, L. M., Filipovic, M. D., Crawford, E. J., et al. 2012a, Revista Mexicana de Astronomía y Astrofísica, 48, 41, doi: 10.48550/arXiv.1109.3945

Bozzetto, L. M., Filipović, M. D., Crawford, E. J., et al. 2012b, Monthly Notices of the Royal Astronomical Society,

420, 2588, doi: 10.1111/j.1365-2966.2011.20231.x
Bozzetto, L. M., Kavanagh, P. J., Maggi, P., et al. 2014, Monthly Notices of the Royal Astronomical Society, 439, 1110, doi: 10.1093/mnras/stu051
Bozzetto, L. M., Filipović, M. D., Vukotić, B., et al. 2017, The Astrophysical Journal Supplement Series, 230, 2, doi: 10.3847/1538-4365/aa653c
Bozzetto, L. M., Filipović, M. D., Sano, H., et al. 2022, Monthly Notices of the Royal Astronomical Society, 518, 2574, doi: 10.1093/mnras/stac2922
Bromm, V., Coppi, P. S., & Larson, R. B. 1999, Astrophysical Journal, 527, L5–L8, doi: 10.1086/312385
Buckingham, E. 1914, Physical Review, 4, 345, doi: 10.1103/PhysRev.4.345
Burrows, A., & Vartanyan, D. 2021, Nature, 589, 29, doi: 10.1038/s41586-020-03059-w
Carter, J. A., & Read, A. M. 2007, Astronomy & Astrophysics, 464, 1155, doi: 10.1051/0004-6361:20065882
Chase, R. C., & VanSpeybroeck, L. P. 1973, Appl. Opt., 12, 1042, doi: 10.1364/AO.12.001042
Chen, L.-W., Fabian, A. C., & Gendreau, K. C. 1997, Monthly Notices of the Royal Astronomical Society, 285, 449, doi: 10.1093/mnras/285.3.449
Chevalier, R. A. 1982, The Astrophysical Journal, 258, 790, doi: 10.1086/160126
Chevalier, R. A., & Fransson, C. 1994, The Astrophysical Journal, 420, 268, doi: 10.1086/173557
Christensen, F. E., & Ramsey, B. D. 2022, X-Ray Optics for Astrophysics: A Historical Review (Springer Nature Singapore), 1–42, doi: 10.1007/978-981-16-4544-0_1-1
Chu, Y.-H., Kim, S., Points, S. D., et al. 2000, The Astronomical Journal, 119, 2242, doi: 10.1086/301331
Cioffi, D. F., McKee, C. F., & Bertschinger, E. 1988, The Astrophysical Journal, 334, 252, doi: 10.1086/166834
Colgate, S. A., & McKee, C. 1969, The Astrophysical Journal, 157, 623, doi: 10.1086/150102
Compton, A. H. 1923, The London, Edinburgh, and Dublin Philosophical Magazine and Journal of Science, 45, 1121, doi: 10.1080/14786442308634208
Cox, D. P., & Anderson, P. R. 1982, The Astrophysical Journal, 253, 268, doi: 10.1086/159632
Cox, D. P., Shelton, R. L., Maciejewski, W., et al. 1999, The Astrophysical Journal, 524, 179, doi: 10.1086/307781
D'Auria, S. 2018, Introduction to Nuclear and Particle Physics, 1st edn., Undergraduate Lecture Notes in Physics (Springer Cham), XII, 192, doi: 10.1007/978-3-319-93855-4
Davis, K. W., Taggart, K., Tinyanont, S., et al. 2023, Monthly Notices of the Royal Astronomical Society, 523, 2530, doi: 10.1093/mnras/stad1433
de Chambure, D., Lainé, R., van Katwijk, K., et al. 1999, ESA Bulletin, 100. https://www.esa.int/esapub/bulletin/bullet100/CHAMBURE.pdf
de Grijs, R., Wicker, J. E., & Bono, G. 2014, The Astronomical Journal, 147, 122, doi: 10.1088/0004-6256/147/5/122
de Horta, A. Y., Filipović, M. D., Bozzetto, L. M., et al. 2012, Astronomy & Astrophysics, 540, A25, doi: 10.1051/0004-6361/201118694
Desai, K. M., Chu, Y.-H., Gruendl, R. A., et al. 2010, The Astronomical Journal, 140, 584, doi: 10.1088/0004-6256/140/2/584
Dickey, J. M., & Lockman, F. J. 1990, Annual Review of Astronomy and Astrophysics, 28, 215, doi: 10.1146/annurev.aa.28.090190.001243
Dopita, M., Hart, J., McGregor, P., et al. 2007, Astrophysics and Space Science, 310, 255–268, doi: 10.1007/s10509-007-9510-z
Dopita, M. A., & Sutherland, R. S. 2003, Astrophysics of the Diffuse Universe, 1st edn., Astronomy and Astrophysics Library (Springer Berlin, Heidelberg), XIV, 441, doi: 10.1007/978-3-662-05866-4
Draine, B. T. 2011, Physics of the interstellar and intergalactic medium, Princeton series in astrophysics (Princeton, NJ: Princeton University Press)
Duffner, G., & Pardo, O. 2023, EB Garamond, https://googlefonts.github.io/ebgaramond-specimen/. https://googlefonts.github.io/ebgaramond-specimen/
Fabjan, C. W., & Schopper, H., eds. 2020, Particle Physics Reference Library, 1st edn., Physics and Astronomy (Springer Cham), IX, 1078, doi: 10.1007/978-3-030-35318-6
Ferrand, G., & Safi-Harb, S. 2012, Advances in Space Research, 49, 1313, doi: 10.1016/j.asr.2012.02.004
Ferrière, K. M. 2001, Reviews of Modern Physics, 73, 1031, doi: 10.1103/RevModPhys.73.1031
Field, G. B., Goldsmith, D. W., & Habing, H. J. 1969, The Astrophysical Journal, 155, L149, doi: 10.1086/180324
Filipovic, M. D., Haynes, R. F., White, G. L., et al. 1998, Astronomy and Astrophysics Supplement Series, 130, 421, doi: 10.1051/aas:1998417
Filipović, M. D., & Tothill, N. F. H. 2021, Principles of Multimessenger Astronomy, 2514-3433 (IOP Publishing), doi: 10.1088/2514-3433/ac087e
Filipović, M. D., Pietsch, W., Haynes, R. F., et al. 1998, Astronomy and Astrophysics Supplement Series, 127, 119, doi: 10.1051/aas:1998369

Filippenko, A. V. 1997, Annual Review of Astronomy and Astrophysics, 35, 309, doi: 10.1146/annurev.astro.35.1.309

Fosco Connect. 2023, Junction Photodiodes. https://www.fiberoptics4sale.com/blogs/wave-optics/junction-photodiodes

Gaensler, B. M., & Slane, P. O. 2006, Annual Review of Astronomy and Astrophysics, 44, 17, doi: https://doi.org/10.1146/annurev.astro.44.051905.092528

Gaia Collaboration, Luri, X., Chemin, L., et al. 2021, Astronomy & Astrophysics, 649, doi: 10.1051/0004-6361/202039588

Gal-Yam, A. 2012, Science, 337, 927, doi: 10.1126/science.1203601

Ghavamian, P., Schwartz, S. J., Mitchell, J., et al. 2013, Space Science Reviews, 178, 633, doi: 10.1007/s11214-013-9999-0

Giacconi, R. 2003, Rev. Mod. Phys., 75, 995, doi: 10.1103/RevModPhys.75.995

Giacconi, R., Gursky, H., Paolini, F. R., et al. 1962, Phys. Rev. Lett., 9, 439, doi: 10.1103/PhysRevLett.9.439

Giacconi, R., Kellogg, E., Gorenstein, P., et al. 1971, The Astrophysical Journal Letters, 165, L27, doi: 10.1086/180711

Giacconi, R., Reidy, W. P., Vaiana, G. S., et al. 1969, Space Science Reviews, 9, 3, doi: 10.1007/BF00187578

Giacconi, R., & Rossi, B. 1960, Journal of Geophysical Research (1896-1977), 65, 773, doi: 10.1029/JZ065i002p00773

Giacconi, R., Branduardi, G., Briel, U., et al. 1979, The Astrophysical Journal, 230, 540, doi: 10.1086/157110

Ginzburg, V. L., & Syrovatskii, S. I. 1965, Annual Review of Astronomy and Astrophysics, 3, 297, doi: https://doi.org/10.1146/annurev.aa.03.090165.001501

Green, D. A. 2002, Highlights of Astronomy, 12, 350

Green, D. A. 2005, Memorie della Società Astronomica Italiana, 76, 534, doi: 10.48550/arXiv.astro-ph/0505428

—. 2024a, An updated catalogue of 310 Galactic supernova remnants and their statistical properties. https://arxiv.org/abs/2411.03367

—. 2024b, A Catalogue of Galactic Supernova Remnants (2024 October version), https://www.mrao.cam.ac.uk/surveys/snrs/

Haberl, F., & Pietsch, W. 1999, Astron. Astrophys. Suppl. Ser., 139, 277, doi: 10.1051/aas:1999394

Harris, C. R., Millman, K. J., van der Walt, S. J., et al. 2020, Nature, 585, 357–362, doi: 10.1038/s41586-020-2649-2

Heger, A., Fryer, C. L., Woosley, S. E., et al. 2003, The Astrophysical Journal, 591, 288, doi: 10.1086/375341

Heiles, C., & Kulkarni, S. R. 1987, in NATO ASI Series, Vol. 210, Physical Processes in Interstellar Clouds, ed. G. E. Morfill & M. Scholer (Springer, Dordrecht), 13–33, doi: 10.1007/978-94-009-3945-5_2

Henke, B. L., Gullikson, E. M., & Davis, J. C. 1993, Atomic Data and Nuclear Data Tables, 54, 181. https://henke.lbl.gov/optical_constants/

Henley, D. B., & Shelton, R. L. 2008, The Astrophysical Journal, 676, 335, doi: 10.1086/528924

Hester, J. J. 2008, Annual Review of Astronomy and Astrophysics, 46, 127, doi: https://doi.org/10.1146/annurev.astro.45.051806.110608

HI4PI Collaboration, Ben Bekhti, N., Flöer, L., et al. 2016, Astronomy & Astrophysics, 594, A116, doi: 10.1051/0004-6361/201629178

Hillebrandt, W., Kromer, M., Röpke, F. K., et al. 2013, Frontiers of Physics, 8, 116, doi: 10.1007/s11467-013-0303-2

Hinton, J. A., & Hofmann, W. 2009, Annual Review of Astronomy and Astrophysics, 47, 523, doi: 10.1146/annurev-astro-082708-101816

Huang, R., Li, J.-T., Cui, W., et al. 2023, The Astrophysical Journal Supplement Series, 268, 36, doi: 10.3847/1538-4365/ace4b8

Hubbell, J. H. 1969, Photon Cross Sections, Attenuation Coefficients, and Energy Absorption Coefficients From 10 keV to 100 GeV, Tech. Rep., National Standard Reference Data System (NSRDS). https://nvlpubs.nist.gov/nistpubs/Legacy/NSRDS/nbsnsrds29.pdf

Hugoniot, M. 1889, Journal de l'École Polytechnique de Paris, 58, 1

Hunter, J. D. 2007, Computing in Science & Engineering, 9, 90, doi: 10.1109/MCSE.2007.55

IAU Central Bureau for Astronomical Telegrams. 2015, List of Supernovae. http://www.cbat.eps.harvard.edu/lists/Supernovae.html

Iben, I., J., & Tutukov, A. V. 1984, The Astrophysical Journal Supplement Series, 54, 335, doi: 10.1086/190932

Janka, H.-T. 2012, Annual Review of Nuclear and Particle Science, 62, 407, doi: 10.1146/annurev-nucl-102711-094901

Jansen, F., Lumb, D., Altieri, B., et al. 2001, Astronomy & Astrophysics, 365, L1–L6, doi: 10.1051/0004-6361:20000036

Joye, W. A., & Mandel, E. 2003, in Astronomical Society of the Pacific Conference Series, Vol. 295, Astronomical Data Analysis Software and Systems XII, ed. H. E. Payne, R. I. Jedrzejewski, & R. N. Hook, 489
Kaastra, J. S., Paerels, F. B. S., Durret, F., et al. 2008, Space Science Reviews, 134, 155, doi: 10.1007/s11214-008-9310-y
Kahn, F. 1976, Astronomy and Astrophysics, vol. 50, no. 1, July 1976, p. 145-148., 50, 145
Kavanagh, P. J., Sasaki, M., Bozzetto, L. M., et al. 2015a, Astronomy & Astrophysics, 573, A73, doi: 10.1051/0004-6361/201424354
Kavanagh, P. J., Sasaki, M., Filipovic, M. D., et al. 2022, Monthly Notices of the Royal Astronomical Society, 515, 4099, doi: 10.1093/mnras/stac813
Kavanagh, P. J., Sasaki, M., Whelan, E. T., et al. 2015b, Astronomy & Astrophysics, 579, A63, doi: 10.1051/0004-6361/201526143
Kiefer, J. 1953, Proceedings of the American Mathematical Society, 4, 502, doi: 10.1090/S0002-9939-1953-0055639-3
Kim, C.-G., & Ostriker, E. C. 2015, The Astrophysical Journal, 802, 99, doi: 10.1088/0004-637X/802/2/99
Kirkpatrick, P., & Baez, A. V. 1948, J. Opt. Soc. Am., 38, 766, doi: 10.1364/JOSA.38.000766
Kirsch, M. G., Briel, U. G., Burrows, D., et al. 2005, in Society of Photo-Optical Instrumentation Engineers (SPIE) Conference Series, Vol. 5898, UV, X-Ray, and Gamma-Ray Space Instrumentation for Astronomy XIV, ed. O. H. W. Siegmund, 22–33, doi: 10.1117/12.616893
Kostić, P., Vukotić, B., Urošević, D., et al. 2016, Monthly Notices of the Royal Astronomical Society, 461, 1421, doi: 10.1093/mnras/stw1381
Koyama, K., Petre, R., Gotthelf, E. V., et al. 1995, Nature, 378, 255, doi: 10.1038/378255a0
Kuntz, K. D., & Snowden, S. L. 2008, Astronomy & Astrophysics, 478, 575, doi: 10.1051/0004-6361:20077912
Kuranz, C. C., Park, H.-S., Huntington, C. M., et al. 2018, Nature Communications, 9, 1564, doi: 10.1038/s41467-018-03548-7
Laming, J. M., & Hwang, U. 2003, The Astrophysical Journal, 597, 347, doi: 10.1086/378268
Leahy, D. A. 2017, The Astrophysical Journal, 837, 36, doi: 10.3847/1538-4357/aa60c1
Leahy, D. A., Williams, J., & Lawton, B. 2017, SNRPy: Supernova remnant evolution modeling, Astrophysics Source Code Library, record ascl:1703.006
Leahy, D. A., & Williams, J. E. 2017, The Astronomical Journal, 153, 239, doi: 10.3847/1538-3881/aa6af6
Lee, J. H., & Lee, M. G. 2014, The Astrophysical Journal, 786, 130, doi: 10.1088/0004-637X/786/2/130
Levenberg, K. 1944, Quarterly of Applied Mathematics, 2, 164, doi: 10.1090/qam/10666
Li, W., Chornock, R., Leaman, J., et al. 2011, Monthly Notices of the Royal Astronomical Society, 412, 1473, doi: 10.1111/j.1365-2966.2011.18162.x
Liang, E., & Keilty, K. 2000, The Astrophysical Journal, 533, 890, doi: 10.1086/308686
Long, K. S., Helfand, D. J., & Grabelsky, D. A. 1981, The Astrophysical Journal, 248, 925, doi: 10.1086/159222
Long, K. S., Blair, W. P., Winkler, P. F., et al. 2010, The Astrophysical Journal Supplement Series, 187, 495, doi: 10.1088/0067-0049/187/2/495
Lopez, L. A., Ramirez-Ruiz, E., Huppenkothen, D., et al. 2011, The Astrophysical Journal, 732, 114, doi: 10.1088/0004-637X/732/2/114
Maggi, P., Haberl, F., Bozzetto, L. M., et al. 2012, Astronomy & Astrophysics, 546, doi: 10.1051/0004-6361/201219708
Maggi, P., Haberl, F., Kavanagh, P. J., et al. 2014, Astronomy & Astrophysics, 561, A76, doi: 10.1051/0004-6361/201322820
—. 2016, Astronomy & Astrophysics, 585, A162, doi: 10.1051/0004-6361/201526932
Maggi, P., Filipović, M. D., Vukotić, B., et al. 2019, Astronomy & Astrophysics, 631, A127, doi: 10.1051/0004-6361/201936583
Maitra, C., Haberl, F., Maggi, P., et al. 2021, Monthly Notices of the Royal Astronomical Society, 504, 326, doi: 10.1093/mnras/stab716
Maitra, C., Haberl, F., Filipović, M. D., et al. 2019, Monthly Notices of the Royal Astronomical Society, 490, 5494, doi: 10.1093/mnras/stz2831
Maoz, D., & Badenes, C. 2010, Monthly Notices of the Royal Astronomical Society, 407, 1314, doi: 10.1111/j.1365-2966.2010.16988.x
Maoz, D., & Mannucci, F. 2012, Publications of the Astronomical Society of Australia, 29, 447, doi: 10.1071/AS11052
Marquardt, D. W. 1963, Journal of the Society for Industrial and Applied Mathematics, 11, 431, doi: 10.1137/0111030
Mathewson, D. S., & Clarke, J. N. 1973, The Astrophysical Journal, 180, 725, doi: 10.1086/152002
Mathewson, D. S., Ford, V. L., Dopita, M. A., et al. 1983, Astrophysical Journal Supplement Series, 51, 345,

doi: 10.1086/190854
—. 1984, Astrophysical Journal Supplement Series, 55, 189, doi: 10.1086/190952
Mathewson, D. S., Ford, V. L., Tuohy, I. R., et al. 1985, Astrophysical Journal Supplement Series, 58, 197, doi: 10.1086/191037
Mathewson, D. S., & Healey, J. R. 1964, in Proceedings of the IAU Symposium, The Galaxy and the Magellanic Clouds, ed. F. J. Kerr, Vol. 20 (Canberra: Australian Academy of Science), 245
McKee, C. F. 1974, The Astrophysical Journal, 188, 335, doi: 10.1086/152721
McKee, C. F., & Hollenbach, D. J. 1980, Annual Review of Astronomy and Astrophysics, 18, 219, doi: 10.1146/annurev.aa.18.090180.001251
McKee, C. F., & Ostriker, J. P. 1977, The Astrophysical Journal, 218, 148, doi: 10.1086/155667
McLean, I. S. 2008, Electronic Imaging in Astronomy: Detectors and Instrumentation, 2nd edn., Springer Praxis Books (Springer Berlin, Heidelberg), XL, 552, doi: 10.1007/978-3-540-76583-7
Mewe, R. 1999, in Lecture Notes in Physics, Vol. 520, X-Ray Spectroscopy in Astrophysics, ed. J. van Paradijs & J. A. M. Bleeker (Springer-Verlag Berlin Heidelberg), 109, doi: 10.1007/978-3-540-49199-6_2
Micelotta, E. R., Dwek, E., & Slavin, J. D. 2016, Astronomy & Astrophysics, 590, A65, doi: 10.1051/0004-6361/201527350
Mills, B. Y., Turtle, A. J., Little, A. G., et al. 1984, Australian Journal of Physics, 37, 321, doi: 10.1071/PH840321
Minkowski, R. 1941, Publications of the Astronomical Society of the Pacific, 53, 224, doi: 10.1086/125315
Moretti, A., Pagani, C., Cusumano, G., et al. 2009, Astronomy & Astrophysics, 493, 501, doi: 10.1051/0004-6361:200811197
Müller, B., Melson, T., Heger, A., et al. 2017, Monthly Notices of the Royal Astronomical Society, 472, 491, doi: 10.1093/mnras/stx1962
Nadezhin, D. K. 1985, Astrophysics and Space Science, 112, 225, doi: 10.1007/BF00653506
Oort, J. 1951, Central Air Document Office, Dayton
Pareschi, G., Spiga, D., & Pelliciari, C. 2021, in The WSPC Handbook of Astronomical Instrumentation (World Scientific Series in Astrophysics), 3–31, doi: 10.1142/9789811203800_0001
Payne, J. L., White, G. L., & Filipović, M. D. 2008, Monthly Notices of the Royal Astronomical Society, 383, 1175, doi: 10.1111/j.1365-2966.2007.12620.x
Pence, W., & Chai, P. 2012, Fv: Interactive FITS file editor, Astrophysics Source Code Library, record ascl:1205.005
Perlmutter, S., Aldering, G., Goldhaber, G., et al. 1999, The Astrophysical Journal, 517, 565, doi: 10.1086/307221
Pietrzyński, G., Graczyk, D., Gallenne, A., et al. 2019, Nature, 567, 200, doi: 10.1038/s41586-019-0999-4
Rankine, W. 1870, Philosophical Transactions of the Royal Society of London, 160, 277
Riess, A. G., Filippenko, A. V., Challis, P., et al. 1998, The Astronomical Journal, 116, 1009, doi: 10.1086/300499
Ritter, A., Parker, Q. A., Lykou, F., et al. 2021, The Astrophysical Journal Letters, 918, L33, doi: 10.3847/2041-8213/ac2253
Röntgen, W. C. 1896, Nature, 53, 274
Sagan, C. 1980, Cosmos (New York: Random House)
Salucci, P. 2019, The Astronomy and Astrophysics Review, 27, 2, doi: 10.1007/s00159-018-0113-1
Santangelo, A., & Madonia, R. 2014, Astroparticle Physics, 53, 130, doi: 10.1016/j.astropartphys.2013.11.005
Santangelo, A., Madonia, R., & Piraino, S. 2023, A Chronological History of X-Ray Astronomy Missions (Springer Nature Singapore), 1–68, doi: 10.1007/978-981-16-4544-0_147-1
Sasaki, M., Breitschwerdt, D., Baumgartner, V., et al. 2011, Astronomy & Astrophysics, 528, A136, doi: 10.1051/0004-6361/201015866
Sasaki, M., Pietsch, W., Haberl, F., et al. 2012, Astronomy & Astrophysics, 544, A144, doi: 10.1051/0004-6361/201219025
Sasaki, M., Knies, J., Haberl, F., et al. 2022, Astronomy & Astrophysics, 661, A37, doi: 10.1051/0004-6361/202141054
Sedov, L. I. 1946, Doklady Akademii Nauk SSSR, 42, 17
—. 1959, Similarity and Dimensional Methods in Mechanics, 4th edn. (New York: Academic Press)
Seok, J. Y., Koo, B.-C., & Onaka, T. 2013, The Astrophysical Journal, 779, 134, doi: 10.1088/0004-637X/779/2/134
Seok, J. Y., Koo, B.-C., Onaka, T., et al. 2008, Publications of the Astronomical Society of Japan, 60, S453, doi: 10.1093/pasj/60.sp2.S453
Shklovskii, I. S. 1960, Soviet Astronomy, 4, 243. https://ui.adsabs.harvard.edu/abs/1960SvA....4..243S
—. 1962, Soviet Astronomy, 6, 162. https://ui.adsabs.harvard.edu/abs/1962SvA....6..162S
Silverman, B. 1986, Density Estimation for Statistics and Data Analysis (London: Taylor and Francis)
Smith, R. C., Chu, Y.-H., Mac Low, M.-M., et al. 1994, The Astronomical Journal, 108, 1266, doi: 10.1086/117152
Smith, R. C., & MCELS Team. 1999, in IAU Symposium, ed. Y.-H. Chu, N. Suntzeff, J. Hesser, & D. Bohlender,

Vol. 190, 28
Snowden, S. L., Collier, M. R., & Kuntz, K. D. 2004, The Astrophysical Journal, 610, 1182, doi: 10.1086/421841
Snowden, S. L., & Kuntz, K. D. 2023, Cookbook for Analysis Procedures for XMM-Newton EPIC Observations of Extended Objects and the Diffuse Background, version 21.0. https://heasarc.gsfc.nasa.gov/FTP/xmm/software/xmm-esas/xmm-esas.pdf
Snowden, S. L., Mushotzky, R. F., Kuntz, K. D., et al. 2008, Astronomy & Astrophysics, 478, 615, doi: 10.1051/0004-6361:20077930
Spiga, D. 2005, PhD Thesis, University of Milano Bicocca. http://www.brera.inaf.it/~canestrari/Thesis-X-ray/PhD_Thesis_Daniele_Spiga.pdf
Stiele, H., Pietsch, W., Haberl, F., et al. 2011, Astronomy & Astrophysics, 534, A55, doi: 10.1051/0004-6361/201015270
Strüder, L., Briel, U., Dennerl, K., et al. 2001, Astronomy & Astrophysics, 365, L18, doi: 10.1051/0004-6361:20000066
Tanabashi, M., Hagiwara, K., Hikasa, K., et al. 2018, Phys. Rev. D, 98, 030001, doi: 10.1103/PhysRevD.98.030001
Tang, S., & Wang, Q. D. 2005, The Astrophysical Journal, 628, 205, doi: 10.1086/430875
Tang, X., & Chevalier, R. A. 2016, Monthly Notices of the Royal Astronomical Society, 465, 3793, doi: 10.1093/mnras/stw2978
Taylor, G. I. 1946, Proceedings of the Royal Society of London. Series A, Mathematical and Physical Sciences, 186, 273, doi: 10.1098/rspa.1946.0043
—. 1950a, Proceedings of the Royal Society of London. Series A, Mathematical and Physical Sciences, 201, 159, doi: 10.1098/rspa.1950.0052
—. 1950b, Proceedings of the Royal Society of London. Series A, Mathematical and Physical Sciences, 201, 175, doi: 10.1098/rspa.1950.0053
Treumann, R. A. 2009, Astronomy and Astrophysics Review, 17, 409, doi: 10.1007/s00159-009-0024-2
Truelove, J. K., & McKee, C. F. 1999, The Astrophysical Journal Supplement Series, 120, 299, doi: 10.1086/313176
Turner, M. J. L., Abbey, A., Arnaud, M., et al. 2001, Astronomy & Astrophysics, 365, L27, doi: 10.1051/0004-6361:20000087
Tutukov, A. V., & Yungelson, L. R. 1981, Nauchnye Informatsii, 49, 3
Tüllmann, R., Gaetz, T. J., Plucinsky, P. P., et al. 2011, The Astrophysical Journal Supplement Series, 193, 31, doi: 10.1088/0067-0049/193/2/31
Urošević, D., Pannuti, T. G., Duric, N., et al. 2005, Astronomy & Astrophysics, 435, 437, doi: 10.1051/0004-6361:20042535
van der Marel, R. P. 2004, The Large Magellanic Cloud: Structure and Kinematics, arXiv. http://arxiv.org/abs/astro-ph/0404192
van der Marel, R. P., Alves, D. R., Hardy, E., et al. 2002, The Astronomical Journal, 124, 2639, doi: 10.1086/343775
VanSpeybroeck, L. P., & Chase, R. C. 1972, Appl. Opt., 11, 440, doi: 10.1364/AO.11.000440
Vink, J. 2011, The Astronomy and Astrophysics Review, 20, doi: 10.1007/s00159-011-0049-1
—. 2020, Physics and Evolution of Supernova Remnants (Springer International Publishing), doi: 10.1007/978-3-030-55231-2
Virtanen, P., Gommers, R., Oliphant, T. E., et al. 2020, Nature Methods, 17, 261, doi: 10.1038/s41592-019-0686-2
von Neumann, J. 1947, Blast Wave Calculations, Tech. Rep. 7, Part II, Chapter 2, Los Alamos Scientific Laboratory
—. 1963, in Collected Works, ed. A. H. Taub (New York: Pergamon), 219–XXX
Wang, B., & Han, Z. 2012, New Astronomy Reviews, 56, 122, doi: 10.1016/j.newar.2012.04.001
Webbink, R. F. 1984, The Astrophysical Journal, 277, 355, doi: 10.1086/161701
Weinberg, S. 1977, The First Three Minutes: A Modern View of the Origin of the Universe (New York: Basic Books), 224
Weisskopf, M. C., Tananbaum, H. D., Speybroeck, L. P. V., et al. 2000, in X-Ray Optics, Instruments, and Missions III, ed. J. E. Truemper & B. Aschenbach, Vol. 4012, International Society for Optics and Photonics (SPIE), 2 – 16, doi: 10.1117/12.391545
Werner, W. 1977, Appl. Opt., 16, 764, doi: 10.1364/AO.16.000764
Westerlund, B. 1997, The Magellanic Clouds, Cambridge Astrophysics (Cambridge University Press). https://books.google.de/books?id=OSiPrgHFOYUC
Westerlund, B. E., & Mathewson, D. S. 1966, Monthly Notices of the Royal Astronomical Society, 131, 371, doi: 10.1093/mnras/131.3.371
Whelan, J., & Iben, Icko, J. 1973, The Astrophysical Journal, 186, 1007, doi: 10.1086/152565
White, R. L., & Long, K. S. 1991, Astrophysical Journal, Part 1 (ISSN 0004-637X), vol. 373, June 1, 1991, p.

543-555., 373, 543
Williams, B. F., Wold, B., Haberl, F., et al. 2015, The Astrophysical Journal Supplement Series, 218, 9, doi: 10.1088/0067-0049/218/1/9
Williams, R. M., Chu, Y.-H., Dickel, J. R., et al. 1999, The Astrophysical Journal Supplement Series, 123, 467, doi: 10.1086/313246
Wilms, J., Allen, A., & McCray, R. 2000, The Astrophysical Journal, 542, 914, doi: 10.1086/317016
Wolter, H. 1952a, Annalen der Physik, 445, 94, doi: 10.1002/andp.19524450108
—. 1952b, Annalen der Physik, 445, 286, doi: 10.1002/andp.19524450410
Woltjer, L. 1972, Annual Review of Astronomy and Astrophysics, 10, 129, doi: 10.1146/annurev.aa.10.090172.001021
Woosley, S., & Janka, T. 2005, Nature Physics, 1, 147, doi: 10.1038/nphys172
Woosley, S. E., & Bloom, J. S. 2006, Annual Review of Astronomy and Astrophysics, 44, 507, doi: 10.1146/annurev.astro.43.072103.150558
XMM-Newton SOC. 2023, XMM-Newton Users Handbook, Issue 2.21 edn., ESA. https://xmm-tools.cosmos.esa.int/external/xmm_user_support/documentation/uhb/XMM_UHB.pdf
Yew, M., Filipović, M. D., Stupar, M., et al. 2021, Monthly Notices of the Royal Astronomical Society, 500, 2336, doi: 10.1093/mnras/staa3382
Zangrandi, F., Jurk, K., Sasaki, M., et al. 2024, First Study of the Supernova Remnant Population in the Large Magellanic Cloud with eROSITA, arXiv. http://arxiv.org/abs/2401.17307
Zyla, P. A., Barnett, R. M., Beringer, J., et al. 2020, Progress of Theoretical and Experimental Physics, 2020, 083C01, doi: 10.1093/ptep/ptaa104


SNR
model
ejecta
distribution
optical
phase
ISM
MCSNR
different
reverse shock
pressure
time
region
background
Galactic
MTL
data
energy
density
observed
based
green
radio
show
velocity
SN
first
particle
result
transition
size
forward shock
ray Evolution
supernovae
CCD
value
detector
structure
galaxy
image
stellar
LMC
given
called
component
explosion
candidate
XMM Newton
Vink
Bh
mass
galaxies
radiative
Vaibhav Shukla
plasma
SNe
powerlaw
two
temperature
electron
scale
using
II
radiation
emission
well
progenitor
shock radius
known
error
thermal
due
calculated
gas
high
photon
line
will
supernova remnant
large
function
interaction
work
study
set
observation
evolution
constant
radius
spectra
left
following
population
properties
spectrum neutrino
shown
keV
core
one
although
LMC SNR
along
type
pn
number
solution
used
imaging
give
current
Table
follow
total
solar
lead
estimate
shell
process
around
right
SNRpy
mirror
remnant
densities
need
explosion energy
Sedov Taylor
seen
discussed
tion
star
See
source
shock
range
age
point
analysis
confirmed
parameter
sample
red
many
mean
use
found
plot
pc
WD
case
absorption
Studies
object
respectively
matter
processes
low
new
EPIC
spectral
small
three
within
free
form
time
pressure
MCSNR
Rfs
survey
M16
expansion
hot
e g
v
Mej
B17
1
d
band
XMM
cm
Thus
typical
n0
example
astrophysical
medium
u
t
o

Declaration of Authorship

I hereby declare that I have authored this work independently and have not used any sources or aids other than those stated.

....

Place, Date *Vaibhav Shukla*